IDENTIFICATION OF THE DEGRADATION MECHANISMS OF ORGANIC SOLAR CELLS: ACTIVE LAYER AND INTERFACIAL LAYERS

by

ISABEL FRAGA DOMÍNGUEZ

Doctor of Philosophy

ASTON UNIVERSITY

October 2015

**IDENTIFICATION OF THE DEGRADATION MECHANISMS OF ORGANIC SOLAR CELLS:
ACTIVE LAYER AND INTERFACIAL LAYERS**

Organic Solar Cells (OSCs) represent a photovoltaic technology with multiple interesting application properties. However, the establishment of this technology into the market is subject to the achievement of operational lifetimes appropriate to their application purposes. Thus, comprehensive understanding of the degradation mechanisms occurring in OSCs is mandatory in both selecting more intrinsically stable components and/or device architectures and implementing strategies that mitigate the encountered stability issues.

Inverted devices can suffer from mechanical stress and delamination at the interface between the active layer, *e.g.* poly(3-hexylthiophene):[6,6]-phenyl-C61-butyric acid methyl ester (P3HT:PCBM), and the hole transport layer, *e.g.* poly(3,4-ethylenedioxythiophene):poly(*p*-styrene sulfonate) (PEDOT:PSS). This work proposes the incorporation of a thin adhesive interlayer, consisting of a diblock copolymer composed of a P3HT block and a thermally-triggerable, alkyl-protected PSS block. In this context, the synthesis of poly(neopentyl *p*-styrene sulfonate) (PNSS) with controlled molar mass and low dispersity (Đ ≤ 1.50) *via* Reversible Addition-Fragmentation chain Transfer (RAFT) polymerisation has been extensively studied. Subsequently, Atomic Force Microscopy (AFM) was explored to characterise the thermal deprotection of P3HT-*b*-PNSS thin layers to yield amphiphilic P3HT-*b*-PSS, indicating that surface deprotection prior to thermal treatment could occur. Finally, structural variation of the alkyl protecting group in PSS allowed reducing the thermal treatment duration from 3 hours (P3HT-*b*-PNSS) to 45 minutes for the poly(isobutyl *p*-styrene sulfonate) (PiBSS) analogous copolymer.

Another critical issue regarding the stability of OSCs is the sunlight-driven chemical degradation of the active layer. In the study herein, the combination of experimental techniques and theoretical calculations has allowed identification of the structural weaknesses of poly[(4,4'-bis(2-ethylhexyl) dithieno [3,2-b:2',3'-d]silole)-2,6- diyl-*alt*-(4,7-bis(2-thienyl)-2,1,3-benzothiadiazole)-5,5'-diyl], Si-PCPDTBT, upon photochemical treatment in air. Additionally, the study of the relative photodegradation rates in air of a series of polymers with systematically modified backbones and/or alkyl side chains has shown no direct correlation between chemical structure and stability. It is proposed instead that photostability is highly dependent on the crystalline character of the deposited films. Furthermore, it was verified that photostability of blends based on these polymers is dictated by the (de)stabilising effect that [6,6]-phenyl-C61-butyric acid methyl ester (PCBM) has over each polymer. Finally, a multiscale analysis on the degradation of solar cells based on poly[4,4' bis(2-ethylhexyl) dithieno[3,2-b:2',3'-d]silole)-2,6-diyl-*alt*-[2,5 bis(3 tetradecylthiophen 2-yl)thiazole[5,4-d]thiazole)-1,8-diyl] and PCBM, indicated that by judicious selection of device layers, architectures, and encapsulation materials, operational lifetimes up to 3.3 years with no efficiency losses can be successfully achieved.

Keywords: organic solar cells, poly(neopentyl *p*-styrene sulfonate), RAFT, photostability, low bandgap polymer

Preamble

This thesis has been developed in the frame of the European-funded ESTABLIS project, a cross-sectoral network combining academic and industrial partners working towards the improvement of the stability of Organic Photovoltaics.

In this context, this specific PhD thesis has been a co-tutelle in between the Université Blaise Pascal in Clermont-Ferrand (France) and Aston University in Birmingham (United Kingdom), integrating work on Degradation Studies (40 %), Polymer Characterisation (35 %) and Synthetic Polymer Chemistry (25 %).

Some of the studied materials and results discussed in this thesis have been obtained in collaboration with other ESTABLIS partners and fellows, namely: Joanna Kolomanska and Dr Harikrishna Erothu from Aston University; Dr Andreas Distler from Belectric OPV; Dr Graham E Morse from Merck Chemicals; and Alberto Gregori, Dr Christine Dagron-Lartigau and Dr Didier Bégué from Université de Pau et des Pays de l'Adour. The author acknowledges the Maxime Defour, PhD student at the Vrije Universiteit Brussel, for performing the RHC measurements, and Camille Bertrand, M2 student at the ICCF, for his collaboration in the degradation studies on polymer and blend films.

Acknowledgements

Table of contents

Abbreviations

[ ]	concentration
°	degree
°C	degree Celsius
1-MN	1-methylnaphtalene
$^1O_2$	singlet oxygen
$^3O_2$	triplet oxygen
Å	ångström
Abs	absorbance
AFM	atomic force microscopy
Ag	silver
AIBN	2,2'-azobis(2-methylpropionitrile)
Al	aluminum
AL	active layer
Al_2O_3	aluminum oxide
ALT	accelerated ifetime test
AM 1.5	air mass 1.5
atm	standard atmosphere
ATR	attenuated total reflectance
ATRP	atom transfer radical polymerisation
BDE	bond dissociation energy
BDT	benzodithiophene
bis-$PC_{60}BM$	bis-substituted [6,6]-phenyl-C61-butyric acid methyl ester
bis-$PC_{70}BM$	bis-substituted [6,6]-phenyl-C71-butyric acid methyl ester
BST	black standard temperature
BT	benzothiadiazole
BTTC-N_3	2-azidoethyl 3-benzylsulfanylthiocarbonylsulfanylpropionate
C	carbon
χ	Flory-Huggins parameter
Ca	calcium
CaF_2	calcium fluoride
CAR/PDMS	carboxen-polydimethylsiloxane
CB	2-chloro-1,3-butadiene
$CDCl_3$	chloroform-d
cm	centimeter
C-PCPDTBT	poly[2,6-(4,4-bis(2-ethylhexyl)-4H-cyclopenta[2,1-b;3,4-b']dithiophene)-*alt*-4,7-(2,1,3-benzothiadiazole)]

CPDT	cyclopentadithiophene
CRP	controlled radical polymerisation
CsF	caesium fluoride
CTA	chain transfer agent
CTC	charge transfer complex
Cu	copper
CuI	copper(I) iodide
Δ	heat
Đ	dispersity
DCB	double cantilever beam
DCC	*N,N'*-dicyclohexylcarbodiimide
DCM	dichloromethane
ΔE	energy difference
DFT	density functional theory
DIPEA	N,N-diisopropylethylamine
dm	decimeter
DMAP	4-dimethylaminopydridine
DMF	dimethylformamide
D_p	degree of polymerisation
DPP	diketopyrrolopyrrole
DPPTT-T	thieno[3,2-b]thiophene–diketopyrrolo-pyrrole
D_p^{th}	theoretical degree of polymerisation
DSC	differential scanning calorimeter/calorimetry
DTBT	dithienylbenzothiadiazole
DTS	dithienosilole
DTTC-N_3	2-azidoethyl 2-(dodecylthiocarbonothioylthio)-2-methylpropionate
e	elementary charge
E	energy
e^-	electron
e.g.	"*exempli gratia*" - for example
E_g	energy/electronic bandgap
EPR	electron paramagnetic resonance
EQE	external quantum efficiency
ER	experienced researcher
ESR	early stage researcher
et al.	"*et alii*" - and others
ETL	electron transport layer
eV	electronvolt

f	volume fraction / initiator efficiency
FF	fill factor
FTIR	fourier transform infrared
FTO	fluorine-doped tin oxide
g	gram
G_c	fracture energy
GC-MS	gas chromatography/mass spectrometry
GHz	gigahertz
GPa	gigapascal
GPC	gel permeation chromatography
H	hydrogen
h	hour
h^+	hole
H_2O	water
HCl	hydrochloric acid
Hg	mercury
HOMO	highest occupied molecular orbital
HPLC	high-performance liquid chromatography
HS-SPME	headspace solid-phase microextraction
HTL	hole transport layer
$h\upsilon$	light
Hz	hertz
I	initiator
i.e.	"*id est*" - that is to say
ICBA	indene-C60 bis-adduct
ICT	intramolecular charge transfer
In_2O_3:Sn	indium tin oxide
IR	infrared
ISC	intersystem crossing
ITO	indium tin oxide
j	current density
J	joule
j_{photo}	photocurrent
j_{sc}	short circuit current density
K	kelvin
k	Boltzmann's constant / reaction constant
k_{add}	addition rate constant
k_{app}	apparent rate of polymerisation
k_β	fragmentation rate constant
kbar	kilobar

KBr	potassium bromide
kcal	kilocalorie
k_d	decomposition rate coefficient
kg	kilogram
kHz	kilohertz
km	kilometer
k_p	propagation rate constant
kPa	kilopascal
k_t	termination rate coefficient
LAM	less activated monomer
LiAc	lithium acetate
LiF	lithium fluoride
LUMO	lowest unoccupied molecular orbital
m	meter
M	molar
mA	milliampere
MAM	more activated monomer
m_{CTA}	relative molar mass of the CTA
MDMO-PPV	poly[2-methoxy-5-(3',7'-dimethyloctyloxy)-1,4-phenylenevinylene]
MEH-PPV	poly[2-methoxy-5-(2-ethylhexyloxy)-1,4-phenylenevinylene]
MeOH	methanol
meV	millielectronvolt
MFT	mean-field theory
mg	milligram
MHz	megahertz
min	minute
mL	milliliter
mm	millimeter
m_M	monomer relative molar mass
mmHg	millimeter of mercury
mmol	millimole
M	monomer
M_n	number average molar mass
M_n^{th}	theoretical molar mass
mol	mole
MoO_3	molybdenum trioxide
MPa	megapascal
M_{PP}	maximum power point
M_w	weight average molar mass

N	degree of polymerisation / Newton / nitrogen
N_2	nitrogen
N_c	effective density of states
NH_3	ammonia
n_i	ideality factor
NIR	near infrared
nm	nanometer
NMP	nitroxide-mediated polymerisation
NMR	nuclear magnetic resonance
nN	nanonewton
N_{Ph}	photon flux density
NSS	neopentyl *p*-styrene sulfonate
O_2	oxygen
O_2^-	superoxide
ODCB	ortho-dichlorobenzene
OE	outdoor exposure
OECT	organic electrochemical transistor
OLED	organic light emitting diode
OSC	organic solar cell
P	polymer
P3HT	poly(3-hexylthiophene)
P3HT-*b*-PSS	poly(3-hexylthiophene)-*block*-poly(*p*-styrene sulfonate)
Pa	pascal
PBD	polybutadiene
PBDTTPD	poly(benzo[1,2-b:4,5-b']-dithiophene–thieno[3,4-c]pyrrole-4,6-dione)
PBSS	poly(n-butyl *p*-styrene sulfonate)
$PC_{60}BM$/PCBM	[6,6]-phenyl-C61-butyric acid methyl ester
$PC_{70}BM$	[6,6]-phenyl-C71-butyric acid methyl ester
PCDTBT	poly[N-9'-hepta-decanyl-2,7-*alt*-carbazole-5,5-(4',7'-di-2-thienyl-2',1',3'-benzo-thiadiazole)
PCE	power conversion efficiency
PDPPTT-T	poly(thieno[3,2-*b*]thiophene–diketopyrrolopyrrole)
PDTSTzTz	poly[4,4' bis(2-ethylhexyl)dithieno[3,2-b:2',3'-d]silole)-2,6-diyl-alt-[2,5-bis(3-tetradecylthiophen 2-yl)thiazole[5,4-d]thiazole)-1,8-diyl]
PE	polyethylene
PEDOT	poly(3,4-ethylenedioxythiophene)
PEI	polyethyleneimine
PEN	poly(ethylene naphthalate)
PET	poly(ethylene terephthalate)
PiBSS	poly(isobutyl *p*-styrene sulfonate)

P_{IN}	incident radiant power
PiPrSS	poly(isopropyl *p*-styrene sulfonate)
PNSS	poly(neopentyl p-styrene sulfonate)
P_{OUT}	maximum power output
P_{oxid}	polymer photooxidation
PP	polypropylene
ppm	parts per million
PPrSS	poly(n-propyl *p*-styrene sulfonate)
PPSS	poly(n-pentyl *p*-styrene sulfonate)
PPV	polyphenylenevinylene
PS	polystyrene
PSS	poly(*p*-styrenesulfonate)
PTB7	poly(thieno[3,4-*b*]thiophene-benzodithiophene)
PTB7-Th	poly[4,8-bis(5-(2-ethylhexyl)thiophen-2-yl)benzo[1,2-b;4,5-b']dithiophene-2,6-diyl-alt-(4-(2-ethylhexyl)-3-fluorothieno[3,4-b]thiophene-)-2-carboxylate-2-6-diyl)]
PTFE	polytetrafluoroethylene
QNM	quantitative nanomechanics
R	leaving/protecting group
RAFT	reversible addition-fragmentation chain transfer
RHC	rapid heat-cool calorimetry / rapid heat-cool differential scanning calorimeter
ROMP	ring-opening metathesis polymerisation
R_p	parallel or shunt resistance
r_p	polymerisation rate
R_q	roughness
R_s	serial resistance
S	sulfur
S_0	singlet ground state
S_1, S_2, …, S_N	singlet excited states
SF	stabilising factor
SF_4	sulfur tetrafluoride
Si	silicon
Si-CPDT	silicon-cyclopentadithiophene
Si-PCPDTBT	poly[(4,4'-bis(2-ethylhexyl)dithieno[3,2-b:2',3'-d]silole)-2,6-diyl-*alt*-(4,7-bis(2-thienyl)-2,1,3-benzo-thiadiazole)-5,5'-diyl]
SnO_2:F	fluorine-doped tin oxide
SPM	scanning probe microscope
T	temperature
t	time
T_1	first triplet excited state
TCO	transparent conducting oxide

TEA	triethylamine
T_g	glass transition temperature
TGA	thermogravimetric analysis/analyser
THF	tetrahydrofuran
TIC	total ion count
TiO_x	titanium oxide
T_m	melting peak temperature
TMS	trimethylsilane
TPD	thieno[3,4-c]pyrrole-4,6-dione
TzTz	thiazolothiazol
UV	ultraviolet
V	volt or voltage
v	volume
V_2O_5	vanadium pentoxide
Vis	visible
V_{oc}	open circuit voltage
W	watt
w	weight
WO_3	tungsten trioxide
WVTR	water vapor transmission rate
XL	crosslinking product
XRD	x-ray diffraction
Z	stabilising group
ZnO	zinc oxide
γ	Langevin recombination constant
δ	chemical shift
η_A	light absorption efficiency
η_{CC}	carrier collection efficiency
η_{ED}	exciton diffusion efficiency
η_{EQE}	external quantum efficiency
θ	contact angle
ϑ_e	equilibrium contact angle
λ	wavelength
μL	microliter
μm	micrometer
μmol	micromole
$\tilde{v}$	wavenumber
Ω	ohm

List of Equations

List of Figures

List of Schemes

List of Tables

General Introduction

The increasing world energy demand has created a dependence upon non-renewable sources that is no longer sustainable. In addition to the cost and limited supply of these resources, their use has incredibly negative effects for the environment. Consequently, increasing attention has been paid over the last two decades to the production of energy from renewable sources, such as wind, hydroelectric, biofuels or sunlight. Among them, sunlight has the highest theoretical potential; in fact, the Earth receives in one hour the necessary energy to supply the human energy consumption needs for a whole year.[1]

Indeed, multiple photovoltaic technologies are currently available to convert sunlight into electricity, such as silicon (Si), gallium arsenide (GaAs), cadmium telluride (CdTe), perovskites, and Organic Solar Cells (OSCs). Among them, OSCs have emerged as an attractive alternative due to the interesting application properties associated with the use of light-absorbing organic semiconductors, *i.e.* flexibility, lightweight, semi-transparency, solution processability, freedom of shape, coloration and low cost.[2] Not in vain, the properties of organic semiconductors have been exploited in other branches of optoelectronics, such as organic electrochemical transistors (OECTs),[3] and organic light emitting diodes (OLEDs).[4] However, OSCs display major drawbacks which impede their broad commercialisation, namely the low power conversion efficiencies (≤ 11.5 %)[5] compared to their inorganic counterparts (≤ 25 % for single-crystal silicon cells),[5] and limited device lifetimes.[6-8]

Whilst most of the research efforts have been focused on the improvement of OSC device performance,[9] less attention has been paid to increasing the operational lifetime of these devices.[6] Degradation pathways in these devices are manifold, and comprise, among others, (photo)chemical and morphological changes in the active layer,[6-7, 10] delamination between layers,[11-12] and oxidation of the metal electrodes.[13-14] Furthermore, the electrical performance of OSCs is strongly affected by the presence extrinsic triggers like oxygen and water,[8, 15-16] to such an extent that device stability (and cost) is ultimately determined by the quality of the employed encapsulation materials. Since the competitiveness of organic solar cells as photovoltaic technology requires a correct balance among efficiency, stability and cost, the fabrication of devices with higher intrinsic stabilities is of prime importance.[17]

The work herein has been developed in the frame of the European-funded ESTABLIS project (Ensuring Stability in Organic Solar Cells), an initial training network of industrial and academic research groups in Europe aiming at the development of organic solar cells with 10-year lifetimes. To this end, the ESTABLIS research team has worked towards the scientific objectives of both clarifying the manifold degradation mechanisms occurring in OSCs *via* combination of experimental results and theoretical calculations, and producing novel materials that overcome the identified stability issues. Among the different sources of instability in OSCs, this dissertation addresses the interfacial adhesion and delamination issues between the active layer and the hole transport layer,[11] and the photochemical degradation of the active layer.[6-7, 10]

The manuscript is organised as follows. Chapter 1 firstly introduces the theoretical aspects necessary to understand the work developed in this thesis, namely the working principle, materials and electrical characterisation of organic solar cells. After which, the role of the active materials and interlayers towards the fabrication of more efficient solar cells is examined, and main degradation mechanisms in organic solar cells are summarised. Chapter 2 explores the synthesis and application of block copolymers as thin interfacial layers to enhance adhesion at the interface between the active layer and PEDOT:PSS. The proposed material, the amphiphilic block copolymer poly(3-hexylthiophene)-*block*-poly(*p*-styrene sulfonate) (P3HT-*b*-PSS), has been selected so that each of the constituting blocks is similar to either a component in the active layer (P3HT block) or a component in the hole transport layer (PSS block). More specifically, the work focuses on the understanding and optimisation of the controlled polymerisation of an alkyl-protected precursor of the PSS block, the surface characterisation of the block copolymer interlayer and the variation of the alkyl-protection on the PSS block to reduce the duration of the thermal treatment necessary for the deprotection of the material. Finally, Chapters 3 and 4 are devoted to the analysis of the photochemical stability of the active layer components, focusing on the photostability of low bandgap polymers synthesised to make better use of the solar spectrum. To this end, Chapter 3 is firstly dedicated to the elucidation of the structural changes occurring upon photooxidation of poly[(4,4'-bis(2-ethylhexyl)dithieno[3,2-b:2',3'-d]silole)-2,6-diyl-*alt*-(4,7-bis(2-thienyl)-2,1,3-benzothiadiazole)-5,5'-diyl], (Si-PCPDTBT). After which, in an attempt to establish a relationship among chemical structure, physicochemical properties and photostability, the photochemical stability of Si-PCPDTBT is compared to that of a series of low bandgap polymers whose backbones and/or side chains have been systematically modified. Finally, Chapter 4 constitutes a multiscale approach to the degradation

of solar cells based on one of the materials in the aforementioned polymer series; a low bandgap polymer constituted by a dithienosilole donor unit and thiazolothiazol as acceptor. Accordingly, chemical and morphological changes in the neat polymer and when blended with PCBM have been probed under a range of conditions, namely thermal stress and natural/artificial photochemical degradation. These results are subsequently compared to the electrical characterisation of the solar cells exposed to illumination using accelerated ageing conditions.

Chapter 1. Organic Solar Cells: Working Principle and Limitations

1.1. Introduction

This chapter discusses fundamental theoretical aspects to understand and contextualise the work contained in this manuscript. Firstly, Organic Solar Cells (OSCs) and their working principles are introduced from a historical point of view, reporting on commonly employed materials and device configurations and describing the electrical characterisation of the cells. The role of the active materials (electron donor and acceptor) and interlayers towards the fabrication of highly efficient solar cells is subsequently examined. Finally, the chapter concludes with an overview of commonly reported degradation mechanisms in OSCs, and briefly introducing the two main stability issues addressed in this work, namely the photochemical degradation of the active layer and interfacial problems detected between the active layer and hole transport layer in inverted devices.

1.2. Organic solar cells

1.2.1. Historical background and working principle

The photovoltaic effect, *i.e.* the creation of current in a material upon exposure to light, was first reported by Becquerel in 1839.[18] In his experiments, small electrical currents were generated when platinum electrodes covered with silver chloride in contact with an acidic solution were exposed to illumination. Later on, in 1873, photoconductivity was also observed in solid systems, namely selenium compounds.[19] Early reports on the photoconductivity of organic compounds date back to the beginning of the 20th century, with the discovery of this property in anthracene molecules.[20] Although conduction along polymer backbones was already reported in the 60s,[21] probably more notable is the finding of Shirakawa, Heeger and MacDiarmid in 1977 who observed increased conductivities when polyacetylene was doped with halogens. They were awarded with the Nobel Prize in Chemistry in 2000 thanks to this ground-breaking discovery.[22]

The basis for conductivity in organic compounds is the so-called conjugation, that is to say the alternation of double and single carbon bonds promoting electron delocalisation (see Figure 1.1). Increasing the numbers of alternating bonds leads to the formation of two band-like orbital groups, one comprising the lower energy bonding π molecular orbitals and other constituted by the antibonding π^*orbitals. For sufficiently high degrees of conjugation, the energy bandgap (E_g), namely the difference between the Highest Occupied Molecular Orbital (HOMO) and the Lowest Unoccupied Molecular Orbital (LUMO), can be overcome by light absorption in the visible wavelength range, thus making these organic materials a very interesting choice for photovoltaic applications.

Figure 1.1 illustrates the reduction of the energy bandgap with increasing conjugation lengths. Electronic transition between these two levels leads to the creation of a singlet exciton (a coulombically bound electron-hole pair), which, for the purpose of organic photovoltaics, needs to be subsequently dissociated into free charges, which must then be extracted to create photocurrent.
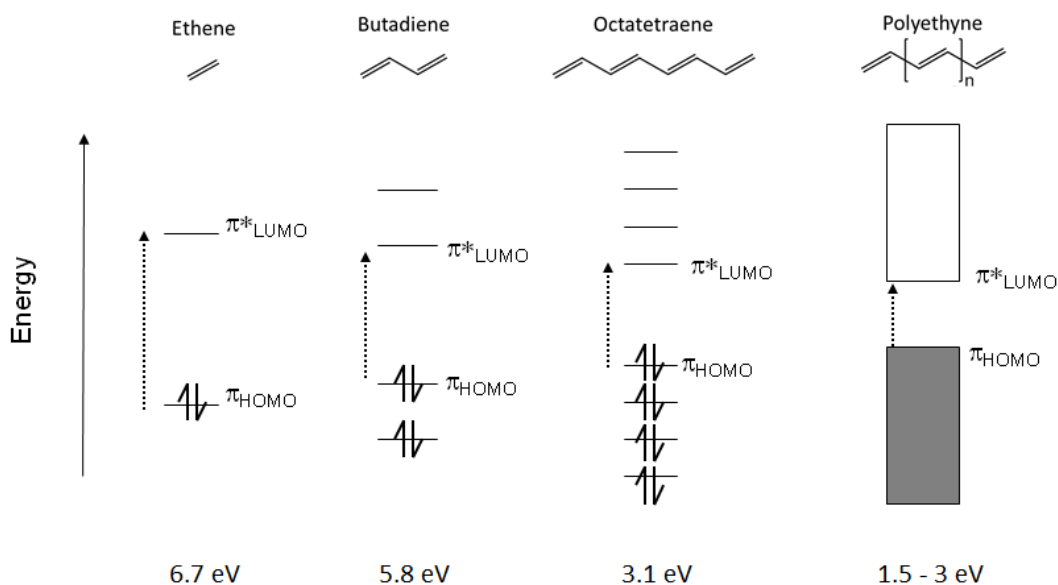
Figure 1.1. Charge delocalisation *via* conjugation in semiconductive polymers. Adapted from reference 23.

The first organic solar cells were based on a monolayer of a conductive material, sandwiched between two electrodes of different work functions. However, these cells exhibited very low performances (below 1%), mainly due to the unfavourable dissociation of the created excitons under these conditions.[24] In organic semiconductors, the binding energy of the created excitons is usually 0.5-1 eV,[25] higher than for their inorganic counterparts (*e.g.* 100 meV for crystalline silicon).[26] Thus, exciton dissociation is unlikely to occur unless it is thermally induced or unless a second material (in this case, the contact electrode) works as an 'electron acceptor', breaking up the excitons into free carriers. Concerning the first, and assuming that the cell achieved 150 °C (423 K) under operating conditions, the corresponding thermal energy (kT = 0.04 eV) would still be insufficient to overcome the exciton binding energy. Secondly, the exciton diffusion length is typically 10 nm,[27] whereas maximum absorption of the incident light is only achieved when the thickness of the conductive layer is above 100 nm. Therefore, in such a monolayer configuration, even if the totality of the excitons could

be created, only a small fraction of them, formed in the vicinity of the electrode, would actually undergo dissociation.
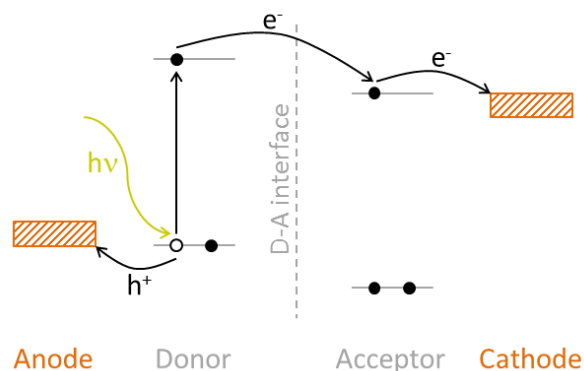
Figure 1.2. Scheme of the working principle of organic photovoltaics.

With the development of bilayer solar cells, the layer of the conjugated 'electron donor' was completed with a second adjacent layer consisting of a strongly electronegative 'electron acceptor'.[28] Roughly speaking, if the energetic characteristics of this second material favour the charge transfer necessary for the exciton to dissociate, the electron will move to the acceptor material, whilst a positive charge or hole will remain on the donor. Subsequently, extraction of these charge carriers towards the respective electrodes leads to the creation of the electrical current. This process, depicted in Figure 1.2, is the working principle of organic solar cells.

In greater detail, the charge generation process consists of a sequence of steps whose success relies on maximising the conversion of photons into extractable electrons (see Figure 1.3). The single processes occurring can be summarised as:

(1) Electronic excitation of the donor to generate a single exciton

(2) Exciton diffusion towards the donor/acceptor interface

(3) Charge transfer from the exciton to the acceptor and formation of an e^-/h^+ polaron pair

(4) Dissociation of the polaron pair into free charges

(5) Charge transport towards the electrodes and charge collection

(1) Exciton generation   (2) Exciton difussion

(3) Exciton dissociation   (4) Polaron dissociation
and polaron pair formation   (5) Transport and collection of free charges
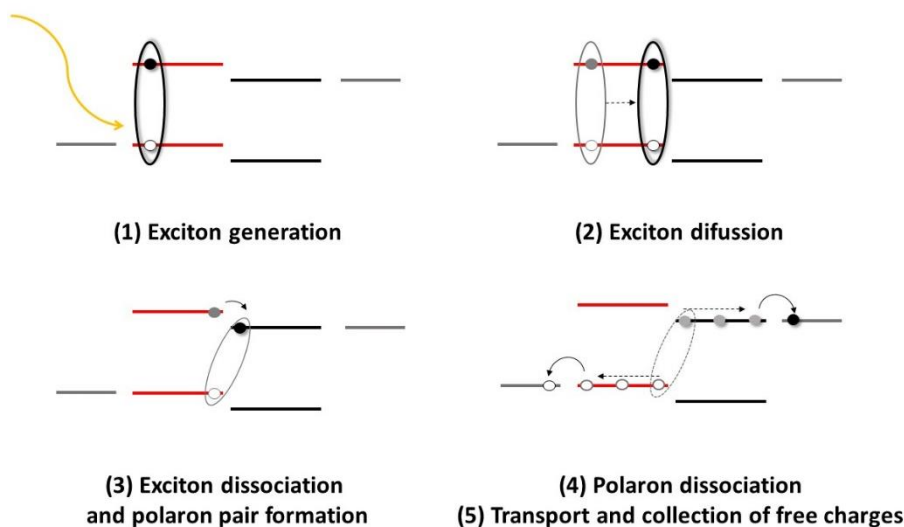
Figure 1.3. Charge generation process in organic solar cells. Adapted from reference 29.

Although the donor/acceptor bilayer conformation delivered an improvement from previous cells, the achieved performances were still very much limited (~1 %).[28] Firstly, exciton creation (1) has to take place within a distance of 10 nm relative to the acceptor to enable sufficient diffusion (2) to contribute to the charge transfer process (3). Secondly, dissociation of the polaron pair intro free charges (4) and their subsequent transport towards the electrodes (5) is favoured by the existence of undisturbed pathways of donor and acceptor, allowing charges to finally reach the electrodes. Although this latter requirement is fully covered by this bilayer disposition, the limited interface between donor and acceptor accounts for the overall poor charge generation.

The development of the bulk-heterojunction (see Figure 1.4) was able to simultaneously fulfil the requirements of sufficient light absorption, and suitable exciton diffusion and charge transport.[30] This concept implies the creation of an interpenetrating network of donor and acceptor domains on a nanometre length scale, achieved by mixing both components in solution and processing them simultaneously. The efficiency of a bulk-heterojunction solar cell is thus dependent to a great extent on the achieved nanoscale organisation of the active layer, and this is, in turn, affected by numerous factors such as donor:acceptor ratio, solvent, processing conditions or post-deposition treatments.[31] Nevertheless, the bulk-heterojunction concept prevails nowadays, being the most widely applied both academically and industrially.
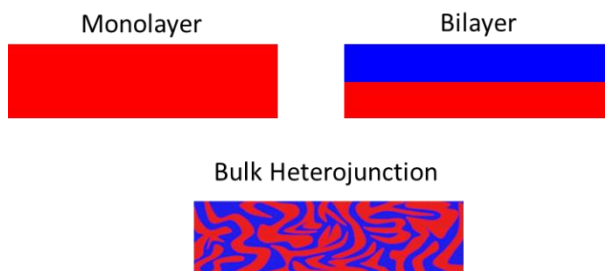
Figure 1.4. Evolution of the active layer in organic solar cells.

It must be noted that the term organic solar cells (OSCs) comprises systems employing 'small' conjugated molecules or polymers as donor components in the active layer. This works deals essentially with polymer solar cells based on the bulk heterojunction concept. Throughout the document, unless specified to the contrary, the term organic solar cells will be employed to refer to polymer-based systems.

1.2.2. Device configuration and materials

Building on the discussion in Section 1.2.1, an organic solar cell can be described as being comprised of three main components: the active layer, containing an organic semiconductor and a suitable acceptor, and two contacts (or electrodes) that deliver the generated current to an external circuit. However, to favour charge carrier flow, two more interlayers are generally implemented, finally leading to a general disposition of five different layers on a transparent glass or plastic substrate (see Figure 1.5).

On top of the substrate, and operating as the bottom electrode, is the transparent conducting oxide (TCO). Typically used TCOs are indium tin oxide (ITO, In_2O_3:Sn) and fluorine-doped tin oxide (FTO, SnO_2:F). Then, the active layer is sandwiched in between two interlayers: the electron transport layer (ETL) on one side and the hole transport layer (HTL) on the other side. These two interlayers help to avoid local shunts and direct the current by selectively directing the charges towards the correct electrode. A commonly used HTL is the ionomeric polymer mixture of poly(3,4-ethylenedioxythiophene) doped with poly(p-styrene sulfonate) (PEDOT:PSS), and the ETL is usually made of metal oxides, such as ZnO or TiO_x. The most widely studied active layer is based on poly(3-hexylthiophene) (P3HT) as the electron donor and [6,6]-phenyl-C61-butyric acid methyl ester (PCBM, also known as $PC_{60}BM$) or [6,6]-phenyl-C71-butyric acid methyl ester ($PC_{70}BM$) as the electron acceptor. Finally, a metal layer, generally calcium, aluminium or silver, serves as the top electrode.
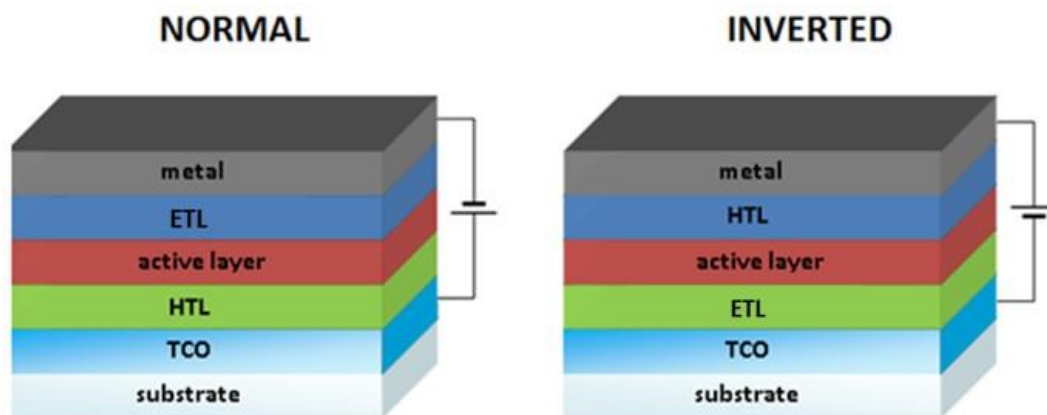
Figure 1.5. Possible device configurations in organic photovoltaic devices.

Which electrode represents the anode or the cathode depends on the order of the interlayers. This fact also leads to the distinction of two different kinds of configurations, normal and inverted, as illustrated in Figure 1.5. The normal configuration comprises the stack substrate/TCO/HTL/active layer/ETL/metal. The top electrode, usually Ca or Al, is a low-work-function metal and works as the negative electrode. The inverted configuration shows an opposite layer sequence, *i.e.* substrate/TCO/ETL/active layer/HTL/metal. In this case, the cathode is the transparent conducting electrode, and a high-work-function metal top electrode, generally Ag, works as the positive electrode. Device architectures can also significantly influence solar cell efficiencies.[9, 32] Notably, the so-called inverted structure has led to more favourable device performances, as well as improved air stabilities due to the use of Ag as top electrode.[7, 32-33] Furthermore, better use of the solar spectrum can be achieved by stacking multiple photoactive layers with complementary absorption spectra (*i.e.*, different E_g) in tandem solar cells, nowadays leading to efficiencies that exceed 10 %.[5, 9, 34]

Flexible OSCs are typically deposited on transparent poly(ethylene naphthalate) (PEN) or poly(ethylene terephthalate) (PET) films. Furthermore, as solar cells are used in ambient atmosphere, they need to be protected by a transparent encapsulation that hinders oxygen and moisture diffusion into the device. Encapsulating materials are usually multilayer films composed of alternating inorganic and organic thin layers, where the inorganic part hinders water and oxygen penetration and the organic layers smooth the coated surface, reducing the presence of nano- and micro-sized defects.

1.2.3. Device physics and characterisation

The photovoltaic performance and electrical behaviour of organic solar cells is commonly evaluated by recording their current-voltage characteristics, *i.e.* measuring the electrical response of a cell subjected to different voltages. Important characteristic parameters can be obtained from the analysis of the recorded current-voltage curves, obtained both under illumination (typically under 1000 W m^{-2} light of AM 1.5 solar spectrum at 25 °C for comparability reasons) and in the dark (see Figure 1.6).
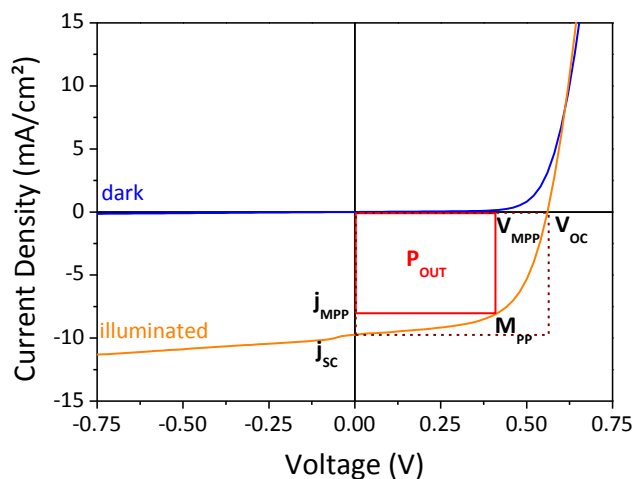
Figure 1.6. Typical illuminated (yellow) and dark (blue) curves of a solar cell. Electrical parameters employed to characterise the cell behaviour are indicated.

The intersection of the light curve with the ordinate axis represents the short circuit current density (j_{sc}), *i.e.* the photogenerated current collected at the electrodes in the absence of an externally applied voltage (V = 0). The value of j_{sc} is determined by Equation 1.1,[2] where: e is the elementary charge, N_{Ph} (λ) is the photon flux density at a wavelength λ and η_{EQE} (λ) is the external quantum efficiency at a wavelength λ.

$$j_{sc} = \int_{AM\ 1.5} e \cdot N_{Ph} \cdot (\lambda) \cdot \eta_{EQE}(\lambda)d\lambda \qquad \text{Equation 1.1}$$

Thus, j_{sc} is essentially dependent on the external quantum efficiency, EQE, which is defined as the fraction of incident photons effectively converted into electrical current and measures the efficiency of the aforementioned steps of the charge generation process, according to Equation 1.2,

where: η_A is the light absorption efficiency, η_{ED} is the exciton diffusion efficiency and η_{CC} is the carrier collection efficiency.

$$\eta_{EQE} = \eta_A \cdot \eta_{ED} \cdot \eta_{CC}$$ **Equation 1.2**

The intersection with the abscissa describes the open circuit voltage, V_{oc}, that is to say the voltage when no current flows in the circuit. V_{oc} values are mainly affected by the difference between the HOMO and the LUMO levels of the donor and acceptor, respectively. Its value is also dependent of other parameters, according to Equation 1.3:[7]

$$V_{OC} = \frac{E_g}{e} - \frac{kT}{e}\left(\frac{(1-P)\cdot\gamma\cdot N_c^2}{PG}\right)$$ **Equation 1.3**

where: E_g is the electronic bandgap, e is the elementary charge, k is the Boltzmann's constant, T the temperature, P, the dissociation of electron-hole pairs into free charges, γ, the Langevin recombination constant and N_c, the effective density of states.

The maximum power point (M_{PP}) is defined by the largest possible product of j_{MPP} and V_{MPP}, which corresponds to the maximum power output P_{OUT} of the device (red box in Figure 1.6). The ratio between the red and the dotted box is called the fill factor (FF) and describes the quality of the j-V curve shape under illumination (Equation 1.4).

$$FF = \frac{j_{MPP}\cdot V_{MPP}}{j_{SC}\cdot V_{OC}}$$ **Equation 1.4**

Finally, the Power Conversion Efficiency (PCE) of the cell is given by the ratio between the device maximum power output P_{OUT} and the incident radiant power P_{IN}, the latter being equal to the irradiance energy (W m^{-2}) multiplied by the area of the solar cell (m^2), see Equation 1.5.

$$PCE = \frac{P_{OUT}}{P_{IN}} = \frac{V_{OC}\cdot j_{SC}\cdot FF}{P_{IN}}$$ **Equation 1.5**

Although all of these parameters are obtained from the illuminated curve, the dark curve also provides with useful information. Ideally, a solar cell under dark conditions behaves like a diode, showing zero resistance against current in one direction and infinite resistance in the other; a certain threshold voltage determining the blocking and conducting regimes. Deviations from ideal behaviour of the diode can be described by an electrical model including a parallel or shunt resistance (R_p), and a serial resistance (R_s). The former, ideally of infinite value, decreases with the presence of leaks

or shorts in the device. In turn, R_s, ideally zero, represents the intrinsic resistivity of the materials in the stack or resistances created at the interfaces. Considering these factors, the electrical behaviour of the cell can be represented by a circuit model consisting of (i) a light-dependent power source, (ii) a diode and (iii) two resistors (R_s and R_p), as depicted in Figure 1.7, where n_i is the ideality factor of the diode and j_{photo} is the photocurrent.[2, 7, 35]
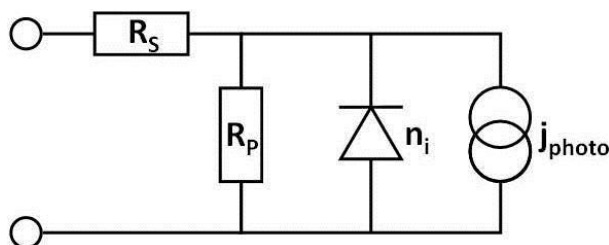
Figure 1.7. Equivalent circuit of a photovoltaic cell. Adapted from reference 2.

1.3. Materials for highly efficient solar cells

A clear requisite to the success and commercialisation of OSCs is the achievement of performances adequate to their application purposes. Maximising the efficiency is possible *via* the selection of adequate materials and device configurations that enhance the V_{OC}, j_{SC} and FF values of the cell (see Equation 1.5). For instance, V_{OC} can be tuned-up by modifying the energy levels of the donor and the acceptor materials in the active layer, and also by optimising the device layout so that shunts and leakages are reduced. High j_{sc} values can be achieved by semiconductors displaying reduced energy bandgaps, whose absorption spectra have a good match with the incident solar spectrum, ideally covering the red and near infrared electromagnetic spectrum. However, as this parameter is also related to the rest of the steps of the power conversion process, exciton diffusion, dissociation and charge transport must be ensured by achieving adequate active layer morphologies. Similarly, good FF values are obtained with optimised cells in terms of their active layer morphologies and device architectures.

This section evaluates the selection of materials for efficient solar cells, focusing on the active layer (donor and acceptor materials) and the interlayers (namely PEDOT:PSS) due to their role in the present work.

1.3.1. Donor materials

The ideal characteristics of a conjugated polymer for its use in organic solar cells comprise (i) low bandgaps to broaden the absorption range and increase j_{sc} values, (ii) low HOMO energy levels to enhance V_{OC}, (iii) suitable LUMO energy levels to ensure efficient electron transfer to the electron acceptor, (iv) crystalline characteristics to facilitate the mobility of charges, and (v) self-organising behaviour leading to appropriate molecular packing and suitable blend microstructures.[26-27] The first polymer donors were based on polyphenylenevinylenes (PPV), such as poly[2-methoxy-5-(3',7'-dimethyloctyloxy)-1,4-phenylenevinylene] (MDMO-PPV), see Table 1.1 for the structure. The absorption characteristics of these materials, limited to wavelengths below 550 nm (2.3 eV bandgap), together with low charge mobilities, account for their limited efficiencies around 3 %.[36-37] Next, polythiophene derivatives were explored; among them, the most notable being poly(3-hexylthiophene), which, with an optical bandgap of 1.9 eV, leads to efficiencies ranging 3-4.4 % depending on its regioregularity and on the chosen acceptor material.[38-39] Despite its restricted absorption to below 650 nm and the limited V_{OC} values of P3HT-based solar cells, this polymer has become a standard absorber, widely studied and employed.[38]

For the past two decades, research efforts have been made to develop polymers with smaller bandgaps and light absorption extended into the infrared.[27, 40-43] These so-called low bandgap polymers are designed with alternating 'push' and 'pull' units, that is to say electron-donating and electron-withdrawing units, allowing an internal charge transfer along the conjugated chain which results in a reduced energy bandgap (typically below 1.5 eV).[27] The HOMO and LUMO levels in a low bandgap polymer are largely localised on the push and pull moieties, respectively (Figure 1.8). Therefore, a weakly electron-donating unit conjugated to a strongly electron-withdrawing unit decreases the bandgap of the polymer while keeping the HOMO level low, this being beneficial for high V_{OC} values. Furthermore, when these polymers are blended with an adequate electron acceptor, light absorption can be further extended into the UV-Vis range, thus increasing j_{sc}.[9]
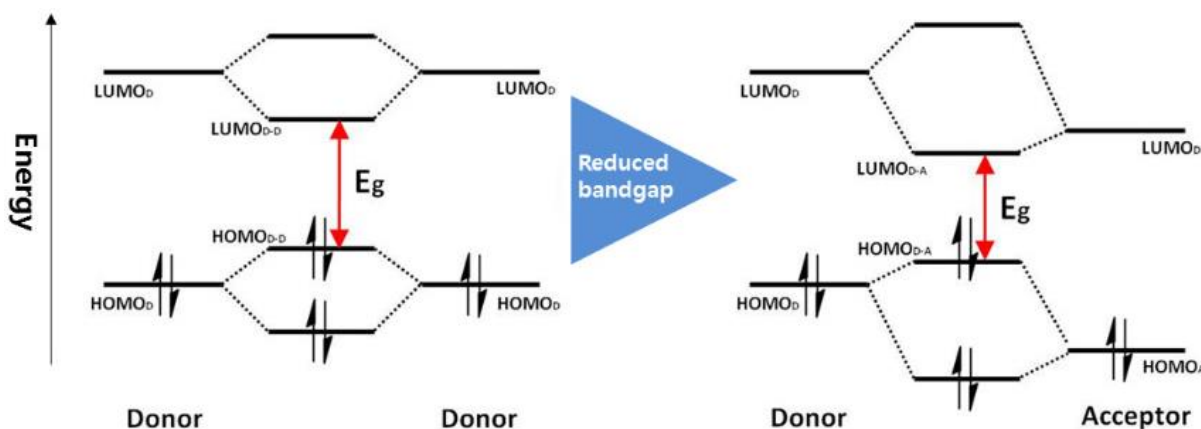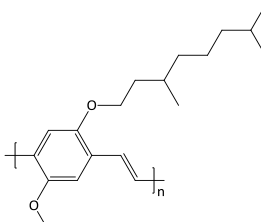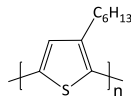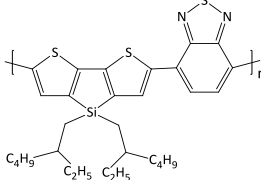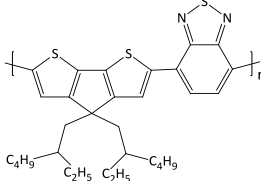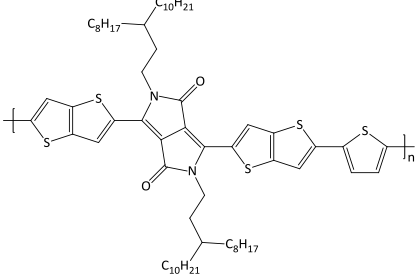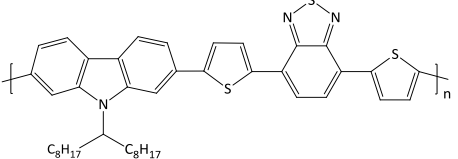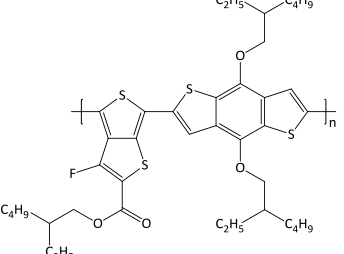
Figure 1.8. Energy scheme to illustrate the creation of a low bandgap polymer by combining push (donor) and pull (acceptor) units.

A great variety of polymers based on different donor-acceptor combinations are nowadays being synthesised, and comprehensive lists of low bandgap polymers are available in the literature.[42-43] Examples of these novel structures can be found in Table 1.1, which summarises the structure, optical bandgap, and highest reported efficiency for commonly employed conjugated polymers (*i.e.*, MDMO-PPV or P3HT) as well as for novel low bandgap polymers based on different donor and acceptor units. Polymers in Table 1.1 have been selected since they have been studied as such in this thesis, and/or because their donor or acceptor units are present also in other polymers studied in this work.

Accordingly, Table 1.1 includes two polymers based on electron-rich cyclopentadithiophene (CPDT) coupled with an electron-deficient benzothiadiazole (BT), namely poly[2,6-(4,4-bis(2-ethylhexyl)-4H-cyclopenta[2,1-b;3,4-b']dithiophene)-*alt*-4,7-(2,1,3-benzothiadiazole) (C-PCPDTBT) and (poly[(4,4'- bis(2-ethylhexyl)dithieno [3,2-b:2',3'-d]silole) -2,6-diyl-*alt*-(4,7-bis(2-thienyl)-2,1,3-benzo-thiadiazole)-5,5'-diyl], (Si-PCPDTBT). The latter is characterised by silicon as bridging atom to the solubilising alkyl side chains in the CPDT unit; in turn, this Si-CPDT unit is also commonly referred to as dithienosilole (DTS). Interestingly, they both displayed a similar electronic bandgap ~1.7 eV,[44-45] but the Si analogous was determined more crystalline than its precursor, leading to improved charge transport properties.[45-46] Nonetheless, these two polymers can both lead to similar efficiencies around 5 % depending on the processing and the structure of the cells.[47-48]

Table 1.1. Optical bandgap and PCE for different conjugated polymers in OSCs.

Name	Structure	E_g eV	PCE %	Ref.
MDMO-PPV		2.3	3.0	37
P3HT		1.9	4.4	39
Si-PCPDTBT		1.7	5.2	48
C-PCPDTBT		1.7	5.5	47
PDPPTT-T		1.4	7.3	49
PCDTBT		1.9	7.5	50
PTB7		1.8	9.2	32

Higher efficiencies were achieved for another benzothiadiazole derivative, in this case combined with a carbazole donor, in poly[N-9'-hepta-decanyl-2,7-carbazole-*alt*-5,5-(4',7'-di-2-thienyl-2',1',3'-benzothiadiazole)] (PCDTBT). This polymer is characterised by an E_g ~1.9 eV,[51] and efficiencies as high as 7.5 % can be obtained with it *via* optimisation of interlayers in the device.[50] Another important family of polymers is that based on electron-deficient diketopyrrolopyrrole (DPP), represented in Table 1.1 by poly(thieno[3,2-*b*]thiophene−diketopyrrolopyrrole) (PDPPTT-T). Devices based on this polymer yield efficiencies ranging from 5.9 to 7.3 % depending on the branching position of the alkyl side chains attached to the DPP unit.[49] Finally, the highest efficiency reported in Table 1.1, 9.2 %, was obtained with poly(thieno[3,4-*b*]thiophene-benzodithiophene) (PTB7), comprising a benzodithiophene (BDT) as donor unit coupled with electron-deficient thieno[3,4-*b*]thiophene.[32, 52] Furthermore, this same polymer including a 2-(2-ethylhexyl)-thienyl group in the BDT unit, so-called PTB7-Th, has led to devices with performances exceeding 10 %.[53]

It is clear from Table 1.1 that reduced bandgaps, although desirable to allow broadening of the absorption range, do not necessarily correlate with higher PCEs. In fact, in addition to appropriate molecular design in terms of the position of the electronic levels, multiple other parameters affecting materials solubility, crystallinity, or molecular packing are to be considered for the purpose of improved solar cell efficiencies.[9, 26] Furthermore, it is noteworthy that the efficiencies reported in Table 1.1 have been achieved *via* optimisation of additional solar cell parameters, for instance processing the active layer with additives[47] or selecting appropriate interlayers[50] and device configurations.[32]

1.3.2. Acceptor materials

The second principal component of the active layer is the acceptor material. The LUMO level in these acceptors must be as high as possible to maximise V_{OC} values, while remaining in between the HOMO and LUMO of the polymer to enable sufficient donor-acceptor electron transfer rates. Solubility, propensity to display crystalline characteristics, and high electron conductivity are other crucial parameters to be considered.
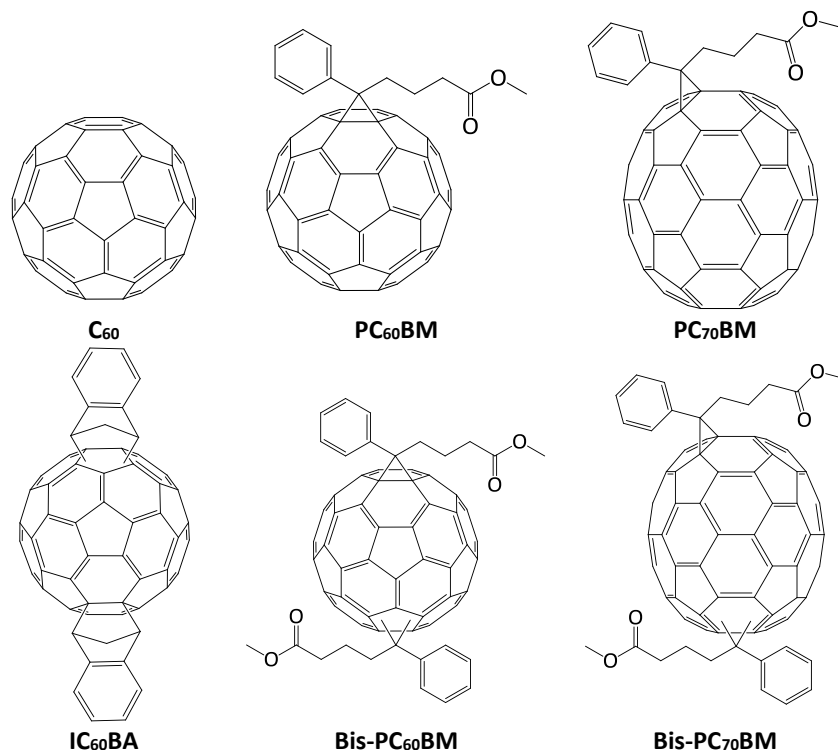
Figure 1.9. Structure of C_{60} and fullerene derivatives of C_{60} and C_{70}.

Fullerene derivatives have been widely employed as electron acceptor materials in organic solar cells (see Figure 1.9 for some selected structures).[54] First reports on fullerene acceptors for OSCs date back to 1992, when Sariciftci *et al.*[55] reported the photoinduced transfer from MEH-PPV onto fullerene C_{60} on a picosecond timescale. However, the lack of solubility of C_{60} limited its application to devices based on a bilayer configuration (see Figure 1.9), thus restricting power conversion efficiencies due to the low diffusion length of the created excitons.[56] Subsequently, the synthesis of soluble fullerene derivatives such as PCBM,[57] together with the implementation of the bulk heterojunction led to a successful combination that is still the most commonly employed nowadays.[30] Currently, the vast majority of cells with good efficiencies utilise soluble fullerene derivatives such as $PC_{60}BM$ or $PC_{70}BM$, the latter generally leading to larger photocurrents thanks to enhanced absorption in the visible range and more favourable interpenetration properties.[54] However, the LUMO values in these two materials (-4.2 eV) limit V_{OC} values, and, as a result, device efficiencies. In this regard, other fullerene derivatives such indene-C_{60} bis-adduct (ICBA),[58] bis-$PC_{60}BM$ or bis-$PC_{70}BM$[59] (see structures in Figure 1.9) display more favourable LUMO levels able to enhance power conversion efficiencies.

While C_{70}-based fullerenes contribute to the creation of photocurrent due to their incremented absorption in the visible range in comparison to C_{60} derivatives, additional absorption in the visible and in the infrared is further desirable to increase PCEs. Notably, this limitation can be overcome by using non-fullerene acceptors, for instance in so-called all-polymer solar cells, where both the donor and acceptor materials are semiconducting polymers. For instance, record 7.7 % power conversion efficiencies have been reported by Hwang *et al*.[60] for all-polymer solar cells based on benzodithiophene-thieno[3,4-*b*]thiophene as the electron donor and a naphthalene diimide-selenophene copolymer as electron acceptor.

1.3.3. Bulk heterojunction morphology

Assuming that the donor and acceptor materials have suitable energetic levels and conduction properties, according to the bulk heterojunction concept, yet an optimum balance between interfacial area, domain sizes and interconnection of materials is to be achieved to prevent non-geminate recombination and maximise the contribution of charges.[61] This morphological control of the active layer can be achieved in different ways: post-deposition treatments like solvent and thermal annealing,[9, 61] use of different solvents or solvent mixtures,[9, 62] and incorporation of several additives.[9, 63] Furthermore, processing can have an impact on the degree of crystallinity or order inside the polymer and fullerene domains. Recently, studies on polymer-fullerene phase diagrams have contributed to the understanding and optimisation of active layer morphologies and, as a result, on photovoltaic performances.[64-66]

Morphological control and crystallinity are also related to the structure of the employed polymers. Notably, the size and disposition (branched/linear) of the alkyl side chains, as well as the introduction of heteroatoms in conjugated polymers, can both affect the self-assembling and crystalline properties of the polymer and the corresponding bulk morphology.[9] For example, replacing branched side chains by linear ones in the BDT moieties of poly(benzo[1,2-b:4,5-b']-dithiophene–thieno[3,4-c]pyrrole-4,6-dione) (PBDTTPD) modifies the bulk morphology to such an extent that device performance drops drastically. While keeping the branched configuration in the BDT units, modulation of the number of aliphatic carbons in the linear N-substituted TPD units was shown to be decisive for improving device performance.[67] Alternatively, Yiu *et al*. highlighted that in polymers based on diketopyrrolopyrrole (DPP) units, nanostructural order can be promoted using long linear side chains instead of branched chains.[68] Improvements to morphology and efficiencies have also been

reported for thieno[3,2-b]thiophene–diketopyrrolo-pyrrole (DPPTT-T) polymers where the branching point was moved away from the polymer backbone.[49] Finally, not only the side chains, but also the presence of heteroatoms can play a role in the morphology and crystalline characteristic of blend thin films. For instance, C-PCPDTBT and Si-PCPDTBT, both combining a cyclopentadithiophene (CPDT) as donor unit and benzothiadiazole (BDT) as acceptor unit and uniquely differing in the bridging atom (C or Si, respectively), exhibit different crystalline properties. The analogous silicon polymer was determined to be more crystalline than its carbon counterpart, leading to improved charge transport properties.[45, 48]

1.3.4. Interlayers

The addition of interlayers between the active layer and the electrodes, indicated in Section 1.2.2, has been proven an efficient method for achieving higher efficiencies *via* optimisation of the charge transport process. Employed interlayers include inorganic materials, such as transition metal oxides (ZnO, TiO_x, V_2O_5, MoO_3, WO_3), inorganic salts (LiF, CsF or LiAc), and polymers, like polyethyleneimine (PEI) and PEDOT:PSS.[9] Due to the role of the latter in the present work, in the following PEDOT:PSS and its contribution to the improvement of solar cell efficiency are briefly described.

PEDOT:PSS is a ionomeric mixture of positively charged poly(3,4-ethylenedioxythiophene), partially balanced by negatively charged poly(styrene sulfonate). The resulting aqueous microdispersion is a polyelectrolyte system with good film forming properties, high conductivity, high light transmission in the visible range, and good stability.[69-70] Furthermore, conductivity of PEDOT:PSS can be further tuned and increased *via* doping with polar solvents.[71] PEDOT:PSS is a widely adopted buffer interlayer in OSCs, and its positive contribution to cell performance is frequently attributed to enhanced hole transportation and electrode selectivity.[72] However, how this material works to improve the overall cell performance is not yet fully understood. For example, contrasting results have been obtained regarding the influence of PEDOT:PSS conductivity on the electrical parameters of the cell. On the one hand, enhanced conductivity in PEDOT:PSS has been observed to positively contribute to PCEs by Hu *et al.,*[72] who reported ethylene glycol-doped PEDOT:PSS improved both the j_{sc} and FF values in the corresponding devices. In turn, Ko and coworkers ascribed the device improvement observed for mannitol-doped PEDOT:PSS mainly to a reduction of series resistance of the layer.[73] On the other hand, several reports indicate that the changes in PEDOT:PSS bulk conductivity do not correlate with

improved performance, but rather relate to enhanced light scattering by the rough surface of PEDOT:PSS (increasing absorption in the active layer),[74] or to other properties at the interface between the buffer and active layers.[75]

1.4. The stability challenge

Whilst device efficiencies continue to improve thanks to the design and selection of favourable materials and device structures, a major limitation of organic solar cells is still their operational lifetimes, which at the moment can still be considered insufficient for establishing themselves on the market.[6-8] Given the complex and multilayer character of polymer solar cells, many factors can contribute to their degradation. Thus, a thorough understanding of all of the failure mechanisms present in organic solar devices is to be achieved in order to tackle the lifetime limitation problem.

1.4.1. Evaluation of OSCs lifetimes

Since the electrical parameters describing the behaviour of solar cells are highly affected by changes in the cell composition and/or operation, studying and monitoring the j-V characteristics of a solar cell over time allows one to obtain valuable information about the degradation processes occurring. However, it is to note that different failure mechanisms can affect similarly the electrical parameters of the cell. For instance, a j_{sc} loss can be, among others, the result of modifications leading to a decreased absorption in the active layer (*e.g.* diminution of polymer conjugation or loss of transparency in the stack), or stem from changes in the active layer morphology and/or interfaces that impair exciton dissociation and the transport of charges.[7]

As a consequence, additional characterisation techniques and evaluations are frequently necessary to discern the degradation causes for each specific case.[7] For instance, monitoring of j-V curves can be completed with the analysis of incomplete or partial devices, individual layers over a substrate, or, even from a more fundamental perspective, with the study of the evolution of individual components. It must be noted that results arising from the evaluation of incomplete devices, individual layers or individual components, although important and informative due to their more simplistic approach, may not always give a true image of what occurs in the actual device, as every other compound present in the cell can strongly influence the studied degradation process.[7] Thus, comprehensive understanding of the degradation mechanisms can only be achieved *via* multiscale approaches, starting with simple systems and increasing in complexity until finally assessing the stability of complete solar devices.

1.4.2. Common degradation mechanisms

A summary of commonly reported degradation mechanisms occurring in polymer solar cells is depicted in Figure 1.10. The list, although not exhaustive, aims to exemplify the complexity of the problem under study: every layer and interface, from the core of the cell to the encapsulation system, is susceptible of undergoing degradation following several chemical and physical processes. The aspects specified in this list are subsequently briefly described.

1	H_2O and O_2 diffusion
2	Degradation of the encapsulants
3	Indium diffusion
4	Photochemical degradation of the AL
5	Formation of Charge Transfer Complexes
6	Polymer oxidation by photosensitised $^1O_2$
7	Polymer chain radical oxidation
8	Morphological changes
9	Interfacial delamination
10	Formation of insulating patches
11	Oxidation of the metal electrode
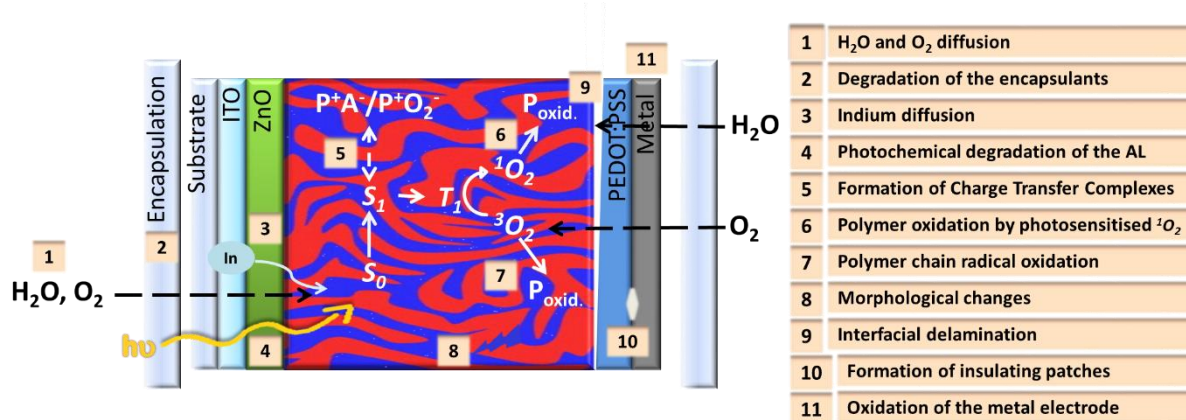
Figure 1.10. Commonly reported degradation mechanisms in OSCs. The notations are described in the text. Adapted from reference 8.

1.4.2.1. Water and oxygen diffusion, degradation of the encapsulation materials

It is generally accepted that the presence of oxygen and water in the device is a limiting factor to the corresponding device lifetimes.[6, 8, 15] Indeed, the interaction of oxygen and water with certain cell components, such as hygroscopic PEDOT:PSS, the active layer (in combination with light), or metal electrodes, triggers or accelerates important degradation processes. These effects are discussed in detail in this section while addressing each of these components. Indeed, oxygen and water can be introduced in the stack upon processing of organic solar cells, especially if industrially produced, for example, using roll-to-roll processes. After processing the whole stack, the main gateway to the device for oxygen and water is penetration or diffusion through the encapsulation material, although diffusion *via* the sides of the device should not be excluded.[7-8] Moreover, once the encapsulation barrier is traversed, oxygen and water diffusion can continue through the outer electrode, mainly *via* nano- or microscopic pinholes or in between the metal grains of the electrode.[76]

Thus, the quality of the encapsulating materials is of major importance to prevent these two components from entering the device. Desirable permeation rates are in the range of

$10^{-5} - 10^{-6}$ g m^{-2} day^{-1} (water) and 10^{-3} - 10^{-5} cm^3 m^{-2} day^{-1} atm^{-1} (oxygen).[7] As aforementioned, a common encapsulation strategy is the use of a barrier film of alternating organic and inorganic layers.[7, 77-78] The resulting stack needs to be resistant against the stress conditions it is subjected to, so that the barrier characteristics, together with other important properties, such as transparency or flexibility, are maintained over time. The main degradation mechanisms concerning barrier materials are linked to the presence of polymeric or organic components, as these are known to be aged by the combined action of light, oxygen, moisture, and heat. Thereby, chemical degradation and reorganisation in these materials can result in an increase in brittleness and modification of their optical properties (polymer yellowing or increment of light scattering), ultimately impairing light absorption by the active materials in the core of the device. These problems are addressed by including UV absorbers or H_2O and O_2 getter materials, and the utilisation of copolymers with elastomeric components able to diminish the material stiffness.[7]

On the contrary, the main cause of degradation for the inorganic components of the barrier is mechanical stress and lack of compatibility between the different layers.[7] When the barrier is composed of layers with different thicknesses and characteristics, residual strains and stresses created upon processing can remain in the stack. In addition, inadequate interlayer adhesion can result in delamination and cracks, which, in the worst case, can propagate through the whole device. These effects can be lowered by an exhaustive selection of the materials in terms of properties and compatibility, in order to enhance the adhesion and stability of the ensemble.

Finally, adhesive materials used to seal the module can release certain by-products detrimental for good cell operation, and can also be an input channel for oxygen and water. Thus, attention must be paid to the selected sealing products, which are usually improved by adding moisture and oxygen getter materials.[79]

1.4.2.2. Chemical degradation of the electrodes

Independent of the device configuration, the generally adopted bottom electrode is ITO. According to its physical characteristics, ITO is a brittle material, and this can represent a problem for its application in devices which are meant to be flexible.[80] Chemically, the polar and hydrophilic characteristics of ITO impair the wetting of the organic active layer if directly coated on top of it.[81] Wetting issues can cause, in turn, limited adhesion between layers hindering charge transport and favouring delamination.[11] This problem can be circumvented by modifying the surface of ITO,

for example, *via* plasma treatments[81] or, most notably, applying buffer layers like PEDOT:PSS[72] or transition metal oxides such as V_2O_5 or MoO_3.[82] However, the application of PEDOT:PSS as a buffer layer, due to the acidic nature of PSS can, in turn, trigger ITO etching, with the diffusion of indium ions across the device.[83-84] Furthermore, water absorption by hydrophilic PEDOT:PSS can lead to the formation of insulating patches located at the interface with the active layer. Alternatively, ITO can be substituted by other (semi)transparent contacts, such as ultrathin metal films, metallic nanowires and nanoparticles, highly conductive polymers, or carbon nanotubes.[7, 80, 85-86]

Concerning the upper electrode, degradation of low work function metals (Ca, Al) is mainly caused by their reaction with oxygen and water, their presence being determined, as aforementioned, by the permeation rate of the employed substrate and barrier layers. Diffusion of oxygen and water through metal pinholes leads to the formation of metal oxides at the active layer/electrode interface, which can act as voids or insulating patches.[13-14, 76] With reference to the high work function metal, usually Ag, although it possesses higher stability against oxidation, there still exist concerns about its possible migration through the layers of the device.[87]

1.4.2.3. Mechanical stress, delamination and interfaces

As indicated when discussing the degradation of encapsulation, maintaining mechanical integrity in a system comprised of layers with different characteristics requires careful consideration, especially if the flexible nature of these devices is to be kept.[11-12, 88] For instance, low adhesion between layers can highly affect stability in flexible devices, as bending the device can provoke delamination problems over time, consequently affecting charge extraction. Although little has been reported concerning the thermomechanical properties of organic solar cells, the interface in between PEDOT:PSS and the active layer has been suggested to be a failure point in inverted devices,[11] creating a need for new solutions and approaches. This subject is further discussed in the introduction to Chapter 2.

1.4.2.4. Photochemical and morphological degradation active layer

The bulk heterojunction is a metastable structure that can evolve over time, even at ambient temperature, consequently disrupting the optimum morphology created for maximising exciton dissociation and charge transport.[6] This effect is enhanced if the device achieves high temperatures upon operation. Notably, common acceptors like PCBM form crystalline domains that grow in size, reducing the interface donor-acceptor and resulting in severe degradation of device performance.[89-90] Stabilisation of the morphology in the active layer has been pursued using different strategies,

for instance using chemically functionalised donor and acceptors, able to crosslink upon thermal or photochemical treatment,[91-92] employing thermocleavable active components,[6] or adding third components or additives that stabilise the morphology over time.[93-94] An interesting approach for stabilising the active layer is represented by the use of block copolymers, which create thermodynamically favoured morphologies that can be preserved over time (see Section 2.1.2 for further details).

Furthermore, the organic components in the active layer are susceptible of undergoing photochemical reactions when exposed to solar irradiation, this effect being enhanced when UV-Vis irradiation is combined with oxygen and/or water.[7, 10, 95] Some of the processes that can occur to the polymer in the active layer are depicted in Figure 1.10, and are subsequently described. When a polymer (P) in its ground state (S_0) absorbs light (hυ) of a suitable wavelength, population of singlet excited states occurs (S_1, S_2, ..., S_N), followed by internal conversion to the first singlet excited state (S_1). Polymer photodoping can then occur when the polymer in its excited state forms a charge transfer complex (CTC) with the acceptor (P^+/A^-) and/or with oxygen (P^+/O_2^-). The latter is regarded as a reversible degradation mechanism highly impairing the PCE of solar cells under photooxidative conditions.[96] Furthermore, the polymer can undergo irreversible modifications, for instance, if the absorbed energy by the polymer in its excited state (S_1) is sufficient for homolytically breaking chemical bonds. In combination with oxygen, polymer photooxidation ($P_{oxid.}$) occurs when molecular oxygen ($^3O_2$) reacts with the polymer following a radical chain oxidation mechanism.[10] The polymer can also be oxidised by highly reactive oxygen species, such as singlet oxygen, $^1O_2$. Singlet oxygen can, in turn, be photosensitised by the polymer in its photoexcited triplet state, T_1 (populated *via* intersystem crossing from the first singlet state S_1).[8] Overall, these reactions lead to a loss of conjugation in the polymer and to the creation of oxidation products that can act as charge traps, leading, in all cases, to cell degradation as they affect light absorption and charge transport.[7] The introduction to Chapter 3 provides further details concerning the photochemical degradation of the polymer donor and the fullerene acceptor on their own, as well as their combination in the blend.

1.5. Conclusions

Two main limitations to the establishment of organic solar cells in the market are the achieved power conversion efficiencies and device stability. Research conducted to increase the performance of organic solar cells has led to very promising results, bringing initial power conversion efficiencies

up to 10 % through the combination of novel materials and device architectures that are able to enhance light absorption, exciton dissociation, and charge transport and collection. However, how the performance is maintained or modified over time is a parameter as crucial as the initial PCE itself. Thus, the successful implementation of these materials and device configurations is only possible if stability issues related to their use are appropriately considered and alleviated, if necessary. In this context, the work herein addresses two sources of instability in organic solar cells, namely the interfacial delamination between the active layer and PEDOT:PSS and the photochemical degradation of the active layer.

Chapter 2.   PSS-based Block Copolymers for Interfacial Stabilisation of Organic Solar Cells

2.1. Introduction

This chapter focuses on the potential application of poly(3-hexylthiophene)-*block*-poly(*p*-styrene sulfonate) (P3HT-*b*-PSS) block copolymers as an interlayer to overcome the wettability and adhesion issues at the interface between PEDOT:PSS and the active layer (P3HT:PCBM).[11] This block combination has been selected so that the P3HT block positively interacts with the active layer and the PSS block does the same with the hole transport layer. Since the proposed material is an amphiphilic diblock copolymer, our synthetic approach is based on the work of Okamura *et al.*,[97] according to which, a sulfonate ester precursor (in this case, neopentyl *p*-styrene sulfonate, NSS) is polymerised, incorporated into the copolymer of interest, and finally (thermally) deprotected to yield the corresponding sulfonic groups. The general strategy is illustrated in Figure 2.1. Firstly, the two building blocks are separately synthesised and subsequently coupled using 'click' chemistry. Following which, the resulting hydrophobic block copolymer can be deposited in the solar cell device using common organic solvents. Finally, thermal treatment at 150 °C permits the removal of the neopentyl protecting groups, producing the target amphiphilic P3HT-*b*-PSS expected to improve adhesion at the aforementioned interface. Within this overall strategy, this work focuses on three main aspects: (1) optimisation of the synthesis of the PNSS block using Reversible Addition-Fragmentation chain Transfer (RAFT) polymerisation; (2) surface characterisation of P3HT-*b*-PNSS thin films by means of Atomic Force Microscopy (AFM); and (3) RAFT synthesis and thermal deprotection of systematically varied R-protected *p*-styrene sulfonate polymers.
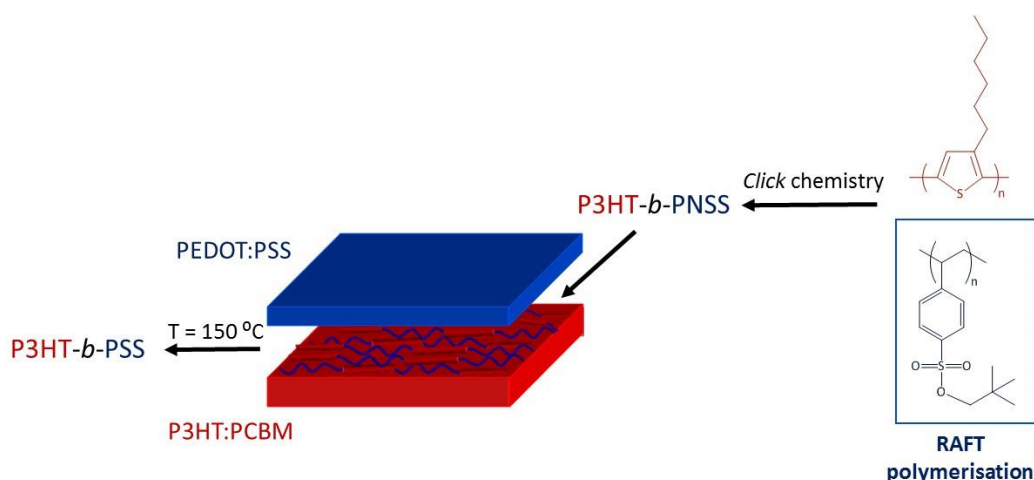
Figure 2.1. General synthetic strategy and application of P3HT-*b*-PSS block copolymers in OSCs. N.B. End group functionalities of the polymer building blocks have not been shown for simplicity purposes.

2.1.1. The interface between PEDOT:PSS and the active layer

2.1.1.1. PEDOT:PSS as hole transport layer

PEDOT:PSS is the most commonly employed hole transport layer (HTL) in both conventional and inverted organic solar cells. As previously described, it comprises an ionomeric mixture of positively charged poly(3,4-ethylenedioxythiophene) balanced by negatively charged poly(p-styrene sulfonate) (see Figure 2.2). PEDOT:PSS is usually commercially available as an aqueous suspension, and can be applied on top of the bottom electrode (normal architecture) or the photoactive layer (inverted structure). In the latter, wettability issues have been observed owing to the orthogonal characteristics of the hydrophobic active layer and the aqueous PEDOT:PSS suspension. Since good wettability and film formation properties are required to allow fabrication of efficient devices, research efforts have been focused on the development of more 'organic' formulations of PEDOT:PSS, which enhance the wetting properties without compromising the conductive properties of the layer.[71, 85]
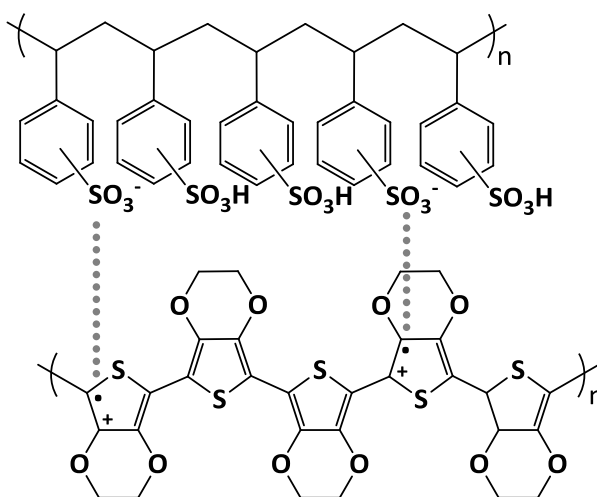
Figure 2.2. Chemical structure of the poly(3,4-ethylenedioxythiophene):poly(p-styrene sulfonate) complex, PEDOT:PSS. Adapted from reference 69.

PEDOT:PSS films, due to their polymeric nature, can undergo irreversible changes at elevated temperatures or when irradiated by light.[98-100] Moreover, the presence of PSS anions confers the complex a highly hygroscopic character and this, in turn, enhances the effects provoked by other external degradation triggers.[100]

2.1.1.2. Stability of PEDOT:PSS-containing solar cells

Overall, PEDOT:PSS is associated with the degradation of solar cells exposed to ambient humidity due to its high hygroscopicity.[13-15, 83, 101-102] In normal architecture devices, water absorption

by this layer can cause ITO etching (due to the acidic nature of PSS)[83] and enhanced cathode oxidation[13-14], whilst in inverted devices (whose stability towards electrode oxidation is enhanced *per se* due to the use of more oxidation-stable metals like Ag), failure mechanisms have been related to chemical changes at the PEDOT:PSS interface with the active layer.[15]

Interestingly, this same interface has been reported to suffer from mechanical stress in inverted devices.[6, 11] Dupont *et al.* have examined the adhesive failure point in inverted solar cells (PET/ITO/ZnO/P3HT:PCBM/PEDOT:PSS/Ag) using a double cantilever beam setup, illustrated in Figure 2.3. Adhesive failure occurred between the hydrophobic P3HT:PCBM and hydrophilic PEDOT:PSS, and the fracture energies were shown to depend on the PCBM content in the active layer.[11]
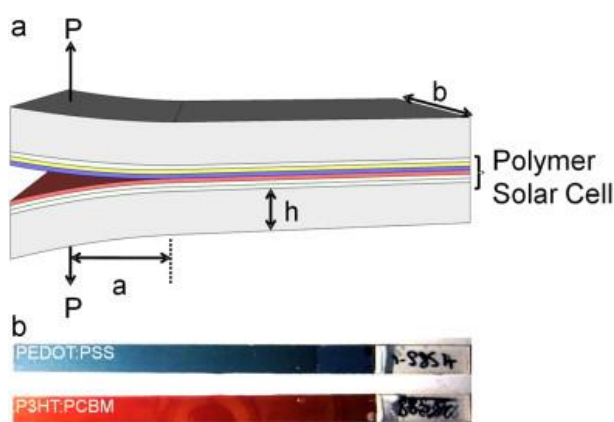
Figure 2.3. (a) Double cantilever beam (DCB) test specimen for the analysis of adhesion in organic solar cells and quantification of fracture energies, G_c. (b) Illustration of the debonded surfaces, PEDOT:PSS (top) and P3HT:PCBM (bottom). Obtained from reference 11.

The negative effects derived from the hydrophilic character of PEDOT:PSS can be eliminated, to an extent, by excluding water ingress into the device with barrier encapsulation systems. However, even under ideal moisture-free conditions, new solutions and approaches are needed to improve wettability and adhesion at this interface and prevent delamination.

2.1.2. Block copolymers

2.1.2.1. Block copolymers for OSCs

Block copolymers are a special type of copolymer that consists of alternating polymeric segments or blocks, which are based on different monomeric units and covalently bonded to each other. These block copolymers can be classified according to the number of distinct blocks (di-, tri-, or multi-block copolymers, for example) and their composition. Owing to the inherent immiscibility of the

different polymer segments, block copolymers undergo a self-assembling process referred to as 'microphase separation', which results in different morphologies with domain sizes on the nanometre length scale. This self-assembling process has been subject of extensive research, and it is probably the most interesting property of block copolymers, responsible for their wide range of applications.[103-105]

According to mean-field theory (MFT), the interactions among the different blocks can be thermodynamically described using the following parameters: N, representing the copolymer total degree of polymerisation, the Flory-Huggins parameter (χ), describing the miscibility of two polymer entities, and f, indicating the volume fraction of a given polymer in the copolymer.[103] In general, negative values of χ indicate favourable interactions between the segments, and positive values suggest unfavourable mixing. However, more pertinent for block copolymers is the analysis of the product χN, which indicates the segregation strength between the different blocks and thus predicts their microphase separation. Overall, when $\chi N < 10$, the system is governed by entropic terms, favouring disordered morphologies; over $\chi N > 10$, enthalpic terms dominate, microphase separation tends to occur (depending on f), and a wide range of structures can be observed depending on the exact χN value and the volume fractions of the polymers.[104] These parameters may be represented for a certain block copolymer using mean-field phase diagrams (see Figure 2.4).[103, 106]
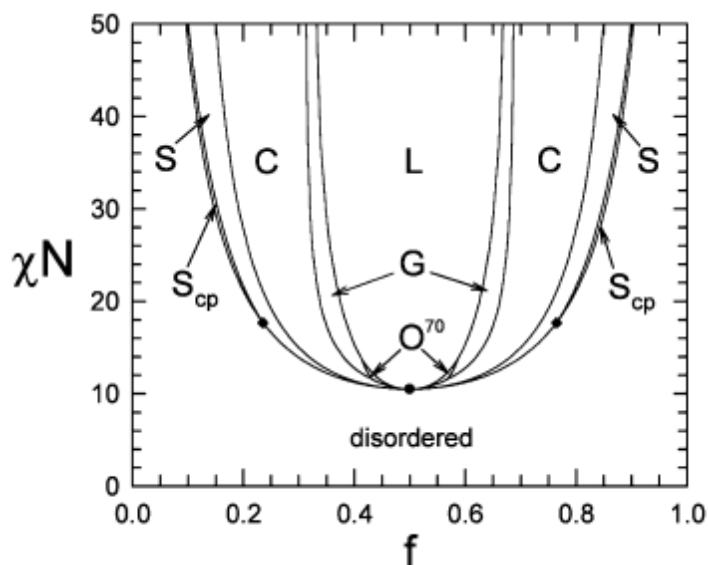
Figure 2.4. Mean-field phase diagrams for melts of an AB diblock copolymer, showing the stability regions of the lamellar (L), cylindrical (C), bcc spherical (S), hcp spherical (Scp), gyroid (G), and Fddd (O^{70}) morphologies. Obtained from reference 106.

The characteristics of the different blocks have an important role in the way the copolymer phase separates and the morphologies that can be created. Two main types of polymer chains can be distinguished: rods and coils. Whilst a coil describes a flexible polymer chain, generally adopting an amorphous conformation, a rod indicates a polymer chain that creates a rigid and crystalline unidirectional block, often due to an overlapping of π-orbitals. Both chain flexibility and electronic properties are two important characteristics to be considered for the design of block copolymers for organic photovoltaics.[104] Figure 2.5 displays common nanostructures observed for coil-coil diblock copolymers.
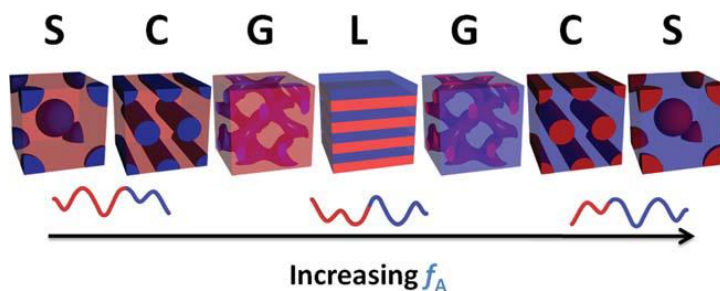
Figure 2.5. Commonly observed nanostructures adopted by coil-coil block copolymers (S = spheres, C = cylinders, G = gyroid, L = lamellae). The blue colour indicates polymer A (with increasing volume fraction, f_A) and the red block indicates polymer B. Obtained from reference 104.

Importantly, the domains created *via* microphase separation of block copolymers and the typical exciton diffusion length in organic solar cells are both on the nanometre length scale. Furthermore, the fact that the achieved nanostructures in block copolymers are thermodynamically favoured confers long-term stability to the created morphologies. This morphological stability is, in turn, of particular importance in the active layer of OSCs, where efficient charge extraction goes hand-in-hand with the creation of well-defined morphologies that are preserved over time.

Indeed, the advantageous characteristics of block copolymers have been explored in OSCs and mainly within the active layer, for instance (i) as main components,[107] (ii) as compatibilisers that improve and/or stabilise the structure of the blend,[108] and (iii) as templating agents for the active layer components.[109] In the first case, block copolymers used as main active layer components have the potential to become efficient materials, able to capture excitons and facilitate charge percolation, whilst minimising recombination. Secondly, their incorporation as additives in the active layer is aimed at improving the blending of immiscible materials by reducing the interfacial energy between them. This is generally achieved when one of the blocks is chemically similar to one of the blend components

and the other segment displays similarities to the other material. Thirdly, block copolymers may be utilised as templating agents, when one of the blocks is easily removable by some kind of degradation after creation of the desired morphology. The mould left by the degraded material can then be filled up with a second material of interest. Finally, whilst the properties of block copolymers are indeed relevant in the quest for efficient and stable active layers, their use can also be extended to other layers in the device, for example electron transport layers[110] or interfacial adhesive layers.[111]

2.1.2.2. Synthesis

Block copolymers can be synthesised by two main procedures, namely 'step growth-like' and 'chain growth-like' approaches (Figure 2.6), also often referred to as 'convergent' and 'divergent' approaches, respectively.[104] In the step growth-like approach, each block is firstly synthesised on its own and coupled afterwards to bind the different segments together. Although this approach permits full optimisation of the synthesis of each block, the overall yield of the procedure highly relies on the coupling step, which is often not quantitative. Thus, effective end-functionalisation of each block and highly efficient coupling methods are required. In this regard, 'click' reactions, proceeding in high yield and with little or no by-products, have been widely adopted, particularly the copper(I)-catalysed 1,3-dipolar cycloaddition between an azide and an alkyne.[112] In the chain growth-like approach, an individual block is polymerised and functionalised with a group capable of initiating (or, in the case of RAFT polymerisation, acting as a chain transfer agent for) the polymerisation of the next block. Such functionalisation converts the polymer into a so-called macroinitiator (or macroCTA) for polymerisation.
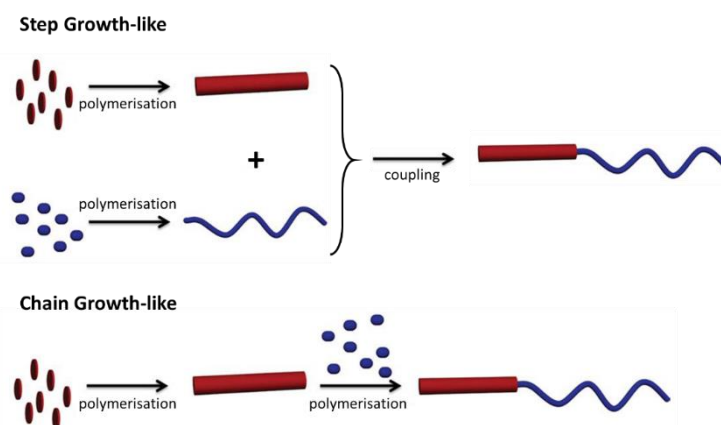
Figure 2.6. Step and chain grow-like synthetic approaches for the preparation of block copolymers. Adapted from reference 104.

As aforementioned, microphase separation in block copolymers is highly dependent on both the chemical characteristics and the size (degree of polymerisation and monomer specific volume) of the different blocks. Thus, and independently of the synthetic approach employed to incorporate the different blocks, fine control over the molar mass of the different blocks is to be achieved. This makes the evolution in the synthetic procedures for the preparation of block copolymers highly related to the development of the controlled or living polymerisation techniques, such as ionic[113] or radical[114] polymerisation and ring-opening metathesis polymerisation (ROMP)[109]. Due to its role in this work, focus herein is on the applicability of controlled radical processes, most specifically, Reversible Addition-Fragmentation chain Transfer (RAFT) polymerisation.

2.1.3. RAFT polymerisation

Controlled radical polymerisation (CRP) processes, such as Atom Transfer Radical Polymerisation (ATRP),[115-116] Nitroxide-Mediated Polymerisation (NMP),[114, 117-118] and Reversible Addition-Fragmentation chain Transfer (RAFT) polymerisation,[114, 119-121] have been revolutionary for the production of well-defined macromolecules with predetermined molar masses. Among them, RAFT polymerisation excels due to its low-cost, simplicity and versatility, as it can be applied to a wide range of monomers under various experimental conditions, showing great tolerance to unprotected functionalities in both monomer and solvent (*e.g.* –OH, –COOH, –NR$_2$, –CONR$_2$), yet providing controlled molar mass polymers with very narrow polydispersities.[121] This is possible thanks to the addition of a suitable agent, denominated RAFT agent or Chain Transfer Agent (CTA) and typically consists of a thiocarbonylthiogroup (S=C-S) with substituents, namely R (leaving group) and Z (stabilising group), that determine its reactivity. According to the RAFT polymerisation mechanism, the newly formed polymer is reversibly deactivated by an active RAFT group, as depicted in Scheme 2.1.
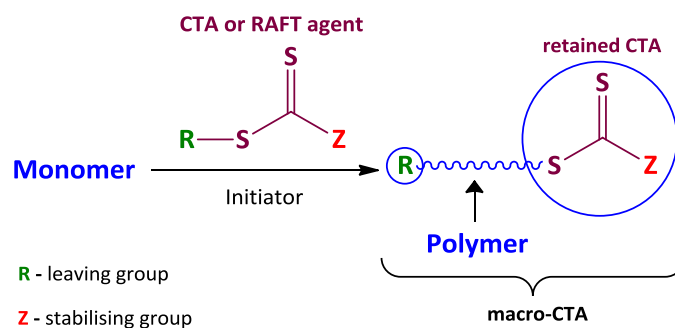
Scheme 2.1. Overall schematic of the RAFT polymerisation process.

2.1.3.1. RAFT polymerisation mechanism

The key aspect in the RAFT mechanism concerns the radical reactions involving the CTA, which provide the process with its controlled or living character. Comparing to a free radical polymerisation, where chains are continuously formed, propagated, and terminated (by radical-radical reactions), in an ideal living polymerisation, chains are initiated at the start of the reaction and then grown at the same rate due to suppression of the termination step. The living behaviour is thus possible using reagents that maintain the majority of the chains in a so-called dormant form *via* reversible processes, reducing the concentration of (growing polymer) radicals at any given time and therefore decreasing the probability of termination. Accordingly, in a free radical process the molar mass of the chains formed in early stages of polymerisation is high, and subsequently lower for the chains formed in later stages due to monomer depletion (leading to $Đ \geq 1.5$). In turn, in a living radical polymerisation, the molar mass linearly increases with conversion, and dispersity values remain low ($Đ \sim 1.1$).

Together with the conventional radical polymerisation steps of initiation and termination, RAFT polymerisation features a sequence of addition-fragmentation equilibria promoted by the addition of the chain transfer agent. In total, the RAFT polymerisation mechanism consists of five main steps, summarised in Scheme 2.2.

1) Initiation
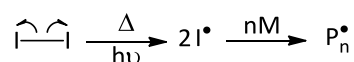
2) Chain Transfer
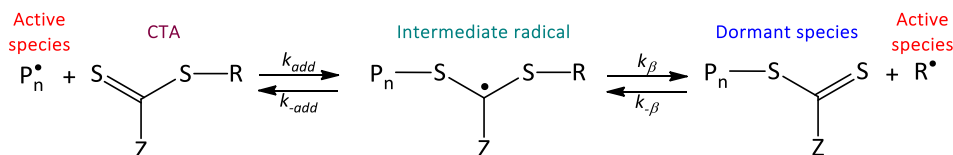
3) Re-initiation
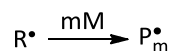
4) Chain Equilibration
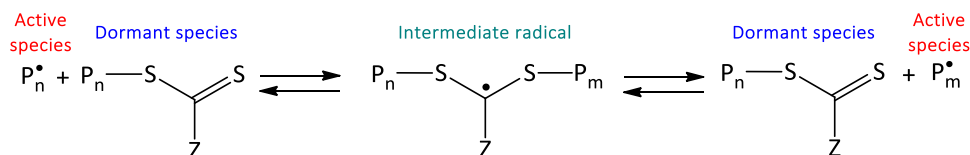
5) Termination
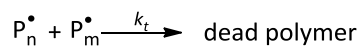
Scheme 2.2. Basic RAFT polymerisation mechanism. Adapted from reference 120.

1)   **Initiation**: The first step involves the generation of radicals by an initiator. This is typically carried out *via* thermal decomposition of azocompounds, such as 2,2'-azobis(2-methylpropionitrile) (AIBN), or alternatively, using photoinitiators, ionising radiation or redox processes.[120] These radicals then react with monomer molecules (M), producing oligomeric radicals ($P_n{}^\bullet$).

2)   **Chain transfer**: During reversible chain transfer, also called pre-equilibrium, oligomeric $P_n{}^\bullet$ radicals react with the Chain Transfer Agent to produce intermediate thiocarbonythio radicals. This intermediate species can either fragment to afford the original CTA and the oligomeric radical, or, more readily, fragment to yield a dormant oligomeric CTA and a reinitiating $R^\bullet$. The pre-equilibrium concludes once the original CTA is fully consumed.

3)   **Reinitiation**: In the reinitiation step, the leaving group radical ($R^\bullet$) initiates the creation of new active polymer chains ($P_m{}^\bullet$).

4)   **Chain equilibration**: This is the main RAFT equilibrium between the active and dormant polymer chains. Rapid exchange at this step favours that the concentration of active polymer chains remains lower than that of the stabilised radical intermediates, thus limiting termination reactions. Ideally, in a rapid interchange process, radicals are equally shared, producing chains with similar lengths and leading to very narrow molar mass distributions.

5)   **Termination:** Given the living character of the RAFT process, termination reactions are limited. However, activated chains may still react through a bi-radical reaction yielding chains that cannot further react (dead polymers). Moreover, radical species can also participate in undesirable side-reactions (*e.g.* radical to monomer, polymer, or solvent), referred to as chain transfer events, leading to inactive species that contaminate the final product.

At the end of the process, and under optimal polymerisation conditions, the majority of the polymer chains will have the CTA structure incorporated. Hence, the created polymer becomes a chain transfer agent itself, a so-called 'macro-CTA', capable of undergoing further polymerisation processes or other chemical reactions.

2.1.3.2. Chain transfer agent or RAFT agent

Based on the general RAFT mechanism discussed above, overall polymerisation control is the result of a good balance among the addition and fragmentation steps, the lifetime of the intermediate radical, and the propagation of the radical species. The effectiveness of RAFT polymerisation is thus highly dependent on the choice of the CTA, where the selected functions R and Z groups can have a great impact on the kinetics of the reaction and the degree of control achieved (see Scheme 2.3).

Reactive double bond

Weak single bond

R must be a good homolytic leaving group, also able to reinitiate polymerisation

Z modifies addition and fragmentation rates

Z stabilises the intermediate radical
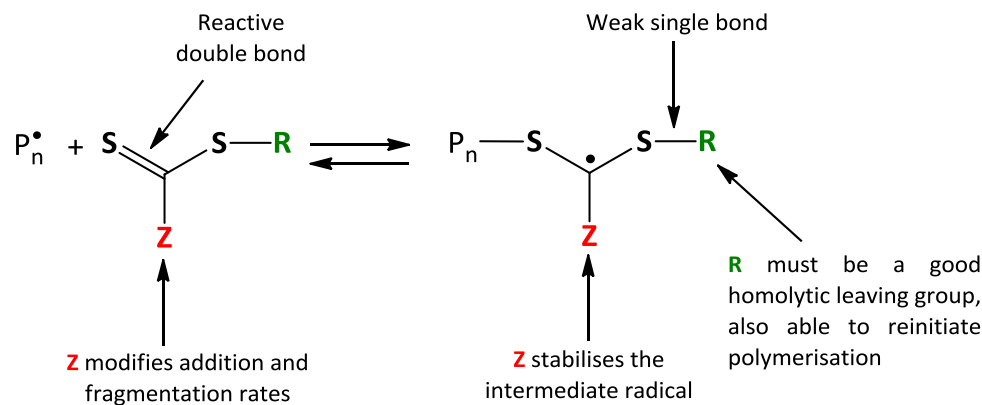
Scheme 2.3. Generic characteristics of the chain transfer agent and its corresponding polymeric adduct. Adapted from reference 120.

The addition process (characterised by the rate constant, k_{add}) is favoured by a high reactivity of the C=S bond, and this is, in turn, influenced by the character of Z group. Importantly, the Z group must be able to stabilise the intermediate radical formed upon addition, but only moderately, so that long induction periods or inhibition of the polymerisation are prevented. For the intermediate radicals to rapidly fragment in the positive direction (k_β), R must be a good homolytic leaving group in relation to the propagating P_n radical, and should as well promote radical propagation after scission to favour the reinitiation step. Since the stabilising and leaving groups are closely related, attention must be paid to the Z/R combinations in order to obtain efficient transfer agents. Commonly employed types of chain transfer agent are depicted in Figure 2.7.

Dithiobenzoates **Trithiocarbonates** **Dithiocarbamates** **Xanthates**
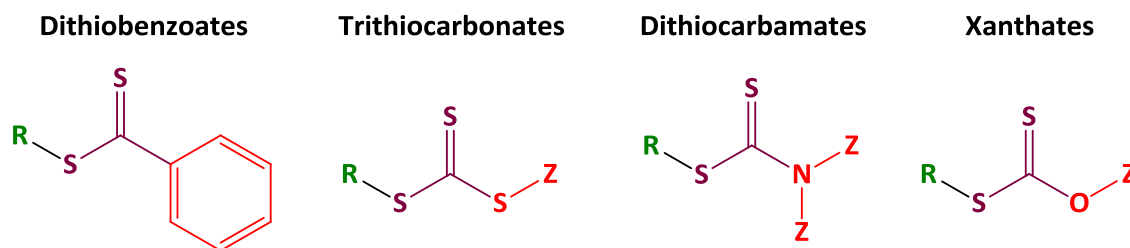
Figure 2.7. Commonly employed chain transfer agents.

Similarly, the CTA effectiveness is dependent on the monomer to be polymerised. Vinyl monomers can be classified as more activated monomers (MAMs), such as styrene, methyl methacrylate or acrylic acid, or less activated monomers (LAMs), such as vinyl acetate, *N*-vinylpyrrolidone or N-vinylcarbazole.[122] Different RAFT agents are recommended depending on the monomer type; for example, very active CTAs are not suitable for the polymerisation of LAMs because

they can inhibit the polymerisaton process. Comprehensive lists of different monomer − CTA combinations are available in the literature.[120]

2.1.3.3. Assessment of RAFT polymerisation: kinetics and influence of experimental conditions

Since in a RAFT process the CTA does not produce radicals, but just distributes them, the kinetics are similar to those of a conventional free radical polymerisation, where the polymerisation rate (r_p) is proportional to the square-root of the initiator concentration, $[I]_0$, and has a first order dependence on the monomer concentration $[M]$, as shown in Equations 2.1 and 2.2.

$$r_p = -\frac{d[M]}{dt} = k[M][I]_0^{1/2}$$

Equation 2.1

A more precise description of the polymerisation rate is given by Equation 2.2:[123]

$$r_p = -\frac{d[M]}{dt} = k_p[M]\sqrt{\frac{fk_d[I]_0 e^{-k_d t}}{k_t}}$$

Equation 2.2

where k_p is the propagation rate constant, f is the initiator efficiency, k_d is the decomposition rate coefficient of the initiator and k_t is the termination rate coefficient. From this expression, it can be deduced that polymerisation rates vary depending on the type of monomer (characterised by certain k_p and k_t values) and its concentration, the initiator concentration and decomposition rate, and are also affected by the employed temperature.

Pseudo first-order kinetic plots (ln$[M]_0$/$[M]$ *versus* time) are often regarded as an indication of the controlled nature of RAFT polymerisation. Linearity in these plots accounts for the establishment of steady state conditions, under which the previous equations are valid. It must be noted that such steady state radical concentrations can be achieved both in free and controlled radical polymerisation by different means; in the former, when displaying similar rates of initiation and termination, and in the latter, when a good balance between activation and deactivation of chains is obtained.[124] Often, because of the different compatibilities among the specific RAFT agent, monomer and reaction conditions, inhibition or retardation of the polymerisation can be observed. Additionally, linearity of this plot during the course of conversion can be employed to assess the existence of diffusion-related processes, such as the Trommsdorff or gel effect, according to which, limited diffusion in bulk or highly concentrated systems can lead to an auto-accelerated polymerisation with an increase in the obtained molar masses.[125-126]

Whilst the rate of polymerisation is independent of $[CTA]_0$, the ratio between initial concentrations of monomer and CTA, $[M]_0/[CTA]_0$, determines the theoretical degree of polymerisation, D_p^{th}, and, concomitantly, the theoretical number average molar mass, M_n^{th}. An effective CTA allows for the preparation of polymers with targeted molar masses by varying this ratio.

The theoretical molar mass, M_n^{th}, can be calculated using the Equation 2.3:[122]

$$M_n = \left(\frac{[M]_0 - [M]_t}{([CTA]_0 + df([I]_0(1 - ek_dt)))}\right).m_M + m_{CTA} \qquad \textbf{Equation 2.3}$$

where $[M]_0$ and $[M]_t$ are the concentration of monomer at t = 0 and t = t, respectively, m_M is the monomer relative molar mass, m_{CTA} is the relative molar mass of the CTA, and $[CTA]_0$ its corresponding initial concentration. The term $df([I]_0(1 - ek_dt))$ reflects the number of initiator-derived chains produced, where d is the average number of chains produced *via* radical-radical termination, f is the initiator efficiency, $[I]_0$ is its concentration, k_d its decomposition rate, and t is the time. In a well-controlled RAFT process, the contribution of this term can be neglected, leading to the commonly employed expression shown in Equation 2.4.[122]

$$M_n = \left(\frac{[M]_0 - [M]_t}{[CTA]_0}\right).m_M + m_{CTA} \qquad \textbf{Equation 2.4}$$
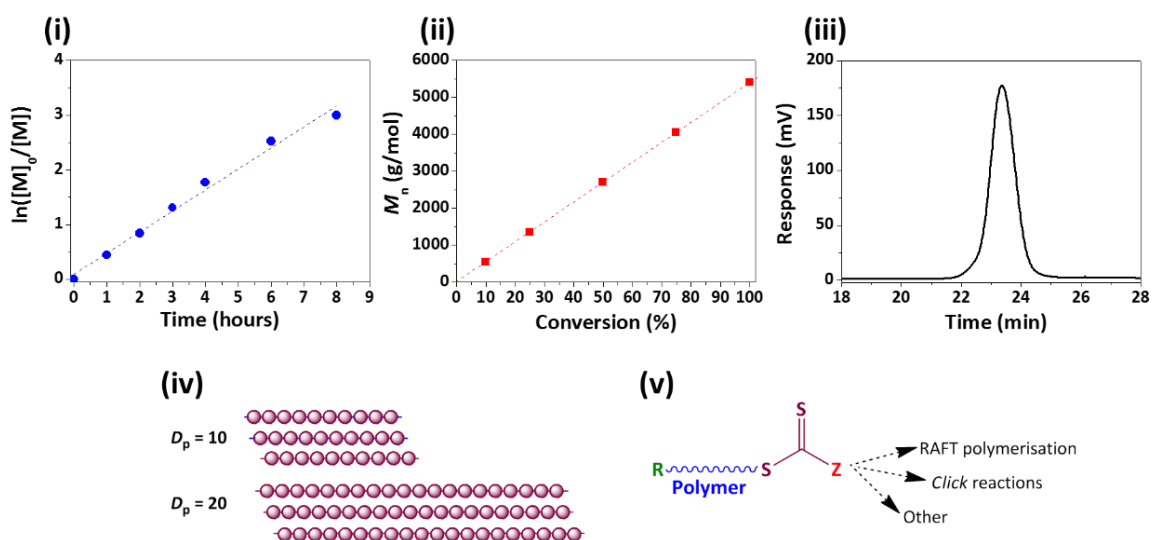
Figure 2.8. Experimental criteria for the assessment of RAFT polymerisation.

Overall, control in RAFT polymerisation can be demonstrated by evaluating the ensemble of the following parameters (Figure 2.8): (i) linearity of the *pseudo*-first order kinetic plot, (ii) linearity of the molar mass evolution with monomer conversion, (iii) narrowness and unimodal character of the molar mass distributions of the created polymers, (iv) accordance between the target and experimental D_p according to predefined stoichiometries, and (v) the ability of the final polymer to take part in subsequent chemical reactions or polymerisations *via* the chain end(s), owing to so-called end group fidelity (*i.e.* incorporation of the CTA end functional groups into the polymer chain).

2.1.3.4. Experimental conditions

The reaction conditions (solvent, temperature, pressure, stoichiometry, and concentration) play a decisive role in the course of polymerisation and in the characteristics of the obtained polymers using RAFT. Although RAFT polymerisation is compatible with numerous reaction media, from common organic solvents, to protic media or ionic liquids,[121] special attention needs to be paid to the CTA choice, as some CTAs have been shown to be prone to hydrolysis.[127] Besides, the solvent type used in free radical polymerisation can influence the polymerisation depending on the affinity of the growing polymer radical to the solvent, having a profound effect on the rate of polymerisation. Charge transfer between the macroradical and the solvent has been shown to reduce the rate of addition of incoming monomer and therefore decrease the rate of propagation.[128-129] However, comparing to the reports that describe marked solvent effects on the course of RAFT polymerisation, other consulted literature indicates that the solvent influence is insignificant, and often, negligible.[130-133]

Overall, higher temperatures lead to higher polymerisation rates, so that shorter reaction times are needed to achieve a given monomer conversion. Moreover, in some cases, increasing the temperature may diminish the retardation period associated with the CTA, and even improve molar mass distributions.[121] The use of very high pressures in RAFT polymerisation (*e.g.* 5 kbar) slows down termination processes, leading to higher polymerisation rates and higher molar mass polymers ($> 10^3$ kg mol^{-1}) than at ambient pressure.[121, 134-135]

As aforementioned, the $[M]_0/[CTA]_0$ ratio sets the theoretical degree of polymerisation, D_p. The $[CTA]_0/[I]_0$ ratio influences the degree of functionalisation of the created polymers, and modifying the $[M]_0/[I]_0$ ratio also has an effect on polymerisation rate. Besides, and frequently neglected in the literature, not only the ratio, but also the concentration of each species in solution, is a parameter which indeed influences the rate of the polymerisation process, *i.e.* higher monomer (and initiator)

concentration results in a higher rate of polymerisation.[122] The scarce reports that analyse the effect of dilution on the RAFT process show contrasting trends concerning the rate of polymerisation, the final monomer conversion achieved and the characteristics of the final polymer, in terms of D_p and dispersity.[131, 133, 136] Furthermore, bulk or highly concentrated systems can display diffusion-related effects, such as the aforementioned Trommsdorff effect (auto-accelerated polymerisation with increased molar masses due to limited diffusion in the system).[125]

2.1.4. Poly(*p*-styrene sulfonate)

As discussed in Section 2.1.1.1, poly(*p*-styrene sulfonate) (PSS) is employed as a polymeric dopant for the conducting material, poly(3,4-ethylenedioxythiophene) (PEDOT)[70, 137-138]. The resulting ionomeric mixture, PEDOT:PSS, is used in organic electronics, such as organic electrochemical transistors (OECTs),[3] organic solar cells (OSCs),[72] or organic light emitting diodes (OLEDs),[4] either as a hole transport layer[4, 70, 72, 139] or as an organic electrode, replacing ITO.[140] Moreover, PSS is an important material in a number of technologies in its own right, with application both in homopolymeric form and incorporated into different copolymers. For instance, it is employed in proton exchange membranes for fuel cells,[141-143] ion exchange materials,[144-145] in photonic sensors,[146] humidity sensors,[147-148] oil additives,[149] water softening,[150] polymeric stabilisers for emulsion polymerisation,[151] and various biomedical applications.[152-155]

The production of PSS is typically carried out *via* sulfonation of polystyrene using concentrated sulfuric acid,[156-157] acetyl sulfate,[148] or gaseous sulfur trioxide.[158] Alternatively, controlled radical polymerisation techniques have been exploited to obtain PSS with low molar mass dispersity directly polymerising corresponding sodium *p*-styrene sulfonate monomer using NMP,[151, 159-160] ATRP,[161-163] and RAFT.[119, 164-165] However, synthesis of PSS containing copolymers by post sulfonation of polystyrene using sulfonating agents is not easily controllable, especially at high sulfonation levels, due to the extremely different polarity between block segments.[166] Similarly, the incorporation of poly (*p*-styrene sulfonate) into hybrid materials with disparate polarities, such as amphiphilic block copolymers,[167-169] can be challenging due to the differing nature of constituents and the difficulty in finding a common solvent system. To circumvent this problem, Okamura *et al.*[97] reported a novel approach to produce amphiphilic PSS-containing copolymers by synthesising a sulfonate ester precursor, neopentyl *p*-styrene sulfonate (NSS), and converting it into its sulfonic derivative, either chemically or by thermal treatment, post polymerisation. This strategy has been subsequently adopted by several groups to

produce PSS-containing copolymers using different types of controlled radical polymerisation techniques; NMP,[170-172] ATRP,[166, 173-175] and RAFT[169] for a wide range of applications.

Given that this approach allows the use of common organic solvents during polymer synthesis, the material can be easily combined with other hydrophobic components, subsequently processed into thin films, and finally deprotected to restore the hydrophilic, ionic character of the sulfonic acid group. This procedure is therefore of great relevance to avoid the processing problems reported for organic electronics, for which the high polarity of PSS and corresponding restriction to polar solvents can create conflicts with other apolar device components, such as polythiophenes or fullerene derivatives.[6, 48, 176] Among the different researchers implementing this strategy, Thelakkat's group demonstrated the RAFT polymerisation of NSS for the first time to produce novel block copolymers for use in organic photovoltaics.[169]

2.1.5. Research focus

The first part of this chapter focuses on the optimisation of the synthetic procedure to obtain poly(neopentyl *p*-styrene sulfonate), PNSS, using Reversible Addition-Fragmentation chain Transfer Polymerisation. The controlled RAFT polymerisation of NSS is examined under a range of conditions, in order to identify an optimum system for producing well-defined PNSS with a systematically variable degree of polymerisation over a controlled molar mass range. To this end, two different CTAs, namely 2-azidoethyl 3-benzylsulfanylthiocarbonylsulfanylpropionate (BTTC-N$_3$) and 2-azidoethyl 2-(dodecylthiocarbonothioylthio)-2-methylpropionate (DTTC-N$_3$), have been investigated, as well as the effect of temperature (60 *versus* 75 °C), diluent (THF, anisole, toluene) and monomer concentration. Once identified, the most successful polymerisation conditions were examined further in order to prepare PNSS with varying molar masses by altering the $[NSS]_0:[DTTC-N_3]_0$ ratio. Finally, to demonstrate the utility and versatility of this approach, whilst simultaneously confirming the presence of the azide moiety on the end of our polymer chains, PNSS-N$_3$ has been 'clicked' to bisalkyne-functionalised polybutadiene, PBD-dialkyne, to produce a hydrophobic block copolymer, PNSS-*b*-PBD-*b*-PNSS. Thermal deprotection of the latter yields an amphiphilic triblock copolymer with poly(*p*-styrene sulfonate) (PSS) end blocks.

The second part of the work concentrates firstly on the surface characterisation of P3HT-*b*-PNSS block copolymers (both pristine and thermally annealed) by means of Atomic Force Microscopy (AFM), used in Tapping Mode and QNM Peak Force Mode. Two block copolymers with

varying PNSS block lengths (P3HT$_{50}$-b-PNSS$_{10}$, P3HT$_{50}$-b-PNSS$_{30}$) and the corresponding individual polymers (P3HT$_{150}$ and PNSS$_{30}$) were separately characterised in terms of roughness, surface morphology, and nanomechanical properties (adhesion tip-sample). Nanomechanical information was also obtained from P3HT:PCBM and PEDOT:PSS, and the effect of the annealing treatment on the active layer was assessed. Finally, in the quest for more readily cleavable protecting groups, which diminish the detrimental effects that thermal treatment can provoke on the active layer and/or the organic solar cell, RAFT polymerisation was explored for the preparation of a series of sulfonate polymers bearing different linear and branched aliphatic protecting groups, namely: n-propyl, isopropyl, n-butyl, isobutyl, n-pentyl, and neopentyl. The thermal deprotection of which was explored using thermogravimetric analysis (TGA). The PSS precursor displaying the most convenient deprotection behaviour (in terms of ease of deprotection and stability at room temperature) was poly(isobutyl p-styrene sulfonate) PiBSS, which was subsequently incorporated into a block copolymer with P3HT (P3HT-b-PiBSS) and then compared to its PNSS counterpart (P3HT-b-PNSS).

2.2. Experimental

2.2.1. Materials

Dimethylformamide (DMF), diethyl ether, methanol (MeOH), dichloromethane (DCM), hexane and ethyl acetate (Laboratory Reagent grade), hexane (Laboratory Reagent grade) were purchased from Fisher Scientific and used as supplied. Sodium chloride (99 %), anhydrous magnesium sulfate (99.5 %), pyridine (99 %) and hydrochloric acid (HCl, 36.5 - 38 %) were purchased from Alfa Aesar, and were all used as received. Thionyl chloride (97 %), sodium-4-styrene sulfonate (technical grade, ≥ 90 %), neopentyl alcohol (99 %), dicarboxy-terminated polybutadiene (M_n ~4200 g mol^{-1}; trans-1,4 = 45 − 65 %, cis-1,4 = 20 − 45 %, vinyl = 13 − 30 %), N,N'-dicyclohexylcarbodiimide (DCC, 99 %) 4-dimethylaminopydridine (DMAP, ≥ 99 %), propargyl alcohol (99 %), copper(I) iodide (99.999 %), triethylamine (≥ 99.0 %), anhydrous tetrahydrofuran (THF, ≥ 99.9 %), anhydrous anisole (≥ 99.9 %), and anhydrous toluene (≥ 99.9 %), and acetone (≥ 99.5 %), were purchased from Sigma Aldrich and used without further purification. Chloroform-d (99.8 % At + 0.05 % TMS, Goss Scientific) and 2,2'-azobis(2-methylpropionitrile) (AIBN, TCl), were used as supplied. 2-Azidoethanol,[177] 3-benzylsulfanylthiocarbonylsulfanylpropionic acid (BTTC),[178] and 2-azidoethyl 2-(dodecylthiocarbonothioylthio)-2-methylpropionate (DTTC-N$_3$)[179] were synthesised according to previous literature procedures. Highly regioregular (> 98 %) P3HT (M_n = 26 kg mol^{-1}, Đ = 1.5) was purchased from BASF. PCBM (99.5 %) was obtained from SES Research Inc. PEDOT:PSS (Clevios HTL Solar) was obtained from Heraeus GmbH. P3HT-*b*-PNSS block copolymers were synthesised by Dr. Harikrishna Erothu, Marie Curie Fellow at Aston University working on the ESTABLIS satellite project SYNABCO.[111] Systematically varied R-protected *p*-styrene sulfonate polymers in Section 2.3.2.3 were synthesised by Joanna Kolomanska, ESR7 in the ESTABLIS project, as described in the literature.[180]

2.2.2. Methods

2.2.2.1. Characterisation

2.2.2.1.1. <u>NMR/GPC</u>

NMR spectroscopy (Bruker Avance ^{1}H 300 MHz, ^{13}C 75 MHz, CDCl$_3$) was used to determine monomer conversion, whereas polymer molar mass (M_n) and dispersity (Đ, M_w/M_n) were measured using gel permeation chromatography (GPC). The GPC systems, operated at 40 °C, were composed of three PL gel 5 μm 300 x 7.5 mm mixed-C columns or two PL gel 10 μm 300 x 7.5 mm mixed-B columns and one PL gel 5 μm 300 x 7.5 mm mixed-C column. In both cases, degassed THF containing 2 % (v/v)

TEA was used as the eluent, at a flow rate of 1 mL min^{-1}. The columns were calibrated with narrow polystyrene standards (M_p = 162 - 6 035 000 g mol^{-1}) and data were analysed using either PL Cirrus software 2.0 or GPC Analysis software packages, which were both supplied by Agilent Technologies.

2.2.2.1.2. FTIR

Fourier transform infrared (FTIR) spectra were accumulated over 16 scans in attenuated total reflectance (ATR) mode using a Thermo Nicolet 380 FTIR spectrophotometer over the range 400-4000 cm^{-1} and a resolution of 4 cm^{-1}. For P3HT-*b*-PNSS samples only, Infrared spectra were recorded by a Thermo Nicolet 760 Magna spectrophotometer working in transmission mode and purged with dry air over the range 400-4000 cm^{-1}, using 32 acquisitions with 4 cm^{-1} resolution.

2.2.2.1.3. TGA

A Mettler Toledo TGA/DSC 1 thermogravimetric analyser (TGA) with StarE software was used to measure the weight changes in PNSS-N$_3$ and PNSS-*b*-PBD-*b*-PNSS as a function of annealing time at 150 °C. Samples of the materials (ca. 5 mg) were accurately weighed into alumina pans. Isothermal analyses were performed at 150 °C for two hours in a N$_2$ atmosphere (flow rate: 75 mL min^{-1}).

For the varying alkyl-protected polymers, 3-4 mg sample of the polymer was placed in a TGA pan and measurements were performed in two modes, a temperature sweep from 25 to 500 °C (at a rate of 10 °C min^{-1}) and an isothermal profile (150 °C) for 120 min.

2.2.2.1.4. Contact angle measurements

The wetting properties of the copolymers were studied using a GBX Digidrop CAM apparatus. Sessile drop static contact angle measurements were made with ultrapure H$_2$O (Fluka). A drop of pure water (2 µL) was released from the Teflon tip of a syringe onto the sample surface. The equilibrium contact angle (ϑ_e) values reported are the average of 15 measurements taken at three locations on the substrate surface.

2.2.2.1.5. P3HT-*b*-PNSS thin films deposition and deprotection

Polymer thin films were coated on glass/KBr substrates *via* doctor blading. P3HT-*b*-PNSS films were deposited from a polymer solution 0.5 mg mL^{-1} in acetone, filtered through a 0.45 µm PTE filter. Thermal deprotection of the polymers was carried out on a hot plate at 150 °C over a period of 5 hours, under inert atmosphere (N$_2$, glovebox).

2.2.2.1.6. <u>AFM analysis</u>

Samples were analysed by an Atomic Force/Scanning Probe Microscope (AFM/SPM) Multimode equipped with an RTESPA probe [0.01- 0.025 Ω cm Antimony (n) doped Si], from Bruker, recommended for samples with Young's modulus comprised between 200 MPa and 2 GPa. Measurements were performed using classical Tapping Mode and PeakForce Quantitative Nanomechanics (QNM) Tapping Mode.

(a)

(b)
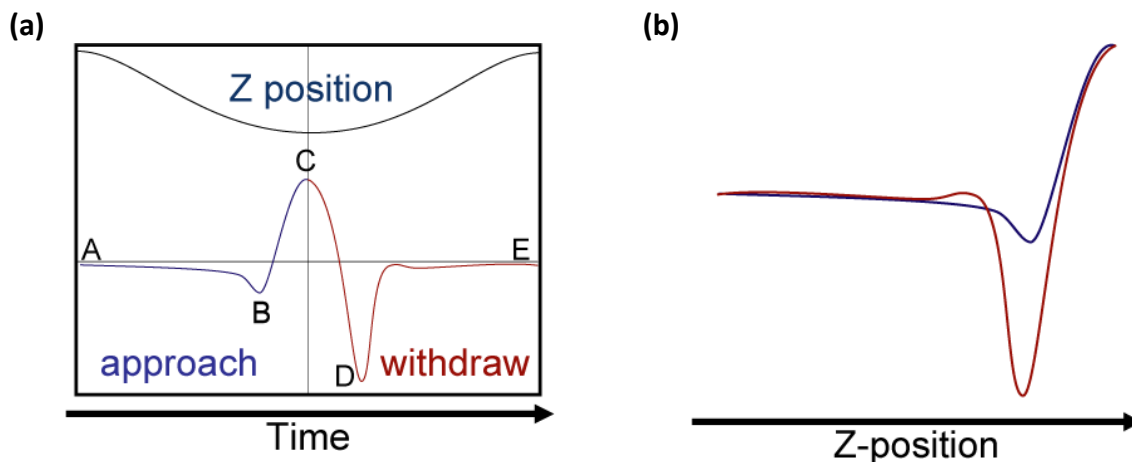
Figure 2.9. Typical force representations obtained from AFM PeakForce QNM.

PeakForce QNM (Quantitative NanoMechanics) allows the collection of quantitative nanoscale material properties such as modulus, adhesion, deformation, and dissipation, *via* the application of a small controlled force with each individual tap of the probe to the sample surface. Accordingly, force curves are recorded at every pixel in the image, and their analysis on the fly allows imaging feedback signals to be obtained corresponding to multiple mechanical properties, together with classical height images. The force *versus* time plot, also known as the 'heartbeat', is displayed in Figure 2.9 (a). The blue line indicates the approach of the probe to the sample, from the initial equilibrium position (A) until the contact point (B), and continuing until the peak force point (C). The red line indicates the withdrawal of the probe from the sample. The extra force (in comparison with point B) displayed in point D, indicates the adhesion forces between tip and sample. The cantilever comes back to its equilibrium position, and a zero force is acquired again (E). Using the Z-position information, the heartbeat can be transformed into a Force – Displacement curve, as shown in Figure 2.9 (b). Analysis of such force curves allows quantification of the nanomechanical properties of a material, as displayed in Figure 2.10. This analysis is automatically performed by the software to obtain feedback images corresponding to the different parameters (Young's Modulus, Adhesion, Deformation…),

see Figure 2.11. Alternatively, 'lines' of force curves can be extracted (Figure 2.12) and manually analysed (Figure 2.13).
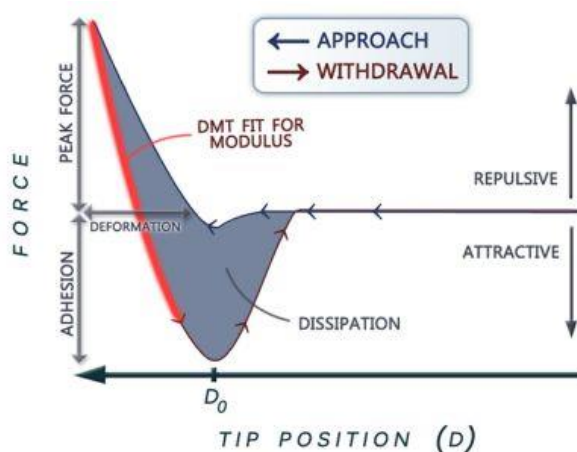
Figure 2.10. Analysis of the approach (trace) and withdraw (retrace) force curves to obtain quantitative nanomechanical properties. Obtained from reference 181.

Quantitative information was obtained after calibration of the probe against a sapphire reference sample, to obtain the values of deflection sensitivity (45 nm V^{-1}) and cantilever spring constant (28.79 Nm^{-1}). Accurate values of DMT Modulus[182] were obtained by adjusting Tip Radius (40.0 nm) and Tip Half Angle (10°) using two other reference samples (polystyrene film, 2.7 GPa and PDMS—Gel, 3.7 MPa). After which, samples under study were measured adjusting Peak Force Set Point so that the resulting deformation depths matched those used during imaging of the reference samples (~5 nm).

It must be noted that in this work, priority was given to obtain high-quality mechanical information from PeakForce measurements and this can sometimes compromise the quality of the recorded height images. Thus, height images presented herein stem from AFM working in classical Tapping Mode, and the rest of the information was obtained from PeakForce QNM mode.

Roughness values

Roughness (R_q) values were calculated as the average of the individual values obtained for three 5 x 5 μm height images, recorded at different points of the sample surface.

Nanomechanical properties (adhesion)

Adhesion values for each sample were obtained as the average of the mean values calculated for three 5 x 5 μm images (adhesion channel), recorded at different points on the sample surface.
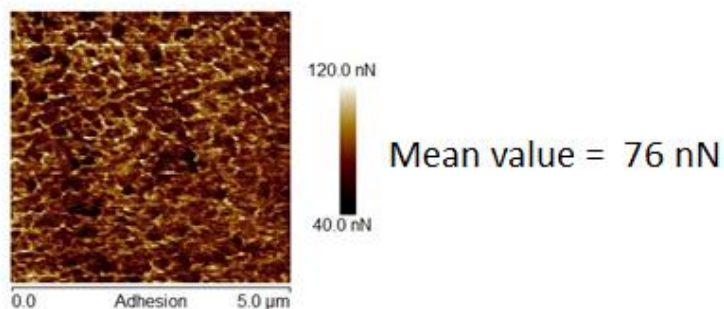
Figure 2.11. Image recorded in the adhesion channel for a pristine sample of P3HT.

The general procedure to obtain the average trace and retrace curves consisted of firstly capturing two force curves in two different areas of the surface, as displayed in Figure 2.12. Then, three representative pairs of curves (trace/retrace) were exported for each data set (captured lines 1 and 2), and separately averaged to obtain the average trace and retrace curves, see Figure 2.13. Curves with anomalous behaviour were discarded. A minimum of three pairs of lines was analysed in all cases.

(a)   **(b)**
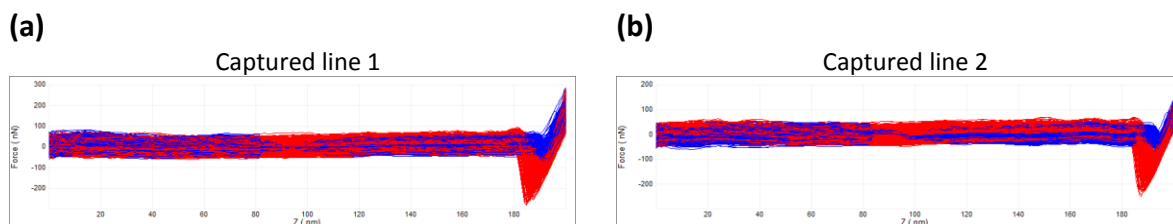
Figure 2.12. Force-displacement curves registered for a pristine PNSS sample. For each data set, the tip was scanning a different surface position.

(a)   **(b)**
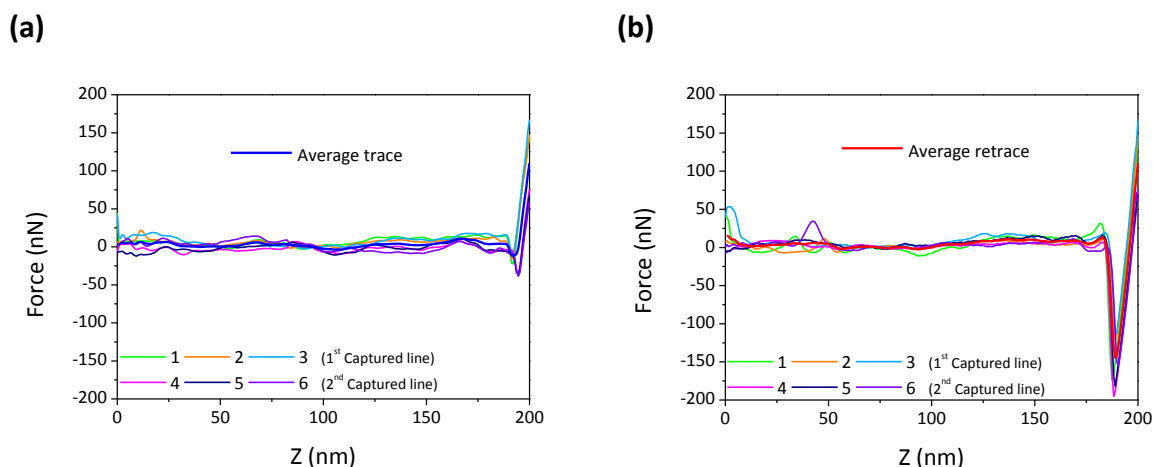
Figure 2.13. General procedure to calculate the average trace (a) and retrace (b) for a particular sample, in this case pristine PNSS.

2.2.2.2. Synthetic procedures

2.2.2.2.1. <u>Monomer synthesis (NSS)</u>

The two-step synthesis of neopentyl *p*-styrene sulfonate (NSS), *via p*-styrene sulfonyl chloride, was performed according to previously reported procedures.[97, 183] The reaction scheme is depicted in Scheme 2.4.
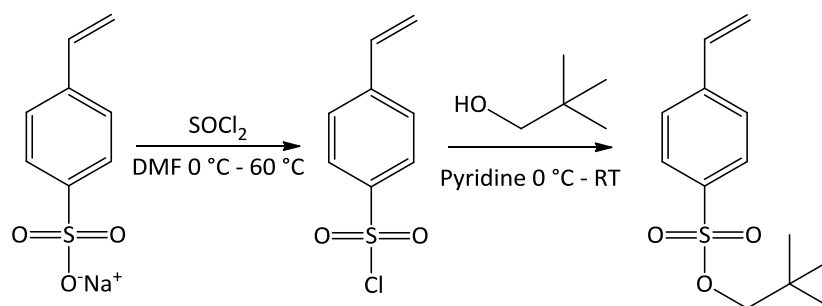
Scheme 2.4. Reaction scheme for the two-step synthesis of neopentyl *p*-styrene sulfonate (NSS).

Synthesis of p-styrene sulfonyl chloride

The synthesis of *p*-styrene sulfonyl chloride was carried out according to the literature with slight modifications.[183] Sodium-4-styrene sulfonate (60 g, 0.29 mol) was slowly added to 200 mL of DMF under a nitrogen atmosphere. The solution was cooled down to 0 °C in an ice bath with stirring maintained for 15 minutes. Subsequently, thionyl chloride (160 mL, 2.205 mol) was added drop-wise to the solution and the reaction mixture was kept stirring for a further 10 minutes at 0 °C before being heated to 60 °C for 6 hours. The mixture was slowly poured into ice-cold water (1 litre) and extracted with several portions of diethyl ether (3 × 200 mL). Finally, the combined organic layers were dried over magnesium sulfate, filtered, and then the solvent was removed under reduced pressure. The resulting product (yellow oil) was completely dried on a vacuum line, and then used in the next step without further purification (44 g, 73 %). The full characterisation has been described elsewhere.[183]

Synthesis of neopentyl p-styrene sulfonate (NSS)

Neopentyl *p*-styrene sulfonate (NSS) was prepared according to the literature procedure with minor modifications.[97] Neopentyl alcohol (21 g, 0.24 mol) was dissolved in pyridine (62.0 mL, 0.77 mol), cooled to 0 °C and then *p*-styrene sulfonyl chloride (44 g, 0.22 mol) was added drop-wise to the solution. The reaction mixture was allowed to return to room temperature and stirred overnight. Following which, the solution was poured onto HCl (1 % solution, 500 mL) and extracted with several

portions of diethyl ether (3 x 200 mL). The organic extracts were combined, washed with water and brine, and dried overnight with magnesium sulfate. After removal of magnesium sulfate by filtration and solvent by evaporation, hexane (300 mL) was added. The mixture was heated to 65 °C and stirred for 15 minutes before the solution was separated from solids by decantation. Hexane was removed under vacuum to give the product (29 g, 52 %) as white crystals. ^{1}H NMR in CDCl$_3$ (δ, ppm): 0.89 (s, 9H), 3.67 (s, 2H), 5.46 (d, 1H, J = 10.8 Hz), 5.90 (d, 1H, J = 17.7 Hz), 6.75 (dd, 1H , J = 17.4, 11.1 Hz), 7.55 (d, 2H, J = 8.4 Hz), 7.85 (d, 2H, J = 8.4 Hz) (Figure 2.14). ^{13}C NMR in CDCl$_3$ (δ, ppm): 26.0, 31.7, 79.6, 118.0, 126.7, 128.3, 135.2, 142.8.
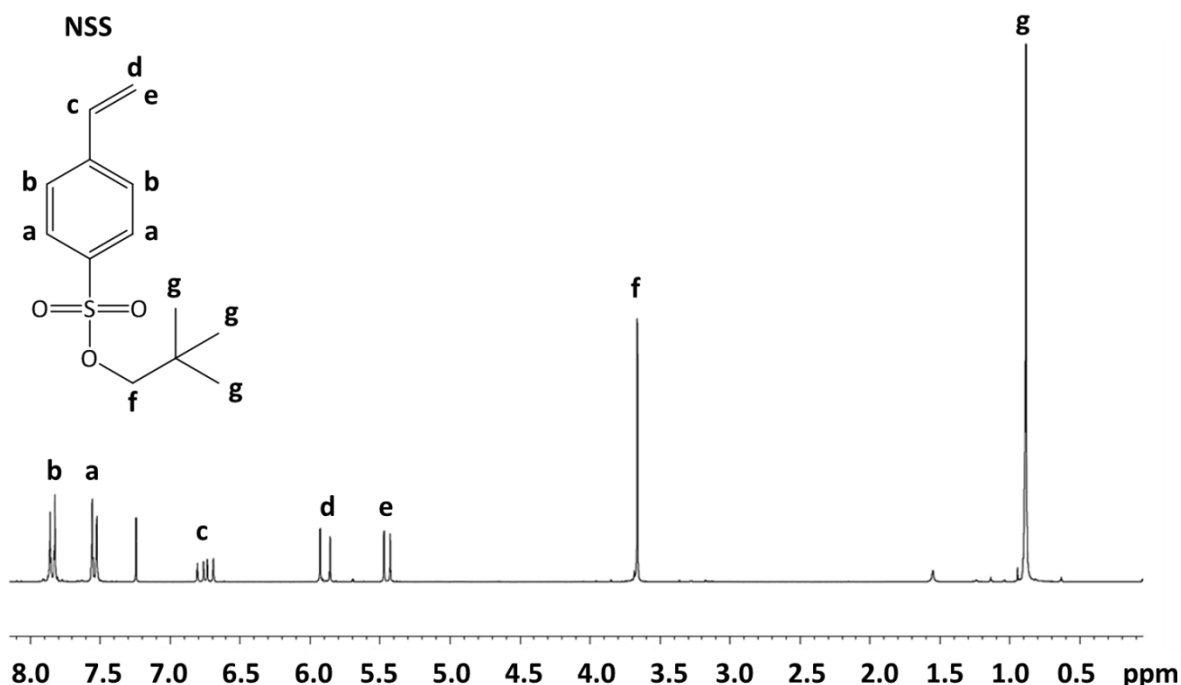
Figure 2.14. ^{1}H NMR spectrum of neopentyl *p*-styrene sulfonate.

2.2.2.2.2. Synthesis of 2-azidoethyl 3-benzylsulfanylthiocarbonylsulfanylpropionate (BTTC-N$_3$)
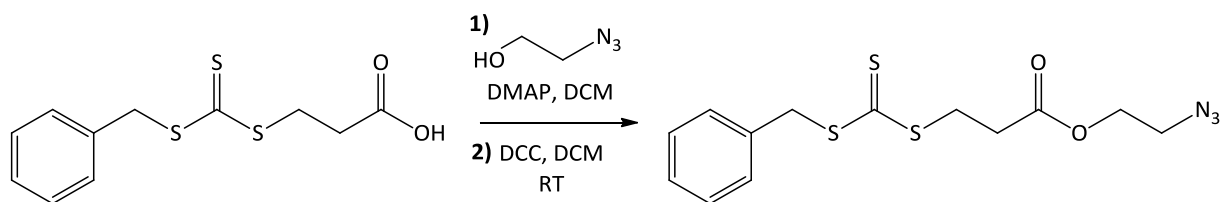
Scheme 2.5. Synthesis of 2-azidoethyl 3-benzylsulfanylthiocarbonylsulfanylpropionate (BTTC-N$_3$).

According to Scheme 2.5, 3-benzylsulfanylthiocarbonylsulfanylpropionic acid (BTTC, 15.0 g, 55 mmol), 4-dimethylaminopyridine (3.3 g, 27 mmol) and 2-azidoethanol (9.6 g, 110 mmol) were dissolved in DCM (500 mL). The reaction was stirred for 15 minutes at room temperature under nitrogen, to which a solution of *N,N'*-dicyclohexylcarbodiimide (DCC, 11.3 g, 55 mmol) in DCM (150 mL) was slowly added and the resulting mixture was then stirred at room temperature for 48 h. Following filtration, DCM was removed under reduced pressure and the resulting crude product was purified by column chromatography using hexane:ethyl acetate as eluent (95:5 v/v) to give the azide-functionalised chain transfer agent, BTTC-N$_3$ (15.6 g, 83 %) as a yellow oil. ^{1}H NMR in CDCl$_3$ (δ, ppm): 2.83 (t, 2H, *J* = 6.9 Hz), 3.47 (t, 2H, *J* = 5.9 Hz), 3.65 (t, 2H, *J* = 6.9 Hz), 4.28 (t, 2H, *J* = 5.4 Hz), 4.61 (s, 2H), 7.32 (m, 5H). ^{13}C NMR in CDCl$_3$ (δ, ppm): 31.1, 33.0, 41.5, 49.7, 63.4, 127.8, 128.8, 129.3, 171.1.

2.2.2.2.3. <u>RAFT polymerisation of neopentyl *p*-styrene sulfonate (NSS)</u>
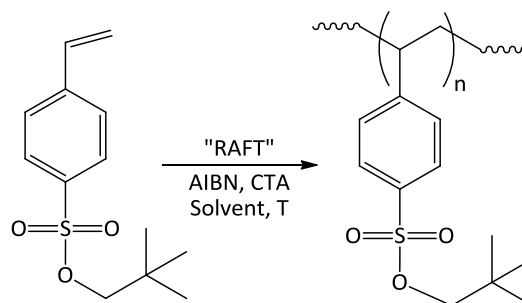
Scheme 2.6. Reaction scheme for the synthesis of poly(neopentyl *p*-styrene sulfonate).

RAFT polymerisation of neopentyl *p*-styrene sulfonate (NSS) was carried out according to Scheme 2.6. The great majority of polymerisations undertaken in this work were performed according to initial conditions [AIBN]$_0$/[CTA]$_0$/[NSS]$_0$ = 0.3/1/20, indicating a target degree of polymerisation (D_p) of 20. In experiments targeting polymers of D_p 100 and 200, the ratio [AIBN]$_0$/[CTA]$_0$/[NSS]$_0$ was varied to 0.3/1/100 and 0.3/1/200, respectively. A 25 mL round bottomed flask, equipped with a magnetic follower, was charged with a mixture of NSS (1 g, 4 mmol), AIBN (10 mg, 0.06 mmol), BTTC-N$_3$ or DTTC-N$_3$ (0.2 mmol), and anhydrous solvent; THF, anisole, or toluene (1, 3 or 5 mL, corresponding to monomer concentrations of 4.0, 1.3 and 0.8 mol dm^{-3}, respectively) under inert atmosphere. The solution was stirred and purged with nitrogen for 15 minutes. Following which, the solution was left under a positive pressure of nitrogen, with stirring, the flask sealed and placed in an oil bath at 60 °C or 75 °C. Aliquots of the solution were taken periodically and the polymerisation was monitored up to high conversion using ^{1}H NMR spectroscopy and gel permeation chromatography (GPC).

The percentages of monomer conversions were calculated by comparison between the region assigned to vinyl terminal protons of the monomer (δ = 5.4 - 5.8 ppm) and the aromatic area, comprising signals of both the growing polymer and the monomer (δ = 7.8 - 7.5 ppm), see Figure 2.15.
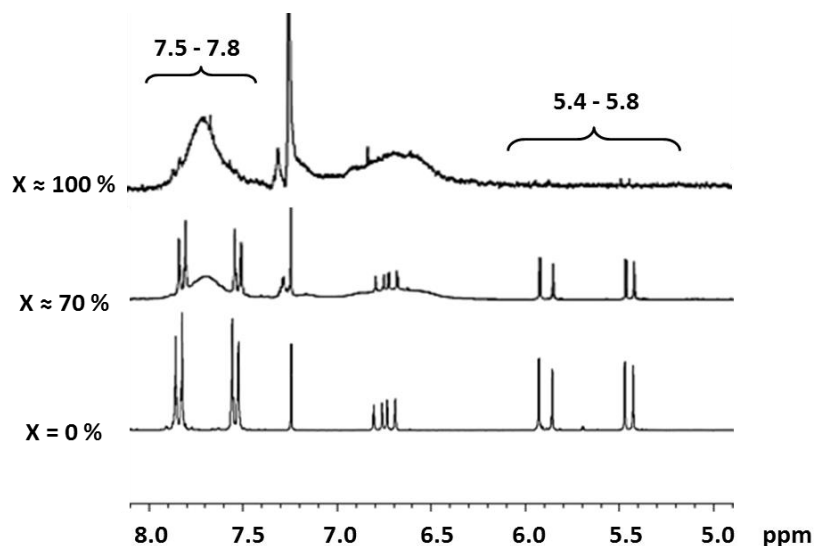
Figure 2.15. ^{1}H NMR spectra corresponding to different stages in the polymerisation of neopentyl *p*-styrene sulfonate in the range δ = 5 − 8.0 ppm. X denotes the monomer conversion (%).

Termination proceeded by rapidly cooling the reaction mixture in ice. Subsequently, the mixture was diluted with 2 mL of THF, and the resulting polymer solution was reprecipitated into 150 mL of methanol. The pale yellow solid was isolated by filtration and dried under vacuum. ^{1}H NMR in CDCl$_3$ (δ, ppm): 0.91 (br, 9H), 1.52 (br, 2H), 1.82 (br, 1H), 3.75 (br, 2H), 6.70 (br, 2H), 7.70 (br, 2H) (see Figure 2.16). Selected IR bands (ATR, cm^{-1}): 2951 m, 2947 m, 2883 w, 2116 w, 1743 w, 1595 w, 1482 m, 1418 m, 1352 s, 1310 w, 1281 w, 1179 s, 1097 m, 1072 w, 1050 w, 992 w, 956 s, 947 s, 833 s, 466 m.

PNSS
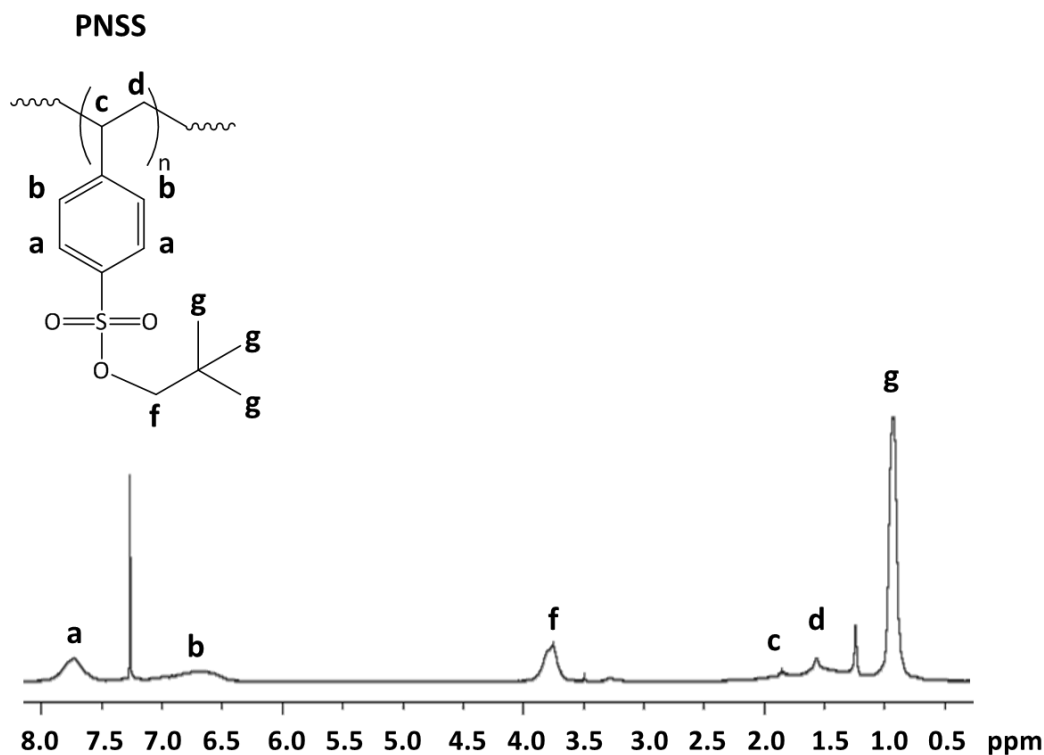
Figure 2.16. ^{1}H NMR spectrum of poly(neopentyl *p*-styrene sulfonate).

2.2.2.2.4. Synthesis of bisalkyne-terminated polybutadiene (PBD-dialkyne)
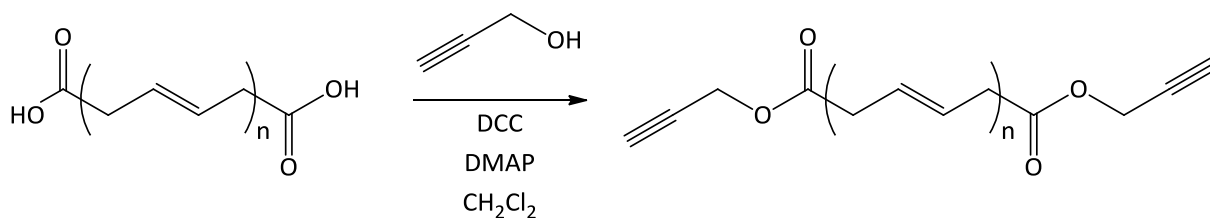
Scheme 2.7. Synthesis of PBD-dialkyne by post-polymerisation functionalisation.

PBD-diCOOH (1.0 g, 0.24 mmol, based on M_n 4,200 provided by supplier), propargyl alcohol (55 µL, 0.95 mmol) and DMAP (11.6 mg, 0.1 mmol) were dissolved in anhydrous DCM (5.0 mL), and the mixture was cooled to 0 °C in an ice bath. A solution of DCC in DCM (950 µL, 1.0 M) was added by syringe. After 1 h, the solution was warmed to room temperature and left to stir overnight. The solids were removed by filtration, and the solvent was evaporated from the filtrate to give a colourless viscous material. Residual propargyl alcohol was removed by washing the polymer repeatedly with MeOH (3 x 5 mL), and drying *in vacuo* (0.1 mmHg, 8 h).

Recovery: 0.88 g (86.3 %). ^{1}H NMR in CDCl$_3$ (δ, ppm): 1.28-1.60 (br m, 0.8H, **e**), 2.03 (br s, 4H, **c** and **f**), 3.20 (s, 0.01H, **a**), 4.70 (d, J = 2.4 Hz, 0.03H, **b**), 4.85-5.10 (m, 0.4H, **h**), 5.20-5.70 (m, 2H, **d** and **g**). Selected IR bands (ATR, cm^{-1}): 3076 w, 3012 w, 3004 w, 2914 m, 2843 m, 2125 w, 1745 w, 1640 w, 1449 m, 1361 w, 1318 w, 1255 w, 1184 w, 1097 w, 1053 w, 964 s, 913 m, 733 m, 691 m. GPC (RI) M_n 9300; M_w/M_n 1.76.
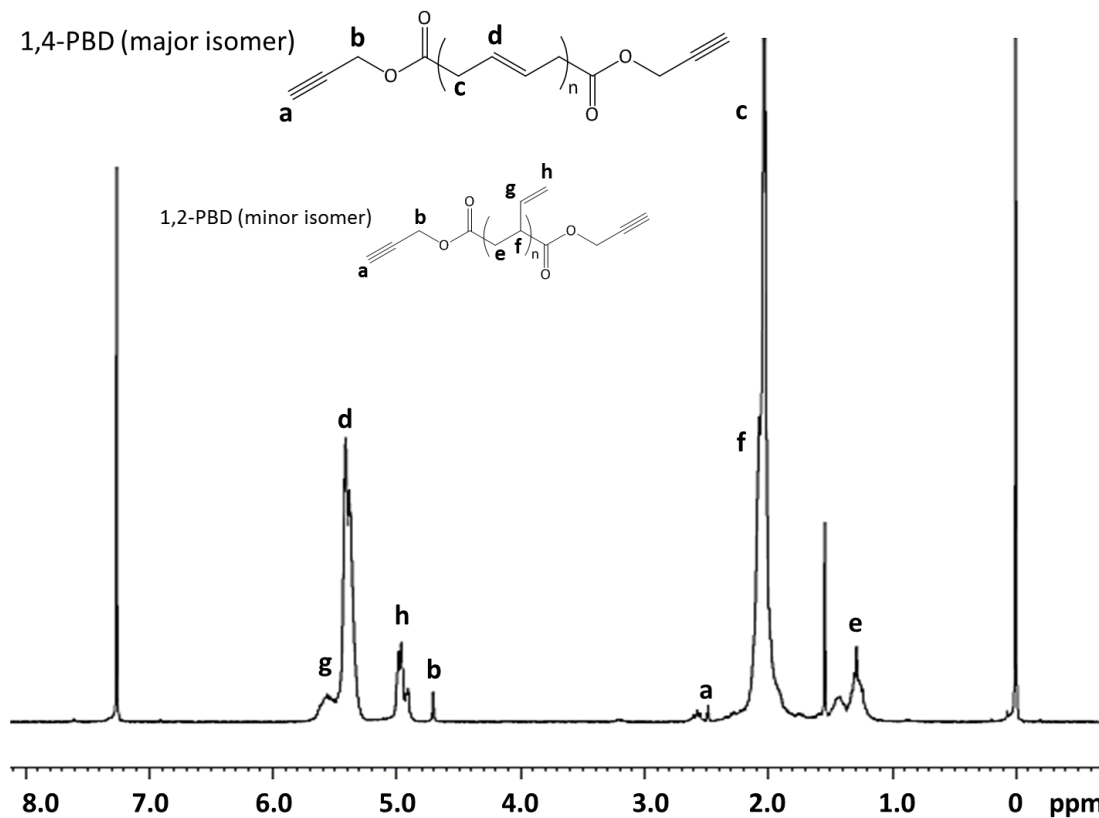
Figure 2.17. ^{1}H NMR spectrum of PBD-dialkyne.

2.2.2.2.5. <u>Synthesis of triblock copolymer, poly(neopentyl *p*-styrene sulfonate)-*block*-polybutadiene- *block*-poly(neopentyl *p*-styrene sulfonate), PNSS-*b*-PBD-*b*-PNSS</u>
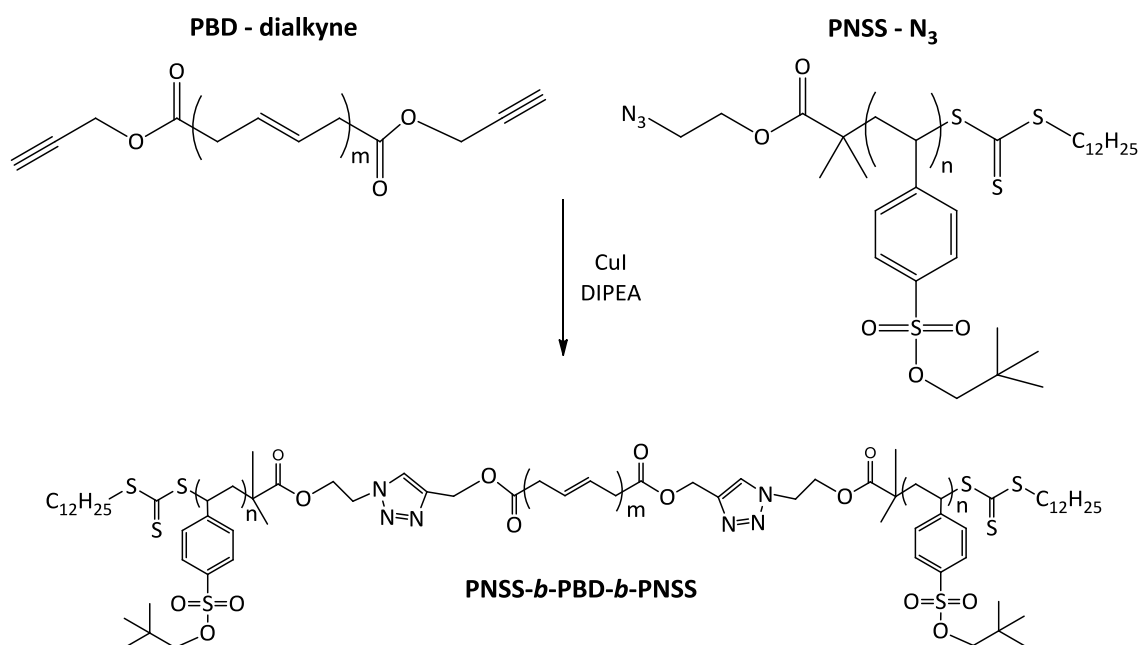
Scheme 2.8. Synthesis of PNSS-*b*-PBD-*b*-PNSS *via* azide-alkyne 'click' coupling. N.B. Only the major *trans*-1,4 isomer of polybutadiene is shown.

For the synthesis of PNSS-*b*-PBD-*b*-PNSS block copolymer (Scheme 2.8), PBD-dialkyne (200 mg, 47 µmol; using the M_n value provided by the supplier plus the mass of groups introduced at the termini, 4,278 g mol⁻¹, and not the GPC M_n value of 9300 g mol⁻¹, which is relative to polystyrene standards), PNSS-N₃ (560 mg, 191 µmol), and CuI (89 mg, 467 µmol) were subjected to three cycles of evacuation and backfilling with N₂ (5 min). THF (20 mL) was added and the mixture was degassed with bubbling N₂ (0.5 h). DIPEA (1.0 mL) was added by syringe and the mixture was stirred at 50 °C for 24 h. The solution was filtered through neutral Al₂O₃ to remove Cu salts, concentrated *in vacuo* to a volume of ca. 5 mL, then poured into MeOH (50 mL) to precipitate the polymer. The polymer was isolated by filtration and dried *in vacuo* (150 mbar, 16 h). Recovery: 190 mg (40.1 %). ¹H NMR (300 MHz, CDCl₃) δ_H, ppm: 0.93 (br s, 18H), 1.10-1.70 (br m, 15H), 2.03 (br s, 46H), 3.24 (br s, 0.14H), 3.75 (br s, 4H), 4.43 (br s, 0.11H), 4.91-4.99 (br m, 5H), 5.22 (br s, H), 5.38-5.56 (br m, 23H), 6.50-7.20 (br m, 4H), 7.50-7.90 (br m, 4H). Selected IR bands (ATR, cm⁻¹): 3087 w, 2920 m, 2846 w, 1740 w, 1646 w, 1601 w, 1481 w, 1451 w, 1420 w, 1360 m, 1314 w, 1279 w, 1180 s, 1103 w, 964 s, 915 m, 832 s, 685 w, 657 m, 587 s, 468 w. GPC (RI): M_n 19300 g mol⁻¹, M_w/M_n = 1.29.

2.2.2.2.6. <u>Thermolysis of poly(neopentyl *p*-styrene sulfonate), PNSS, to poly(*p*-styrene sulfonate), PSS</u>

PNSS-*b*-PBD-*b*-PNSS (25 mg) was dissolved in DCM (750 μL) and a film sample was prepared by depositing 50 μL of the polymer solution onto a glass cover slip. The sample was left in a covered petri dish for 2 h in order to evaporate the majority of the solvent, and residual DCM was removed *in vacuo* (120 mbar, 4 h). Following which, the film was heated at 150 °C for 2 h under a constant flow of N$_2$ in order to remove the neopentyl protecting groups from the PNSS blocks, generating hydrophilic PSS segments. Selected IR bands for PSS-*b*-PBD-*b*-PSS (ATR, cm^{-1}): 3387 br, 2926 s, 2851 s, 1707 m, 1600 w, 1501 w, 1445 m, 1411 w, 1365 w, 1127 s, 1035 s, 1003 s, 965 s, 909 m, 829 m, 772 w, 674 m, 578 m.

2.3. Results and discussion

2.3.1. Controlled synthesis of poly(neopentyl *p*-styrene sulfonate) *via* RAFT polymerisation

The work described in this Section 2.3.1 corresponds to the following article:

Fraga Domínguez, I.; Kolomanska, J.; Johnston, P.; Rivaton, A.; Topham, P. D., Controlled Synthesis of Poly(Neopentyl *p*-Styrene Sulfonate) *via* Reversible Addition-Fragmentation Chain Transfer Polymerisation. *Polymer International* **2015**, *64*, 621-630.

The controlled polymerisation of neopentyl *p*-styrene sulfonate (NSS) was performed using Reversible Addition-Fragmentation Chain Transfer Polymerisation (RAFT). In order to optimise the conditions for the preparation of well-defined poly(neopentyl *p*-styrene sulfonate) (PNSS), the effect of chain transfer agent (CTA), monomer concentration, solvent and temperature, on the polymerisation kinetics and the quality of the final polymer, has been assessed systematically, as shown in Table 2.1.

2.3.1.1. CTA choice

Initial screening was undertaken to identify a suitable CTA for the RAFT polymerisation of neopentyl *p*-styrene sulfonate (NSS). The CTAs selected were 2-azidoethyl 3-benzylsulfanylthio-carbonylsulfanylpropionate (BTTC-N$_3$) and 2-azidoethyl 2-(dodecylthiocarbonothioylthio)-2-methylpropionate (DTTC-N$_3$), which differed in the Z stabilising group; aliphatic chain (DTTC-N$_3$) or aliphatic ester with terminal azide functionality (BTTC-N$_3$) attached to sulfur, and in the R leaving group radical; tertiary (DTTC-N$_3$) or primary (BTTC-N$_3$) (as shown in Figure 2.18). These trithiocarbonates were selected based on their previous success (in their carboxylic acid or azide-functionalised form) for polymerising more-activated monomers (MAMs), such as styrene,[184-185] *N,N*-dimethylacrylamide,[184] methyl methacrylate,[185] *N*-isopropylacrylamide,[186-188] ethyl acrylate, acrylic acid, and *N-tert*-butyl acrylamide.[189] Furthermore, the azide functionality was designed in our work to furnish each homopolymer with a handle to allow linkage to other materials (*via* 'click' chemistry).[190-193] This provides access to well-defined functional, hybrid or block copolymer materials using facile coupling chemistry of otherwise incompatible building blocks.

Table 2.1. Summary of reaction conditions, molar mass data, and monomer conversions of the polymerisation of neopentyl *p*-styrene sulfonate.

Exp.	Solvent	T °C	[M] mol dm^{-3}	CTA	Time h	M_n[a] g mol^{-1}	D_p[a,b]	Đ[a] (M_w/M_n)	Monomer conversion[c] %
1	THF	75	0.80	BTTC-N$_3$	96	5600	21	1.26	97
2	THF	75	0.80	DTTC-N$_3$	96	4400	17	1.14	98
3	Anisole	75	0.80	BTTC-N$_3$	145	4300	16	1.23	67
4	Anisole	75	0.80	DTTC-N$_3$	145	2500	8	1.10	60
5	Toluene	75	0.80	BTTC-N$_3$	117	4200	15	1.16	52
6	Toluene	75	0.80	DTTC-N$_3$	117	2100	7	1.08	53
7	THF	60	0.80	BTTC-N$_3$	196	7200	27	1.28	92
8	THF	60	0.80	DTTC-N$_3$	196	3800	13	1.21	98
9	THF	60	1.3	DTTC-N$_3$	48	4100	14	1.07	99
10	THF	60	4.0	DTTC-N$_3$	24	4000	14	1.13	98
11	Anisole	60	0.80	DTTC-N$_3$	72	2500	8	1.07	70
12	Anisole	60	1.3	DTTC-N$_3$	48	3200	11	1.07	90
13	Anisole	60	4.0	DTTC-N$_3$	24	4000	14	1.08	95
14	Toluene	60	0.80	DTTC-N$_3$	72	3400	12	1.08	86
15	Toluene	60	1.3	DTTC-N$_3$	48	3700	13	1.08	89
16	Toluene	60	4.0	DTTC-N$_3$	24	4200	15	1.12	93
17	Anisole	75	4.0	DTTC-N$_3$	8	3600	13	1.10	95
18	Toluene	75	4.0	DTTC-N$_3$	4	3800	13	1.10	91

(a) Calculated by THF GPC against polystyrene standards;
(b) $D_p = (M_n$ polymer $- M_r$ CTA$)/M_r$ monomer; and
(c) calculated by ^{1}H NMR spectroscopy.
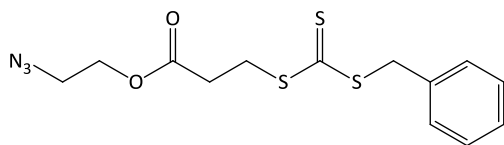
(a)   **(b)**

2-azidoethyl 3-benzylsulfanylthiocarbonylsulfanylpropionate
(BTTC-N$_3$)
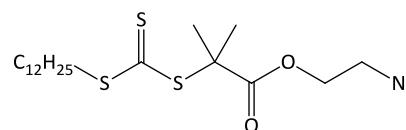
2-azidoethyl 2-(dodecylthiocarbonothioylthio)-2-methylpropionate
(DTTC-N$_3$)

Figure 2.18. Structures of the two chain transfer agents trialled in this study, (a) BTTC-N$_3$ and (b) DTTC-N$_3$.

For the initial CTA screening, the RAFT conditions employed were [AIBN]$_0$/[CTA]$_0$/[NSS]$_0$ = 0.3/1/20, at 75 °C, using a monomer concentration of 0.80 M in three different solvents (THF, anisole and toluene). Table 2.1 (rows 1 to 6) shows the results obtained for the different

CTAs. The most noticeable difference is the final polymer molar mass produced; with BTTC-N_3 affording higher molar mass PNSS than DTTC-N_3 despite setting identical target degrees of polymerisation. However, regardless of the solvent used, DTTC-N_3 produced polymers with lower dispersities ($Đ \leq 1.14$) and unimodal GPC traces [Figure 2.19 (a)], whereas BTTC-N_3 afforded PNSS with higher dispersities and, in a number of cases, resulted in GPC peaks with shoulders [Figure 2.19, (b)]. Clearly, the more stable tertiary radical leaving group, which affords a higher fragmentation rate, offers a higher degree of control over the polymerisation. The final achievable monomer conversion, on the other hand, appears to be independent of CTA in these systems. Both CTAs allow a near identical conversion to be attained when performing the polymerisation in the same solvent.

(a)   **(b)**
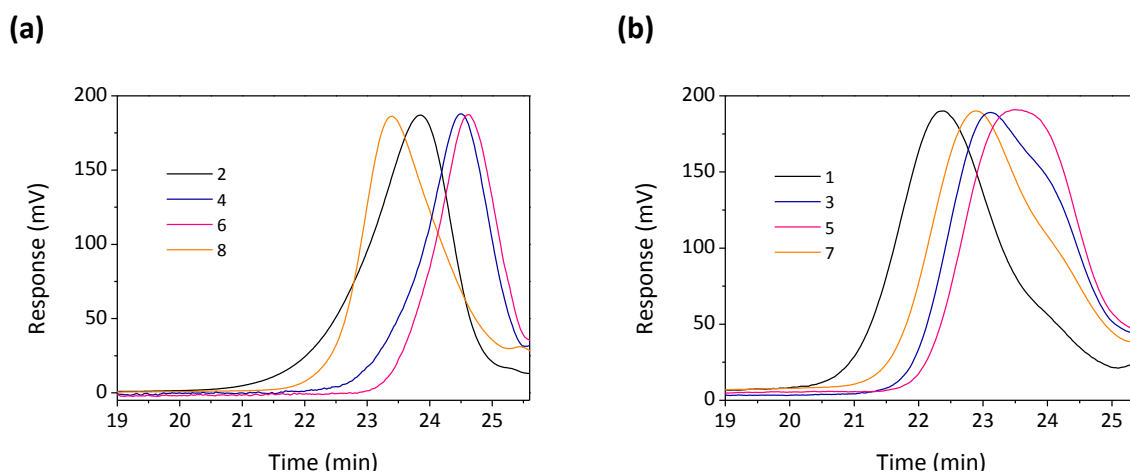
Figure 2.19. GPC traces for the final polymers in experiments 2, 4, 6 & 8, using DTTC-N_3 as CTA (a) and experiments 1, 3, 5 & 7, using BTTC-N_3 as CTA (b).

To extend the screening further, identical experiments were undertaken in THF at a lower temperature (60 °C). Indeed, the same trends were observed (see Figure 2.20); higher molar mass polymer was achieved with BTTC-N_3, but with shouldered distributions and higher dispersities throughout the course of the polymerisation. In this case, however, DTTC-N_3 also gave marginally higher monomer conversion (98 % *versus* 92 %). It is noteworthy that DTTC-N_3 produces a negligible amount of low molar mass impurities in a number of cases [Figure 2.19 (a)]. Decreasing the temperature of the reaction led to reduced polymerisation rates compared to the corresponding systems at 75 °C, although better linear fits (for the first order plots) were obtained for both CTAs when the polymerisations were conducted at lower temperatures (Figure 2.21). In particular, the *pseudo*-first order plot for DTTC-N_3 at 75 °C deviates somewhat from a single linear dependence. At both temperatures, DTTC-N_3 showed higher rates (0.061 h^{-1} at 75 °C and 0.025 h^{-1} at 60 °C) than its

primary counterpart BTTC-N_3 (0.041 h^{-1} and 0.021 h^{-1} at 75 °C and 60 °C, respectively). The fits were obtained for the linear regime during the first 48 hours of polymerisation. In summary, DTTC-N_3 was selected for further investigation as it produced PNSS with narrower, and more uniform, molar mass distributions in all three solvents studied.
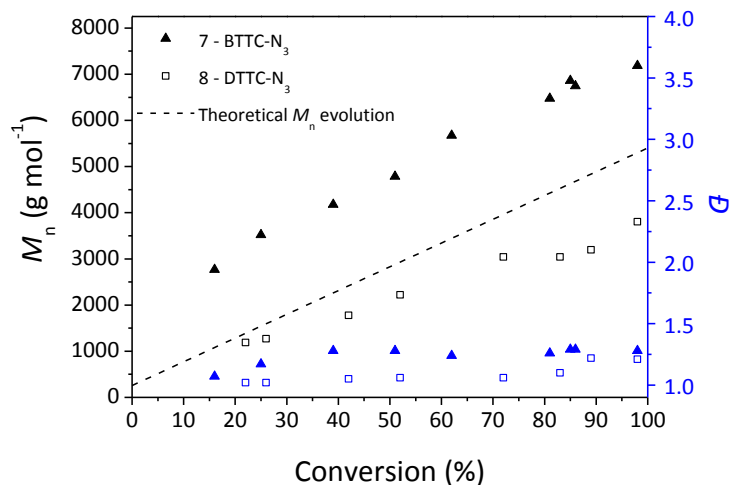
Figure 2.20. Plot of molar mass, M_n (black symbols), and dispersity, Đ (blue symbols), *versus* monomer conversion for the polymerisation of neopentyl *p*-styrene sulfonate using BTTC-N_3 (exp. 7) and DTTC-N_3 (exp. 8) in THF at 60 °C The dotted line indicates the theoretical M_n evolution for the target D_p = 20 (M_n = 5400 g mol^{-1}).
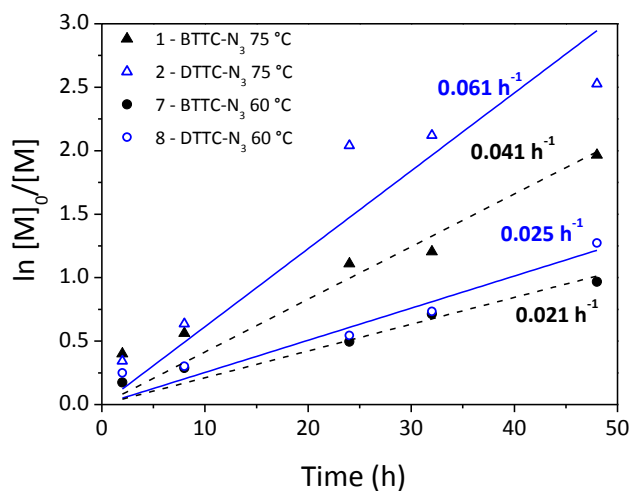
Figure 2.21. *Pseudo*-first order kinetic plots for the polymerisation of neopentyl *p*-styrene sulfonate using BTTC-N_3 and DTTC-N_3 in THF at 75 °C (exp. 1 and 2) and 60 °C (exp. 7 and 8), initial monomer concentration 0.80 M.

2.3.1.2. Monomer concentration

In an attempt to speed up the polymerisation, whilst maintaining control over the final polymer properties, the effect of monomer concentration was studied in the three different solvents (THF, anisole, and toluene). In the literature, many articles fail to report the concentration of each species in solution, a parameter which indeed influences the rate of the polymerisation process.[122] Interestingly, the scarce reports that do exist on the effect of monomer concentration on the RAFT process show contrasting trends. Wood *et al.*[131] compared different amounts of toluene (9.1, 23.1, 41.2, and 66.6 % w/w toluene contents) on the RAFT polymerisation of methyl acrylate. Although they report negligible effects of the dilution in the early stages of polymerisation for the three more concentrated systems, they indicate that the overall rate of polymerisation is significantly lower for the most dilute system, as expected. They also revealed lower monomer conversions for the most dilute system (66.6 % w/w of toluene). Similar results were obtained by Cauët *et al.*[136] for the polymerisation of *p*-acetoxystyrene in 1,4-dioxane. Three concentrations were assessed (33.3, 50 and 66.6 % v/v 1,4-dioxane contents), resulting in lower polymerisation rates for the most diluted systems. They also indicated a slight loss of molar mass control at higher dilutions. In contrast, Abreu *et al.*[133] report higher monomer conversions at higher dilution for the RAFT polymerisation of vinyl chloride in THF, together with lower molar masses and higher dispersities. In their study, the solvent contents studied were 50, 75, and 83.3 % (v/v THF contents) and their somewhat anomalous results were attributed to side reactions from the growing macroradicals to the solvent.

In our work herein, the effect of monomer concentration was studied in the three different solvents (THF, anisole, and toluene) using DTTC-N$_3$ at 60 °C. Accordingly, the solvent content was varied from 83.3 % to 75 % and 50 % (w/v solvent content), corresponding to monomer concentrations of 0.80, 1.3, and 4.0 M, respectively (see rows 8 to 16 in Table 2.1). N.B. these concentrations do not take into account the relatively small quantities of initiator and CTA. Firstly, in THF, high monomer conversions were achieved at all concentrations and the corresponding degrees of polymerisation (ca. 14), approximated by GPC analyses, were close to the target D_p of 20. It should be noted that the molar mass data obtained from GPC are relative to PS standards only and, due to differences in the radii of gyration of PNSS and the PS calibrants in THF, absolute molar mass data are not obtained. Typically, ^{1}H NMR spectroscopy can be used to determine a more accurate value of M_n for low molar mass polymers, however this was not possible because CTA peaks were not sufficiently discernable in the polymer NMR spectra. As expected (and in line with the work of Wood *et al.*[131] and

Cauët *et al.*[136]) the rate of polymerisation was faster for higher initial monomer concentrations; with less time required to achieve almost complete monomer conversion. Concurrently, the dispersity decreased significantly from 1.21 to 1.07 going from 0.80 to 1.3 M, but then increased slightly to 1.13 in the most concentrated reaction trialled, 4.0 M. Our general trend, however, where diluted systems offer less control over the polymerisation, is more in line with the work of Abreu *et al.*[133] and is attributed to the increased probability of chain transfer to solvent. Although there was no observed change in dispersity of the final polymer, the overall effect of concentration was more pronounced in anisole and toluene than THF, with a marked increase in monomer conversion with increasing monomer concentration, particularly in anisole. Concomitantly, the achieved degrees of polymerisation approached the target D_p as the concentration was increased in all cases. Additionally, the effect of monomer concentration on the apparent rate of polymerisation (k_{app}) was closer to a linear dependence in anisole and toluene (see Figure 2.22).
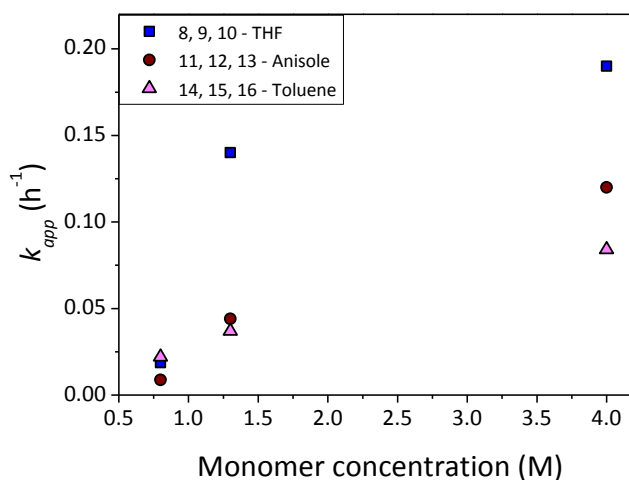
Figure 2.22. Calculated k_{app} *versus* initial monomer concentration for polymerisations performed in the three trialled solvents (THF, exp. 8-10; anisole, exp. 11-13; toluene, exp. 14-16), at 60 °C and using DTTC-N$_3$ as CTA.

When using the highest concentration (4.0 M), the systems behave similarly, independent of solvent choice, producing polymers close to their target D_p with narrow molar mass distribution ($Đ$ ~1.10) and high monomer conversions (> 90 %) after only 24 hours in each case. These more concentrated systems are better suited to industrial applications where the reduced amount of (relatively harmful) solvents and significantly shorter reaction times will reduce costs and the environmental impact of the process.

2.3.1.3. Solvent effect

In general, the influence of the solvent type used in free radical polymerisation is related to the affinity of the growing polymer radical to the solvent and has a profound effect on the rate of polymerisation. Charge transfer between the macroradical and the solvent has been shown to reduce the rate of addition of incoming monomer and therefore decrease the rate of propagation.[128-129] On the other hand, reports on the effect of solvent type used in RAFT polymerisation indicate that the influence is insignificant, and often, negligible. For example, Benaglia *et al.*[130] investigated the effect that benzene, acetonitrile, and dimethylformamide had on the RAFT polymerisation of methyl methacrylate mediated by dithiobenzoates. The authors indicate relatively minor effects of the solvent on the process, although slightly lower conversions and *Đ* were observed in reactions in benzene. Wood *et al.*[131] studied the effect of solvent polarity on the trithiocarbonate-mediated RAFT polymerisation of methyl acrylate, using toluene, *N*,*N*'-dimethylformamide, and methyl ethyl ketone. All systems were shown to exhibit identical *pseudo* first-order rate plots during the early stages of polymerisation. However, for the polymerisation of 2-chloro-1,3-butadiene (CB), our group recently found that the solvent had a marked effect over the control and rate of PCB synthesis, with THF showing and enhanced control over xylene.[132] Similarly, Abreu *et al.*[133] showed distinct differences on the polymerisation of vinyl chloride performed in dichloromethane, cyclohexanone, and THF; once again with THF giving rise to the most successful results.

According to our data herein, varying results are observed depending on the solvent chosen. The systems with the most polar solvent, THF, were more robust, achieving high monomer conversions and good quality polymers independent of the employed conditions. On the contrary, systems using anisole and toluene were more sensitive to monomer concentration. In these aromatic diluents, higher solvent content suppressed the progress of the polymerisation, particularly at 75 °C, and only permitted 50 - 70 % monomer conversion to be reached. Similarly, at 60 °C, the most dilute anisole system could only attain 70 %, however, the toluene system was actually only marginally affected by dilution, reaching 86 % (instead of 93 % at 4.0 M). In terms of monomer conversion, the general trend of THF > anisole > toluene is observed, which follows the trend of relative polarity. Here, the higher the polarity, the higher the achievable monomer conversions. Concomitantly, the rate of polymerisation (demonstrated by the value of the apparent rate constant for propagation, k_{app}) also follows this dependence. At 60 °C and $[M]_0$ = 4.0 M, reactions using the most polar solvent, THF, had a k_{app} of 0.154 h^{-1}, 0.12 h^{-1} when employing anisole, and 0.064 h^{-1} in the less polar solvent

toluene (Figure 2.23). Although the first order plots are not strictly linear in every case, these trend lines have been selected to display the general rate of the reactions and establish a comparison among the different solvent systems. The reactions in aromatic solvents show similar behaviour during the first 10 hours, and the most significant differences can be observed beyond this timeframe. Our findings are in line with the theory that the higher the affinity of the growing macroradical to the solvent, the slower the polymerisation. Hence, our relatively non-polar monomer will favour interaction with non-polar solvents giving rise to the observed trends. This theory also helps to explain the lack of sensitivity of the THF system towards changes in initial monomer concentration, compared to the aromatic solvents for which the affinity of the macroradical to solvent is higher. Thus, according to our results, modifying the concentration of the system is intimately related to the solvent employed for the polymerisation, and the dilution of the system reflects not only the changes in concentration, but also the specific behaviour that each solvent displays towards a certain monomer and/or propagating radical.
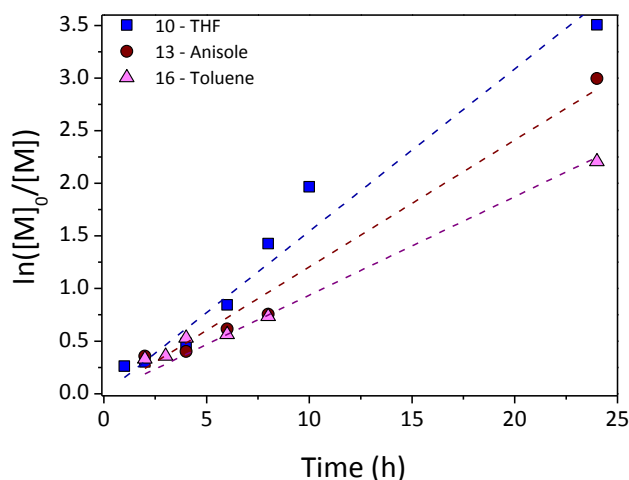
Figure 2.23. *Pseudo*-first order kinetic plots with DTTC-N$_3$ at 60 °C, monomer concentration 4.0 M, in THF (exp. 10, ■), anisole (exp. 13, ●), and toluene (exp. 16, ▲).

Overall, the anisole system at the highest concentration (4.0 M) was the most promising in terms of low molar mass dispersity with relatively high monomer conversion. Although this system has been shown to be the most optimum for the polymerisation of neopentyl *p*-styrene sulfonate, the performance of the other solvents at the same initial monomer concentration was similar and can also be highlighted as acceptable systems for the controlled synthesis of PNSS.

2.3.1.4. Effect of the temperature

Finally, in a further attempt to reduce polymerisation time, whilst maintaining control over the system, the effect of increasing the temperature to 75 °C was studied in systems at the most effective monomer concentration (4.0 M). It should be noted that only anisole and toluene were investigated under these conditions, as manipulating THF reactions became impractical at such a low dilution and high temperature (THF boiling point = 66 °C).

(a)   **(b)**
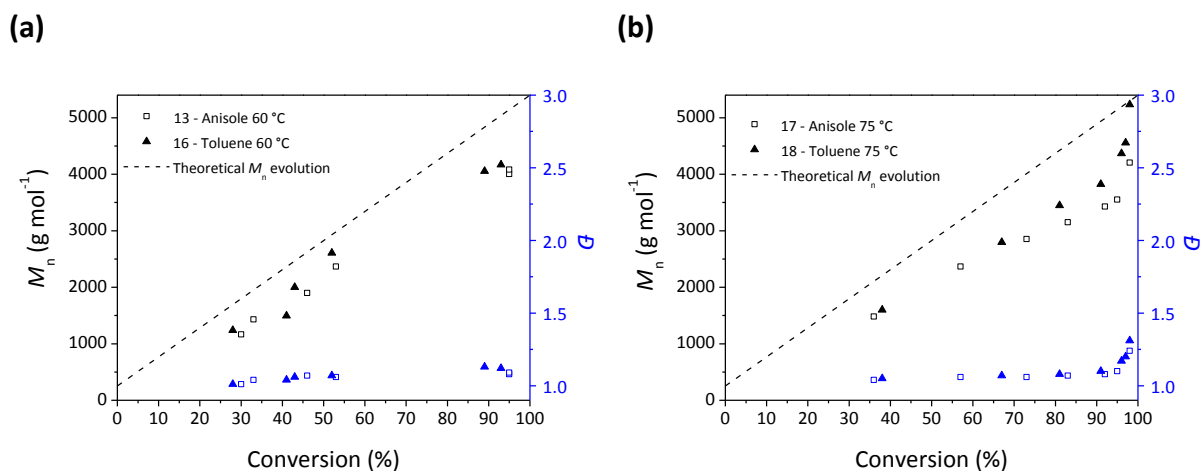
Figure 2.24. Molar mass, M_n (black symbols), and dispersity, $Đ$ (blue symbols), *versus* monomer conversion employing DTTC-N₃, initial monomer concentration 4.0 M in anisole (exp. 13, 17) or toluene (exp. 16, 18), at (a) 60 °C and (b) 75 °C. The dotted line indicates the theoretical M_n evolution for the target D_p = 20 (M_n = 5400 g mol⁻¹). The increase in $Đ$ in the latter stages of polymerisation in (b) is due to the formation of high molar mass products as shown in Figure 2.25.
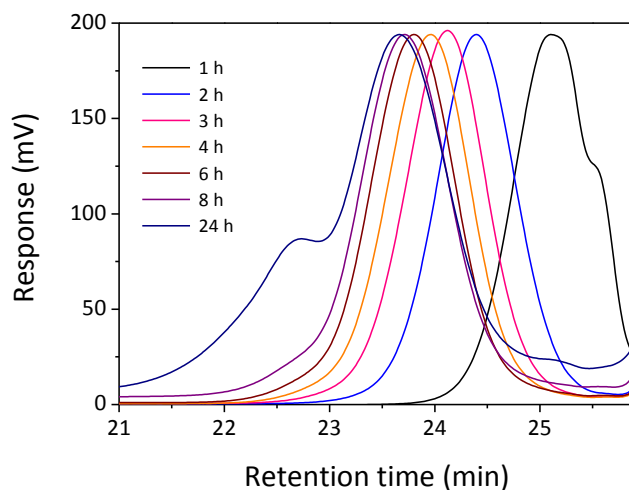
Figure 2.25. Evolution of the GPC traces for experiment 17. After 24 hours, a bimodal distribution is observed with formation of higher molar mass products.

As expected, the results show that the polymerisations are considerably faster at elevated temperature, achieving monomer conversions above 90 % after 8 and 4 hours in anisole and toluene, respectively (compared to 24 hours at 60 °C for both systems). Higher conversions (98 %) could be obtained at longer polymerisation times, however, this came with a loss of control over the system, where distributions became bimodal and dispersities increased significantly (Figure 2.24 and Figure 2.25).
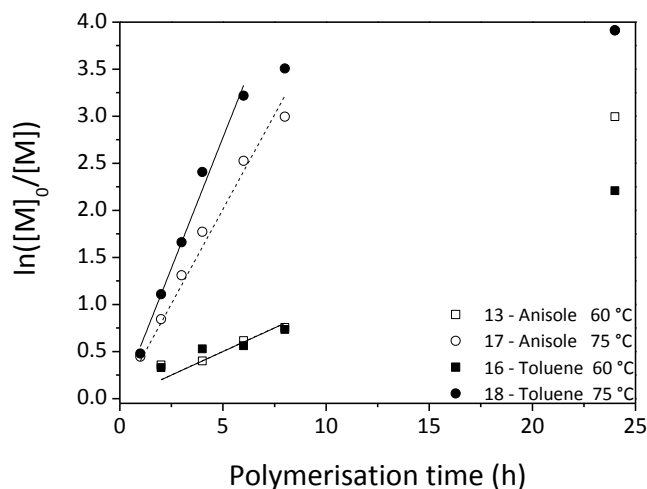
Figure 2.26. *Pseudo* **first-order kinetic plots in anisole (exp. 13, 17) and toluene (exp. 16, 18) at 60 °C and 75 °C. N.B. The trend lines for anisole and toluene at 60 °C are completely coincident within the first 8 hours.**

Semi-logarithmic plots for these polymerisations (in anisole and toluene at 60 °C and 75 °C) demonstrate linear *pseudo* first-order kinetics, as expected for controlled polymerisation (see Figure 2.26). In fact, the reactions in anisole and toluene become approximately 4 and 6 times faster, respectively, on moving to 75 °C (Exp. 13, k = 0.100 h^{-1}; Exp. 17, k = 0.40 h^{-1}; Exp. 16, k = 0.100 h^{-1}; Exp. 18, k = 0.55 h^{-1}). It is clear that increasing the temperature led to enhanced rates and, moreover, improved linear fits in the first eight hours of polymerisation. In summary, increasing the temperature to 75 °C has allowed us to drastically reduce the polymerisation time without compromising control; high monomer conversion (particularly in anisole) with low molar mass dispersity (*Đ* = 1.10) and moderate agreement of achieved molar mass with that targeted. Interestingly, for the reactions in toluene at the highest dilution (0.80 M), the decrease in temperature to 60 °C led to better results in terms of both monomer conversion and molar mass of the obtained polymer (Table 2.1; rows 6 and 14).

2.3.1.5. Extending the scope of the polymerisation; effect of [PNSS]$_0$:[CTA]$_0$ ratio

For the following experiments, the system comprising anisole at 75 °C with initial monomer concentration of 4.0 M, was selected due to its rapidity, linear evolution of the molar mass and good quality of the obtained polymer (Table 2.1, row 17). This system was employed to synthesise higher molar mass PNSS with relatively narrow molar mass distributions. The initial monomer:CTA ratio (target D_p) was modified in order to target polymers of D_p = 20, 100, and 200. Figure 2.27 shows the GPC traces and molar mass data of the produced polymers. The discrepancy between the data reported for this same system in Table 2.1 and the data concerning D_p = 20 in Figure 2.27 arises from the course of polymerisation in both cases. While data in Table 2.1 stem from the characterisation of PNSS whose polymerisation process has been monitored (thus, sample aliquots have been periodically extracted from the system), data in Figure 2.27 derives from the characterisation of samples directly produced (*i.e.* no intermediate sample extraction) *via* the polymerisation conditions designed as optimal.

$D_p{}^{th}$	$D_p{}^{exp}$	$M_n{}^{GPC}$	Đ
20	15	4300	1.09
100	36	9700	1.30
200	65	17000	1.50
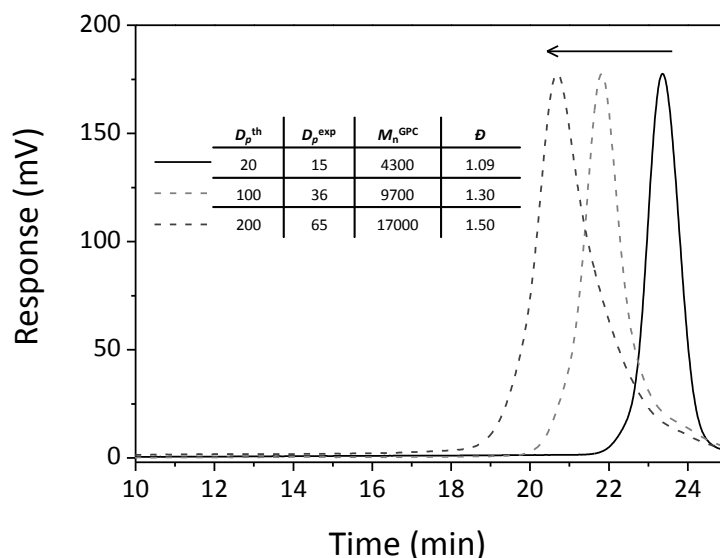
Figure 2.27. GPC traces of PNSS with varying target molar masses, synthesised by RAFT using DTTC-N$_3$ in anisole at 75 °C at 4.0 M NSS. M_n values were calculated relative to polystyrene standards.

Data reported in Figure 2.27 indicate that the molar mass dispersity of the polymers increases with molar mass, yet all afford unimodal distributions over a controlled range of molar masses. The measured degrees of polymerisation (D_p = 15, 36, and 65, respectively), by GPC, are significantly lower than those targeted, which is partially attributed to differences in the hydrodynamic volumes of PNSS and the PS calibration standards from which these calculations are derived (as aforementioned).

Having said this, it is difficult to attribute such vast differences between obtained and theoretical molar masses to this phenomenon alone and therefore it should be noted that although we can alter the final degree of polymerisation of the polymer by varying the $[\text{monomer}]_0:[\text{CTA}]_0$ ratio, it is difficult to obtain high molar mass PNSS with the systems reported herein. Nevertheless, the polymerisation conditions identified here produce an extremely versatile material with two key features; a reactive end-group and a thermally responsive protective moiety, that can be exploited for the construction of more complex and structurally diverse materials.

2.3.1.6. Proof of concept: Synthesis and deprotection of a PNSS-based triblock copolymer

In order to briefly demonstrate how the azide-functionalised PNSS (PNSS-N_3) can be utilised for the construction of block copolymers, a hydrophobic triblock copolymer, poly(neopentyl *p*-styrene sulfonate)-*b*-polybutadiene-*b*-poly(neopentyl *p*-styrene sulfonate) (PNSS-*b*-PBD-*b*-PNSS) was synthesised, which was then subjected to thermal treatment (150 °C for 2 hours) to convert the PNSS blocks to hydrophilic poly(*p*-styrene sulfonate) segments (Scheme 2.9). For the purposes of clarity and to emphasise the styrene sulfonic acid functionality generated on thermolysis, the thermally treated material is denoted as PSS-*b*-PBD-*b*-PSS. However, it is important to note that the PBD midblock crosslinks during thermal treatment. Copper(I)-catalysed azide-alkyne 'click' chemistry was employed to couple bisalkyne-functionalised polybutadiene (PBD-dialkyne, M_n ~9300 g mol^{-1}, M_w/M_n = 1.76) to our azide-functionalised PNSS (M_n ~2600 g mol^{-1}, M_w/M_n = 1.11) to yield PNSS-*b*-PBD-*b*-PNSS (M_n ~19300 g mol^{-1}, M_w/M_n = 1.29; *it is important to note that although the M_n value of polybutadiene provided by the supplier (4278 g mol^{-1}) was used to calculate the reagent stoichiometry for the synthesis of the triblock copolymer, the GPC M_n values here have been used to allow direct comparison between the polymer building blocks and the final copolymer*). Figure 2.28 shows the ^{1}H NMR spectrum of PNSS-*b*-PBD-*b*-PNSS, displaying signals corresponding to the two building blocks. Additionally, Figure 2.29 shows the GPC traces and FTIR spectra of the separate blocks and the resulting triblock copolymer. Clearly, the GPC traces show the expected unimodal increase in molar mass for the block copolymer, with no detectable homopolymer impurities. Moreover, UV detection (at λ = 270 nm) confirms that the final triblock copolymer product contains covalently bound, UV-active, PNSS (whereas the GPC traces for PBD alone show no UV-active species). Concomitantly, FTIR characterisation indicates that the block copolymer spectrum is a combination of the individual building blocks with the removal of azide and alkyne bands (2116 cm^{-1} in PNSS-N_3 and 2125 cm^{-1} in PBD-dialkyne, respectively) as expected. Finally, it should be noted that the efficiency of

the 'click' reaction (40.1 %) for this polymer-polymer coupling is moderate, as only a maximum of 77 % of the PNSS chains should be furnished with azide functionality due to the high initiator quantity employed in this work (assuming an initiator efficiency, f, of 0.5 for AIBN).
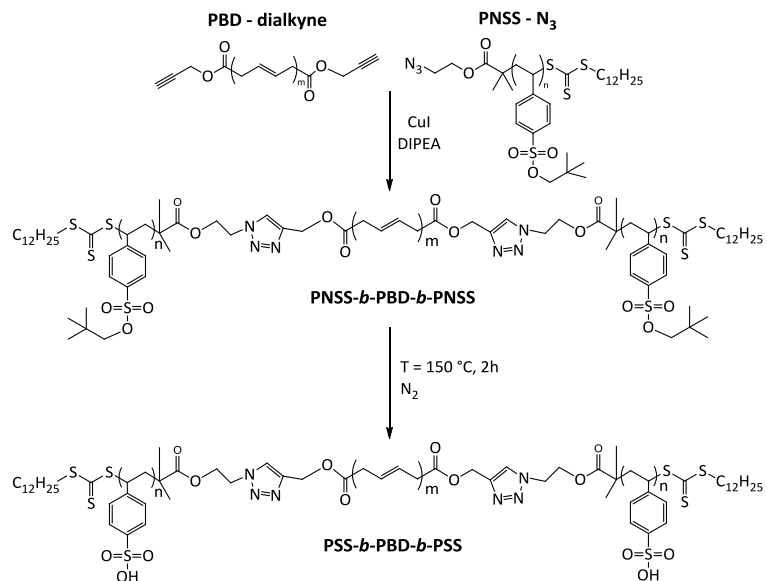
Scheme 2.9. Synthesis of PNSS-*b*-PBD-*b*-PNSS and thermolysis of poly(neopentyl *p*-styrene sulfonate) blocks to yield PSS-*b*-PBD-*b*-PSS. N.B. Only the major *trans*-1,4 isomer of polybutadiene is shown.
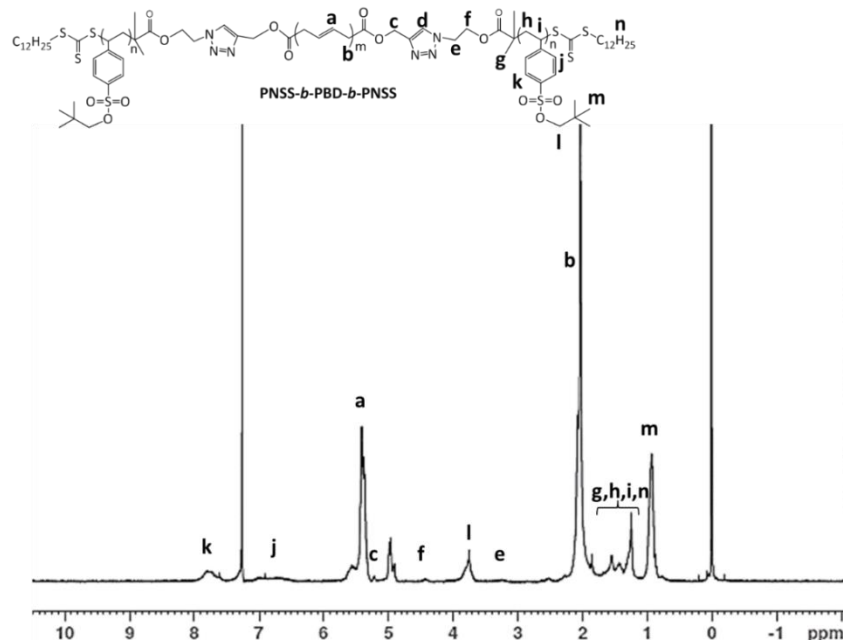
Figure 2.28. Assigned ¹H NMR spectrum of PNSS-*b*-PBD-*b*-PNSS (proton 'd' is not discernible, expected at approximately 7.5-7.6 ppm).

(a)

(b)
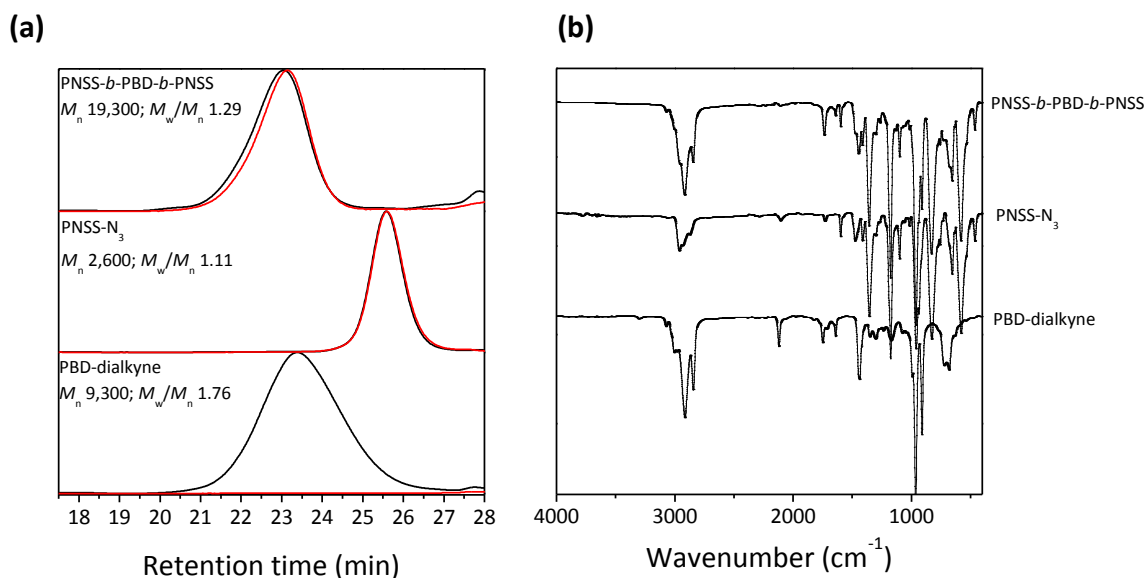
Figure 2.29. GPC traces (a) and FTIR spectra (b) of the PNSS-*b*-PBD-*b*-PNSS block copolymer and its corresponding building blocks, PNSS-N$_3$ and PBD-dialkyne. Refractive index signals in the GPC traces (a) are shown in black, while UV signals (λ$_{270\ nm}$) are shown in red.

In a second step, thermal annealing of the resulting PNSS-*b*-PBD-*b*-PNSS (150 °C, 2 h, N$_2$) was applied to deprotect the PNSS blocks and yield the corresponding poly(*p*-styrene sulfonate) counterparts. To confirm the thermal deprotection of the PNSS-*b*-PBD-*b*-PNSS block copolymer to produce an amphiphilic material, thermal gravimetric analysis, TGA, contact angle measurements and FTIR spectroscopy have been employed (see Figure 2.30 and Figure 2.31). TGA shows a mass loss of 10.9 % for the block copolymer during thermal treatment at 150 °C, which is attributed to the loss of the neopentyl protecting group. The theoretical mass loss for complete removal of the neopentyl group in our block copolymer is 12.6 % and the discrepancy observed herein is attributed to a Friedel-Crafts side reaction, where an extremely small portion of the neopentyl groups are attacked by (and thus attach to) the aromatic rings on the sulfonate repeat units, as reported in the literature.[174-175] Upon thermolysis, this block copolymer becomes amphiphilic as the PNSS block is deprotected to generate poly(*p*-styrene sulfonate) (PSS) end blocks, as previously shown for PNSS-*b*-poly(*n*-butyl acrylate).[174]
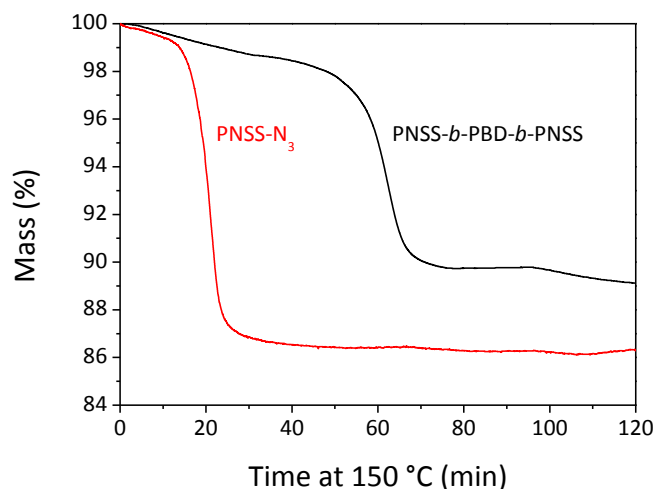
Figure 2.30. Mass loss profiles obtained from isothermal thermogravimetric analysis of PNSS-N₃ and PNSS-*b*-PBD-*b*-PNSS (150 °C, 2 h, N₂ flow rate: 75 mL min⁻¹). Observed mass loss for PNSS-*b*-PBD-*b*-PNSS is 10.9 % (expected 12.6 %) and for PNSS-N₃ is 13.7 % (expected 23.5 %).

(a)   **(b)**
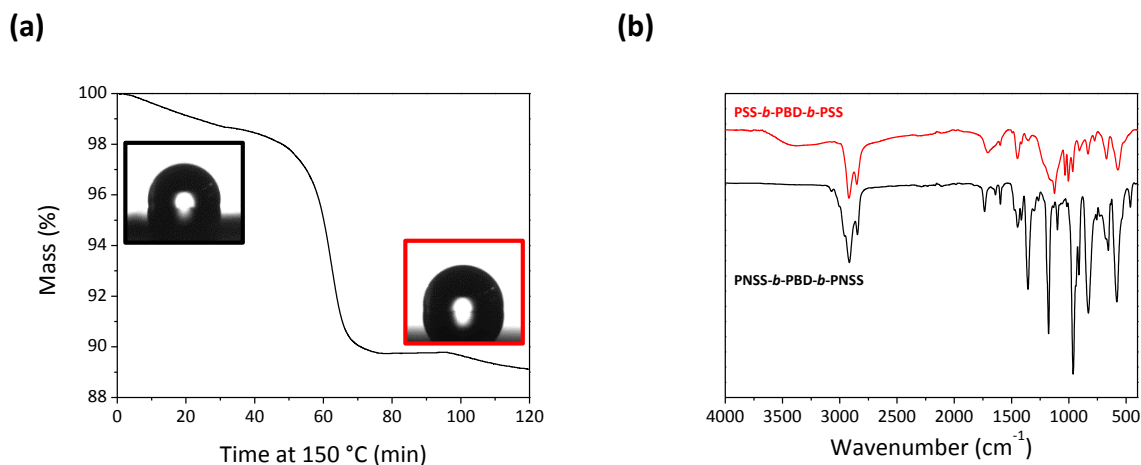
Figure 2.31. (a) Thermal Gravimetric Analysis during isothermal treatment at 150 °C and contact angle images before (PNSS-*b*-PBD-*b*-PNSS) and after (PSS-*b*-PBD-*b*-PSS) this thermal treatment. (b) FTIR spectra of the PNSS-*b*-PBD-*b*-PNSS and PSS-*b*-PBD-*b*-PSS block copolymers (*i.e.* before and after treatment at 150 °C for 2 hours, respectively).

As further proof of the success of the deprotection step, FTIR spectroscopy [Figure 2.31 (b)] reveals the appearance of a broad band in the region of 3387 cm⁻¹, indicative of the presence of the deprotected sulfonate group, alongside the disappearance of the sulfonate ester group around 1350 cm⁻¹. Following deprotection, the contact angle (with deionised water) decreased slightly from 100.1° ± 0.7° to 95.7° ± 1.6°. While this change represents only a marginal increase in surface hydrophilicity, it is clear from the TGA analysis and infrared spectra in Figure 2.31 that thermolysis of

PNSS-*b*-PBD-*b*-PNSS successfully generates the expected sulfonic acid groups. The small change in the contact angle following thermolysis is therefore attributed to a known phenomenon of molecular reordering of the polybutadiene segments to the hydrophobic air-polymer interface to reduce its free energy.[194]

2.3.2. P3HT-*b*-PSS block copolymers as adhesive interlayer

Poly(neopentyl styrene *p*-sulfonate) produced *via* RAFT polymerisation was 'clicked' to poly(3-hexylthiopene) synthesised by Dr. Harikrishna Erothu using Grignard metathesis (GRIM) polymerisation, to obtain a series of poly(3-hexylthiophene)-block-poly-(neopentyl *p*-styrene sulfonate), P3HT-*b*-PNSS, with varying PNSS block lengths.[111] Whilst the work of Erothu *et al.*[111] extensively characterised these materials using multiple techniques, in the piece of work herein, focus is placed on the characterisation of two of these block copolymers ($P3HT_{50}$-*b*-$PNSS_{10}$ and $P3HT_{50}$-*b*-$PNSS_{30}$) under application conditions, *i.e.* thin films deposited and annealed following the same procedures as for incorporation into solar cell devices. With this aim, these block copolymers were dissolved in acetone (0.5 mg mL^{-1}), filtered through a PET film, and coated on top of glass substrates using doctor blading. This solvent was selected to enable coating on top of the active layer without washing it off. To guarantee complete removal of the neopentyl groups, thermal treatment was carried out at 150 °C for 5 hours, since TGA analysis of the polymer powder revealed that 3 hours of treatment was not sufficient for those polymers with the smallest PNSS segments.[111] The characterisation of these materials is mainly based on AFM measurements, employed both in classical Tapping mode (height images) and QNM Peak Force mode. The latter allows the surface characterisation in terms of the nanomechanical properties.

2.3.2.1. Characterisation of P3HT-*b*-PNSS and separate blocks

2.3.2.1.1. <u>Height and roughness analysis (AFM tapping)</u>

In a first step, the surface morphology of the two separate homopolymers (commercially available P3HT, D_p = 150 and PNSS, D_p = 30) and two block copolymers with varying PNSS segment lengths ($P3HT_{50}$-*b*-$PNSS_{10}$, $P3HT_{50}$-*b*-$PNSS_{30}$) was analysed using AFM working in classical Tapping Mode, before and after thermal treatment. Table 2.2 and Table 2.3 display the height images obtained for each material (1 x 1 μm), together with the roughness values after evaluation of three 5 x 5 μm images. The analysis of the separate blocks (P3HT and PNSS) in Table 2.2 indicates that, whilst for P3HT no noticeable changes in morphology can be observed, for the case of PNSS an important reorganisation of the film morphology occurs after thermal treatment at 150 °C. In both cases, the applied thermal annealing provoked an increase in surface roughness as indicate the values accompanying the images. The same analysis for the block copolymers, displayed in Table 2.3, indicates a very strong morphological organisation from the start, which seems not to be modified after thermal treatment. Contrary to what observed for the separate blocks, no changes in roughness values can either be

identified. This evolution is summarised in Figure 2.32, with an increase in roughness for both P3HT and PNSS, no modification for $P3HT_{50}$-b-$PNSS_{10}$ and slight decrease in roughness for $P3HT_{50}$-b-$PNSS_{30}$. It was expected that similar modifications to those observed for PNSS before and after thermal treatment were observed for the block copolymers, since the same process (neopentyl removal *via* thermal treatment, with formation of sulfonic groups) has been proven to occur in both cases.[111]

Table 2.2. AFM height images (1 x 1 μm) obtained for P3HT and PNSS thin films deposited *via* doctor blading, before and after thermal treatment. The accompanying roughness values were obtained for each sample after evaluation of three 5 x 5 μm images.
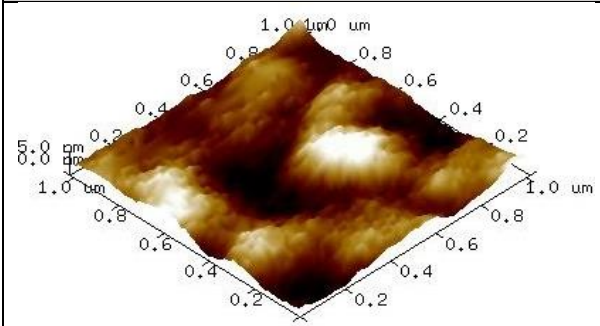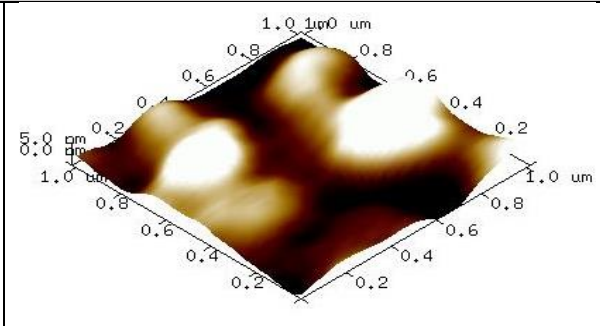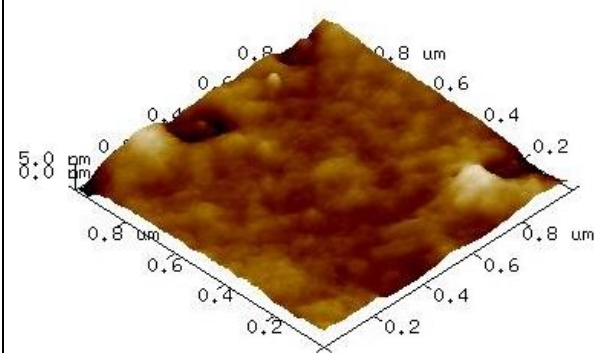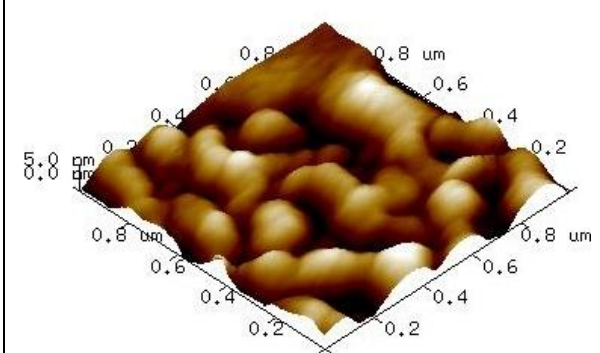
Pristine film	Film after 5 h @ 150 °C (N₂)
P3HT (D_p = 150)	
R_q = 3.4 ± 0.6 nm	R_q = 5.7 ± 0.9 nm
PNSS (D_p = 30)	
R_q = 2.5 ± 0.4 nm	R_q = 3.6 ± 0.9 nm

Table 2.3. AFM height images (1 x 1 μm) obtained for P3HT$_{50}$-*b*-PNSS$_{10}$ and P3HT$_{50}$-*b*-PNSS$_{30}$ thin films deposited *via* doctor blading, before and after thermal treatment. The accompanying roughness values were obtained for each sample after evaluation of three 5 x 5 μm images.

Pristine film	Film after 5 h @ 150 °C (N$_2$)
P3HT$_{50}$-*b*-PNSS$_{10}$	
R_q = 1.8 ± 0.3 nm	R_q = 2.1 ± 0.4 nm
P3HT$_{50}$-*b*-PNSS$_{30}$	
R_q = 2.6 ± 0.4 nm	R_q = 2.1 ± 0.2 nm
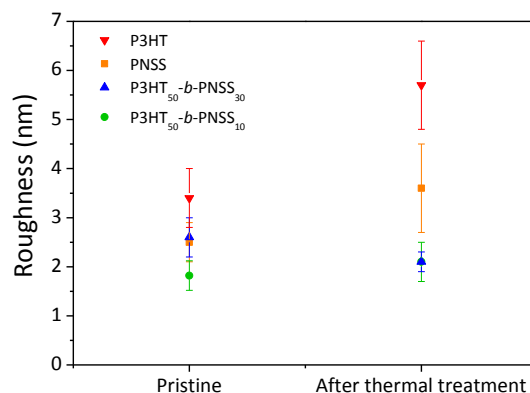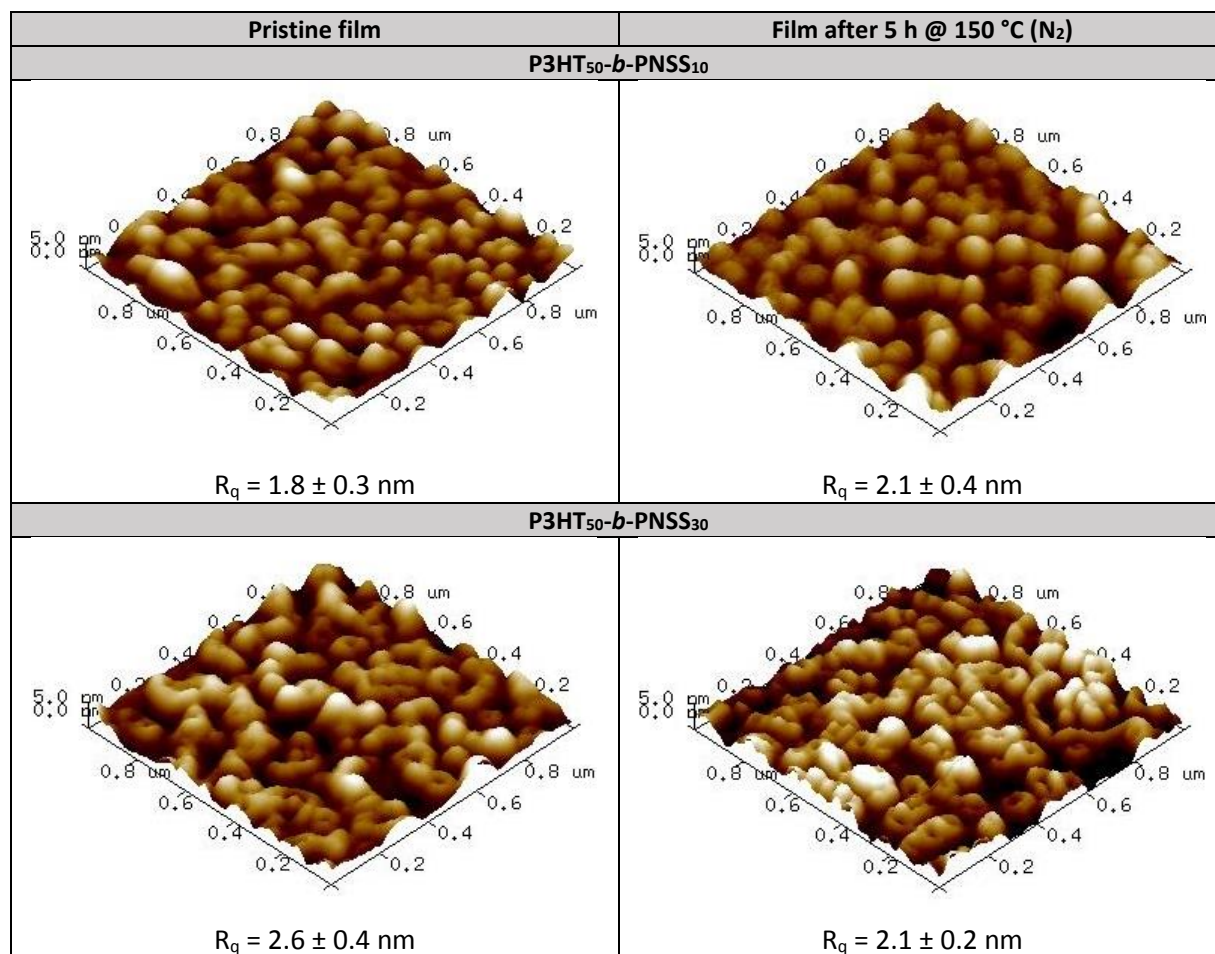
Figure 2.32. Roughness values obtained for thin films before and after thermal deprotection.

2.3.2.1.2. <u>Surface nano-mechanical properties (AFM Peak Force QNM)</u>

Further information was obtained from the analysis of the surface nanomechanical properties of these four materials using AFM in Peak Force Mode. This mode permits quantitative nanoscale material properties, such as modulus or adhesion, to be obtained *via* the application of a small and controlled force with each individual tap of the probe (RTESPA - Antimony doped Si) to the sample surface (see Section 2.2.2.1.6). Thus, this technique was examined for surface characterisation of the nanoscale properties of the different materials.

According to the literature, the Young's Moduli of P3HT and PSS display very similar values.[195] This makes it arduous to characterise them depending on the sensitivity of the technique, as the differences between them can be comprised within the method. In a first attempt, the Young's moduli were analysed as characterised in the corresponding feedback image. The calculated values (not shown) were of the same order of magnitude as the values reported in the literature, however, no trends or accurate values could be obtained from this analysis.

Table 2.4 shows average force-displacement curves for the homopolymers, P3HT and PNSS, before and after thermal treatment. Trace and retrace curves are the result of averaging at least three pairs of curves deriving from two captured lines (see Section 2.2.2.1.6 for further explanation). As can be observed, the adhesion values (understood as the peak force below the baseline at Force = 0 nN in the retrace curves) dramatically change for both materials after thermal annealing, from -90 nN to -30 nN in P3HT, and from -150 nN to -20 nN for PNSS. Since this parameter was sufficiently distinctive in each of these materials, as well as clearly modified upon annealing, focus was placed on the established tip-sample adhesion forces to characterise both homopolymers and the resulting block copolymers.

The same characterisation was performed for the two block copolymers, displayed in Table 2.5. Firstly, both pristine block copolymers exhibited adhesion values [Table 2.5 (a) and (c)] intermediate between those obtained for the corresponding pristine P3HT and PNSS blocks [Table 2.4 (a) and (b)]. Contrary to what was observed for the separate block constituents, these values remained unmodified after the thermal treatment of the two copolymers. Interestingly, $P3HT_{50}$-*b*-$PNSS_{30}$ (with a higher PNSS content), displayed slightly higher (absolute) adhesion values than $P3HT_{50}$-*b*-$PNSS_{10}$.

Table 2.4. Average trace (approach) and retrace (withdraw) curves acquired for P3HT and PNSS before (left) and after (right) thermal treatment.

Pristine film	Film after 5 h @ 150 °C (N$_2$)
P3HT (D_p = 150)	

| PNSS (D_p = 30) | |
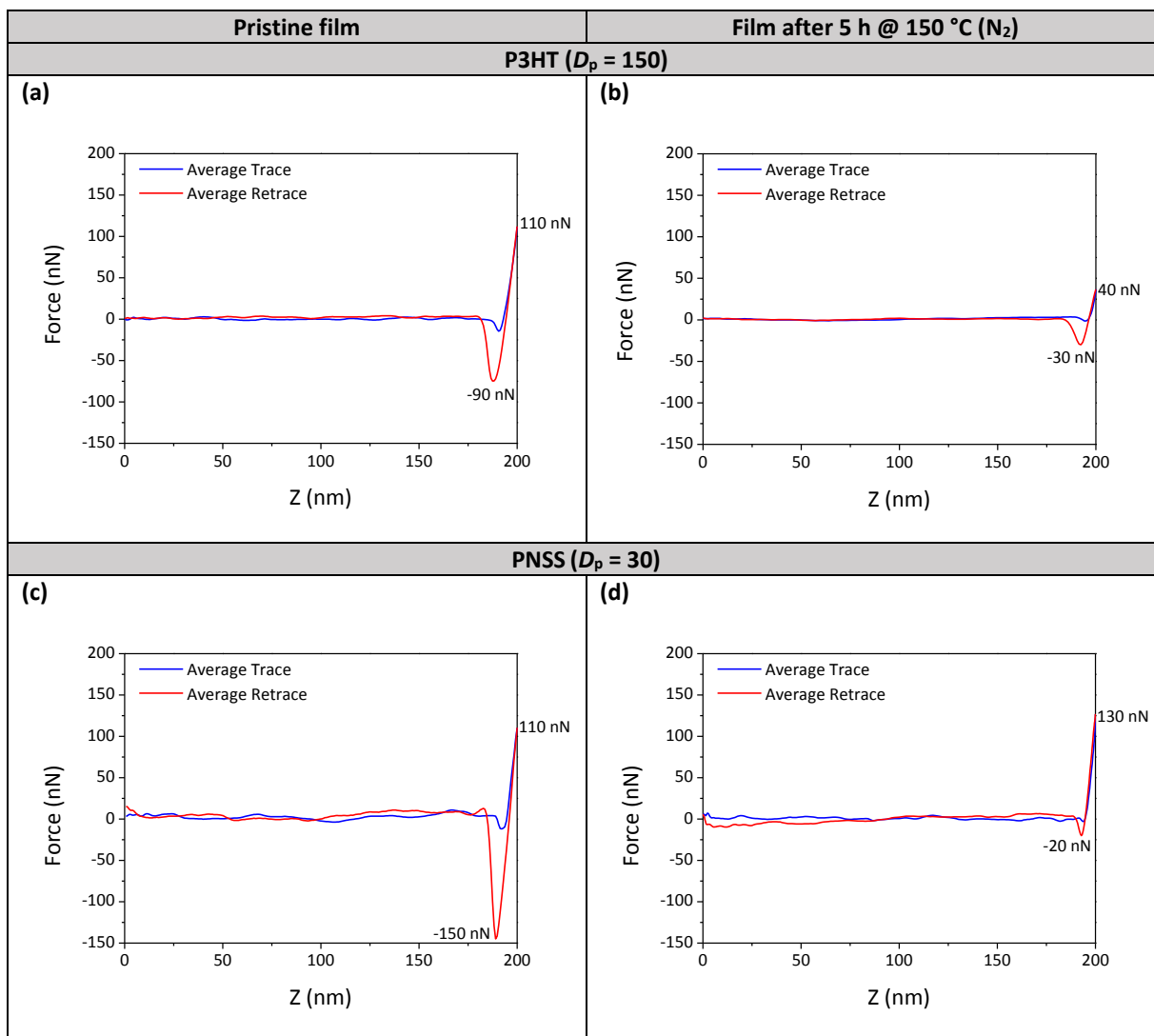
Table 2.5. Average trace (approach) and retrace (withdraw) curves acquired P3HT$_{50}$-*b*-PNSS$_{10}$ and P3HT$_{50}$-*b*-PNSS$_{30}$ before (left) and after (right) thermal treatment.

Pristine film	Film after 5 h @ 150 °C (N$_2$)
P3HT$_{50}$-*b*-PNSS$_{10}$	
(a)	(b)
(c)	(d)

P3HT$_{50}$-*b*-PNSS$_{30}$
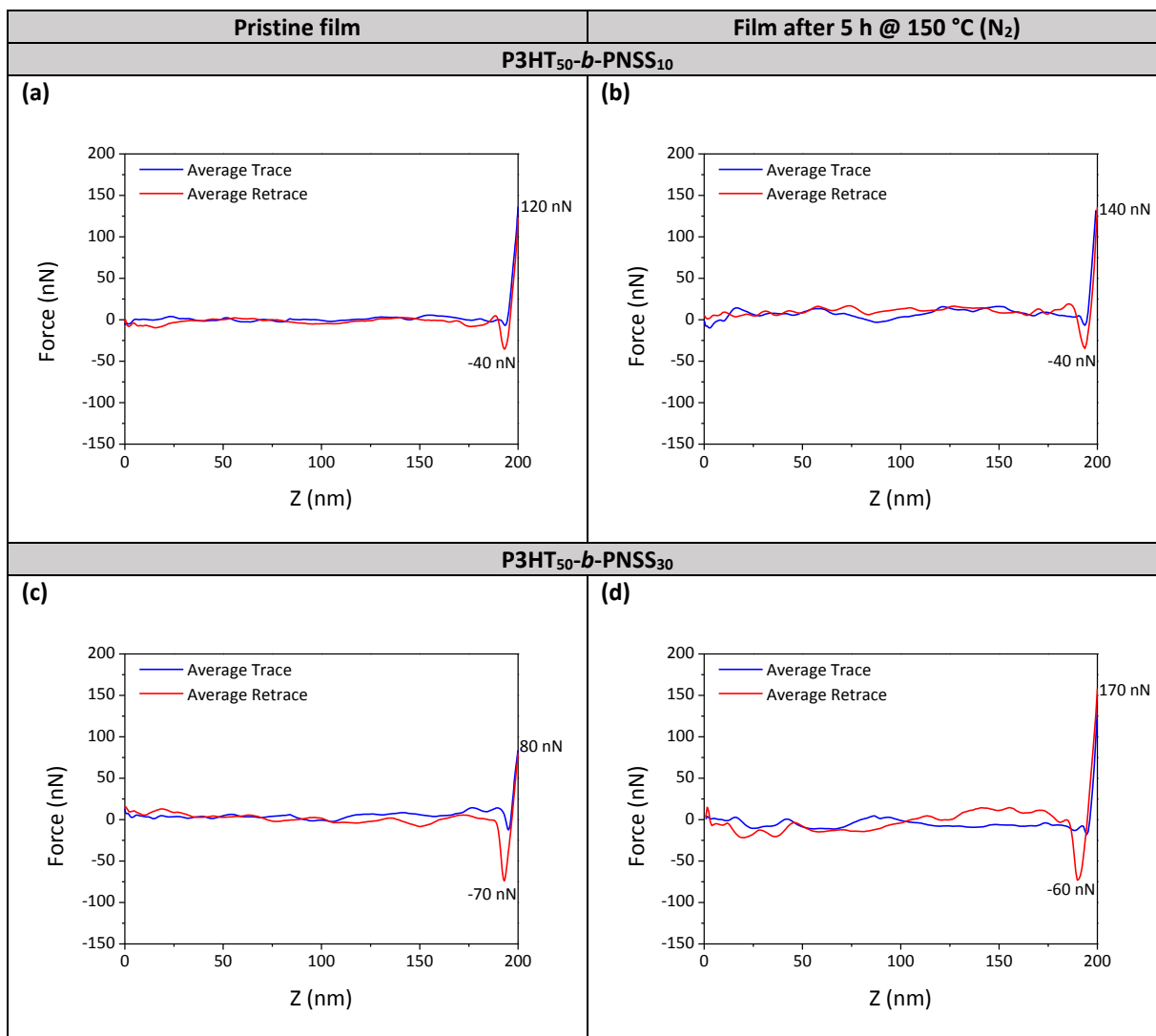
Operation of AFM in QNM Peak Force mode allows for the simultaneous acquisition of height images and mapping of nanomechanical properties *via* analysis, on the fly, of all the individual peak force curves obtained at each pixel of the image (*i.e.*, with each approach of the tip to the surface). Thus, adhesion values can be extracted as well from the evaluation of the images obtained from mapping this parameter. Figure 2.33 displays, as an example, images obtained for pristine P3HT, corresponding to the height (a) and adhesion (b) channels, together with the height-adhesion combined 3D plot (c). The mean adhesion value calculated for this particular adhesion image is as well displayed in (c). Mean adhesion values calculated for three 5 x 5 μm images for each material (P3HT,

PNSS and the two block copolymers) are displayed in Figure 2.34 (b) together with the absolute values calculated for the average retrace curves displayed in Table 2.4 and Table 2.5 [Figure 2.34 (a)].

(a)

(b)

(c)
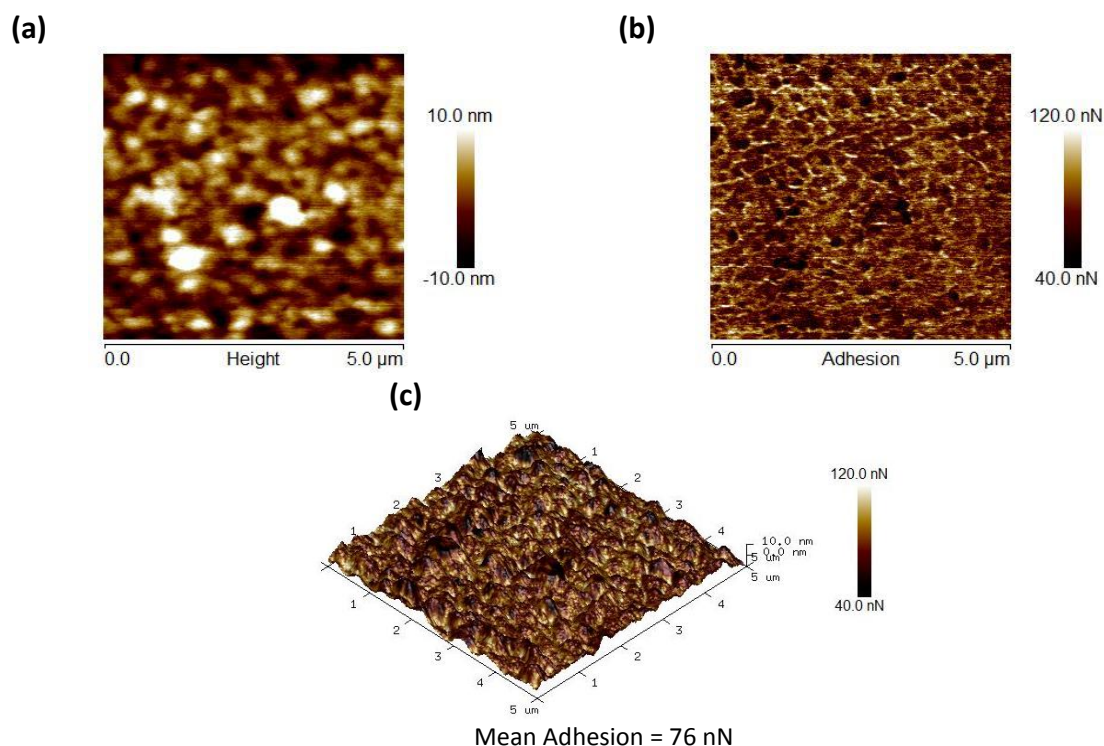
Mean Adhesion = 76 nN

Figure 2.33. (a) Height (b) Adhesion and (c) 3D image combining height and adhesion, together with the corresponding mean adhesion value, for a pristine P3HT sample.

(a)

(b)
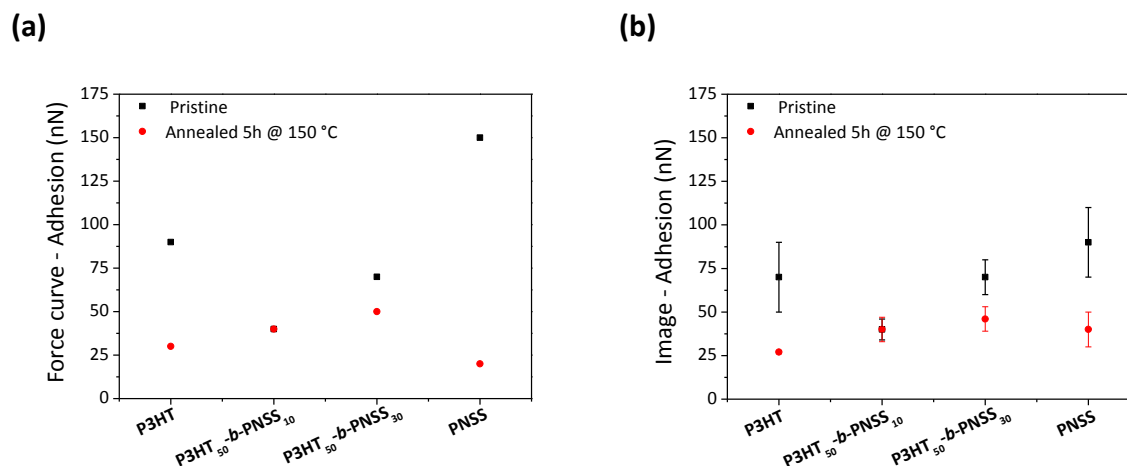
Figure 2.34. Adhesion values before (black) and after (red) thermal treatment for the different materials, as evaluated (a) from the analysis of the average retrace curves displayed in Table 2.4 and Table 2.5 (as absolute values), and (b) from the mean value recorded in the adhesion channel. N.B. Pristine and annealed values for P3HT-b-PNSS$_{10}$ are coincident.

Firstly, when comparing Figure 2.34 (a) and (b), very similar values and trends were obtained, independently of the method utilised for the characterisation of the parameter. Adhesion values decreased for all materials after annealing, with the exception of P3HT$_{50}$-b-PNSS$_{10}$, for which the value kept constant. Interestingly, this same block copolymer showed no noticeable modification in its roughness values before and after annealing (Figure 2.32). The strongest adhesion was observed for pristine PNSS exhibiting a marked decrease in adhesion after the conversion of protected sulfonate groups. Likewise, P3HT$_{50}$-b-PNSS$_{30}$ shows a slighter decrease in its adhesion after annealing, with both the values as pristine and annealed material located in between those observed for the PNSS homopolymer. Finally, P3HT$_{50}$-b-PNSS$_{10}$, with shorter PNSS segments, revealed no differences in adhesion with thermal annealing. In the following, values extracted from the adhesion feedback images are used for comparing the different materials, since these accumulate data corresponding to three 5 x 5 µm sample areas.

Overall, increasing the length of the PNSS blocks in the block copolymers leads to behaviour more similar to that of the PNSS homopolymer, as expected. In P3HT$_{50}$-b-PNSS$_{10}$, the coincident adhesion values before and after annealing (~40 nN) are similar to those obtained for both annealed P3HT (~27 nN) and annealed PNSS, *i.e.* PSS, (~40 nN). With a shorter PNSS segment, it could be expected that the material performs more similar to P3HT. However, if this was the case, higher adhesion (~90 nN) should be observed for the block copolymer as a pristine material, since P3HT itself only shows lower adhesion values after thermal annealing. An adhesion value of this magnitude (~40 nN) even before the thermal treatment is applied could also be explained by the fact that the PNSS is located at the surface of the sample, and possibly deprotected from the start. This second hypothesis is further supported by the high degree of morphological organisation observed for pristine P3HT$_{50}$-b-PNSS$_{10}$ and the fact that no roughness evolution is noticeable after thermal treatment (in contrast to what occurred for both P3HT and PNSS upon annealing). On the other hand, P3HT$_{50}$-b-PNSS$_{30}$ behaves more similarly to PNSS, with higher adhesion values as a pristine material (~70 nN), but lower than for the corresponding homopolymer (~90 nN), and decrease in adhesion after thermal treatment (~46 nN). The latter value is reasonably in line with the values obtained for PSS (~40 nN). Yet, the values for the pristine material (~70 nN) could be both due to resemblance to pristine P3HT (~70 nN) or PNSS partial deprotection (intermediate value between 90 and 46 nN). Again, the absence of changes in terms of morphology and roughness (Table 2.3, Figure 2.32) somewhat indicate the absence of modifications at

the surface level upon annealing, which could be due to a partial deprotection of the PNSS block at the surface.

In addition, Figure 2.35 displays the IR transmission spectra for P3HT$_{50}$-*b*-PNSS$_{30}$, before and after thermal annealing. Clearly, thermal treatment induces a huge modification of the band at 3200 cm^{-1}, related to the formation of –OH groups proving the loss of the neopentyl protecting group as a volatile byproduct, as well as a modification in the fingerprint region due to the conversion of the sulfonate groups to sulfonic acids. However, from this IR data is noticeable that even initially, a broad band in the hydroxyl domain can be observed, which further increases after thermal treatment. This could be due to the suspected partial deprotection at a surface level.
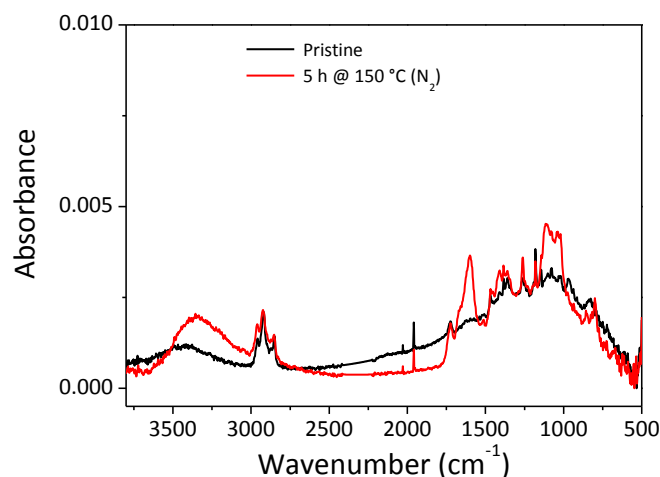
Figure 2.35. IR transmission spectra for P3HT$_{50}$-*b*-PNSS$_{30}$ deposited on KBr following the same deposition technique pristine (grey line) and after thermal treatment (red line).

The behaviour in terms of morphology, roughness, and tip-sample interaction (adhesion) suggests that, for the studied block copolymers, PNSS blocks could be located at the surface of the sample and partially deprotected already in the pristine material. This finding questions the need for applying a complete thermal treatment when introducing this material as an interfacial adhesive layer in the solar cell stack, since the film surface (in contact with PEDOT:PSS in an inverted structure) would be containing PSS even without thermal treatment. However, it must be noted that the segregation of the materials to the surface is highly dependent on the substrates employed for the analysis. Accordingly, the fact of coating the active layer below the interlayer (block copolymer) could indeed

modify the behaviour and segregation of the material. Similarly, different interactions could be created in a complete device.

2.3.2.2. Characterisation of PEDOT:PSS and P3HT:PCBM

In order to obtain further information about the possible interactions with the layers below and above, the same adhesion characterisation was performed for pristine P3HT:PCBM and PEDOT:PSS. It must be recalled that calculated adhesion values correspond to the interactive forces established between the tip and the samples surface, and have been employed to characterise the different materials. However, this does not provide any direct information about the adhesion *between* layers, as can be obtained *via* other methods like the double cantilever beam.[11]

Figure 2.36 displays the average trace-retrace curves obtained for pristine P3HT:PCBM (a) and PEDOT:PSS (b), and Figure 2.37 summarises the adhesion values evaluated from the feedback images for both layers, together with the two studied block copolymers before and after thermal annealing.

(a)   **(b)**
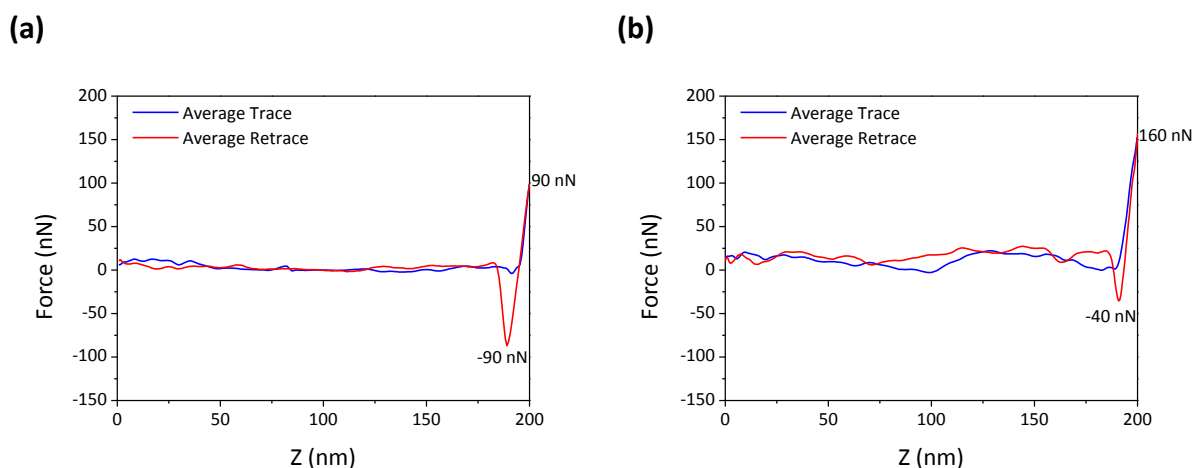
Figure 2.36. Average trace (approach) and retrace (withdraw) curves acquired pristine (a) P3HT:PCBM and (b) PEDOT:PSS.

As can be observed from Figure 2.37, and in comparison with Figure 2.34 (b), adhesion in P3HT:PCBM (~70 nN) is similar to P3HT (~70 nN), whereas PEDOT:PSS displayed lower adhesion values (~32 nN), comparable to PNSS after deprotection (~40 nN). Besides, the adhesion values displayed by the block copolymers are intermediate between the two materials, and more in line with that of PEDOT:PSS, especially after deprotection in the case of P3HT$_{50}$-*b*-PNSS$_{30}$. It must be noted that the average retrace for P3HT:PCBM stems from rather disparate retrace curves [see Figure 2.38, (a)].

This behaviour is attributed to the different interactions established with the P3HT and PCBM domains in the sample.
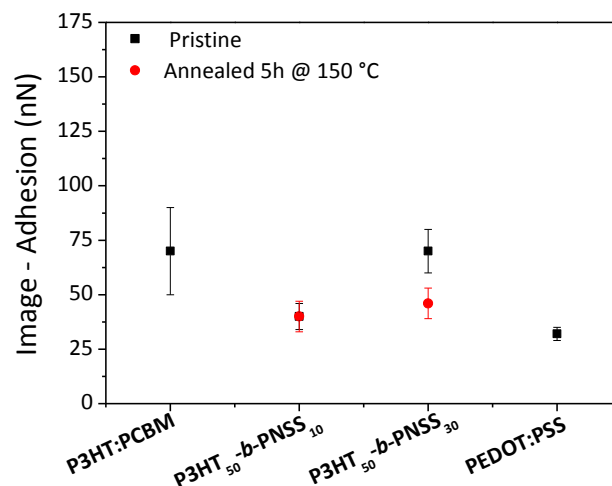
Figure 2.37. Adhesion values before (black) and after (red) thermal treatment for the different materials, as evaluated from the mean value recorded in the adhesion channel.

(a)   **(b)**
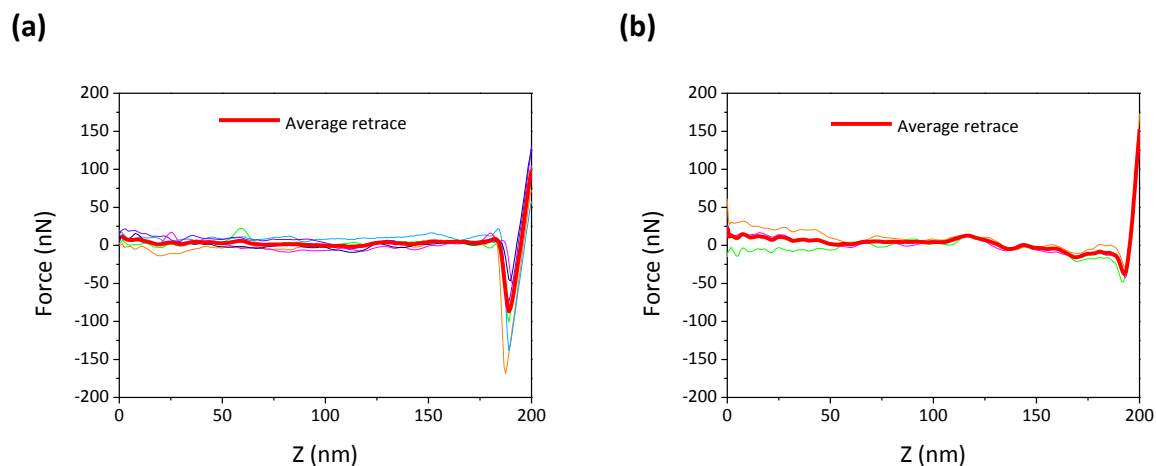
Figure 2.38. In colours, the analysed retrace curves to obtain the red average retrace curve for (a) pristine P3HT:PCBM and (b) annealed P3HT:PCBM in each case.

For the purpose of enhancing adhesion between P3HT:PCBM and PEDOT:PSS in inverted devices, the block copolymers are to be coated on top of the active layer. Thus, the effects that the annealing treatment (5 h at 150 °C) had on the active layer were analysed. Interestingly, such treatment led to a more distinctive behaviour in terms of the force-displacement curves [Figure 2.38, (b)] compared to the variance recognised before annealing [Figure 2.38 (a)]. Additionally, the average

retrace curve for annealed P3HT:PCBM clearly presents lower adhesion values than the pristine material. This behaviour is ascribed to an enhanced content of PCBM on the surface, as reported throughout the literature,[89-90] which, in turn, led to lower sample-tip interactions.

(a)

(b)

(c)
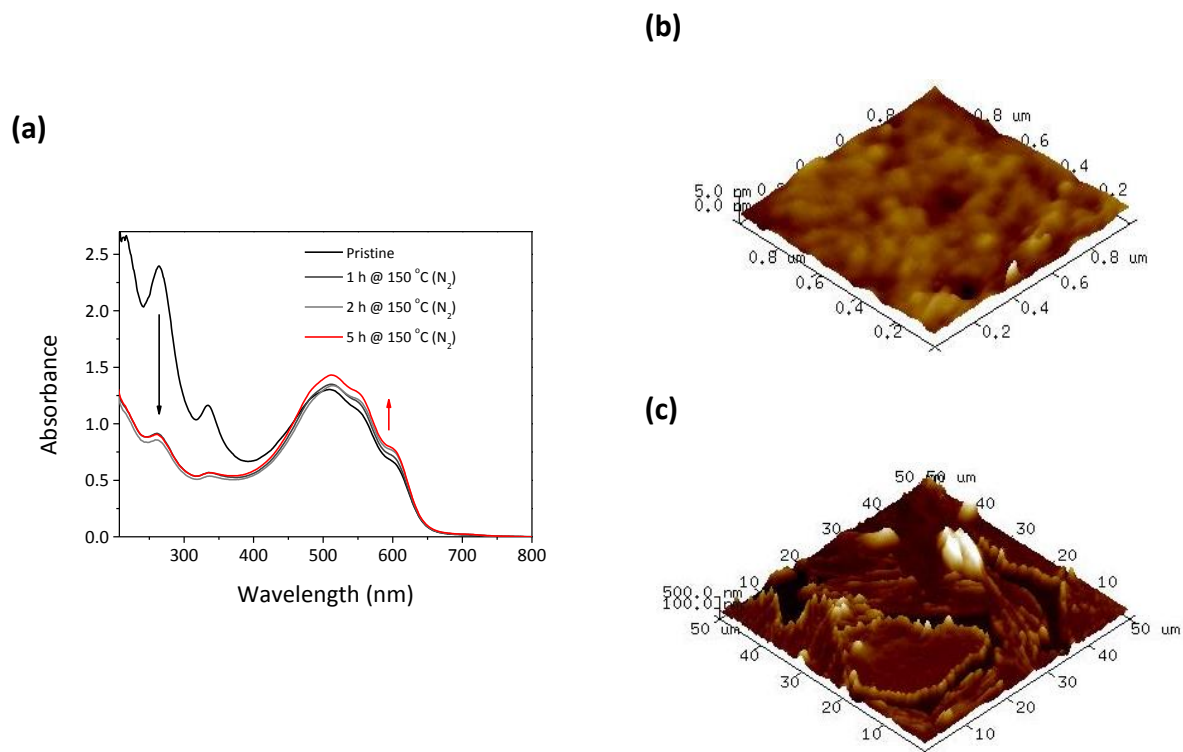
Figure 2.39. (a) UV-Vis spectra recorded upon annealing of P3HT:PCBM thin films at 150 °C for 5 hours. (b) AFM height image (1 x 1 μm) obtained for a pristine P3HT:PCBM. (c) AFM height image (50 x 50 μm) obtained for a P3HT:PCBM sample annealed for 5 hours. The image size was selected to better illustrate the PCBM crystallites on the surface.

Finally, P3HT:PCBM samples were examined upon annealing using UV-Vis spectroscopy [Figure 2.39, (a)] and AFM, the latter to obtain morphological information in the corresponding height images obtained for pristine [Figure 2.39 (b)] and annealed [Figure 2.39 (c)] samples. The UV-Vis spectra show a dramatic decrease in the bands in the range 200-350 nm, characteristic of PCBM, as well as a slight increase of the band at 500 nm, corresponding to P3HT. This evolution is the result of a morphological rearrangement of the two materials in the blend: PCBM migrates to the surface and aggregates to big crystallites there, leading to an inhomogeneous lateral distribution of PCBM and consequently to a drop of the overall absorption in the UV region. The slight increase at 500 nm indicates an enhanced π-π stacking of P3HT due to a higher degree of crystallinity in the polymer domain as well. Concurrently, AFM height images illustrate the evolution from a smooth and

homogenous pristine surface [Figure 2.39 (b)] to the formation of big PCBM crystallites after thermal annealing [Figure 2.39 (c)], in line with the literature.[89-90] These data evidence that such thermal treatment is very detrimental for the active layer, for which keeping appropriate domain sizes of donor and acceptor is mandatory for achieving satisfactory device efficiencies. Thus, if an interlayer material needs to be fully deprotected after coating on top of the active layer *via* thermal annealing, such annealing should occur either at lower temperatures or using substantially shorter deprotection times.

2.3.2.3. Modification of the PSS protecting group

AFM findings on the analysis of P3HT-*b*-PNSS copolymers coated on glass substrates suggest that surface removal of the neopentyl groups occurs even before the thermal treatment is applied. According to these results, coating of the pristine copolymer already leads to a disposition of PSS groups at the surface of the layer and this could, in principle, directly enhance chemical interactions with PEDOT:PSS without any thermal treatment. However, it must be recalled that different behaviour and interactions may be observed when implementing this interlayer in a complete cell. Besides, suitable charge transport properties of the interlayer are to be considered, for which appropriate domains of the two polymer blocks with full removal of the protecting groups to yield PSS could be required throughout the entire thickness of the layer, and not only at its surface.

TGA studies on these copolymers concerning the conditions required for full removal of the neopentyl groups from PNSS homopolymer and P3HT-*b*-PNSS copolymers indicated that the deprotection time at 150 °C varies from 30 minutes (in PNSS) to 3 hours or more depending on the PNSS length in the corresponding P3HT-*b*-PNSS copolymers.[111] This long annealing treatment limits the application of these materials in OSCs, particularly in inverted structures, which, in turn, are those which would be theoretically benefited from the application of this interfacial adhesive layer in between P3HT:PCBM and PEDOT:PSS. However, when processing such inverted devices, the interlayer is to be coated on top of the active layer; after which, thermal treatment at 150 °C to deprotect PNSS for at least 3 hours would follow. This long annealing time at such temperature is, nonetheless, detrimental for the active layer coated below in terms of morphology, and as a result, for the solar cell performances.

Whilst the general approach to prepare the amphiphilic P3HT-*b*-PSS copolymers through the synthesis of an alkyl-protected PSS has been successful, shorter deprotection times are desirable to prevent unfavourable effects in the solar cell devices. In the quest for more suitable materials, our

research group utilised RAFT polymerisation to synthesise a systematic range of styrene sulfonate polymers bearing different linear and branched aliphatic protecting groups, namely: *n*-propyl, isopropyl, *n*-butyl, isobutyl, *n*-pentyl and, to ensure the same characteristics as the rest of the polymers, again neopentyl, see Figure 2.40. The thermal lability of the various protecting groups was then systematically assessed using thermogravimetric analysis (TGA) to identify a well-defined, readily processable poly(*p*-styrene sulfonate) precursor to be incorporated to a diblock copolymer together with P3HT.
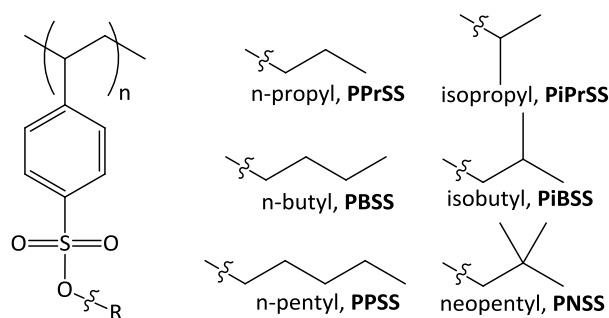
Figure 2.40. *p*-styrene sulfonate protected polymers designed and synthesised by Kolomanska *et al.*[180]

2.3.2.3.1. RAFT polymerisation of systematically varied alkyl protected PSS

The RAFT system explored for the polymerisation of NSS in section 2.3 was applied to the polymerisation of systematically varied R-protected *p*-styrene sulfonate monomers to yield the polymers in Figure 2.40. More specifically, each monomer in the series was polymerised *via* RAFT using DTTC-N$_3$ [see Figure 2.18 (b)], in THF (37 % w/v) at 60 °C for 120 hours. Comparing to the conditions previously selected as optimal for the polymerisation of NSS (DTTC-N$_3$, Anisole 4.0 M, 75 °C), the only variable that was kept was the use of the aliphatic DTTC-N$_3$, which afforded more controlled polymerisations, yielding polymers with narrower molar mass distributions (and also lower M_n, compared to BTTC-N$_3$). Concerning the solvent, THF was selected as it proved to be the most robust solvent system, achieving good quality polymers independently of the monomer concentration or temperature. Finally, the overall system dilution (1.5 M) enabled adequate sample uptake throughout the polymerisation, and the lower temperature (60 °C) was employed to avoid premature sample deprotection during polymerisation.

To follow the progress of each reaction, samples were taken periodically and analysed by GPC and ^{1}H NMR spectroscopy. High monomer conversion after 120 h (> 80 %) was observed in all reactions,

except the polymerisation of isobutyl *p*-styrene sulfonate, where an acceptable 69 % was reached. It is noteworthy that partial removal of the isopropyl protecting group was observed during polymerisation after 120 h at this temperature. Thus, to obtain poly(isopropyl *p*-styrene sulfonate) of a similar molar mass to the remaining polymers in the series, polymerisation to obtain PiPrSS was repeated using 0.04 eq. CTA (target D_p = 25) and stopped after 72 h to avoid premature thermolysis. Indeed, GPC analyses show that the attained molar masses for all polymers were within the range of 3000 to 3900 g mol^{-1}, all products displaying unimodal GPC traces with low molar mass dispersities ($Đ \leq 1.11$), see Table 2.6.

Table 2.6. RAFT polymerisation to yield polymers in Figure 2.40.

Product	R	$M_n^{th\ a}$ g mol^{-1}	Time h	Monomer conversion[b] %	M_n^c g mol^{-1}	$Đ$ $(M_w/M_n)^c$
PPrSS	n-propyl	4870	120	97	3300	1.09
PiPrSS	isopropyl	5590	72	92	3800	1.08
PBSS	n-butyl	5150	120	98	3800	1.09
PiBSS	isobutyl	5150	120	69	3000	1.08
PPSS	n-pentyl	5430	120	94	3900	1.08
PNSS	neopentyl	5430	120	97	3500	1.11

(a) Target degree of polymerisation, D_p = 20, with the exception of PiPrSS (target D_p = 25), which required a higher final target to achieve a similar M_n to the others in the study because prolonged polymerisation times (> 72 h) induced thermal deprotection of the polymer;
(b) determined by ^{1}H NMR spectroscopy; and
(c) determined by THF GPC (PS standards).

2.3.2.3.2. <u>TGA analysis</u>

TGA was employed to examine the thermal modification profiles of our R-protected polymers to produce poly(*p*-styrene sulfonate), PSS. Measurements were performed in two modes; a temperature sweep from 25 to 500 °C (at a rate of 10 °C min^{-1}) and an isothermal profile (150 °C) for 120 minutes, see Figure 2.41. The data clearly show that the weight loss of the branched polymers, occurring at approximately 150 °C (PiPrSS) and 200 °C (PiBSS, PNSS) in the temperature sweep experiment [Figure 2.41 (a)], occurs more readily than the weight loss in the linear counterparts (PPrSS, PBSS, PPSS), observed at approximately 230 °C. For the isothermal (150 °C) treatment, a significant weight loss is observed after 7 min for PiPrSS, 30 min for PiBSS, and 80 min for PNSS, whereas for the linear polymers only a minor decrease of weight is observed after 120 minutes.

The observed weight loss is attributed to the removal of the protecting group from the sample. However, it is noteworthy that the initial obtained weight loss percentage observed in Figure 2.41 (b) differs from the theoretically calculated values in the case of isobutyl and neopentyl derivatives;

11 % (PiBSS) and 12 % (PNSS) compared to the respective 21 % and 25 % theoretical values (including release of nitrogen from the azide group),[196-197]. This difference is attributed to a Friedel-Crafts side reaction which results in attachment of some of the alkyl protecting groups to the aromatic ring of the polymer at the *meta* position. Observation of this phenomenon has already been described for poly(neopentyl *p*-styrene sulfonate).[174,175] Interestingly, the observed weight loss closely matches the theoretically calculated values for the polymer with isopropyl protecting group (PiPrSS). Isothermal TGA [Figure 2.41 (b)] shows the differences in the time required for protecting group removal, indicating the ease of deprotection in the following order (starting with the most readily deprotected): isopropyl > isobutyl > neopentyl. Owing to the fact that the isopropyl group is easily cleavable, the degradation of PiPrSS was observed during storage at room temperature. This highlights that the design of polymers with fast cleavable groups, for processes where sustained thermal treatments are undesired, requires a compromise between lability (for application) and stability (for synthesis and short-term storage) of protecting groups. In this case, the isobutyl group providing both features was investigated further for its thermal processing behaviour and as the switchable component in P3HT-*b*-PiBSS copolymer.

(a) **(b)**
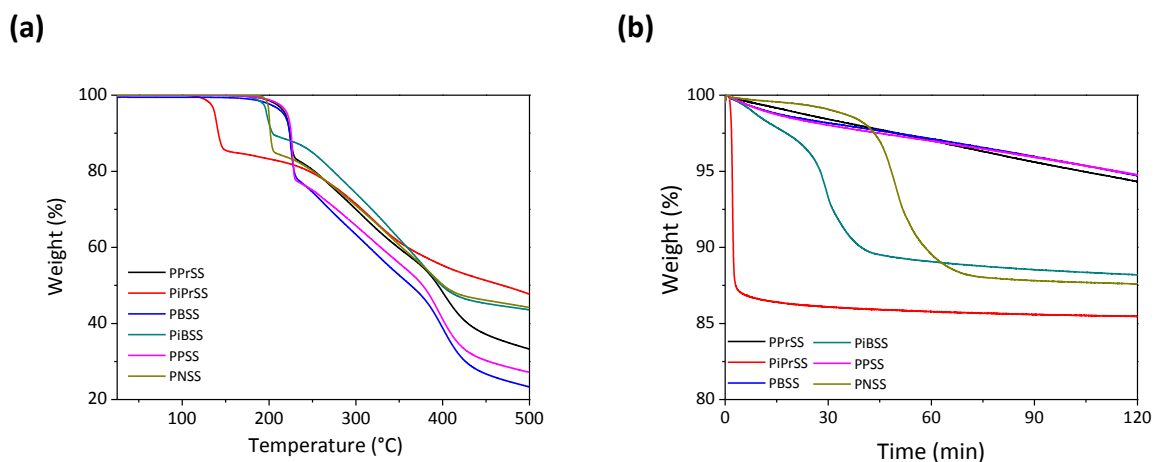
Figure 2.41. TGA thermograms of the different R-protected polymers for (a) a thermal sweep at a rate of 10 °C min^{-1} and (b) isothermal degradation at 150 °C.

2.3.2.3.3. Thermal deprotection of P3HT-*b*-PiBSS

P3HT$_{50}$-*b*-PiBSS$_{14}$ diblock copolymer was synthesised *via* 'click' coupling of alkyne-functionalised P3HT (P3HT-ethynyl) and PiBSS-N$_3$, according to previously published procedures.[111, 180] The thermal modification behaviour of the PiBSS-N$_3$ homopolymer and corresponding P3HT-*b*-PiBSS diblock copolymer was investigated by isothermal TGA (150°C, 3 h), water contact angle

measurements, and FTIR spectroscopy (before and after thermal treatment) as shown in Figure 2.42. TGA confirmed complete removal of the isobutyl group from P3HT-*b*-PiBSS (observed 6.5% weight loss, expected 6.3% weight loss for complete deprotection). The water contact angle of a film of the diblock copolymer concomitantly changed from 99.4° to 89.7° after heating at 150°C for 3 h, indicating the expected increase in surface hydrophilicity due to the formation of free sulfonic acid groups in the block copolymer. Consistent with the aforementioned isothermal experiments (Figure 2.41), the control PiBSS-N_3 homopolymer only underwent 49.8% of the expected mass loss (observed 10.2% compared to the theoretical 20.5%). This is attributed to the Friedel-Crafts rearrangement occurring in PiBSS homopolymer, but not observed in P3HT copolymer.[111] Nevertheless, the surface hydrophilicity increased significantly as a result of the thermal treatment, giving rise to a water contact angle of 51.4° compared with a contact angle of 85.9° measured for PiBSS-N_3 prior to thermal treatment. Regardless of the extent of deprotection observed by TGA for thermally treated PiBSS-N_3 and P3HT-*b*-PiBSS, the FTIR spectra of both materials displayed broad bands around 3300 cm^{-1} which clearly implies free sulfonic acid groups are formed upon thermal treatment [Figure 2.42 (b)].

(a)   **(b)**
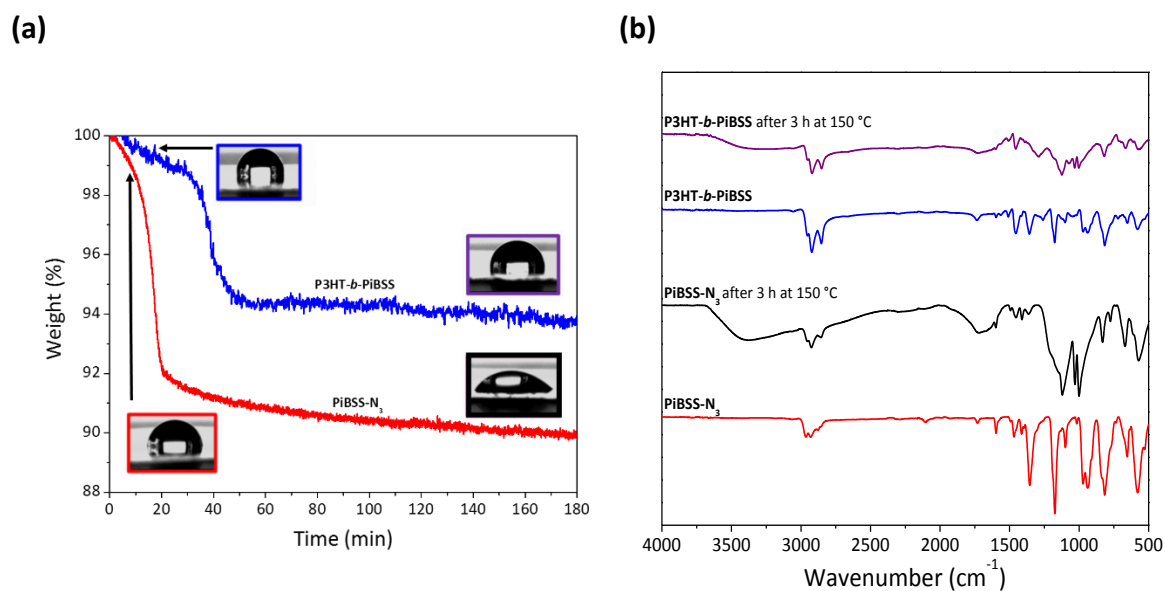
Figure 2.42. (a) Isothermal TGA profiles for P3HT$_{50}$-*b*-PiBSS$_{16}$ and PiBSS$_{16}$-N_3 (150°C, 3 h); insets show water contact angles for P3HT$_{50}$-*b*-PiBSS$_{16}$ and PiBSS$_{16}$-N_3 before and after thermal treatment (150 °C, 3 h). Contact angles for P3HT$_{50}$-*b*-PiBSS$_{16}$ are: θ = 99.4 ± 2.2° and θ$_{150°C}$ = 89.7 ± 3.9°; contact angles for PiBSS$_{16}$-N_3 are: θ = 85.9 ± 2.0° and θ$_{150°C}$ = 51.4°. (b) FTIR spectra of P3HT$_{50}$-*b*-PiBSS$_{16}$ and PiBSS$_{16}$-N_3 before and after thermal treatment (150°C, 3 h).

Replacing the neopentyl group in P3HT$_{50}$-*b*-PNSS$_{16}$ with the isobutyl protecting group used in the current diblock material (P3HT$_{50}$-*b*-PiBSS$_{14}$), resulted in a decrease in the required deprotection time (at 150°C) from 3 h (for P3HT$_{50}$-*b*-PNSS$_{16}$) to around 45 minutes (for P3HT-*b*-PiBSS). This thermal processing behaviour renders P3HT-*b*-PiBSS a better candidate for application in solar cell devices, for which long annealing temperatures should be avoided.

2.4. Conclusions

Studies of the RAFT polymerisation of neopentyl *p*-styrene sulfonate have been performed to identify optimum synthetic conditions. Two chain transfer agents were trialled, 2-azidoethyl 3-benzylsulfanylthiocarbonylsulfanylpropionate (BTTC-N$_3$) and 2-azidoethyl 2-(dodecylthiocarbonothioylthio)-2-methylpropionate (DTTC-N$_3$), where the latter, characterised by a tertiary (and therefore more stable) leaving group with higher fragmentation rates, offered more control as shown by the unimodal GPC traces and lower dispersities of the produced polymers. The effect of the initial monomer concentration (0.8, 1.3 or 4.0 M) was assessed, indicating higher polymerisation rates for more concentrated systems. Faster reactions and higher monomer conversions were observed with the most polar solvent (THF), attributed to the lower affinity of the relatively non-polar monomer radicals for the solvent. Promising results were obtained for the three solvents when [NSS]$_0$ = 4.0 M, with anisole leading to marginally better dispersity values (*Đ* < 1.10). As expected, the polymerisation rate could be increased by increasing the temperature from 60 to 75 °C, without compromising control over the process. The most successful conditions ([NSS]$_0$ = 4.0 M, DTTC-N$_3$ in anisole at 75 °C) were employed to obtain well-defined PNSS of varied molar masses with unimodal distributions (*Đ* ≤ 1.50 in all cases). Finally, to demonstrate the utility of this synthetic approach, a poly(neopentyl *p*-styrene sulfonate)-*b*-polybutadiene-*b*-poly(neopentyl *p*-styrene sulfonate) triblock copolymer was synthesised by azide-alkyne 'click' chemistry (highlighting good retention of the azide functionality on the PNSS chains) and subsequent thermolysis produced an amphiphilic copolymer containing poly(*p*-styrene sulfonate) segments.

Following the same strategy, our research group synthesised P3HT-*b*-PNSS block copolymers with varying PNSS block lengths for application as interlayer in OSCs.[111] The surface characterisation of P3HT$_{50}$-*b*-PNSS$_{10}$, P3HT$_{50}$-*b*-PNSS$_{30}$, P3HT and PNSS thin films, was carried out by means of AFM. Both pristine and thermally annealed (5 hours at 150 °C) films have been characterised using AFM working in classical Tapping mode (height images) and QNM Peak Force mode (nanomechanical properties). Analysis of the adhesion forces established between the AFM tip and the sample showed increasing similarity between the behaviour of the block polymers and that of PNSS when the length of the PNSS block was incremented. However, no morphological or roughness changes were observed after annealing of the block copolymers, contrary to the increase in roughness (for both P3HT and PNSS) and morphological order (for PNSS) after annealing. This somewhat unexpected behaviour, together with the fact that the adhesion values displayed by the block copolymers after thermal annealing were close

to those obtained for PSS, led to the conclusion that PNSS block is possibly located at the surface level and at least partially deprotected. This calls into question the need for full deprotection of the block copolymers when using it as interlayers in the devices, as this requires long temperature treatments that, in turn, can be detrimental for the active layer and device performance. Finally, on the analysis of PEDOT:PSS and P3HT:PCBM thin films, the former displayed similar adhesion behaviour to PSS, whilst P3HT:PCBM adhesion values were markedly affected by the thermal treatment applied to the active layer. On the one hand, the characterisation of the active layer provided further evidence about an enhanced content of PCBM upon thermal annealing (5 hours at 150 °C), thus negatively affecting the bulk-heterojunction morphology. On the other hand, the consistent adhesion values obtained for these materials depending on their composition (*i.e.* PEDOT:PSS showing similar values to PSS) validate the method as a tool for surface characterising thin films.

To overcome long temperature treatments reported for the full deprotection of P3HT-*b*-PNSS (≥ 3 hours at 150 °C), collaborative work with Kolomanska *et al.*[180] has been undertaken to produce a series of systematically modified R-protected *p*-styrene sulfonate polymers *via* RAFT. The complete series comprises styrene sulfonate polymers bearing different linear and branched aliphatic protecting groups, namely: *n*-propyl, isopropyl, *n*-butyl, isobutyl, *n*-pentyl, and, to ensure the same characteristics as the rest of the polymers (since the polymerisation conditions were modified), again neopentyl. The conditions employed, based on the results obtained for the optimisation of the RAFT synthesis of NSS, resulted in high quality polymers with comparable M_n (3000 to 3900 g mol^{-1}), low molar mass dispersities (Đ ≤ 1.11) and unimodal GPC traces in all cases. Thermogravimetric analysis (TGA) of the different R-varied polymers identified poly(isobutyl *p*-styrene sulfonate) as the best poly(*p*-styrene sulfonate) candidate for incorporation into a diblock copolymer with P3HT to yield the target P3HT-*b*-PSS, due to a better lability upon thermal treatment and stability at room temperature. Thermogravimetric analysis on the thermal behaviour of P3HT$_{50}$-*b*-PiBSS$_{14}$, synthesised *via* 'click' coupling of P3HT-ethynyl and PiBSS-N$_3$, indicated shorter deprotection times (around 45 minutes) compared to the 3 hours required for the previously studied P3HT$_{50}$-*b*-PNSS$_{16}$ copolymer. This significantly improves the deprotection conditions required for implementation of this kind of thermally triggerable block copolymers as an interlayer in OSCs, designed to enhance interactions between the active layer (P3HT:PCBM) and the hole transport layer (PEDOT:PSS).

Chapter 3.   Photochemical Stability of Low Bandgap Polymers for the Active Layer

3.1. Introduction

One of the most crucial factors limiting lifetime in organic solar cells is the photochemical degradation of the active layer components.[6-8] Indeed, the employed polymers, as organic materials, are unstable and degrade when exposed to solar irradiation, this effect being more enhanced when UV-Vis radiation is combined with oxygen ingress into the device.[95, 198] Therefore, elucidation of the mechanisms and parameters responsible for polymer photodegradation is a key point to develop strategies that decrease or prevent the loss of the functional properties of these materials.

Accordingly, this chapter focuses on the photochemical stability of a series of low bandgap polymers, synthesised for the purpose of enhanced solar cell performances. Firstly, the photochemical pathways of poly[(4,4'-bis(2-ethylhexyl)dithieno[3,2-b:2',3'-d]silole)-2,6-diyl-*alt*-(4,7-bis(2-thienyl)-2,1,3-benzothiadiazole)-5,5'-diyl] (Si-PCPDTBT) are elucidated by experimentally monitoring and theoretically analysing the structural changes occurring upon photooxidation. In the second part of the chapter, the relative photochemical stability of a series of low bandgap polymers (P1 - P4, P5a - c, see structures in Figure 3.24) of systematically modified backbones and/or side chains is assessed, with the aim of establishing a relationship between the chemical structure and the resulting photostability. In order to obtain information relevant to the use of these polymers in solar cell devices, their stability when blended with PCBM is also investigated. These aspects are summarised in Figure 3.1.
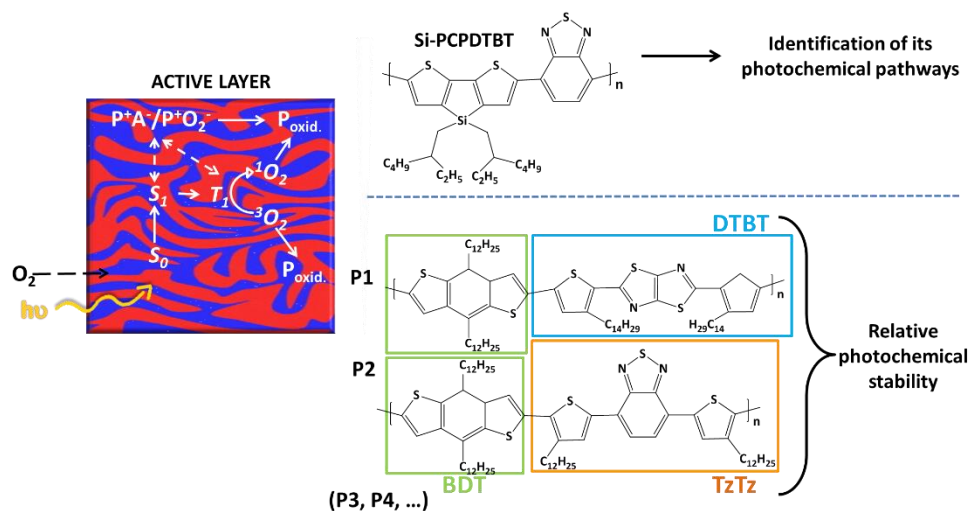
Figure 3.1. Summary of the aspects treated in this chapter, dealing with the photostability (mainly in presence of oxygen) of low bandgap polymers (P) designed for the active layer. The reader is directed to Section 1.4.2.4 for detailed description of the abbreviations describing the photochemical pathways in the active layer. BDT, benzodithiophene; DTBT, dithienylbenzothiadiazole; TzTz, thiazolothiazol.

3.1.1. Photochemical stability of the active layer

3.1.1.1. Photochemical degradation of p-type polymers

As described in Section 1.2.1, the most characteristic structural feature in p-type polymers is the alternation of single and double bonds, which creates a highly delocalised π-electron system, able to absorb visible photons and transport charges along the polymer chain. In this regard, any physico-chemical processes diminishing the degree of conjugation and the ordering of polymer chains can contribute to cell degradation. Whilst many processes can impair light absorption and transport in the active layer,[6-8] in the following, focus is placed on light induced processes (in the presence or absence of oxygen) that are responsible for polymer degradation.

3.1.1.1.1. <u>Photochemical degradation in presence of oxygen</u>

Conjugated polymers are known to rapidly lose their absorption and charge transport properties in the combined presence of light and oxygen. It is generally recognised that two different types of processes are responsible for this degradation; so-called reversible and irreversible degradation.[16] On the one hand, reversible photochemical effects are attributed to the creation of a charge transfer complex (CTC) between O_2 and the polymer. On the other hand, irreversible degradation proceeds *via* a chain radical oxidation mechanism, or reaction with a highly reactive oxygen species, such as singlet oxygen, $^1O_2$.

3.1.1.1.2. <u>Reversible degradation - charge transfer complex with oxygen</u>

Studies attribute reversible degradation to the photoinduced formation of a charge transfer complex (CTC) by electronic transfer between O_2 and the polymer.[199] This complex has been detected in commonly employed p-type polymers by means of electronic paramagnetic resonance.[200-201] Although the existence of this charge transfer complex is light dependent, its persistency under ambient conditions and in the dark has been observed. However, the formation of this complex, which has also been detected in presence of the PCBM, can be overcome by applying heat or vacuum, as summarised in Figure 3.2.[200-201] Moreover, the CTC has been associated with irreversible degradation, for example, if the relaxation of the P^+/O_2^- complexes produces highly reactive singlet oxygen states $(^1O_2)$[201] Importantly, formation of the charge transfer complex has been proven to be the main cause for performance loss of P3HT:PCBM solar cells under photooxidative conditions.[96]
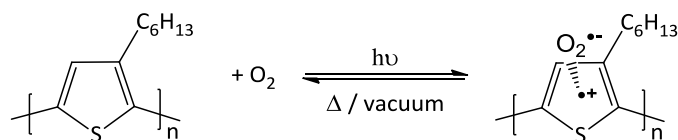
Figure 3.2. Formation of the Charge Transfer Complex (CTC) of P3HT with oxygen. Adapted from reference 199.

3.1.1.1.3. Radical oxidation mechanism

P-type polymers can degrade following the degradation mechanisms reported for commonly employed aliphatic polymers such as polyethylene (PE) or polypropylene (PP).[10] The main steps of the radical oxidation mechanism are reported in Scheme 3.1.

Initiation	$r^\bullet + PH \longrightarrow P^\bullet + rH$	**(1)**
Propagation	$P^\bullet + {}^3O_2 \longrightarrow PO_2{}^\bullet$	**(2)**
	$PO_2{}^\bullet + PH \longrightarrow PO_2H + P^\bullet$	**(3)**
Termination	$PO_2{}^\bullet + PO_2{}^\bullet \longrightarrow$ *inactive species*	**(4)**
	$P^\bullet + P^\bullet \longrightarrow$ *inactive species*	**(5)**
Branching	$PO_2H \xrightarrow{h\upsilon,\,\Delta} PO^\bullet + {}^\bullet OH$	**(6)**
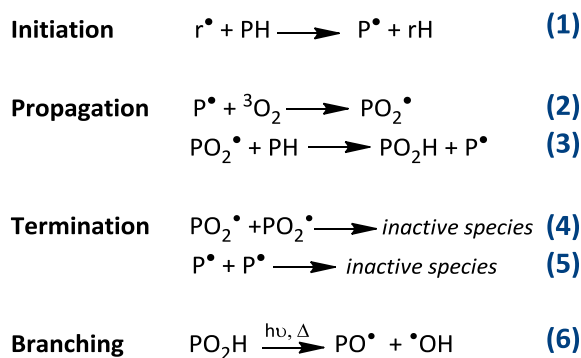
Scheme 3.1. Main steps of the radical oxidation mechanism. Adapted from reference 10.

In the initiation step **(1)**, the polymer (PH) undergoes hydrogen abstraction by free radicals ($r^\bullet$), formed *via* photonic excitation of chromophoric species. In the propagation steps **(2, 3)**, the created macroradical ($P^\bullet$) reacts with oxygen, yielding a peroxy radical ($PO_2{}^\bullet$) that rapidly evolves to hydroperoxide (PO_2H) by abstraction of a labile hydrogen atom. The so-formed hydroperoxides can then decompose thermally or photochemically to give macroalkoxy radicals and hydroxyl radicals, capable of undergoing further radical reactions **(6)**. Finally, termination occurs when two radical species react with each other to yield inactive species **(4, 5)**.

According to what previously described, the process starts by excitation of a chromophore; the identification of the species acting as chromophore is, however, subject of discussion.[10] Sunlight wavelengths reaching the surface of the Earth extend from the IR to the UV region, with a cut-off of 290-300 nm depending on the atmospheric conditions. Since aliphatic polymers (such as PE or PP) do not absorb light in this domain, initiation in the chain radical oxidation mechanism is attributed to the presence of material impurities acting as chromophoric species. In the case of polypropylene,

hydroperoxides (weakly absorbing up to 360 nm) were identified as the moieties most likely to be responsible for the production of reactive free radicals.[202] For p-type polymers, whose absorption is extended into the visible domain, the polymer on its own can act as a chromophore able to initiate the radical oxidation.[10] Alternatively, free radicals can be photosensitised by material impurities, such as residual metal catalysts or organic impurities, resulting from the polymer synthesis.[203] Remarkably, a relationship has been established between the quantity of paramagnetic species in conjugated polymers, their photochemical and thermal stability, and ultimately the resultant device performance.[204-205]

Radical oxidation has been reported for many relevant polymers in OSCs.[206-213] According to the commonly accepted radical mechanism for the benchmark P3HT, the oxidative process starts by hydrogen abstraction at the α-carbon atom of the hexyl side chain.[214] The low C-H bond dissociation energy at this point is justified by the stabilisation of the created radical by the adjacent π-electron system of the backbone. It is noteworthy that this mechanism is valid for the majority of p-type polymers, since they all possess alkyl side chains, necessary to render the polymers soluble in commonly employed organic solvents.
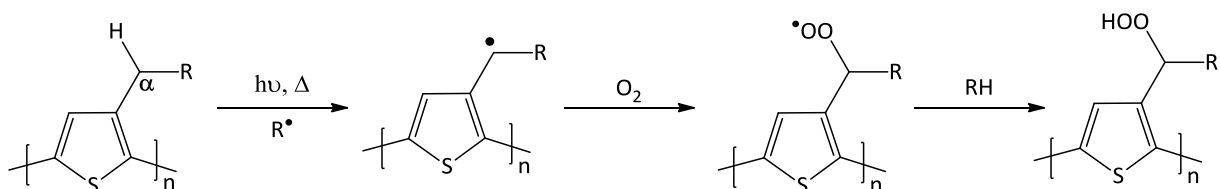
Figure 3.3. Radical oxidation mechanism in P3HT, starting at C$_\alpha$ of the side chain. Adapted from reference 214.

After oxidation of the C$_\alpha$ (see Figure 3.3), oxidation propagates through the entire macromolecule. According to Manceau *et al.*,[214] and based on the identification of the degradation products by infrared spectroscopy, the degradation mechanism of the alkyl side chain involves the formation of alcohols, ketones, aldehydes, and carboxylic acids, as illustrated in Figure 3.4. Additionally, degradation of the backbone is dominated by oxidation of the sulfur atoms into sulfoxides, sulfones and eventually into sulfinic acids (see Figure 3.5).
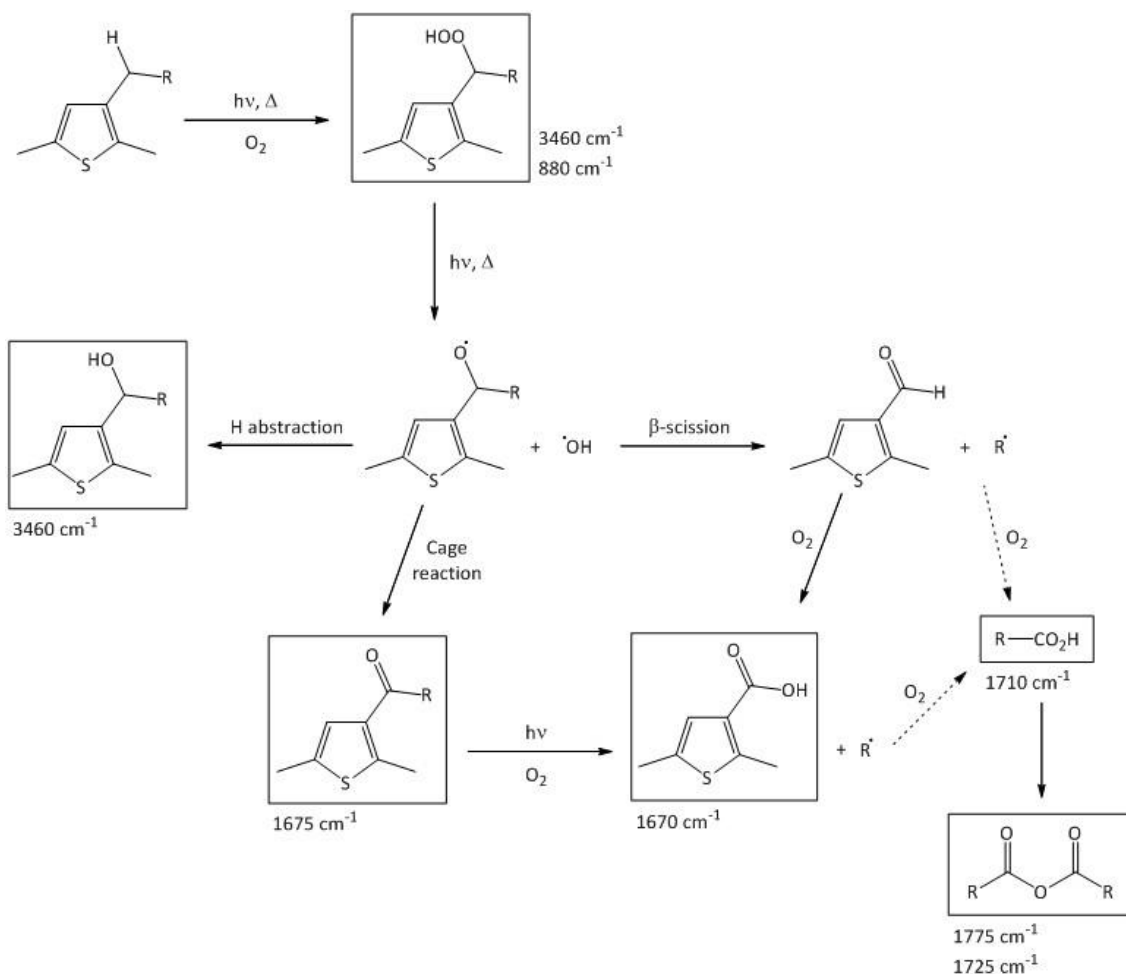
Figure 3.4. Oxidation of the alkyl side chain in P3HT. Adapted from reference 214.
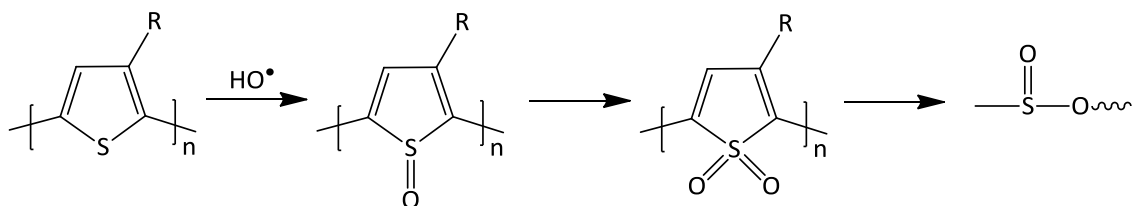
Figure 3.5. Oxidation of the conjugated backbone in P3HT. Adapted from reference 214.

3.1.1.1.4. <u>Reaction with singlet oxygen ($^1O_2$)</u>

Another photodegradation mechanism is the reaction of polymers with singlet oxygen ($^1O_2$), formed *via* energy transfer from photoexcited T_1 state of the polymer to adsorbed oxygen molecules in the ground state ($^3O_2$), as depicted in Figure 3.6. For this exchange to take place, intersystem crossing ($S_1 \rightarrow T_1$) in the polymer needs to be sufficiently favoured, and populate a long-living T_1 state that is higher in energy than the oxygen singlet state (0.98 eV).[8]
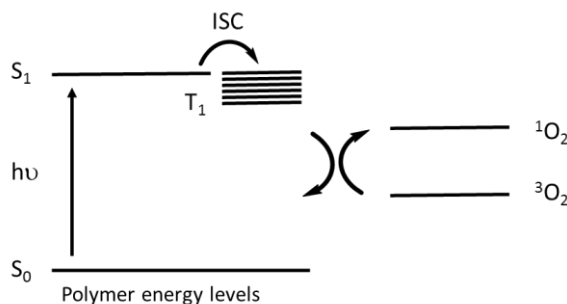
Figure 3.6. Energetic diagram corresponding to the formation of singlet oxygen ($^1O_2$) *via* energy transfer from the T_1 state of the polymer to adsorbed oxygen in the ground state ($^3O_2$). Polymer T_1 state is populated *via* intersystem crossing (ISC) from photoexcited S_1 state. Adapted from reference 8.

Once formed, singlet oxygen can undergo a Diels-Alder cycloaddition with the π-electron system of the polymer. After formation of an intermediate endoperoxide, disruption of the π-conjugation, or even polymer chain scission, can occur. As an example, Figure 3.7 illustrates singlet oxygen addition to the vinylene bond in PPV. Just as for radical oxidation, reaction with singlet oxygen has been reported for commonly studied p-type polymers for OSCs, both in solution and films.[215-218]
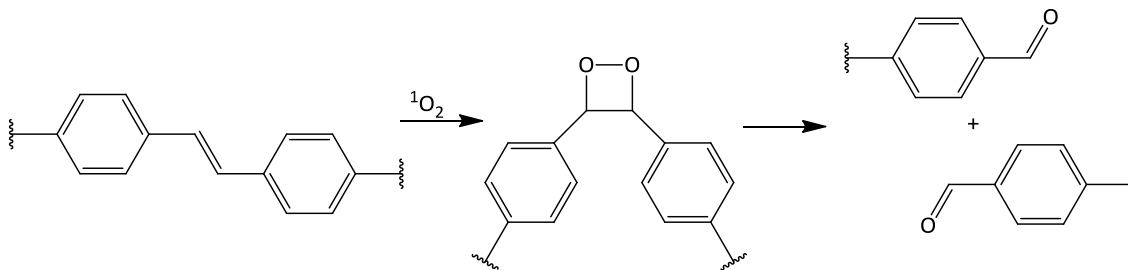
Figure 3.7. Reaction of a PPV polymer with singlet oxygen ($^1O_2$). Adapted from reference 8.

3.1.1.1.5. <u>Prevalence of the different mechanisms</u>

The prevalence of one of these degradation mechanisms over the other depends on the characteristic of each specific polymer and the degradation conditions. For example, degradation of P3HT by means of $^1O_2$ has been reported in solution,[215] but has been discarded in the case of polymer films by Manceau *et al.*,[219] proposing instead a chain radical oxidation mechanism.[214] This mechanism occurred both under photooxidation and thermooxidation, suggesting that singlet oxygen is not the main intermediate in the degradation process. Interestingly, Hintz *et al.*[212] have suggested that both mechanisms account for the degradation of P3HT depending on the irradiation conditions. Whilst illumination in the visible region (525 nm) favoured direct degradation of the π-conjugated

system (suggesting attack by singlet oxygen), illumination with more energetic UV photons (365 nm) indicated a radical mechanism initiated by hydrogen abstraction at the side chains of the polymer and subsequently extending to the conjugated backbone. Conversely, Tournebize *et al.*[220] have proposed that radical chain oxidation operates both under UV and visible illumination, and the distinct degradation behaviour observed was ascribed to the different reactivity of the created oxidation products under these conditions. In fact, the apparent higher reactivity of the alkyl side chains under UV irradiation was explained by the creation of certain oxidation species (*e.g.* hydroperoxides or ketones) that can further decompose when irradiated with UV light (but not with visible light), notably promoting migration of the side chains as volatile by-products. Recently, photooxidation of the high-performing polymer thieno[3,4-b]thiophene-alt-benzodithiophene (PTB7)[32] has been shown to occur *via* singlet oxygen attack both in solution and films.[216]

3.1.1.2. Photochemical degradation in absence of oxygen

Whilst the combination of light and oxygen is especially destructive for p-type polymers, the suppression of oxygen does not guarantee the absence of photochemical reactions. Nonetheless, the photodegradation rate is dramatically reduced in the absence of oxygen, to varying extents, depending on the polymer.[221-223] It is important to note that certain chemical bonds can be homolitically broken *via* light absorption in the UV-Vis domain, such as C-N or C-O.[208, 223] For example, cleavage of the C-O bond in MDMO-PPV leads to scission of the alkyl side chains, creating free radicals that can further react with the macromolecule. In this way, the overall loss of absorbance upon irradiation without oxygen has been explained by saturation of the highly reactive exocyclic double bond by free radicals, thus breaking the conjugation.[223] A similar mechanism has been proposed for P3HT irradiated without oxygen, for which reduction of the conjugated length can arise from saturation of the aromatic rings by alkyl moieties. The lower reactivity of aromatic rings and alkyl side chains compared to the exocyclic double bonds and alkoxy side chains would explain the higher stability of P3HT compared to MDMO-PPV.[222]

As stated in Section 3.1.1.1.1, defects or impurities in the material, such as residues of metal catalyst or organic impurities (unreacted monomers, coupling by-products, oligomers, and other reagents resulting from polymer synthesis or purification), are able to promote photochemical degradation.[204, 224-225] To this end, many research efforts have been made over the past years to minimise polymer impurities and defects in the materials, both upon synthesis[226-227] and purification.[228]
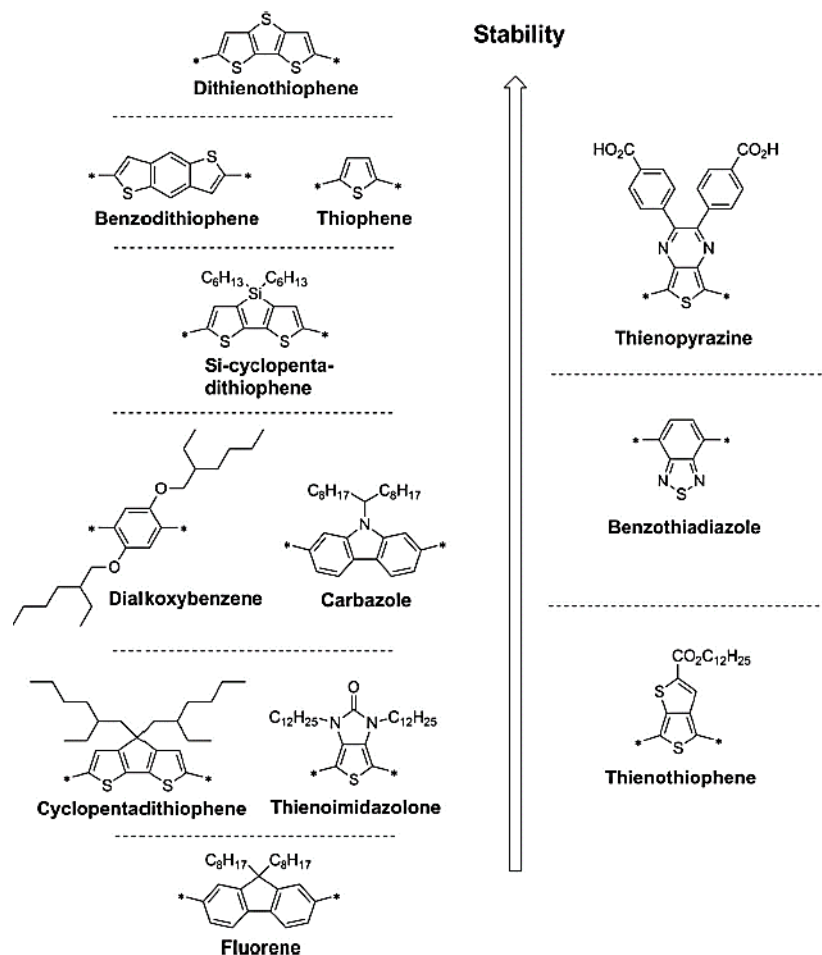
Figure 3.8. Photostability ranking of donor (left) and acceptor (right) units commonly employed in OSCs polymers, as determined by Manceau *et al*.[210] Obtained from reference 6.

3.1.1.3. Influence of chemical structure

P-type polymers are described in terms of their conjugated backbone and the corresponding alkyl side chains. This conjugated backbone can be constituted by purely donor units (such as thiophene monomers in P3HT) or, in the case of low bandgap polymers, by the alternation of electron-rich (donor) and electron-poor (acceptor) groups. Since both the variety of monomer structures and the possibilities of combination are manifold, a great variety of polymers are currently being synthesised.[42-43] This somewhat makes it arduous to trace photochemical (in)stability back to a specific building block or to a certain structural combination (especially if one considers the additional parameters influencing photostability, see Section 3.1.1.4). Accordingly, Manceau *et al.*[210] studied a broad range of polymer types and chemical structures, establishing a stability ranking for different donor and acceptor units (see Figure 3.8), providing guidelines for the design of photostable polymers.

A clear outcome from this study was that the side chains play a key role in conjugated polymer degradation, both in what refers to the nature of the pendent chain and the employed bridging atoms, *i.e.* the atoms that link the side chain to the conjugated backbone. For instance, the presence of readily cleavable bonds in the structure (such as C–N or C–O) was found to limit stability, in line with mechanisms proposed in the literature.[206, 208, 229-230] Interestingly, the authors indicated that the simple modification of C by Si as the bridging atom increased the photostability of the corresponding polymers.[210] Concerning the nature of the pendent chains, ester and alkoxy substituents led to lower stabilities, and higher photoresistance was observed in the absence of side chains. However, as aforementioned, the presence of side chains is necessary to ensure solubility and processability and may also affect other material properties, such as the energy levels or molecular packing.[231] Manceau *et al.*[232] thus proposed an elegant approach consisting in the thermal cleavage (post-deposition) of the pendent side chains, after which, polymer photostability improved. Nevertheless, such procedures must also suit the processing requirements for fabrication of complete devices, where excessively high temperatures (or long thermal treatments) can be detrimental for good functioning of the cell.

3.1.1.4. Other influencing factors

In addition to the chemical structure, a number of parameters are known to influence polymer photostability, such as different external factors (water, temperature, ozone, or irradiation wavelengths), polymer physico-chemical characteristics (molar mass, dispersity, purity, regioregularity, or crystallinity), and the processing conditions (morphology, thickness, or post-deposition treatments). The influence of these factors is subsequently described.

3.1.1.4.1. <u>Extrinsic parameters</u>

Hintz *et al.*[233] investigated in detail a range of environmental factors influencing the photooxidation of P3HT. Photooxidation of P3HT was accelerated with increasing temperature or in the presence of water. Furthermore, water can participate as a reactant, also modifying the kind of products being formed.[233] Importantly, P3HT films were also degraded by ozone, which, in turn, can be produced by the xenon lamps frequently utilised to irradiate samples.[211] Finally, the light source employed to irradiate the samples greatly influences the photooxidative process. Hintz *et al.*[212] described the effects caused by irradiating the polymer with different wavelengths, influencing the

degradation rates, the kind of predominant mechanism (see 'Prevalence of the different mechanisms' in Section 3.1.1.1.1) and the modifications in the polymer structure.

3.1.1.4.2. Intrinsic parameters

As aforementioned, impurities or defects in the synthesised polymer can lead to lower photoresistance. In line with this, Kong *et al.*[225] observed that device performance and stability (upon light and oxygen exposure) of PCDTBT-based solar cells could be significantly improved by selecting only unimodal fractions containing the longest polymer chains, associated with a lower content in impurities/defects. Similarly, Mateker *et al.*[224] have reported the relationship between the presence of polymer organic and inorganic impurities and impaired device performances and stabilities of PBDTTPD cells. As such, Electronic Paramagnetic Resonance (EPR) has been shown as a powerful tool to quantify the amount of defects in different polymer batches and qualify them for their use in organic photovoltaic devices,[205] and the photo(thermal) stability of several polymers has been successfully traced back to the rate of accumulation of radicals as identified by means of EPR.[204]

Dupuis *et al.*[234] investigated the photostability of several batches of P3HT, exhibiting differences in regioregularity, molar mass, and purity. In this study, higher photostability was associated with higher regioregularity, crystallinity, and purity, whereas the molar mass of the examined batches had negligible effects. In the same way, Hintz *et al.*[180] and Madsen *et al.*[184] observed better stabilities to photooxidation for regioregular P3HT. Indeed, polymer regioregularity influences molecular conformation and film morphologies, as confirmed by the different shapes of the UV-Vis spectra of pristine polymers. While regioregular P3HT forms semicrystalline films, regiorandom films are disordered. Crystallinity is, in turn, associated with a higher resistance towards oxygen, either due to a lower oxygen-permeability or due to the achievement of overall longer conjugation lengths, since oxygen tends to attack at points where conjugation is disrupted (*i.e.* chain ends or kinks).[233-235] In line with this, the typical blue-shift of the absorption peak, indicative of a loss of π-conjugation (observed for oligomers with less than 20 thiophene units), was found to appear later for more regioregular films.[233] In agreement with Dupuis *et al.*,[183] Madsen *et al.*[184] observed no influence of molar mass on the photodegradation kinetics, suggesting that the actual length of the polymer chains is much less important than the achieved conjugation length.

3.1.1.4.3. <u>Experimental conditions: processing</u>

Consistently, post-deposition annealing of regioregular P3HT films led to increased conjugation lengths, which, in turn, increased the stability of the films.[235] In a similar way, PBDTTPD samples obtained from the same polymer batch upon different processing conditions displayed different photooxidation rates, due to changes in polymer packing and crystallinity.[213]

When comparing the relative photostability of different polymers, attention must be paid to the thickness of the samples, since penetration of both light and oxygen vary accordingly. Tromholt *et al.*[236] systematically assessed the relative stabilities of six different polymers with varying film thicknesses, and found a great dependence of the degradation rate with this parameter (thicker films being more photostable). However, the authors recalled that the study did not address other experimental parameters that may influence the resulting resistance to photooxidation of the different polymers, *e.g.* film morphology and crystallinity. On the study of P3HT films of different thicknesses, Madsen *et al.*[235] reported lower stability and higher sensitivity to variations in film thickness for thin films (< 60 nm), whereas for mediumly sized films (75 ≤ x ≤ 175 nm), degradation was observed to scale up with the initial number of thiophene rings. For thicker films (> 175 nm), depth-dependent oxidation rates were observed (either due to light shielding or to different oxygen contents at different film depths), with lower layers showing lower degradation rates.[235] In line with this, Chambon *et al.*[206] indicated that the oxidative degradation of MDMO-PPV films with thicknesses between 100 and 1000 nm was determined by the penetration of light into the sample, and suggested that the heterogeneity of the degradation could be limited in films of thickness < 300 nm.

3.1.2. Photostability of the active layer: the role of PCBM

Photochemical stability of polymers is normally studied by monitoring the UV-Vis absorbance loss (photobleaching) upon irradiation, in air or without air, as a function of time.[10] This information can be used for establishing the relative photostability of different polymers, if the aforementioned factors influencing photostability are appropriately considered. Nevertheless, extrapolation of these results to the behaviour of solar cells based on these polymers also requires consideration of the effects of mixing polymer and PCBM, according to the bulk-heterojunction concept. Indeed, due to the ability of PCBM to stabilise/destabilise the polymer upon light exposure and to undergo photochemical modifications itself, the relative photochemical stability of the isolated polymers and that of their blends with PCBM may be inequivalent.[237] Importantly, good correlation between photochemical modifications on isolated active layers and performance loss of the corresponding cells has been

reported, indicating that the study of blend films is a valid approach to predict the stability of cells based on these materials.[238]

3.1.2.1. Photochemical behaviour of PCBM

PCBM can undergo, on its own, several chemical reactions when exposed to light and oxygen. For instance, irreversible addition of oxygen atoms to the fullerene cage can occur, the main oxidation products being epoxides ($C_{60}>O$), single bonds (C–O), and carbonyl groups (C=O).[239-240] In the absence of oxygen, irradiation of C_{60} and C_{70} induces fullerene polymerisation.[241-242] Mono-substituted fullerenes (such as PCBM) have been reported to dimerise upon illumination, following a [2+2] cycloaddition between two parallel 6-6 double bonds on adjacent fullerenes.[243-246]

3.1.2.2. Photochemical behaviour of the active layer

Under photooxidative conditions, PCBM modifies the photooxidation rate of π-conjugated polymers, imparting both stabilising and destabilising effects.[237, 247] Considering the stabilising effects first, fullerenes possess the ability to scavenge free radicals, and this can, in turn, hinder the degradation of polymers by a radical-based mechanism.[248] Moreover, fullerenes can quench polymer excited singlet states, or act as inner filter for UV radiation, thus shielding the polymer from the action of the most effective irradiation. On the other hand, destabilising effects have been related to the photosensitisation of reactive oxygen species,[249] which, as aforementioned, are able to trigger polymer degradation. For example, PCBM possesses a triplet energy of 1.5 eV,[250] according to which, energy transfer to molecular oxygen to produce singlet oxygen can occur (the energy diagram shown in Figure 3.6 is also valid for fullerene). In the active layer, PCBM is able to accept electrons from the excited polymer, creating a charge transfer complex ($P3HT^{+}/PCBM^{-}$), after which, population of the triplet state of the polymer can occur.[237] Sensitisation of singlet oxygen can follow depending on the energy of the polymer triplet state. Additionally, Grancini *et al.*[251] have related photoexcited interfacial charge transfer state to the generation of reacting species, such as the superoxide anions ($O_2^{\bullet-}$), *via* electron transfer to present species such as $^{\bullet}OH$ or $^{\bullet}OOH$. The involvement of superoxide anions in the initial steps of degradation of P3HT (in solution) has been confirmed by Chen *et al.*[252] In turn, and consistent with a mechanism involving $O_2^{\bullet-}$, Hoke *et al.*[247] have found faster photooxidation rates for blends containing fullerenes with smaller electron affinities.

Just as for the degradation of p-type polymers, the illumination of blends in the absence of oxygen leads to considerable higher stability compared to photooxidation.[222-223]

Importantly, Distler *et al.*[243] ascribed the main modifications of the blend under these conditions to photoinduced dimerisation of PCBM, resulting in a loss of power conversion efficiency. Interestingly, this same dimerisation process has been indicated to increase the stability of the active layer under thermal stress.[245-246] Tournebize *et al.*[253] also proposed that, after the creation of radicals *via* photoinduced scission of the N-C bond in PCDTBT, reaction of these radicals with the fullerene cage can follow, leading to the stabilisation of the active layer morphology. Furthermore, photochemistry has been intentionally used for stabilising the metastable morphology of the bulk heterojunction. Accordingly, photochemical treatment of bulk heterojunctions, where the polymer and/or PCBM have been chemically functionalised, can lead to the crosslinking of the film.[91-92]

3.1.3. Research focus

The first part of this chapter is devoted to elucidation of the photochemical mechanisms responsible for the loss of optical properties of a low bandgap polymer, namely Si-PCPDTBT, poly[[(4,4'-bis(2-ethylhexyl) dithieno[3,2-b:2',3'-d]silole)-2,6-diyl-*alt*-(4,7-bis(2-thienyl)-2,1,3-benzothiadiazole)-5,5'-diyl], to photooxidative conditions. The evolution of polymer films under exposure has been monitored using a range of analytical techniques, namely UV-Vis and IR spectroscopy, Atomic Force Microscopy (AFM), and profilometry. Furthermore, headspace solid-phase microextraction (HS-SPME) coupled with gas chromatography/mass spectrometry (GC-MS) has been exploited to elucidate any gas phase low molar mass by-products released during degradation. Finally, the results obtained with these analytical techniques have been jointly analysed with results acquired from theoretical predictions based on molecular modelling. This has allowed for a more complete elucidation of the radical-based photochemical processes responsible for the degradation of Si-PCPDTBT under the exposure conditions, focusing on both polymer backbone oxidation and alkyl chain-derived oxidation products. Special focus has been placed on the role that the solubilising side chains, and, more specifically, the silicon-bridging atom, had on the initiating steps of photooxidation (macroradical formation *via* hydrogen abstraction).

The second part of the chapter examines the influence that systematic modifications (in the backbone and of side chains) in a series of low bandgap polymers have on their photochemical stability. With this aim, the photooxidation of a series of low bandgap polymers based on two different donor units (BDT and DTS), three different acceptor units (DPP, DTBT, TzTz), and three alkyl side chains (in the case of the DTS-PDD combination), has been monitored using UV-Vis spectroscopy. In addition, the different polymers have been characterised (as pristine materials) using different

techniques (X-ray Diffraction, Rapid Heat-Cool Calorimetry and Electronic Paramagnetic Resonance), in order to assess the influence that other relevant parameters (*e.g.* crystallinity or purity) could have on their photochemical behaviour. The general considerations derived from the study of the polymers were finally re-evaluated after the analysis of the corresponding blends with PCBM, photochemically oxidised under the same conditions.

3.2. Experimental

3.2.1. Materials

Si-PCPDTBT (M_n = 18.5 kg mol^{-1}, Đ = 2.85) was provided by Belectric OPV GmbH and was used without further purification. P3HT (M_n = 26 kg mol^{-1}, Đ = 1.5) was obtained from Rieke Materials. C-PCPDTBT was provided by Dr. Christine Dagron-Lartigau from the Université de Pau et des Pays de l'Adour (UPPA). P5a (M_n = 21.9 kg mol^{-1}, Đ = 3.5), and P5c (M_n = 31.5 kg mol^{-1}, Đ = 4.0) were synthesised by Alberto Gregori (ESR2 in the ESTABLIS project) at UPPA and were used as received. P1, P2, P3 (M_n = 32 kg mol^{-1}, Đ = 1.7), P4 (M_n = 45 kg mol^{-1}, Đ = 3.5) and P5b were synthesised by Dr Graham E Morse (ER3 in the ESTABLIS project) at Merck Chemicals, and were used without further purification. *Ortho*-dichlorobenzene (ODCB) and *para*-xylene were obtained from Sigma-Aldrich, HPLC grade (99 %).

3.2.2. Methods

3.2.2.1. Thin films preparation

Si-PCPDTBT films, discussed in Section 3.3.1, were fabricated *via* spin coating using a G3P-8 Cookson Electronics Equipment from a polymer solution in ODCB (1.5 or 2 mg mL^{-1}), stirred overnight at 80 °C. Sample thicknesses were determined using a KLA Tencor Alpha Step IQ profilometer. The experimental conditions allowed the preparation of deposits with absorbance values around 0.5 and 1.3 at the maximum absorption wavelength, equivalent to sample thicknesses of 100 and 200 nm, respectively. Different substrates (glass, KBr, CaF$_2$) were chosen as a function of the ageing experiment and characterisation technique employed in each case.

Films discussed in Section 3.3.2 (corresponding to polymers P1-P5c, P3HT, Si-PCPDTBT, C-PCPDTBT) were fabricated on glass substrates using doctor blading (Erichsen Coatmaster 809 MC) from a polymer solution 0.9 % (w/w) in *para*-xylene:ODCB (7:1) that had been stirred overnight at 100 °C. The initial absorbance of the deposits was approximately 0.5 at the maximum absorption wavelength.

3.2.2.2. Characterisation

3.2.2.2.1. <u>GPC</u>

Gel permeation chromatography (GCP) was performed with an Agilent Technologies 1260 infinity eluted at 1 mL min^{-1} with 50˚C HPLC grade chlorobenzene (Aldrich) through a PL gel 10 μm Mixed-B (300 × 7.5 mm) GPC column. The polymers were analysed with a refractive index

detector calibrated with narrow polystyrene standards. Samples were dissolved in HPLC grade chlorobenzene at a concentration of 1-4 mg mL^{-1} and filtered before injection. The measurement and the calculation of molar mass and dispersity of the polymers was performed by Dr. Graham Morse at Merck Chemicals Ltd in the framework of the ESTABLIS project. Whilst the effect of molar mass (above a certain threshold) has been reported negligible in terms of the photostability of the polymers;[234-235] polymer dispersity, and more specifically the unimodal/multimodal character of the GPC traces has been identified as important in terms of the resulting cell photostability and, hence, its device stability.[224-225]

3.2.2.2.2. <u>Electronic Paramagnetic Resonance</u>

Electronic Paramagnetic Resonance (EPR) was employed to quantify the paramagnetic defects in the polymer samples. Borosilicate glass tubes containing 2 mg of polymer powder (weighed and introduced in the tubes under ambient air conditions) were placed in the interior of the cavity of an X-band Bruker EMX spectrometer operating at 9.24 GHz. EPR spectra were recorded at room temperature, and the intensity of the signal in each case was employed to compare the quantity of paramagnetic defects in the polymers.

3.2.2.2.3. <u>Rapid Heat-Cool Calorimetry</u>

Rapid Heat-Cool Calorimetry (RHC) analysis were carried out by Maxime Defour, PhD student at the Vrije Universiteit Brussel. The measurements were performed on a TA Instruments Rapid Heat-Cool Differential Scanning Calorimeter (RHC) using a liquid nitrogen cooling system and purged with neon (12 mL min^{-1}). The RHC cell is heated by four quartz halogen lamps with an almost instantaneous response. More details on the procedure can be found in the literature.[254]

3.2.2.2.4. <u>X-ray diffraction</u>

X-ray diffraction (XRD) analyses were made using a PANalytical XPert Pro diffractometer equipped with a X'Celerator detector and a Cu anticathode (Kα1/Kα2). The instrument was used in the θ-θ reflection mode, fitted with a nickel filter, 0.04 rad Soller slits, 5 mm mask, 1/160° fixed divergence slit, and 1/32° fixed antiscatter slit. XRD data were measured over a range of 1-40° (2θ) with a step size of 0.0167° and a total counting time of about 3 h.

3.2.2.3. Ageing experiments

3.2.2.3.1. <u>Photochemical degradation</u>

Illumination of the samples was performed using two different irradiation setups, namely SEPAP 12/24 device and Suntest CPS/XLS Atlas device. SEPAP 12/24 consists of a square reactor containing a rotating carousel to hold the samples and four medium-pressure mercury vapour lamps (Mazda MA 400) located in each corner of the chamber. Wavelengths below 300 nm are filtered by the borosilicate glass envelope of the lamps. The carousel has capacity for 24 samples, placed at 20 cm distance from the lamp axis, and turns 4 times per minute. Chamber temperature is maintained at 60 °C during all experiments, controlled by a platinum probe in contact with a polyethylene film placed on the carousel. The relative humidity level inside the chamber was 7 % (60 °C). Suntest CPS/XLS Atlas device is provided with a xenon lamp from ATLAS (NXE1700) configured at 750 W m^{-2} (300 – 800 nm); a cryostat maintains the Black Standard Temperature (BST) at 80 °C (experiments described in Section 3.3.1) or 60 °C (Section 3.3.2), corresponding to a temperature inside the chamber of 45 or 35 °C, respectively. Samples are irradiated in a fixed position, and UV irradiance under 300 nm and IR irradiation are filtered. The differences between the characteristics of the irradiation using both setups are described in Section 3.3.1.3.2.

The vast majority of experiments described in this chapter were performed under ambient air conditions. The presence of oxygen in these experiments justifies the use of the term photooxidation when referring to them. Some samples were irradiated with the exclusion of oxygen, in so-called photolysis experiments. To this end, samples were glass-encapsulated inside borosilicate tubes under secondary vacuum (10^{-6} Pa).

3.2.2.3.2. <u>Thermal degradation</u>

Thermal ageing of samples was performed inside a thermoregulated oven at 100 °C.

3.2.2.4. Spectroscopy analysis

UV-Vis absorption spectra were obtained using a Shimadzu UV-2600 spectrophotometer provided with an integration sphere. Infrared (IR) spectra were recorded by a Nicolet 760 Magna spectrophotometer working in transmission mode and purged with dry air. The parameters used were 32 acquisitions and 4 cm^{-1} resolution.

3.2.2.5. Identification of photoproducts

3.2.2.5.1. Chemical derivatisation treatments

Identification of the polymer oxidation products was performed *via* chemical derivatisation treatments using sulfur tetrafluoride (SF₄) and ammonia (NH₃) in combination with IR spectroscopy. These reagents are capable of selectively reacting with certain products present in the sample, leading to the formation of new products with characteristic IR signals (Table 3.1).[255] At ambient temperature and atmospheric pressure, sulfur tetrafluoride reacts with acids, alcohols, and hydroperoxides exchanging the hydroxyl groups with fluorine atoms. Under these conditions, SF₄ also reacts with sulfinic acids and esters yielding sulfynil fluorides. However, it does not react with other carbonyl compounds such as aldehydes, ketones, or esters. Ammonia (NH₃) reacts with carboxylic acids, forming ammonia salts, and with esters and anhydrides, yielding amides. It also reacts with sulfinic acids to form ammonia sulfinates, but not with their esters.

Table 3.1. Chemical modifications upon derivatisation treatment with SF₄ (left) and NH₃ (right). Wavenumbers associated to the different chemical groups before and after treatment are specified.

SF₄ treatment	
$R-C(=O)OH \xrightarrow{SF_4} R-C(=O)F + HF + SOF_2$ $\nu_{C=O} \approx 1720 - 1680\ cm^{-1}$ (left); $\nu_{C=O} \approx 1850 - 1800\ cm^{-1}$ (right)	$R-S(=O)OX \xrightarrow{SF_4} R-S(=O)F + XF + SOF_2$ X=H: $\nu_{S=O} \approx 1090 - 990\ cm^{-1}$; X=R: $\nu_{S=O} \approx 1140 - 1110\ cm^{-1}$ (left); $\nu_{S=O} \approx 1260\ cm^{-1}$ (right)

NH₃ treatment	
$R-C(=O)OH \xrightarrow{NH_3} R-C(=O)O^- + NH_4^+$ $\nu_{C=O} \approx 1720 - 1680\ cm^{-1}$ (left); $\nu_{CO} \approx 1695 - 1540\ cm^{-1}$, $\nu_{CO} \approx 1460 - 1335\ cm^{-1}$ (right)	$R-C(=O)OR' \xrightarrow{NH_3} R-C(=O)NH_2 + R'OH$ $\nu_{C=O} \approx 1750 - 1710\ cm^{-1}$ (left); $\nu_{C=O} \approx 1690 - 1650\ cm^{-1}$, $\nu_{N-H} \approx 3215\ cm^{-1}$ (right)
$R-S(=O)OH \xrightarrow{NH_3} R-S(=O)O^- + NH_4^+$ $\nu_{S=O} \approx 1090 - 990\ cm^{-1}$ (left); ν_{SO} (asym) $\approx 1030\ cm^{-1}$, ν_{SO} (sym) $\approx 980\ cm^{-1}$ (right)	$R-C(=O)-O-C(=O)-R' \xrightarrow{2\ NH_3} R-C(=O)NH_2 + R'CO_2^- + NH_4^+$ $\nu_{C=O} \approx 1850 - 1780\ cm^{-1}$, $\nu_{C=O} \approx 1760 - 1710\ cm^{-1}$ (left); $\nu_{C=O} \approx 1690 - 1650\ cm^{-1}$, $\nu_{N-H} \approx 3215\ cm^{-1}$ (right)

Pristine and oxidised Si-PCPDTBT films were initially characterised using IR spectroscopy. After which, samples were placed inside a Teflon® (SF$_4$) or polyethylene (NH$_3$) reactor and N$_2$ purged (5 min). Then, the reagent was flown inside the closed reactor for 30 seconds, and reaction was allowed for 15 min (NH$_3$ treatment) or 1 hour (SF$_4$ treatment). Finally, the reactor was repurged with N$_2$ and samples were immediately analysed by IR. Films subjected to SF$_4$ treatment were deposited on CaF$_2$ substrates.

3.2.2.5.2. <u>HS-SPME-GC-MS</u>

Headspace solid-phase microextraction (HS-SPME) coupled with gas chromatography/mass spectrometry (GC-MS) was employed to collect and analyse the volatile compounds created upon photooxidation of Si-PCPDTBT films. Polymer films were introduced in 20 mL flasks sealed with a silicon septum under ambient air conditions. After which, samples were irradiated for 70 hours in the SEPAP 12/24 chamber. Appropriate blank samples (ambient air, non-irradiated films) were also prepared. Flasks were heated at 60 °C for 1 hour to ensure desorption of the products from the film matrix before the fibre was introduced in the flasks for 5 minutes to adsorb the volatile compounds. Then, the fibre was manually transferred to the chromatographic injector where analytes desorbed at 280 °C for 2 seconds. The column temperature was kept at 35 °C for 10 min, followed by a two-step ramp (5 °C min^{-1} up to 60 °C, 10 °C min^{-1} up to 200 °C). The final temperature (200 °C) was maintained for 15 min. The temperature of the transfer line was kept at 280 °C, and the ions source temperature was fixed at 230 °C. Ionisation was produced by electronic impact with 70 eV energy. The mass spectra as well as the reconstructed chromatograms were obtained by mass scanning in the interval m/z 20-400.

The SPME fibre used was a 75 mm carboxen-polydimethylsiloxane (CAR/PDMS) fibre provided by Supelco (BelleFonte, PA, USA), conditioned at 280 °C prior to every use. GC-MS equipment consisted of a gas phase chromatograph Network System 6890N, from Agilent Technologies, coupled with a mass spectrometer Network Mass Selective Detector MSD 5973. The fused silica capillary column, of dimensions 30 m x 0.25 mm, contained a stationary phase Carbowax 20 M (Supelco, BelleFonte, PA, USA). The carrier gas was helium at a constant pressure of 38 kPa and 50 mL min^{-1} flow.

3.2.2.6. Atomic Force Microscopy

A Nanoscope IIIa Atomic Force Microscope from Veeco Instruments was used to obtain surface topographic measurements and perform nanoindentations using a Nanoscope 7.20 software.

Measurements were performed with a diamond tip (64.05 kHz), of spring constant of 160 N m^{-1} and a curvature radius of 25 nm.

Surface roughness values were obtained as the average of 10 x 10 µm images obtained at three different surface positions for each degradation step. The evolution of the mechanical properties as a function of irradiation time was determined using nanoindentations. To this end, force-displacement curves were recorded under a constant load (10 µN), and nanohardness values were obtained from the analysis of the load-unload curves using the Oliver-Pharr's method.[256] Average values were obtained from the analysis of three sets of 25 nanoindentations at each degradation time. This methodology has been previously described in-depth.[208]

3.2.2.7. Computational details

Computational calculations were performed by Prof. Didier Begué at the Université de Pau et des Pays de l'Adour in the frame of the ESTABLIS project.

The near infrared (NIR) spectra were fully interpreted by applying a method developed for efficient automatic computation of both the infrared wavenumbers and intensities. The employed procedure uses Parallel Variational Multiple Window Configuration Interaction wave functions, the so-called P_VMWCI2 algorithm, which incorporates both mechanical and electrical anharmonic effects. It has been shown that inclusion of anharmonicities is crucial to correctly assigning the fundamental, combination, and overtone vibrational frequencies in the infrared spectrum of the target system.

Molecular geometries of model compounds were fully optimised within Density Functional Theory (DFT) method, using two double-ζ polarised basis-sets (6-31G* and +6-31+G**).[257-259] DFT calculations used a B3LYP exchange-correlation function.[260] Where required, the open-shell wave function was set to an unrestricted type (UHF/UKS). Modelling of hydrogen-abstracted geometries was performed with a doublet multiplicity in a neutral state. Bond dissociation energies (BDEs) were calculated with respect to the ground state. All calculations were performed using Gaussian 09 software.[261] Spin distribution was extracted from the Löwdin partition.[262-263]

3.3. Results and discussion

3.3.1. Unravelling the photodegradation mechanisms of Si-PCPDTBT by combining experimental and modelling approaches

The majority of the work contained in this Section 3.3.1 has been described in the article:

Fraga Domínguez, I.; Topham, P. D.; Bussière, P.-O.; Bégué, D.; Rivaton, A., Unravelling the Photodegradation Mechanisms of a Low Bandgap Polymer by Combining Experimental and Modeling Approaches. *The Journal of Physical Chemistry C* **2015**, *119*, 2166-2176.

The work herein describes the photochemical behaviour of the low bandgap polymer Si-PCPDTBT under photooxidative conditions, artificially obtained using a SEPAP 12/24 device. The evolution of polymer thin films under exposure is monitored using a range of analytical techniques, namely UV-Vis and IR spectroscopy, Atomic Force Microscopy, and profilometry. Furthermore, headspace solid-phase microextraction (HS-SPME) coupled with gas chromatography/mass spectrometry (GC-MS) has been exploited to elucidate any gas phase low molar mass byproducts released during degradation. Finally, the results obtained with these analytical techniques are combined with molecular modelling, allowing for a complete elucidation of the photochemical processes responsible for the degradation of Si-PCPDTBT under the exposure conditions.
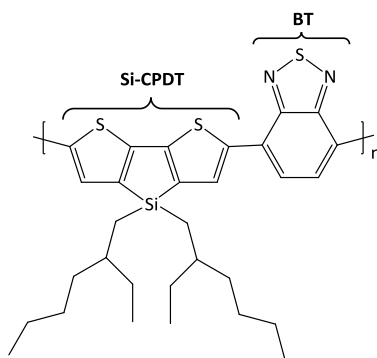
Figure 3.9. Chemical structure of Si-PCPDTBT, poly[(4,4'-bis(2-ethylhexyl)dithieno[3,2-b:2',3'-d]silole)-2,6-diyl-*alt*-(4,7-bis(2-thienyl)-2,1,3-benzothiadiazole)-5,5'-diyl].

3.3.1.1. Morphological analysis

The morphology of pristine Si-PCPDTBT films spin-coated on glass substrates and their corresponding evolution upon ageing was characterised by Atomic Force Microscopy. Figure 3.10 shows the AFM surface images and profiles obtained for pristine films and films exposed to photooxidation in SEPAP 12/24 for 150 hours. Prior to irradiation, the surface of the film has a relatively

even and homogeneous appearance. After 40 hours of ageing, although the topographic image does not appear to have significantly changed, when plotting the surface profile [Figure 3.10 (b)], a variation in the surface height is already noticeable. A dramatic modification is observed in both the surface image and the corresponding profile after 100 hours of irradiation, characterised by the formation of a multitude of small spherical features. Finally, 50 hours later, these features coalesce and create a smaller number of larger aggregates. For previously studied conjugated polymers, such as PCDTBT (poly[N-9'-hepta-decanyl-2,7-carbazole-alt-5,5-(4',7'-di-2-thienyl-2',1',3'-benzothiadiazole)]), this type of evolution with the formation of spherical features has been related to a new arrangement of the polymer macromolecules, namely π-π stacking, indicated by changes in the UV-Vis spectra.[209] However, no such evidence has been observed in the case of Si-PCPDTBT films.

(a)   **(b)**
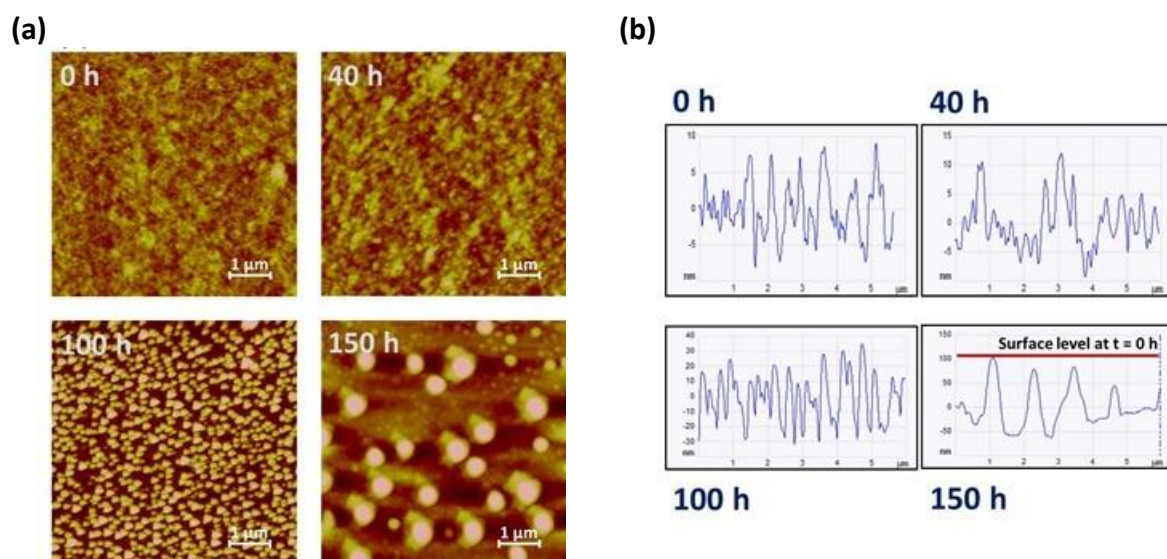
Figure 3.10. (a) Height images obtained by Atomic Force Microscopy, indicating the surface evolution of Si-PCPDTBT films at different stages of photooxidation. (b) Surface profiles corresponding to the height images displayed in (a). Thickness data, shown in Figure 3.11, were used to set up a bar (−) comparing the final surface profile to the initial surface position and show that the there is a 100 nm average decrease in thickness after 150 hours.

Consistent with the described evolution, Figure 3.11 (a) shows that roughness values extracted from AFM topographic images remain constant and around 4-6 nm during the first 60 hours of exposure. Following on from this exposure time, the roughness dramatically increases together with the heterogeneity of the surface, the latter indicated by the augmentation in the error bars (z values). Usually, this evolution of surface roughness can be related to the formation and subsequent loss of low molar mass species from the polymer. Additionally, thickness values obtained by profilometry, also

reported in Figure 3.11, show a rapid decrease after 60 hours of exposure, finally reaching approximately half of its initial value after 150 hours. The increased error associated with each measurement in the later stages of degradation reveals once again the augmentation of surface heterogeneity with degradation time. Thickness values have been employed to set up a bar in the surface profile evolution in Figure 3.10 (b), indicating the position of the initial surface height in comparison with the final surface level. This gives account for the important loss of materials that occurs during light exposure. It must be noted that surface degradation can highly influence the active layer interfaces in terms of mechanical, adhesive or charge extraction properties, all of which ultimately having drastic consequences on the performance of the device.[264]

(a)   **(b)**
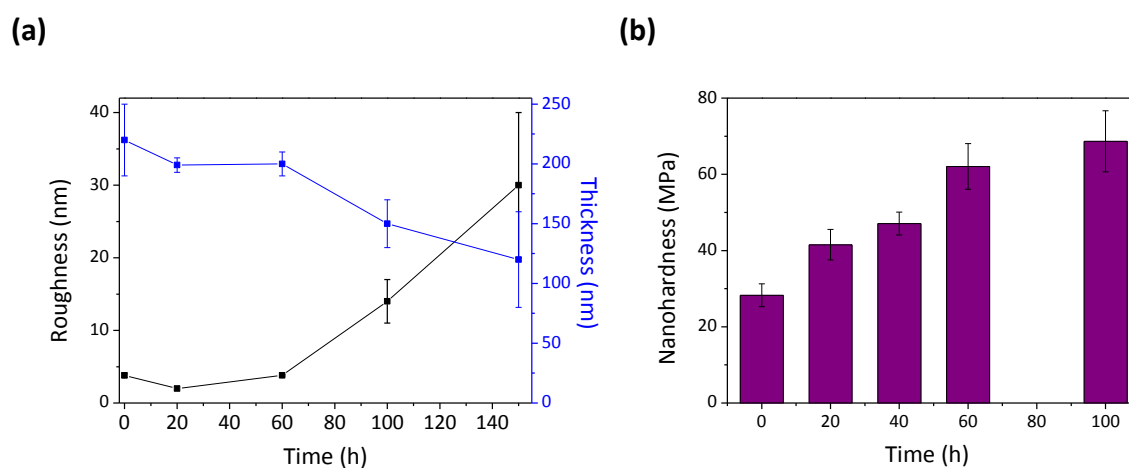
Figure 3.11. (a) Roughness and thickness evolution of Si-PCPDTBT thin films deposit upon 150 hours photooxidation, extracted from AFM profiles and profilometric analysis, respectively. (b) Nanohardness evolution upon 100 hours of photooxidation, as calculated using AFM nanoindentations. After 100 hours of exposure, it was not possible to obtain accurate reproducible hardness values due to the high increase in roughness and heterogeneity of the sample surface.

AFM nanoindentations were subsequently performed using a constant load or force, allowing any variation in mechanical properties of the sample to be monitored. During the whole irradiation period, particular attention was paid to the employed force to avoid taking into account the mechanical properties of the glass substrate. Quantitative values of the nanohardness of the material were estimated using the Oliver and Pharr procedure,[256] showing a steady increase in stiffness with oxidation time [Figure 3.11 (b)]. As previously suggested for PCDTBT, the most relevant hypothesis is that radicals involved in the chain radical oxidation process can recombine, provoking crosslinking of the sample, and therefore increasing stiffness.

3.3.1.2. Chemical evolution

The observed changes in thickness, morphology and stiffness originate from modification of the chemical structure of the polymer macromolecular chains and the formation of degradation products. Accordingly, these chemical changes have been monitored using Infrared Spectroscopy (IR) in combination with chemical derivatisation treatments and analysis of the gas phase using HS-SPME-GC-MS, in order to identify the oxidation products and ultimately propose a degradation mechanism.As displayed in Figure 3.9, Si-PCPDTBT is composed of a silicon-cyclopentadithiophene (Si-CPDT) donor group bearing two alkyl solubilising side-chains linked to the silicon atom and a benzothiadazole (BT) unit as a withdrawing group. Due to the complexity of the IR spectrum, the different structures in the polymer were identified by matching the experimental IR data with theoretical predictions in solution based on B3LYP/6-31G* anharmonic calculations (see Table 3.2).[265-266] It is noteworthy that experimental and computational spectra are in good agreement.

Table 3.2. Attribution of the IR bands of Si-PCPDTBT; IR intensities (km mol^{-1}) are included as values in parentheses.

$\tilde{\nu}$ / cm^{-1}			Assignment
Experimental	B3LYP/6-31G*		
613	610 (29.3)		ω thiophene ring + ω benzothiadiazole
749	741 (29.2)		ω benzothiadiazole
	752 (29.3)		
794	788 (56.0)		benzothiadiazole and thiophene rings deformations+ C$_4$Si ω
	799 (17.9)		benzothiadiazole
881	870 (21.0)		δ thiophene ring + υ_{CS} thiophene + $\upsilon_{C\text{-}Si}$
1105	1096 (43.3)		α_{CCC} rings + δ_{CH} alkyl chains
	1109 (12.9)		υ_{CC} rings + δ_{CH} alkyl chains
1184	1180 (37.4)		δ_{CC} thiophene ring + $\delta_{C\text{-}H}$ alkyl chain
	1183 (37.1)		
1245	1231 (19.4)		'breathing' C$_4$Si cycle + $\delta_{C\text{-}H}$ alkyl chain
	1262 (30.4)		
	1263 (17.0)		
1360	1375 (39.0)		$\upsilon_{a,C=C}$ C$_4$Si ring + $\upsilon_{C=C}$ all rings
	1395 (60.2)		
1498	1494 (125.2)		$\upsilon_{C=C}$, $\upsilon_{C=N}$, α_{CCC} benzothiadiazole
	1495 (13.6)		
1568	1532 (77.1)		$\upsilon_{C=C}$ benzothiadiazole
	1599 (24.0)		
2858	2923-2961	(45.5)	υ_s CH$_2$ alkyl side chain
2869		(37.7)	υ_s CH$_3$ alkyl side chain
2926	2972-3034	(84.6)	υ_a CH$_2$ alkyl side chain
2956		(95.8)	υ_a CH$_3$ alkyl side chain
3000-3060	3100-3173 (26.5)		υ =C-H

Exposing the polymer to photooxidative conditions provoked a gradual disappearance of the different chemical functionalities of Si-PCPDTBT, as well as the appearance of new bands corresponding to the oxidation products. Figure 3.12 (a) shows the IR spectrum (in transmission mode) of a Si-PCPDTBT film before and after two different irradiation times (50 and 205 hours). Subtraction of the initial spectrum (*i.e.* before irradiation) from the spectra recorded after irradiation permits observation of the global shape of the absorption bands that are formed or consumed [Figure 3.12 (b)]. The parts of the spectra above the base line (dashed line) correspond to the formation of oxidation products, and the parts below the baseline to the disappearance of the functional groups of the polymer upon photooxidation.
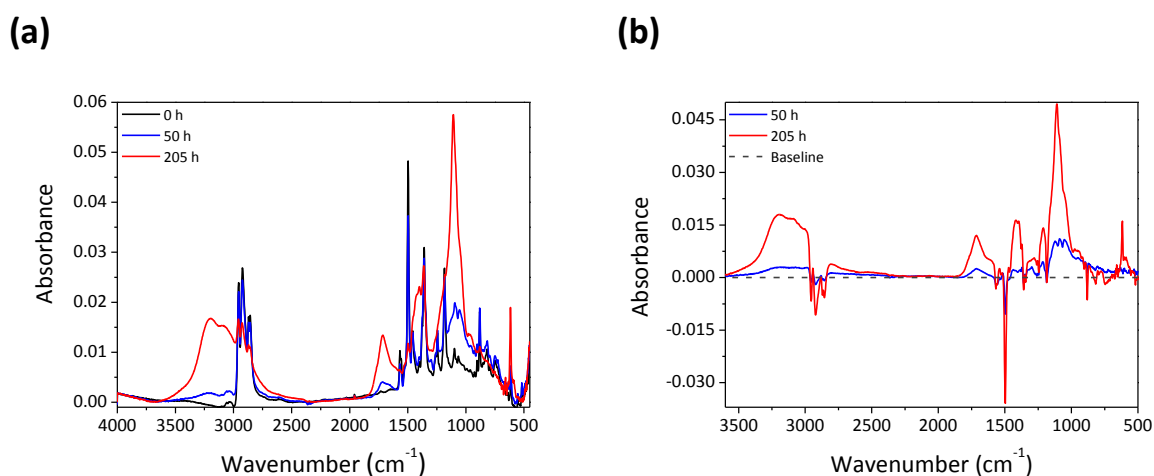
Figure 3.12. (a) IR spectra of Si-PCPDTBT thin films during photooxidation in the SEPAP device; before irradiation (black); after 50 hours (blue) and 205 hours (red) of photooxidation. (b) IR difference spectra (non-irradiated sample spectrum subtracted from the irradiated sample spectrum) of Si-PCPDTBT thin films irradiated for 50 hours (blue line) and 205 hours (red line) in the SEPAP device.

The changes in the initial spectrum include a decrease of the bands related to the alkyl side chain (2858 - 2956 cm^{-1}), thiophene (1184 cm^{-1}, 881 cm^{-1}), benzothiadiazole (1568 cm^{-1}, 1498 cm^{-1}), and C-Si bond (1245, 881 cm^{-1}). In parallel, new bands appear in the carbonyl (1800-1600 cm^{-1}) and hydroxyl (3600-3000 cm^{-1}) regions in addition to the fingerprint region (1500-500 cm^{-1}). In order to facilitate a complete understanding of the degradation mechanism, the different parts of the polymer have been individually addressed. First, particular attention has been paid to the evolution of the alkyl side chain and its corresponding mechanism, before evolution of the units of the conjugated backbone (Si-CPDT and BT) was analysed.

3.3.1.2.1. <u>Alkyl side chain photooxidation</u>

The IR bands associated with the alkyl side chain (2956, 2926, 2869, 2858 cm^{-1}) steadily decrease from the beginning of light exposure, indicating that the moiety is being consumed or modified. It has been repeatedly reported that the side-chains needed to render conjugated polymers soluble in organic solvents are actually the Achilles' heel of these structures (in terms of photooxidation), being the first moiety to oxidise and subsequently start a chain radical oxidation that leads to the degradation of the conjugated backbone.[206, 214, 221, 267] More specifically, it has been demonstrated that the process starts by hydrogen abstraction on the alkyl chain, notably in the alpha position to the conjugated backbone, as demonstrated for P3HT.[214]

Low molar mass oxidation products

HS-SPME-GC-MS analysis was performed in order to ascertain the migration of volatile photoproducts and identify their structures. The Total Ion Count (TIC) chromatograms (Figure 3.13) corroborate the presence of low molar mass oxidation products in the gas phase for samples irradiated for 70 hours, a time that corresponds to a significant loss in thickness and increase in roughness, *vide supra*. Identification of the main products, displayed in Table 3.3, was carried out by comparison with the software spectral library. No products containing the backbone heteroatoms (S, N) were identified, and the structures of the determined species clearly suggest that their origin is the oxidation of the alkyl chain of the polymer.
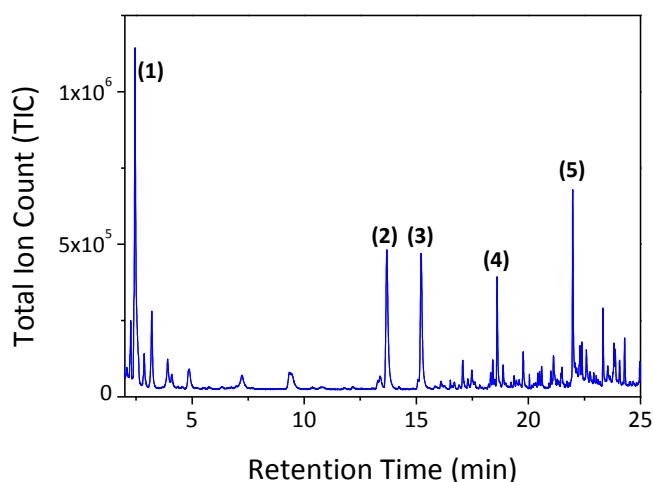
Figure 3.13 Total ion count chromatogram corresponding to HS-SPME-GC-MS analysis of a Si-PCPDTBT sample irradiated for 70 hours. The numbers in parentheses refer to the identified products as indicated in Table 3.3.

Table 3.3 Main volatile organic compounds released from irradiated Si-PCPDTBT films, identified by HS-SPME-GC-MS.

Compound	Retention time min	Identification
1	2.5	3-methylene-heptane
2	13.7	3-heptanone
3	15.2	2-ethylhexanal
4	18.6	3-heptanol
5	22.0	2-ethyl-hexan-1-ol

Chain oxidation products

In order to identify the chain oxidation products that remained in the films, focus was placed on the evolution of the IR spectra in the carbonyl and hydroxyl regions (Figure 3.14). From the beginning of exposure, the most significant spectral changes were noted in the 1600-1800 cm^{-1} region, characteristic of C=O vibrations. The carbonyl band is centred around 1714 cm^{-1}, usually ascribed to carboxylic acids in the dimer form. In the hydroxyl region, a broad band around 3200 cm^{-1} again suggests the formation of carboxylic OH groups, and no band attributed to alcohols (usually observed at 3400 cm^{-1}) is observed.

(a)

(b)
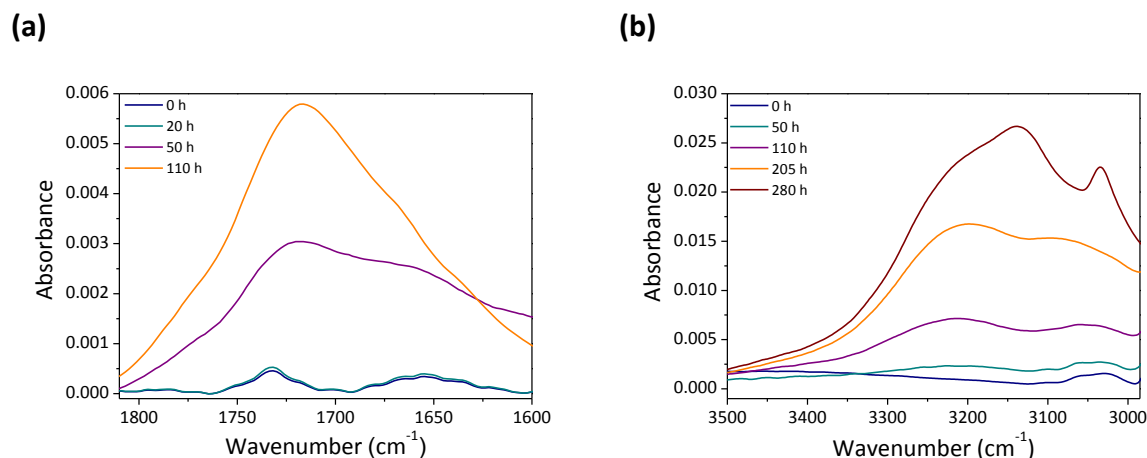
Figure 3.14. (a) IR spectral changes in the carbonyl region (1820 – 1600 cm^{-1}) and (b) in the hydroxyl region (3500-2900 cm^{-1}) region of Si-PCPDTBT thin films, caused by photooxidative ageing.

Photooxidised samples were then chemically treated with NH$_3$ and SF$_4$ to better identify the nature of the carbonylated products.[255, 268] NH$_3$ treatment permitted the identification of carboxylic acid species in the sample, as their reaction with NH$_3$ yields ammonium salts with distinctive bands at 1575 cm^{-1} ($v_{C=O}$ asymmetric stretch) and 1475 cm^{-1} ($v_{C=O}$ symmetric stretch), see Figure 3.15 (a) and (b).

Additionally, the formation of derivative bands around 1660 cm^{-1} ($\nu_{C=O}$) and 3215 cm^{-1} ($\nu_{N=H}$) indicated the existence of esters and/or anhydrides that react with NH$_3$ to yield primary amides (see Figure 3.15).

(a)

(b)

(c)
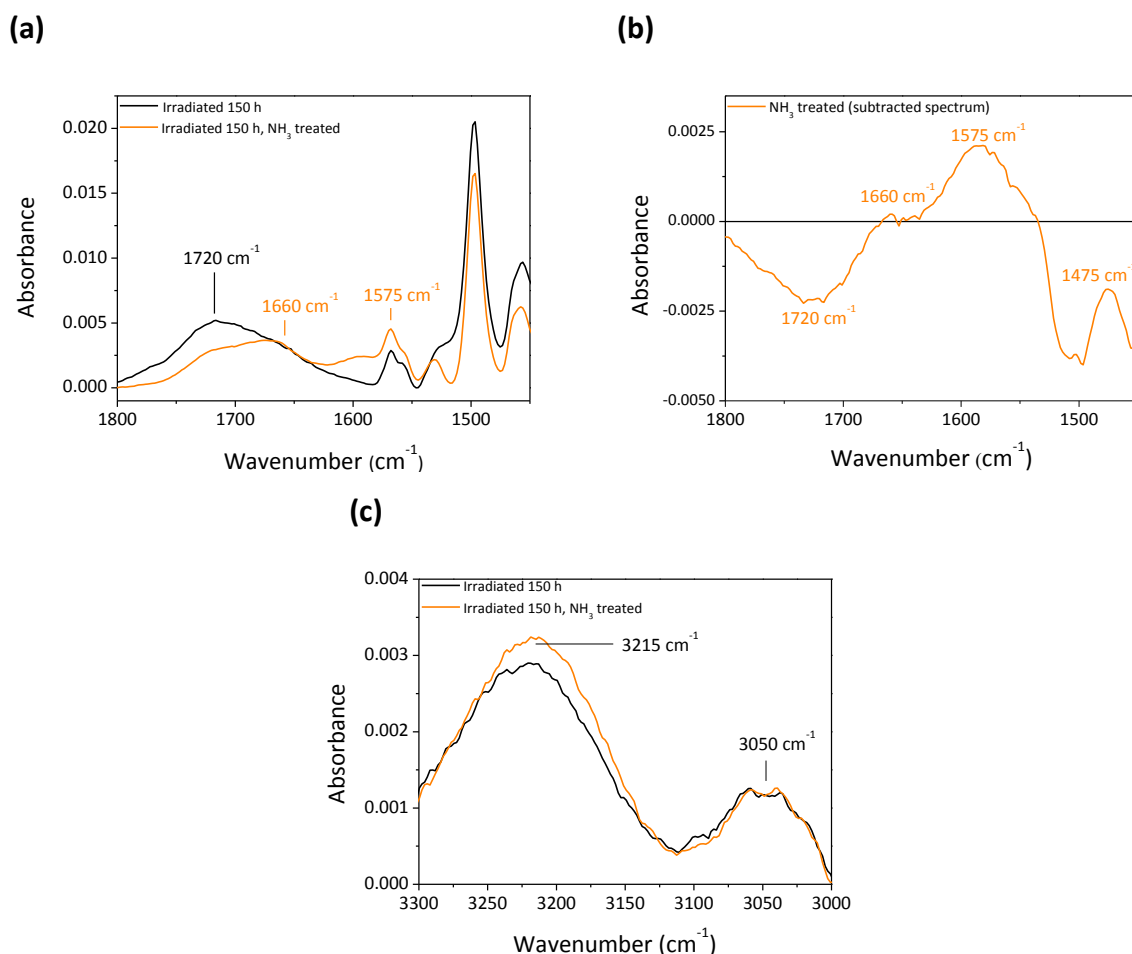
Figure 3.15. IR evolution of a photooxidised Si-PCPDTBT film (irradiated for 150 hours) upon chemical treatment with NH$_3$ (a) in the carbonyl region, (b) corresponding subtracted spectrum (NH$_3$ treated - Irradiated), (c) IR evolution in the hydroxyl region.

The presence of carboxylic acids was also revealed by SF$_4$ treatment. The reaction of saturated carboxylic acids (1710 cm^{-1}) with SF$_4$ provoked the formation of a band at 1840 cm^{-1} stemming from the formation of acyl fluorides, see Figure 3.16 (a) and (b). Correspondingly, the signals in the hydroxyl region (3210 cm^{-1}, 3050 cm^{-1}), assigned to carboxylic acids, decreased after SF$_4$ treatment [Figure 3.16 (c)]. The band at 3350 cm^{-1} has not been assigned.

Finally, after this same treatment, the existence of a remaining band at 1720 cm^{-1} (slightly shifted to 1730 cm^{-1}) indicates that the sample still contains carbonyl products that do not react with

SF$_4$, such as esters, aldehydes, ketones or anhydrides [Figure 3.16 (a)]. Also, the band at 1790 cm^{-1} is generally detected when aromatic polymers are treated with SF$_4$.

(a)

(b)

(c)
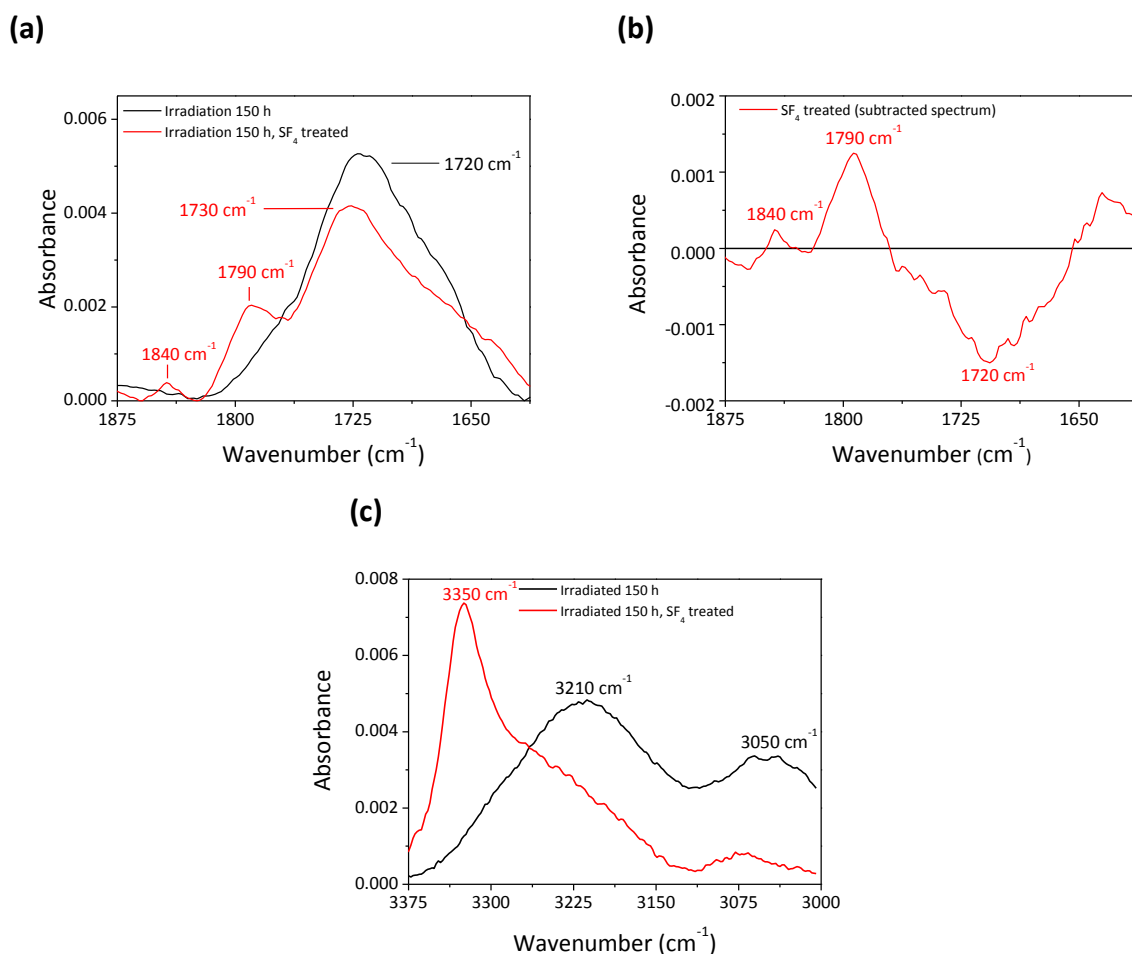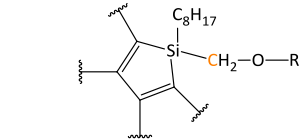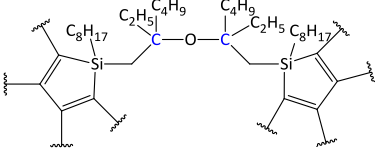
Figure 3.16. IR evolution of a photooxidised Si-PCPDTBT film (irradiated for 150 hours) upon chemical treatment with SF$_4$ (a) in the carbonyl region, (b) corresponding subtracted spectrum (SF$_4$ treated - Irradiated), (c) IR evolution in the hydroxyl region.

Crosslinking reactions

The reported increase in nanohardness [see Figure 3.11 (b)] indicates an increase in stiffness, usually associated with crosslinking of the polymer.[208-209] To further confirm this hypothesis, modelling was employed to identify possible C-O-C links, which have been shown to be more prevalent than the formation of direct C-C bonds in photooxidative degradation.[207, 220, 229] Theoretical calculations were undertaken to identify the frequencies associated with crosslinking at the alkyl chain positions, C$_\alpha$ and C$_\beta$. The results indicated that C-O-C bonds show frequencies in the range of 1200 to 1260 cm^{-1}

depending on the number of alkyl substituents directly linked to the carbon involved in the ether linkage (Table 3.4).

Table 3.4. Proposed products of crosslinking (XL), produced *via* ether linkage at the C_α and C_β positions of the alkyl side chain. Theoretical predictions based on B3LYP/6-31G* for the C-O-C groups are compared to data of experimental IR bands within an interval of ± 15 cm^{-1} around the predicted value.

Name	Proposed chemical structure	$\tilde{\nu}$/ cm^{-1}	
		B3LYP/6-31G*	Experimental
XL$_\alpha$		781 1076 **1262**	- 1089 **1251, 1267**
XL$_\beta$		784 1014 **1216**	- - **1215**
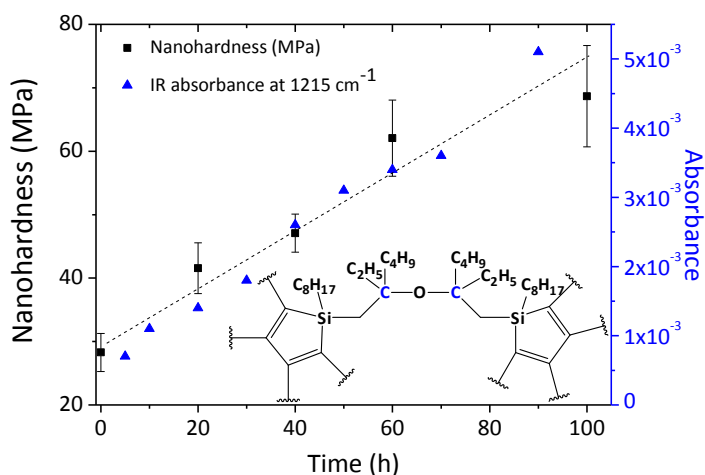
Figure 3.17. Evolution of nanohardness values and the IR band at 1215 cm^{-1} assigned to XL$_\beta$ structure (insert) during the first 100 hours of irradiation.

During the first 100 hours of exposure, there is an increase in the band at 1215 cm^{-1} that fits the calculated value (1216 cm^{-1}) for the structure XL$_\beta$ (see Table 3.4), which involves a C-O-C crosslink through the tertiary atom of the alkyl chain. The other two calculated modes associated with this structure are located at 1014 cm^{-1} and 784 cm^{-1}, regions which are difficult to monitor due to the convoluted growth of bands. Additionally, there is the appearance of low intensity bands at 1251 cm^{-1}

and 1267 cm^{-1}, more in accordance with the calculated modes for XL_{α} (Table 3.4), suggesting the formation of C-O-C bonds involving carbons with less substituents. Figure 3.17 displays the increase in the band at 1215 cm^{-1} (attributed to the formation of the XL_{β} structure within the polymer matrix) together with the increase in nanohardness, highlighting their good agreement and providing strong evidence for the relationship between the evolution of the chemical structure (crosslinking *via* ether linkages) upon irradiation and the effect on nanomechanical properties.

Alkyl side chain photooxidation mechanism

As aforementioned, the first step of the degradation process is hydrogen abstraction at the alkyl side chain. It is well known that the lability of hydrogen atoms depends on the stability of the corresponding radical created, and this is strongly linked to the substitution of the involved carbon atom, *i.e.* attached substituents create a stabilising inductive effect on the formed radical.[269] As highlighted in Figure 3.18, the alpha position in Si-PCPDTBT is a secondary carbon (C_{α}), whereas the beta position is a tertiary carbon (C_{β}). Thus, the tertiary carbon of the polymer (C_{β}) is expected to be more susceptible to hydrogen abstraction than the secondary (C_{α}) one. The C-H bond dissociation energies at the C_{α} and C_{β} positions (in relation to Si) were calculated within B3LYP/6-31+G** theory level, showing values of 100.4 and 97.4 kcal mol^{-1} for C_{α} and C_{β}, respectively. As expected, the tertiary beta position requires a slightly inferior energy value to dissociate the C-H bond; however, on proposing a degradation mechanism, the formation of radicals at the alpha position is also possible and should not be excluded.
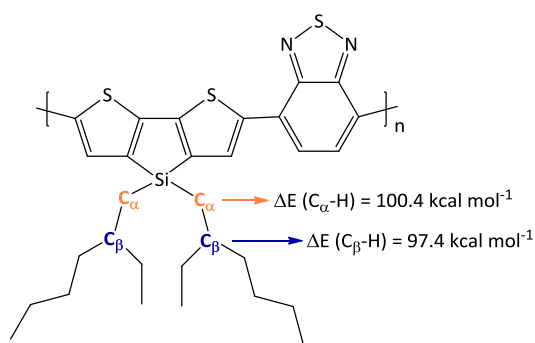
Figure 3.18. Chemical structure of Si-PCPDTBT, highlighting the studied C_{α} and C_{β} positions in the alkyl side chain and including their corresponding C-H bond dissociation energies as calculated within B3LYP/6-31+G theory.**

(a)

(b)
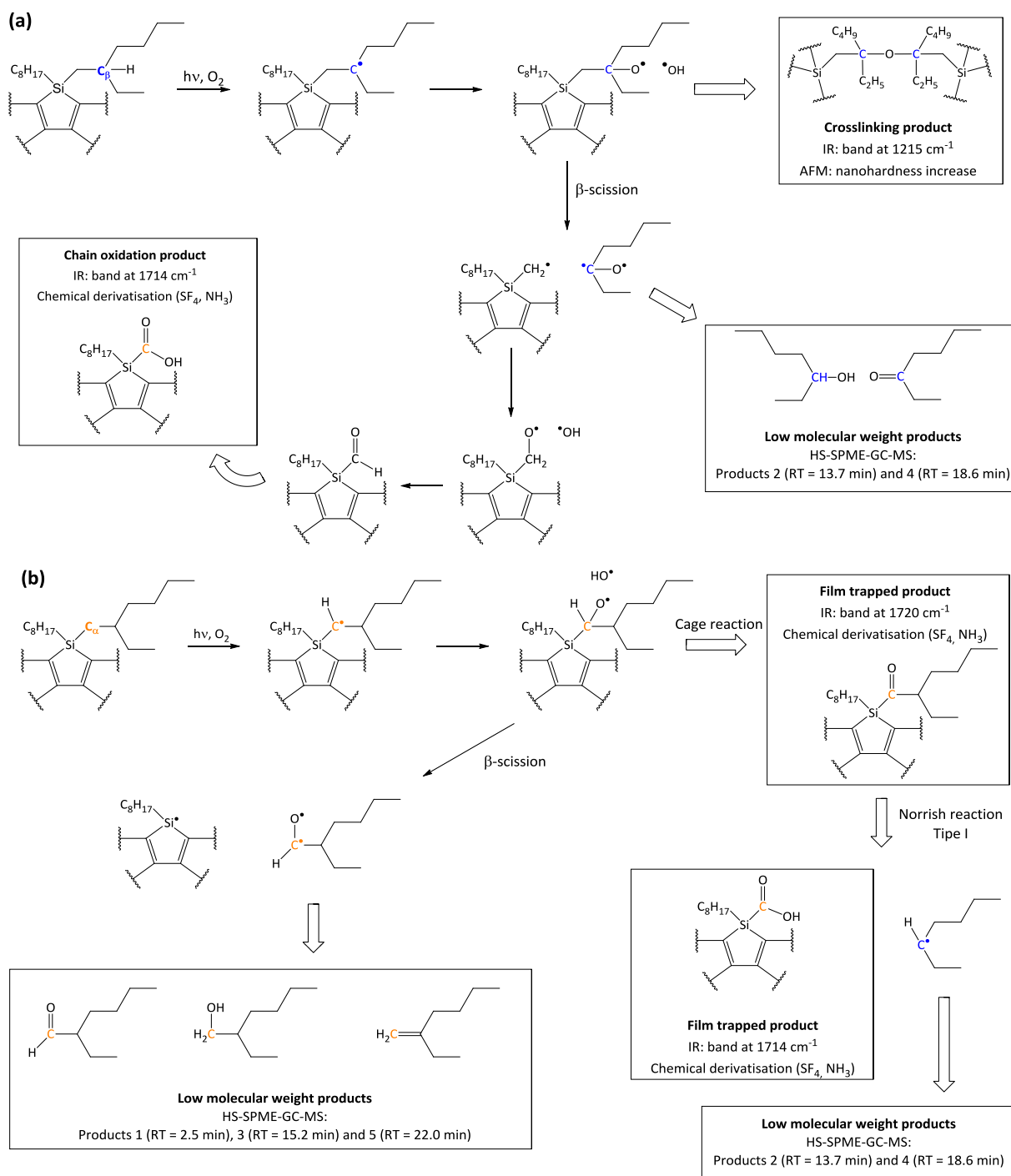
Scheme 3.2. Main routes involved in the oxidation of Si-PCPDTBT alkyl side chain; (a) mechanisms starting by hydrogen abstraction at C_β [$\Delta E(C_\beta$-H) = 97.4 kcal mol^{-1}] (b) mechanisms starting by hydrogen abstraction at C_α [$\Delta E(C_\alpha$-H) = 100.4 kcal mol^{-1}].

After hydrogen abstraction, and according to the fundamental aspects of the photooxidation of polymers, the prime oxidation products created, namely hydroperoxides, rapidly decompose

(thermally or photochemically) to give hydroxyl radicals and macroalkoxy radicals. The latter can further evolve through three main routes; (i) formation of alcohols by hydrogen abstraction; (ii) cage reaction to produce chain ketones and (iii) beta scission processes. It is noteworthy that cage reactions comprise the main route of evolution when oxidation involves secondary carbon atoms, whereas for tertiary carbon atoms, the main route is beta scission, which leads to the formation of acids.[95, 198, 270-272]

Combining these basic rules of polymer photodegradation and the results obtained in this study, the main steps of the Si-PCPDTBT alkyl side-chain photooxidative mechanism have been identified (Scheme 3.2). Oxidation of the alkyl side-chain starting at the most labile position, the tertiary carbon (C_β), can proceed through crosslinking to yield product XL_β (IR band at 1215 cm^{-1}) or go *via* chain scission to produce chain end carboxylic acids (identified by an IR band centred at 1714 cm^{-1} and confirmed by SF_4 and NH_3 treatments) and low molar mass oxidation products (namely products **2** and **4** in Table 3.3, as identified by HS-SPME-GC-MS). On the other hand, oxidation of the secondary carbon atom (C_α) produces chain ketones (IR band at 1720 cm^{-1}) and low molar mass oxidation products (**1**, **3** and **5** in Table 3.3), analysed by HS-SPME-GC-MS.

3.3.1.2.2. Conjugated backbone photooxidation

Radicals involved in the side-chain photooxidative process can also react with moieties of the conjugated backbone, initiating their oxidative degradation. As observed in Figure 3.12, the characteristic bands of the polymer backbone [benzothiadiazole (1498 cm^{-1}), thiophene (1184 cm^{-1}), C_4-Si (1245 cm^{-1}), and the signal at 881 cm^{-1}, corresponding to both Si-C and thiophene moieties] decrease during the irradiation period. In parallel, the appearance of new bands in the fingerprint region is also observed, indicating the transformation of chemical structures present in the polymer.

Oxidation of the thiophene ring in P3HT has been proposed to occur through oxidation of the sulfur atom to produce sulfoxides (R-SO-R), sulfones (R-SO$_2$-R) and, by decomposition of the latter, sulfinic esters (R-SO-OR).[214] The same steps were observed upon oxidation of the thiophene units of PCDTBT.[209] Based on this, modelling was employed to identify the bands associated to these different stages of sulfur oxidation in the two sulfur-containing structures of the polymer, BT and Si-CPDT. Table 3.5 shows theoretical and experimental data for the selected oxidised structures. Oxidation of the sulfur atom in the BT unit (BT-sulfoxide) was calculated to show one band in the interval

153

1115 – 1133 cm^{-1}, and an additional feature at 1317 cm^{-1} for the sulfonic derivative. Experimental infrared spectra (Figure 3.19) show bands in these regions, specifically at 1122, 1107 and 1297 cm^{-1}. Good agreement was again observed for the first and second oxidation of the sulfur atoms in the thiophene units, showing the growth of one band at 1051 cm^{-1} (corresponding to Si-CPDT-sulfoxide formation) and bands at 1089 cm^{-1} and 1215-1234 cm^{-1}, (attributed to Si-CPDT-sulfone). As occurred for P3HT, bands associated to sulfinic esters (617 cm^{-1}) appear at a later stage of degradation, in this case after 70 hours of irradiation. It must be noted that the second band related to this structure (1122 cm^{-1}) also fits with the calculated theoretical wavenumber of oxidation of the sulfur in the BT unit. This could explain its growth from the beginning of irradiation (instead of after 70 hours, like the band at 617 cm^{-1}). According to these data, it seems likely that the same step by step sulfur oxidation mechanism proposed for P3HT and PCDTBT is prevalent in Si-PCPDTBT.

(a)   **(b)**
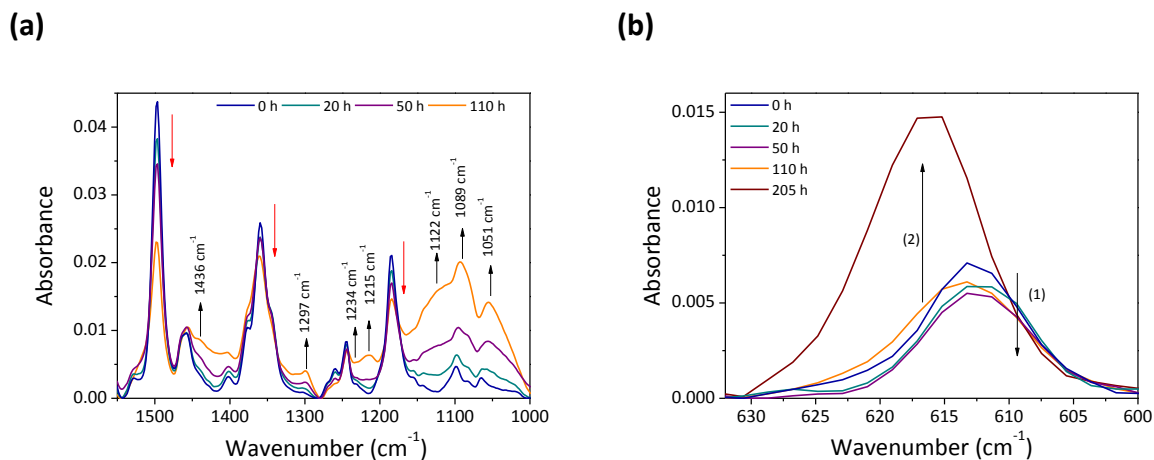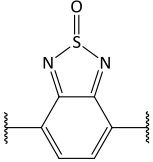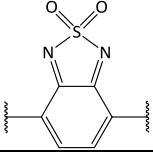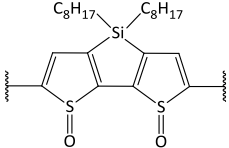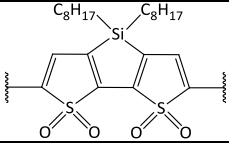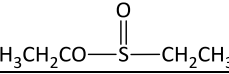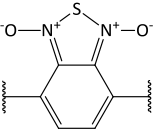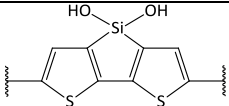
Figure 3.19. Evolution of the IR spectrum of Si-PCPDTBT during photooxidation in the fingerprint region; (a) 1500 – 1000 cm^{-1}; (b), 632 – 600 cm^{-1}.

Oxidation of the nitrogen of the BT unit (BT-nitroxide) was also investigated in combination with theoretical calculations (Table 3.5). Accordingly, the band associated with the oxidation of this atom is theoretically located towards 1460 cm^{-1} if just one nitrogen atom is oxidised, and in the range 1436-1520 cm^{-1} when oxidation occurs in both nitrogen atoms. In the IR spectra, three low intensity bands can be distinguished at 1430, 1515 and 1540 cm^{-1}. This same IR region was investigated for P3HT and PCDTBT; the latter also containing a benzothiadiazole unit. Similar low intensity bands were also observed in PCDTBT infrared spectra, but not in those of P3HT. This further suggests that these bands are not associated with thiophene ring oxidation, but to the oxidation of a different structure. However, their intensity is significantly more inferior to the pronounced evolution of the bands

associated with the thiophene rings. In fact, the IR spectra in the late stages of oxidation are clearly similar for these three polymers, showing bands in three main areas (1390, 1110 and 617 cm^{-1}), attributed to oxidation of the sulfur atoms of the thiophene rings.

Finally, modelling was employed to identify oxidation of the silicon atom in the polymer (Si-CPDT-silanol in Table 3.5). The characteristic bands of bending and deformation of the Si-OH group are localised between 780 and 900 cm^{-1}, with two principal components at 816 and 822 cm^{-1}. The development of a sharp band at 828 cm^{-1} was only observed at very late stages of degradation of the polymer, after 360 hours of irradiation.

Table 3.5. Theoretical predictions (based on B3LYP/6-31G**) for the most characteristic IR bands for model oxidised backbone structures, confronted to experimental IR bands increasing in the interval of the predicted values.

Description	Proposed chemical structure	$\tilde{\nu}$/ cm^{-1}	
		B3LYP/6-31G**	Experimental
BT-sulfoxide (R-SO-R)		1133	1122[a]
BT-sulfone (R-SO$_2$-R)		1115 1317	1107 1297
Si-CPDT-sulfoxide (R-SO-R)		1035-1048	1051
Si-CPDT-sulfone (R-SO$_2$-R)		1057-1100 1256-1262	1089 1234
Sulfinic ester (R-SO-OR)		627 1121	617 1122[a]
BT-nitroxide		1436-1520	1440, 1515
Si-CPDT-silanol		816-822	828

(a) This experimental band that can be attributed to both the formation of BT-sulfoxide and sulfinic ester.

Photooxidation mechanism of the conjugated backbone

The decrease in intensity of the characteristic IR bands (see Figure 3.12) indicates that all of the moieties are oxidised in parallel. Indicative model oxidised molecules (Table 3.5) were employed to predict the oxidation of the polymer by combining the evolution of the bands in the IR recorded spectra with theoretical calculations. These proposed structures may differ from the actual products, as the different moieties of the polymer are all oxidised at the same time. That said, good agreement between the calculated modes and the recorded bands indicates that the heteroatoms present in the backbone are indeed susceptible to oxidation. More specifically, vibrations corresponding to the oxidation of the sulfur atoms in BT and DT have been identified from the beginning of the irradiation. These bands indicate that the sulfur steadily evolves, leading to sulfoxide, sulfone and sulfinic species (the latter appearing after 70 h of oxidation). Oxidation of the bridging silicon atom is only observed at very late stages of degradation (360 hours of irradiation). Finally, although the appearance of low intensity bands at 1430, 1515, and 1540 cm^{-1} suggests that nitrogen could also be susceptible to oxidation, the intensity and general evolution of the ensemble of IR bands indicates that the main degradation of the backbone is due to oxidation of thiophene sulfur atoms, as already reported for P3HT and PCDTBT.[209, 214]

3.3.1.3. Evolution of optical properties

3.3.1.3.1. UV-Vis absorbance decay: degradation profile

Figure 3.20 (a) shows the UV-Vis spectra recorded upon irradiation of Si-PCPDTBT thin films in the SEPAP 12/24 device under ambient air conditions. Prior to irradiation, the absorption spectrum of the polymer shows a main band centred at 700 nm, characteristic of the π-electronic system, with two maxima located at λ = 690 and 760 nm. Three more energetic bands are observed at λ = 425, 320 and 250 nm. The two different maxima around 700 nm stem from different vibrational transitions and their relative ratio correlates with the crystallinity of the polymer. The initially well-pronounced low-energy band at 760 nm indicates a very high degree of crystallinity in Si-PCPDTBT films, in line with the literature[46] and with the results presented in the Section 3.3.2.

(a)

(b)
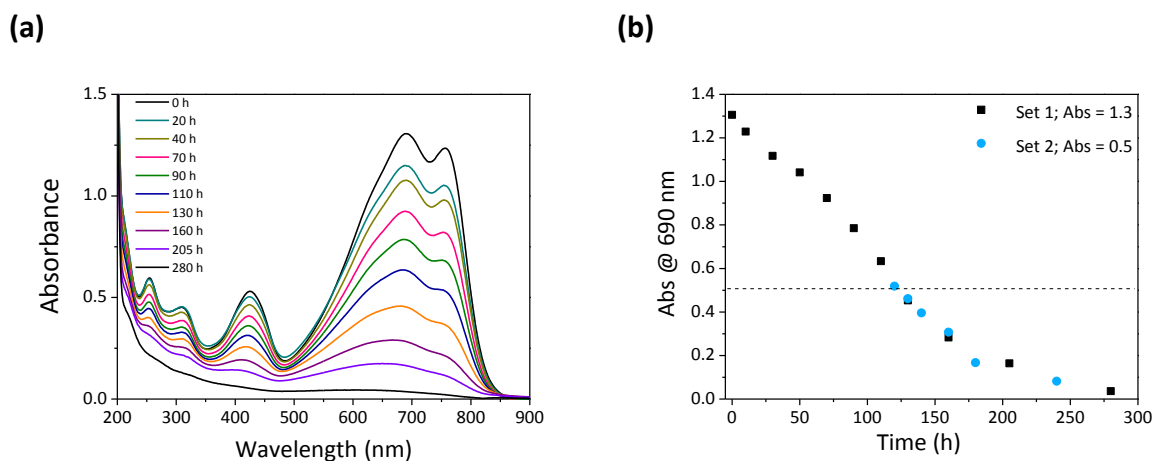
Figure 3.20. (a) Evolution of Si-PCPDTBT UV-Vis spectra upon photooxidation. Abs decay at 690 nm for Si-PCPDTBT films (■ initial Abs 1.3, ● initial Abs 0.5).

Irradiation in the presence of air provokes a continuous decrease in the UV-Vis absorption bands indicating that the π-system of the polymer is diminished or destroyed, which finally leads to complete bleaching of the sample (Figure 3.20). Remarkably, only a slight blue-shift of the absorbance bands is observed in the latter stages of the degradation. The crystalline character of this polymer (together with its high molar mass) creates long conjugation lengths, and thereby minimises oxygen attack at random positions of the backbone, as oxygen tends to attack amorphous regions where the conjugation is disrupted (*i.e.* chain ends or kinks).[211, 233, 235] Consequently, extensive π-conjugation can be preserved for a long time during the degradation progress, which in turn delays a blue-shift of the absorption bands.

Furthermore, both oxygen diffusion and light penetration can create a depth dependent degradation that keeps lower layers of the material intact as photooxidation proceeds, *i.e.* upper parts of the layer facing the incident light and oxygen are likely to be more strongly oxidised than the lower buried parts closer to the substrate. In this regard, since crystalline regions exhibit lower permeability to oxygen than amorphous regions, [234] as degradation proceeds disrupting the π-conjugation of the upper layers exposed to oxygen, more crystalline layers can be preserved below, thus explaining the delayed blue-shift.

Oxidative degradation of the films can be limited by the penetration of light into the sample, effectively determined by the film thickness.[206] According to the thickness evolution for Si-PCPDTBT films depicted in Figure 3.11 (a), after 100 hours of exposure (corresponding to marginally less than 50 % absorbance loss) the thickness of the sample has already decreased by approximately 25 %.

Nevertheless, the shape of the absorption spectrum does not change significantly (besides a faster decrease of the band at 760 nm, indicating a reduction in crystallinity), which suggests that intact, long π−conjugated material is still present in the lower part of the sample, after the upper polymer layers have already completely degraded. Related to this, the thickness decrease cannot solely account for the decrease in absorbance, as the main absorption band at 700 nm decreases faster than the film thickness [compare Figure 3.11 (a) and Figure 3.20 (a)].

In addition, Figure 3.20 (b) displays the absorbance decay at 690 nm of two sets of samples; set 1, with initial Abs ~1.3 and corresponding to the UV-Vis spectra in Figure 3.20 (a), and set 2, with initial Abs ~0.5. The absorbance decay of this second dataset has been plotted in the graph starting from the point in which the thicker film reaches 0.5 in absorbance. Interestingly, despite the increase in absorbance in the visible and, more markedly, in the UV domain for the thicker sample, the absolute degradation rate (ΔAbs *versus* time) exhibits no dependency on the initial thickness of the films in both sets.

Finally, the finding that a pristine film with Abs approximately 0.5 photooxidises with the same rate as a film which has been previously photoxidised (Abs = 1.3 → 0.5) corroborates the aforementioned idea of a layer-by-layer degradation profile. In light of these results, such a degradation profile is limited by the oxygen permeability of the crystalline/amorphous regions, whereas the penetration of light in these samples did not play a significant role.

3.3.1.3.2. Influence of the irradiation setup (SEPAP 12/24 *versus* Suntest CPS/XLS)

The photooxidative behaviour of Si-PCPDTBT thin films using SEPAP 12/24 was then compared to degradation using Suntest CPS/XL as irradiation source, each of these devices having different irradiation sources of characteristic spectral distributions (Figure 3.12). In this regard, it has been demonstrated that the photodegradation rate (and also mechanism) of a P3HT layer can be different depending on the UV or visible content of the light source used for the experiments.[212, 220] Furthermore, in line with exposures used in the studies in Section 3.3.1.3.1, light penetration (and thus the creation of light-dependent degradation profiles) can be influenced by the wavelengths irradiating the sample.[206]

Given that SEPAP 12/24 and Suntest irradiate the sample with a different quantity of UV and visible photons, the influence that the different irradiation devices had on the kinetics of the

Si-PCPDTBT degradation was examined. At this point, the possible differences in the resulting degradation mechanisms were not addressed.
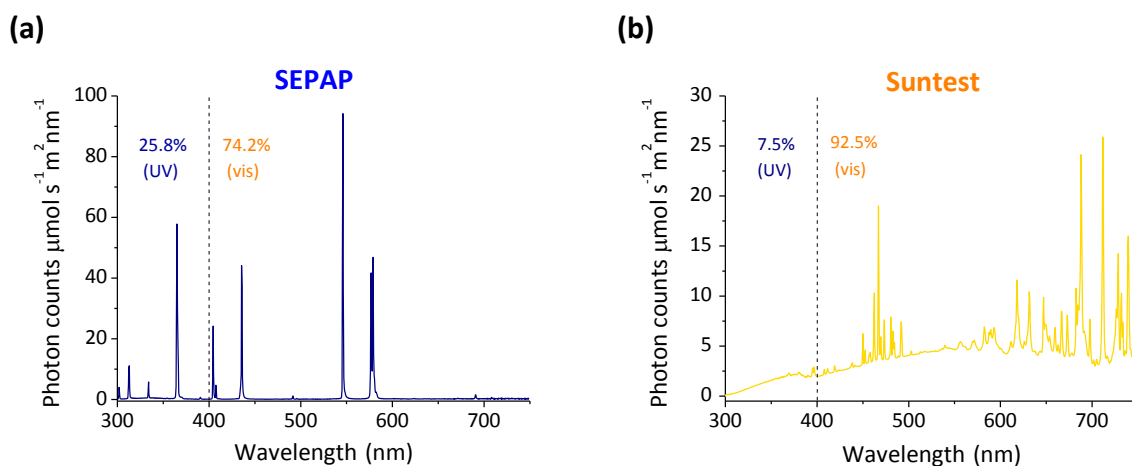
Figure 3.21. Spectral distribution (photon counts) of SEPAP 12/24 (a) and Suntest CPS/XLS (b). The percentages correspond to the content in UV (λ < 400 nm) and visible (λ > 400 nm) photons for each device.

Device	Slope m² mol⁻¹	Total Photon Count mol m⁻²
SEPAP	-4.5 ± 0.2 10⁻³	220
Suntest	-8.3 ± 0.2 10⁻⁴	1130
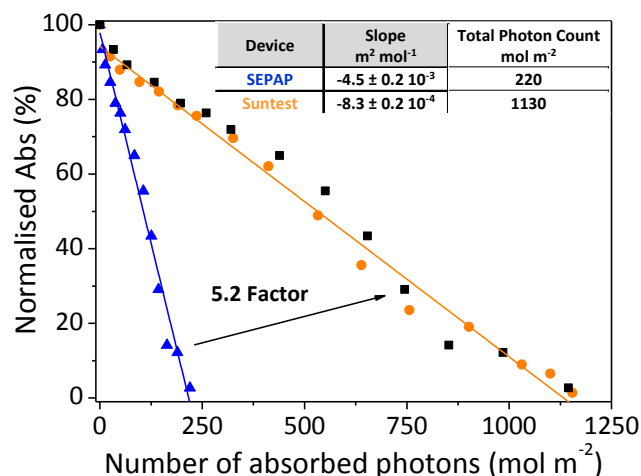
Figure 3.22. Photooxidation kinetics for Si-PCPDTBT, presented as normalised Abs at λ = 690 nm *versus* number of absorbed photons. (▲) Absorbance decay for a sample irradiated in SEPAP 12/24. The straight line indicates the linear fit applied. (●) Absorbance decay for a sample exposed to irradiation in Suntest. The straight line indicates the linear fit applied. (■) Absorbance decay for a sample submitted to irradiation in SEPAP 12/24, applying a factor of 5.2.

The photooxidation kinetics, in terms of the number of absorbed photons, for irradiations performed in SEPAP or Suntest, are displayed in Figure 3.22. As shown, the decay is faster in the case of the degradation in SEPAP. This device, having a higher content of the more energetic UV photons,

requires fewer absorbed photons to achieve complete photobleaching of the polymer. Interestingly, even though the main absorption band of the polymer lies in the visible region, the UV photons still lead to a faster destruction of the π-conjugated system of Si-PCPDTBT. A linear fit was applied to both datasets to calculate the number of absorbed photons needed to achieve a final null absorbance for the devices. According to which, 5.2 times more photons are needed from Suntest in comparison with SEPAP to get total bleaching of the polymer. Furthermore, application of this 5.2 factor to the initial SEPAP data creates a new dataset with good correlation with the Suntest kinetic decay.

3.3.1.3.3. <u>Absorbance loss relative to other polymers: the role of silicon</u>

The absorbance loss kinetics of Si-PCPDTBT under photooxidative conditions was then compared to that of previously studied P3HT and PCDTBT, also reported to undergo degradation following a radical chain oxidation mechanism.[209] Thin films of the three materials exhibiting the same initial absorbance were irradiated under identical conditions, and the absorbance was periodically recorded throughout exposure at the respective maximum absorbance wavelengths. As shown in Figure 3.20 (b), the initial velocities, calculated from t = 0 until 50 % absorbance loss, are 0.0256 h^{-1} for P3HT, 0.0120 h^{-1} for PCDTBT and 0.00446 h^{-1}, for Si-PCPDTBT. Accordingly, approximately 50 and 150 hours of irradiation were needed to achieve complete bleaching of P3HT and PCDTBT, respectively, whereas Si-PCPDTBT was only fully degraded after 280 hours.
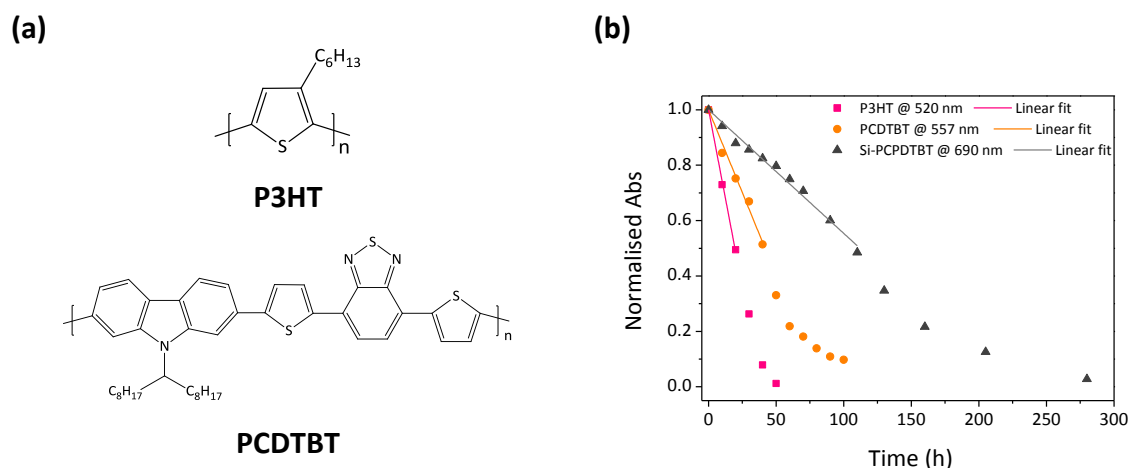
Figure 3.23. (a) Chemical structure of P3HT and PCDTBT. (b) UV–Vis normalised Abs decay (normalised to the corresponding initial values) for P3HT, PCDTBT, and Si-PCPDTBT exposed to photooxidation.

Interestingly, these three polymers share common structural features (thiophene and benzothiadiazole units), with a notable difference being the way in which the alkyl side chain is attached to the polymer backbone in each case [see Figure 3.9 and Figure 3.23 (a)]. In P3HT, where the hexyl chain is directly linked to the thiophene ring, degradation has been reported to start by hydrogen abstraction on the alpha carbon (to the thiophene ring).[214] The great lability of this hydrogen atom can be explained in terms of the stabilisation of the corresponding radical by delocalisation through the conjugated backbone. On the other hand, in PCDTBT, irradiation provokes direct scission of the bond between the N atom of the carbazole unit and the pendant alkyl side chain.[209] Finally, the alkyl side chain of Si-PCPDTBT is attached to the CPDT unit through a silicon bridging atom. Thus, our interest focused on understanding the role of Si on the oxidation of the polymer, and more precisely, on the oxidation of the alkyl side chain identified as the starting point of the degradation.

Calculations were performed for both Si-PCPDTBT and the analogous polymer C-PCPDTBT, solely differing on the bridging atom, Si or C. Initially, the relative hydrogen labilities at the C_α and C_β positions, in relation to the respective bridging atoms, were determined in terms of the C-H bond dissociation energies. Subsequently, the corresponding macroradicals, formed after hydrogen abstraction at the most labile position identified for each polymer, were evaluated in terms of their thermodynamic stability and electron delocalisation (Table 3.6).

Table 3.6. Calculated bond dissociation energies and thermodynamic stabilities in Si-PCPDTBT and C-PCPDTBT within B3LYP/6-31+G** theory level.

		Si-PCPDTBT	C-PCPDTBT
Bond dissociation energy (kcal mol^{-1})	**C_α-H**	100.4	101.9
	C_β-H	97.4	98.7
Thermodynamic stability of R$^\bullet$ (kcal mol^{-1})		-15.3	-18.3

The bond dissociation energies reported in Table 3.6 firstly indicate that, independent of the bridging atom (Si or C), C_β-H is more labile than C_α-H, as expected, due to their tertiary character. Higher bond dissociation energies, and thus stronger C-H bonds, are observed in the presence of carbon in comparison to the silicon counterpart. Nevertheless, variation in the bond dissociation energies between both polymers is small (+1.5 and +1.3 kcal mol^{-1} for C_α and C_β, respectively). These differences were further explored by examining the stability of macroradicals created after abstraction of the most labile hydrogens, *i.e.* those in the β position. The corresponding macromolecular stabilities were assessed using DFT calculations of overall energy gains for performing

the reaction RH + OH$^\bullet$ → R$^\bullet$ + H$_2$O.[273-274] According to the data reported in Table 3.6, C-PCPDTBT gives rise to the most stable structure (-18.3 kcal mol^{-1}), thus significantly favouring radical formation. Finally, the spatial delocalisation of unshared electrons in the created macroradicals was evaluated. In C-PCPDTBT, the unpaired electron is localised with a partition coefficient of 0.59 at the native carbon (from which the hydrogen was abstracted) and 0.16 over the C$_5$ ring. In Si-PCPDTBT, the coefficient on the native carbon increases up to 0.74, and sharply decreases to 0.06 over the cycle. This indicates that hydrogen abstraction in C-PCPDTBT produces a more delocalised macroradical, and therefore more stabilised than the equivalent abstraction in Si-PCPDTBT. In fact, the silicon atom blocks the unpaired electron from moving towards the ring[275-276] producing a less stable macroradical, and thus disfavouring the general process of hydrogen abstraction.

All of these computational data converge to the conclusion that introducing a silicon atom as a bridge to the solubilising alkyl side-chains is a good strategy to warrant improved photostability of the resulting polymer. This is, in turn, supported by the comparative absorbance decay shown in Figure 3.23 (b), which clearly shows an increased resistance to photooxidation for Si-PCPDTBT. However, on assessing the relative stabilities of different polymers, it should be noted that not only the chemical structure but also other parameters, such as purity, regioregularity, crystallinity, or morphological order obtained upon deposition play a decisive role (see Section 3.1.1.4). For example, if these three materials are compared with one another, in terms of the structural order obtained upon deposition, both regioregular P3HT and Si-PCPDTBT films exhibit rather crystalline properties which are known to increase stability towards photooxidation,[46, 233-235] whereas PCDTBT forms mainly amorphous films.[277] Thus, despite the differences in the nature of the side chains and/or bridging atoms, and the overall differences in their chemical backbones, the higher photoresistance of Si-PCPDTBT could also be explained in terms of the (semi)crystalline character of the films. Furthermore, on the comparison of the Si/C bridging atom, recent publications indicated that photodegradation rate in the initial steps of degradation is actually higher for Si-PCPDTBT compared to C-PCPDTBT.[237, 278] Based on surface analysis with XPS, the authors claim a higher reactivity of Si and the carbon atoms bonded to it towards photooxidation, which, in turn, delays the oxidation of sulfur and nitrogen atoms compared to the reactivity of C-PCPDTBT.[278] It must be noted that the authors also observed the presence of an initially oxidised Si compound in the samples, which did not belong to the polymer.[278] This can, indeed, have an influence on the results under discussion, and highlights again the need for appropriate purification procedures on the synthesis of low bandgap polymers for organic solar cells.

3.3.2. Characterisation and photochemical degradation of systematically modified p-type polymers

The work in Section 3.3.1 constitutes a detailed description on the photochemical pathways of the low bandgap polymer Si-PCPDTBT, considering a predominant chain radical degradation mechanism with the alkyl side chains identified as the starting point of degradation. The photobleaching rate in Si-PCPDTBT was compared to that of other polymers (P3HT, PCDTBT), and the differences in photostability were approached from a structural point of view. More specifically, focus was placed on understanding the role of silicon (or carbon) as the bridging atom to the side chains. The differences in the chemical backbones of the compared polymers, along with other intrinsic or extrinsic parameters influencing polymer photostability, have not been addressed.

In this section, the aim is to first establish a relationship between polymer structure and the resulting photostability in air of a series of low bandgap polymers. To this end, collaborative work with Gregori *et al.* and Morse *et al.* has been developed to synthesise low bandgap polymers with a systematically modified backbone and/or alkyl side chain structures. More specifically, two different donor units (benzodithiophene, BDT, and dithienosilole, DTS) and three different acceptor units (diketopyrrolopyrrole, DPP, dithienylbenzothiadiazole, DTBT, and thiazolothiazol, TzTz) have been combined to yield the polymers P1 - P5. Also, for the pair DTS-DPP (P5), it was varied the length and nature (linear or branched) of the side chains in the acceptor DPP unit, creating the sub-series P5a - P5c. The ensemble of the low bandgap polymers under study is depicted in Figure 3.24. For comparison, Si-PCPDTBT has been included again to the study using the same processing conditions as the rest of the polymers, as well as the carbon analogous C-PCPDTBT and the well-known P3HT (see Figure 3.25). Secondly, as described in Section 3.1.1.4, not only the chemical structure, but also other parameters (such as crystallinity, morphology or content in paramagnetic species) can determine polymer photooxidation rates. Thus, all polymers have been characterised using a range of techniques (XRD, RHC, and EPR) with the aim of establishing possible relationships between their physicochemical properties and corresponding photodegradation rates. Finally, the effect of blending the polymers with fullerene acceptor PCBM has on photochemical behaviour has been assessed.

Acceptor / Donor	DTBT	TzTz	DPP
BDT	P1	P2	-
DTS	P3	P4	P5a,b,c

P1 [BDT – DTBT]

P2 [BDT – TzTz]

P3 [DTS – DTBT]

P5 [DTS – DPP]

P4 [DTS – TzTz]
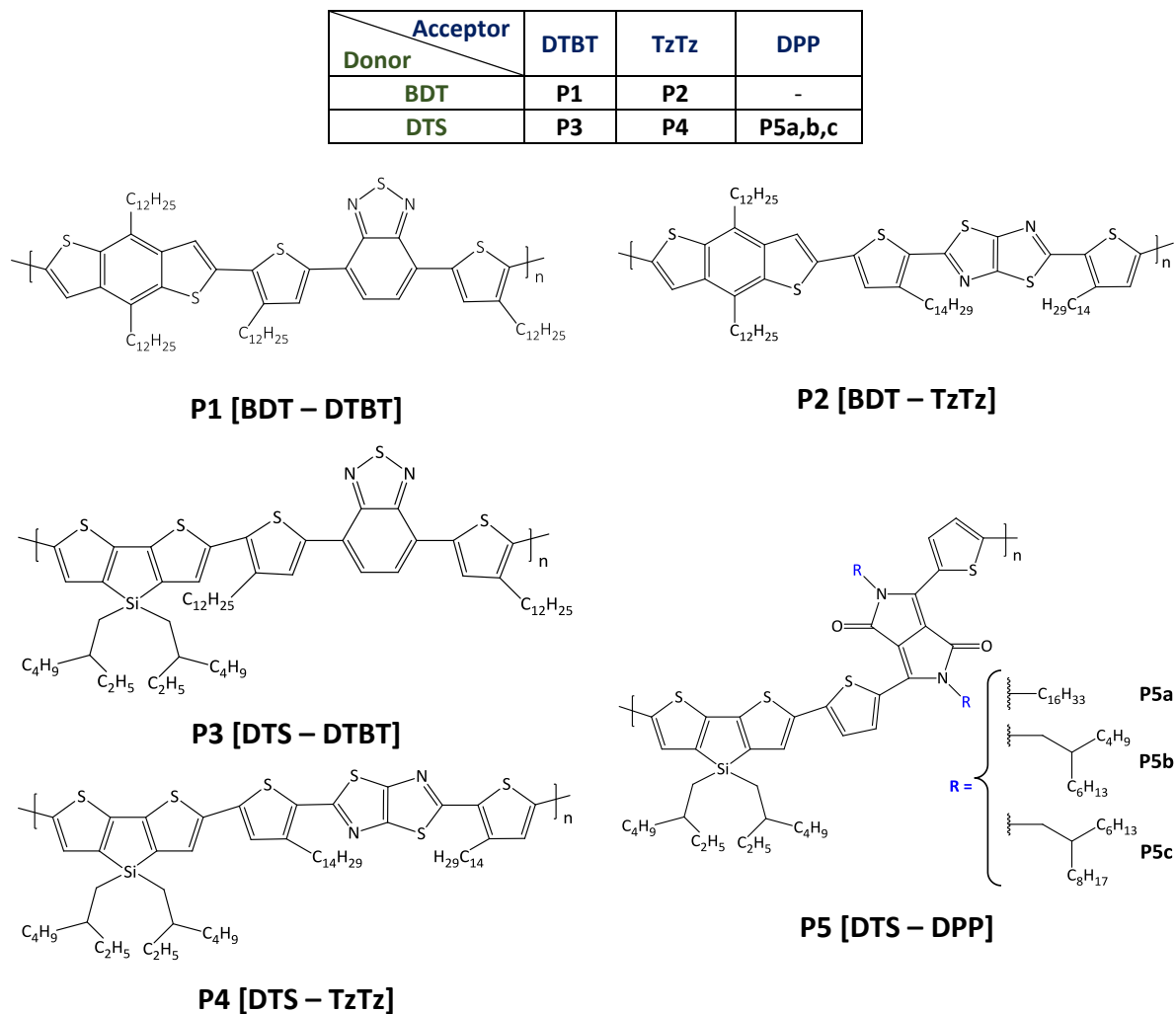
Figure 3.24. Low bandgap polymers under study.

Si-PCPDTBT [DTS – BT]   **C-PCPDTBT**   **P3HT**
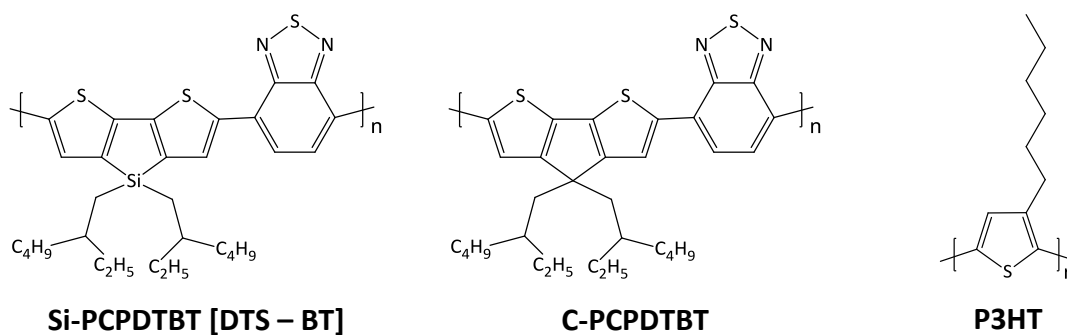
Figure 3.25. Reference polymers used in this study: Si-PCPDTBT, C-PCPDTBT, and P3HT.

3.3.2.1. Polymer characterisation

3.3.2.1.1. <u>Paramagnetic species content</u>

The paramagnetic species content was determined using Electronic Paramagnetic Resonance (EPR), as shown in Figure 3.26. All of the polymers studied displayed a characteristic signal, centred at a magnetic field of approximately 3500 Gauss, with the intensity ranging, in the majority of cases, from 1×10^4 to 2×10^4. Two of the polymers displayed higher intensity values, around 8×10^4 in the case P5a and 1×10^5 for C-PCPDTBT. Since the same amount of polymer (2 mg) was measured in all cases, a higher signal indicates a higher paramagnetic species content, which, in turn, can be detrimental for the functioning of the solar cell and can also trigger degradation. Importantly, these signals are not caused by metallic catalysts, since those signals would usually be observed at much lower g-factor (low field region),[201] but could stem from organic impurities, such as low molar mass organics (oligomers or unreacted/deactivated monomers), degradation products or other by-products that remain within the polymer.[224]
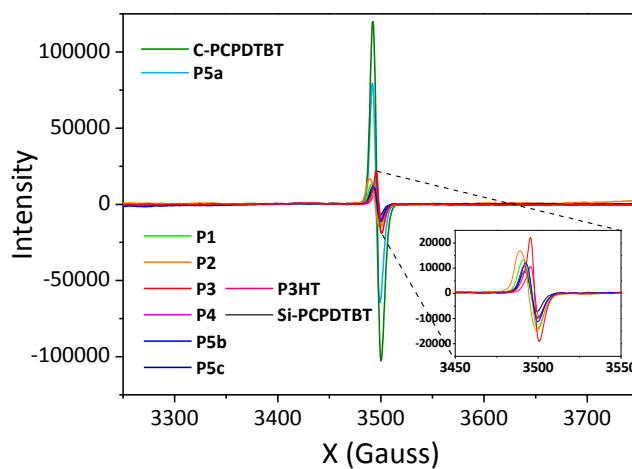
Figure 3.26. EPR traces displayed for the polymers under study (2 mg, as powder).

3.3.2.1.2. <u>Optical properties</u>

Figure 3.27 (a-c) displays the UV-Vis spectra of all pristine polymer films, together with a table summarising the absorption characteristics of the polymers in (d). All polymers have been processed following the same procedure, and no optimisation or post-deposition treatment (such as thermal annealing) to enhance crystallinity/packing have been applied. Overall, low bandgap polymers display two absorption bands, one at lower wavelength, corresponding to $\pi \rightarrow \pi^*$ transitions, and a second

main absorption band at higher wavelength due to the intramolecular charge transfer (ICT) from the donor to the acceptor unit. In some cases, the band corresponding to the $\pi \rightarrow \pi*$ transitions may be not observed due to the cut-off of the glass substrates (< 300 nm).

Concerning the synthesised low bandgap series (P1 – P5c), and firstly analysing of the BDT-based polymers (P1 and P2), it is shown that the combination BDT-DTBT (P1) yields a polymer of main absorption at 635 nm. The main absorption band shows some structuration (690 nm), as well as a very strong $\pi \rightarrow \pi*$ band at 430 nm. BDT is known to easily form π-π stacking due to its large planar structure.[279] In turn, P2 (BDT-TzTz), displays a main absorption band around 560 nm, with two clearly resolved features at 545 and 585 nm. These features seem somewhat related to the presence of the TzTz unit, since they appear also for polymer P4 (DTS-TzTz).

Comparing the series containing DTS units (P3, P4, P5), it can be seen that a lower bandgap (higher absorption wavelength) was displayed by the combination of DTS-DPP (P5) [see Figure 3.27 (a)]. Interestingly, P1 and P3 display similar spectra (main band at 640 nm, and strong $\pi \rightarrow \pi*$ band at 430-455 nm), however with higher structuration in the case of P1. As aforementioned, P4 exhibits a very similar absorption spectrum to P2, shifted to slightly higher wavelengths (~600 nm).

Polymers in the P5 series (comprising a DTS-DPP backbone with varying side chains), show two main bands, one around 450 nm ($\pi \rightarrow \pi*$ transitions), and another around 800 nm (donor-acceptor ICT). A low bandgap achieved is achieved thanks to the DPP unit, whose planar and highly conjugated lactam structure confers the unit a high electron withdrawing effect. [280] Whilst the position of the main absorption band is very similar for the three polymers, the nature of the side chain linked to the nitrogen in the lactam units imparted some structuration to it. Accordingly, the spectrum of P5a (bearing a linear C16 side chain) exhibits a broad featureless band at 800 nm, but the spectra of P5b and P5c (bearing branched side chains of different lengths) show slightly pronounced shoulders in the main band, see Figure 3.27 (b).

Figure 3.27 (c) groups the UV-Vis absorption spectra of pristine P3HT, Si-PCPDTBT and C-PCPDTBT. P3HT films exhibit a broad band centred at 520 nm, with low-resolved features at 550 and 600 nm. An increase in these features can be obtained when highly ordered domains are created.[233-235] According to the literature, Si-PCPDTBT forms more crystalline films due to strong aggregation and stacking of the polymer chains, whilst C-PCPDTBT creates mainly amorphous films.[46, 278] This difference is manifested in the UV-Vis absorption spectra of the polymers, both displaying a main absorption band

around 700 nm, and in the case of Si-PCPDTBT featuring two resolved vibronic shoulders at 690 nm and

760 nm. Interestingly, while the Si-PCPDTBT spectrum presented in the Section 3.3.1.3 (Figure 3.20)

displayed the highest absorbance in the first vibronic shoulder (at 690 nm), in Figure 3.27 (c), the

feature at 760 nm is the most intense. The feature at higher wavelengths is related to the

aggregation/crystallinity; [278, 281] thus, it reflects changes in the processing conditions leading to different

conjugation lengths or aggregation. Indeed, the two spectra correspond to samples processed

differently, *i.e.* spin coating in one case (Section 3.3.1.3), and doctor blading in the other (this section).

Interestingly, according to the presence or absence of vibronic shoulders, Si-PCPDTBT films also seem

more crystalline than P3. However, the overall backbone structure of these two polymers is the same,

only including alkyl-substituted thiophene spacers in the acceptor BT unit in the case of P3.

(a)

(b)

(c)

(d)

Polymer	$\pi \rightarrow \pi^*$ (nm)	ICT (nm)
P1	430	**635**, 690
P2	-	**545**, 585
P3	455	**640**
P4	-	**585**, 630
P5a	450	780
P5b	450	730, **810**, 830
P5c	450	720, **790**
Si-PCPDTBT	430	690, **760**
C-PCPDTBT	415	700, **750**
P3HT	**520**, 550, 600	-
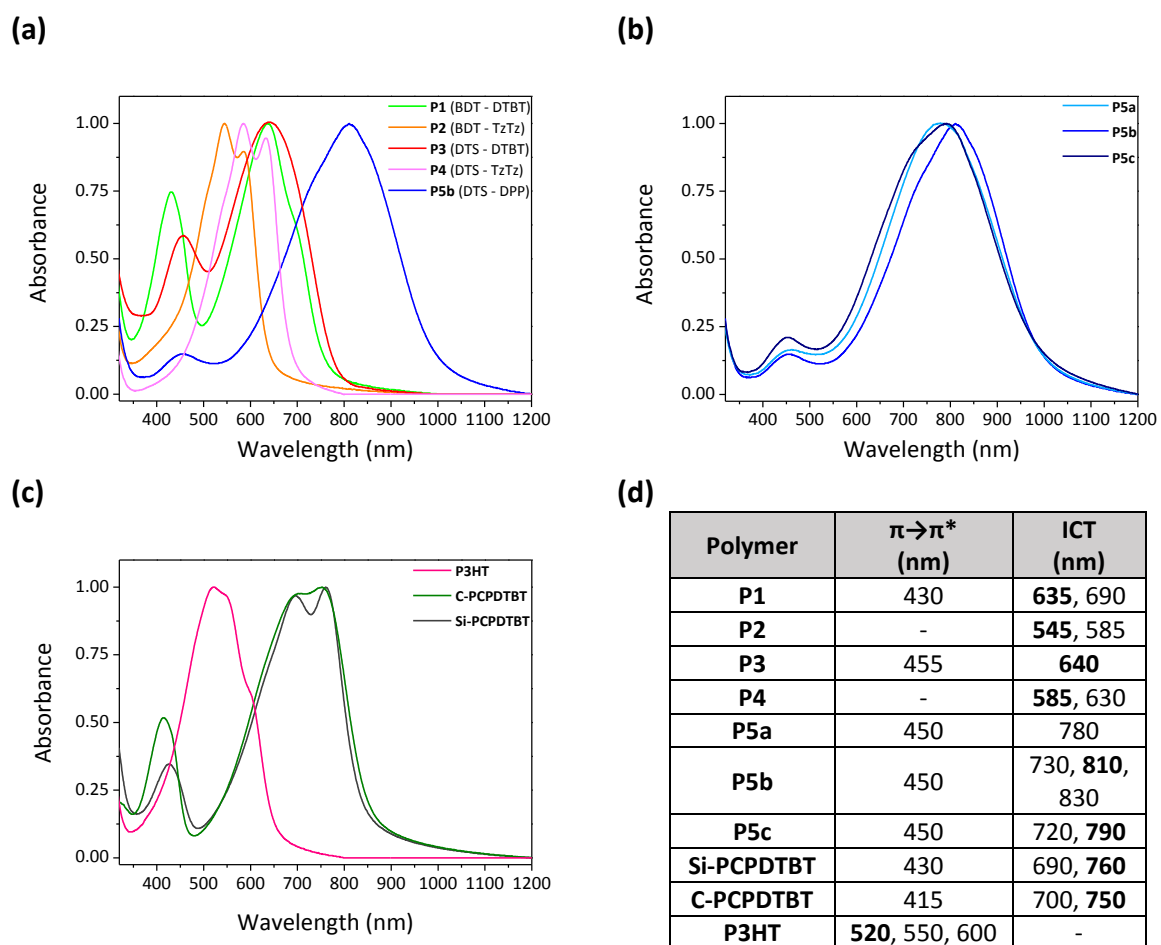
Figure 3.27. UV-Vis absorption spectra of the polymers under study: (a) P1-P5, (b) P5a-c, bearing different side chains in the DPP acceptor unit, and (c) reference polymers regioregular P3HT, C-PCPDTBT, and Si-PCPDTBT.

3.3.2.1.3. Crystallinity

Rapid Heat-Cool Calorimetry

Information about the crystallinity of the different polymers was obtained using Rapid Heat-Cool Calorimetry (RHC). Table 3.7 summarises the thermal information obtained for the ensemble of polymers, directly analysed as the solid materials obtained from the suppliers. Only the second heating run was taken into account and the different values have been determined for a heating and cooling rate of 500 K min^{-1} and 20 K min^{-1}, respectively. The corresponding thermograms are shown in the Annex (page 251).

The melting temperature obtained for reference P3HT (T_m = 231 °C) is in fair agreement with the consulted literature.[64-65, 282] Unfortunately, identification of the T_g value (expected around 12 °C)[64, 282] was unsuccessful due to baseline instability. However, no crystallinity was observed for Si-PCPDTBT, despite the reported crystalline characteristics of the polymer (as films),[46] nor for C-PCPDTBT. Regarding the low bandgap polymers under study, P2, P3 and P5a-c displayed some crystalline behaviour, as indicate the identified melting temperatures displayed in Table 3.7. Among them, P2 (solid at room temperature) displayed a marked transition at low temperature (4 °C) which could be due to the presence of a liquid crystalline phase in the polymer. The melting peak for P5a was too broad, making it arduous to assign a credible T_m value and calculate the corresponding melting enthalpy. In several cases (P2-P4, P5b-c, and Si-PCPDTBT), T_g values remained undetermined.

Whilst these data provide interesting information about the polymers and can give an idea about their crystalline properties, it is important to note that the solid-state microstructure is heavily influenced by all of the crystallisation phenomena that can take place.[66] The results presented in Table 3.7 have been obtained from the analysis of the different polymers as received in bulk from the suppliers; however, in this work, the photostability of the different polymers has been assessed as solution-processed films, both as single components or blended with PCBM. Since processing from solution leads to different behaviour than melt-processing, the crystallinity of the polymer films may differ from that of the solid material obtained directly after synthesis and purification. Indeed, thermal analysis of the polymer powders (or blends) as-cast from solution is more pertinent to obtain information about the crystalline character of the polymer films under study.[65]

Table 3.7. Glass transition temperature (T_g), melting peak temperature (T_m), and melting enthalpy, as determined using Rapid Heat-Cool Calorimetry (heating and cooling rate of 500 K min^{-1} and 20 K min^{-1}, respectively).

Polymer	T_g / °C	T_m / °C	Melting enthalpy J g^{-1}
P1	146	-	-
P2	a	a	a
P3	-	135	8.2
P4	-	-	-
P5a	135	b	b
P5b	-	270	12.1
P5c	-	250	14.1
P3HT	-	231	23.8
Si-PCPDTBT	-	-	-
C-PCPDTBT	176	-	-

(a) P2 displayed a transition at low temperature (4 °C), see Annex. The associated enthalpy remained undetermined due to difficulties establishing a baseline for the calculation; and
(b) P5a, T_m was too broad and the enthalpy difficult to quantify.

X-ray diffraction

With the aim of obtaining a more appropriate picture about the (semi)crystalline or amorphous character of the polymer films under study, X-ray diffraction (XRD) measurements were performed on pristine films (see Figure 3.28). These measurements were carried out only to provide a qualitative picture in assessing the main character of the different polymer samples, *i.e.* predominantly amorphous or predominantly crystalline. Among the different donor-acceptor combinations, P1 (BDT – DTBT) and the P5 variant (DTS – DPP) seem to yield the most crystalline films. Interestingly, no crystallinity was detected for P2 nor P3 in the probed length scales in this study, contrary to what was observed for RHC characterisation of the polymer powder (Table 3.7). In line with the literature, and according to what previously described, P3HT films display a marked crystalline character, and Si-PCPDTBT films were more crystalline than the corresponding C-PCPDTBT films.[46] For the ensemble of polymers, the observed XRD peaks were located at 2θ = 4-5.5,° corresponding to a distance of 23-16 Å, most likely related to the spacing between adjacent chains set by pending side chains in each case.[46] The results in Figure 3.28 are also valid for the corresponding blends with PCBM (ratio 1:2), with the exception of P1:PCBM, for which no diffraction peaks were detected (results not shown).

(a)

(b)

(c)
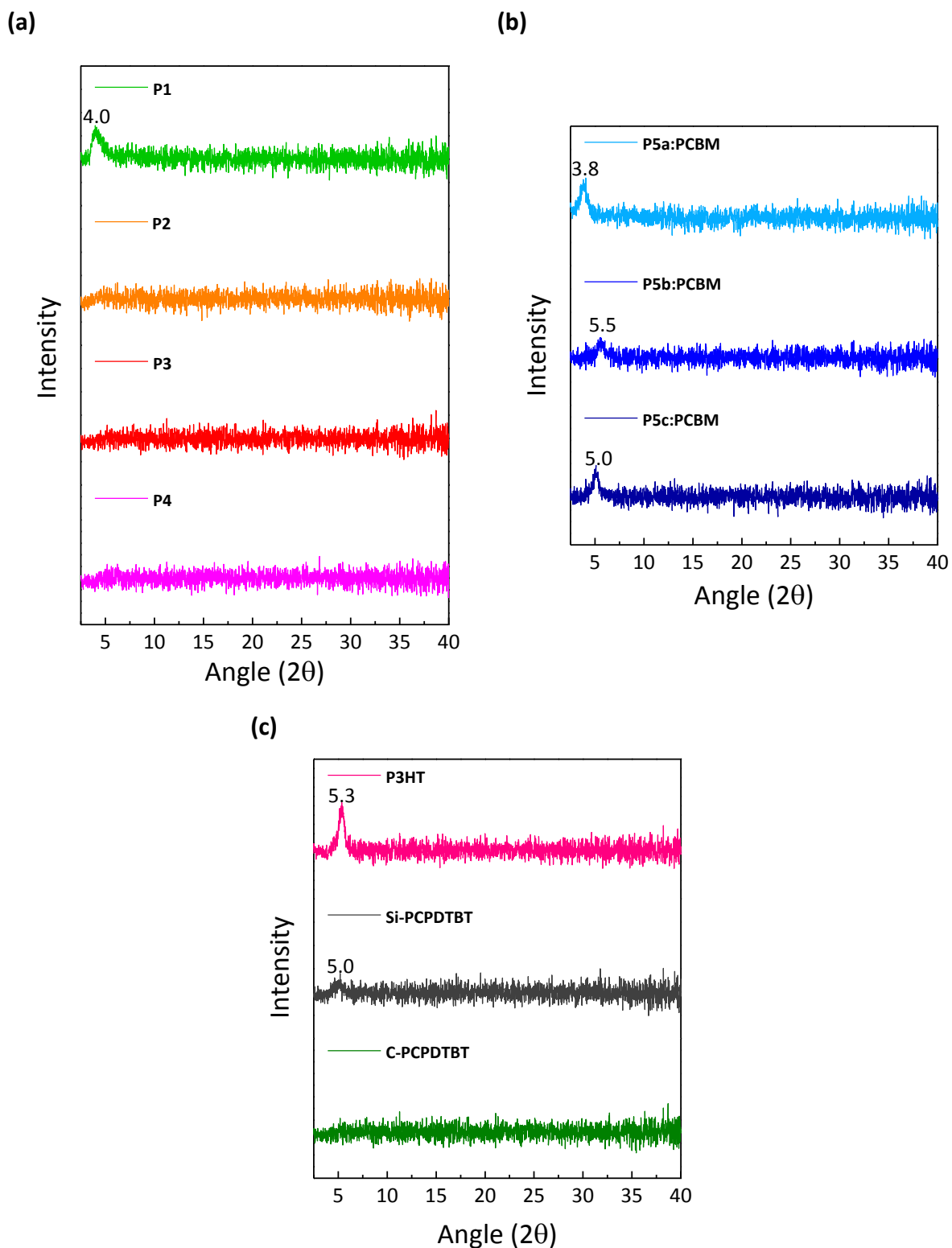
Figure 3.28. XRD profiles of pristine polymer films, prepared *via* doctor blading (a) Polymers P1-P4, with varying donor-acceptor units (b) P5a-c, of same conjugated backbone (DTS – DPP) and varying alkyl side chains (c) Reference polymers P3HT, Si-PCPDTBT, and C-PCPDTBT.

In summary, XRD results are in line with RHC characterisation in the case of P5b, P5c, and P3HT, showing predominantly crystalline polymers according to both techniques, as well as for P4 (predominantly amorphous in both cases). In contrast to this, RHC results indicated crystalline character for P2 and P3 (rather amorphous according to XRD) and lack of crystallinity in the case of P1, P5a, and Si-PCPDTBT (displaying diffraction peaks in XRD). The discrepancy in the results obtained *via* both characterisation techniques can result from the fact that RHC analysis was performed on the polymers as-powder, whilst XRD data were obtained from the analysis of polymer films.[66] Furthermore, the characterisation *via* XRD (*e.g.*, 2θ range) was not optimised; as consequence, information about the crystallinity of the films can be missing in the presented results. Thus, these results, although revealing some information, are not comprehensive. Future work could include both the optimisation of the acquisition conditions using XRD and the calorimetric analysis of solution-processed polymer films.

3.3.2.2. Evaluation of polymer photostability

3.3.2.2.1. <u>Polymer photooxidation</u>

Evaluation of photostability was performed by exposing polymer thin films to UV-Vis irradiation (Suntset CPS/XL) under ambient air conditions (photooxidative conditions). In all cases, irradiation provoked a continuous decrease in intensity of the UV-Vis absorption bands indicating a destruction of the π-conjugated system of the polymer, finally leading to complete bleaching of the samples (see Figure 3.29 and Figure 3.30). Interestingly, the loss of absorbance followed different patterns depending on the polymer concerning the shift of the maximum absorbance to lower wavelengths (blue-shift), characteristic of the loss of conjugation in the films. While P1 and the polymers in the P5 series showed no blue-shift (Figure 3.29), P3 and P4 exhibited a very marked blue-shift from the very beginning of the irradiation. Finally, a blue-shift in P2 was observed towards the end of the exposure time, as can be seen in Figure 3.30.

In order to obtain information about the photooxidation kinetics in each case, the normalised absorbance value (at the maximum absorbance wavelength for each polymer) was plotted *versus* time for the ensemble of the polymers, and compared also to the reference neat P3HT, Si-PCPDTBT, and C-PCPDTBT samples, see Figure 3.31 (a). The photodegradation rates of all polymers (calculated from the linear fit of the data between t_{1h} and t_{15h}) are summarised in Figure 3.31, from the lowest rate (P1; $r_{P1} = -0.0121$ h^{-1}) to the highest (P2; $r_{P2} = -0.059$ h^{-1}). Concerning the stability of the reference polymers,

both Si-PCPDTBT and C-PCPDTBT displayed very similar, low photooxidation rates around -0.015 h^{-1}, whilst the photooxidation rate of P3HT had an intermediate value (r_{P3HT} = -0.036 h^{-1}) among all the investigated samples. Accordingly, the photooxidation rates of the low bandgap polymers under study can be grouped into three categories. Firstly, those that exhibited higher photostability, with lower photooxidation rates closed to that of the PCPDTBT polymers (around -0.015 h^{-1}), namely P1 and P5c. Secondly, those whose photooxidation rates had intermediate values (set by the photooxidation rate of P3HT; -0.036 h^{-1}), *i.e.* P5a, P5b, and P4. Finally, those with photooxidation rates higher than that of P3HT, namely P3 and P2. This classification is discussed in Section 3.3.2.2.3.
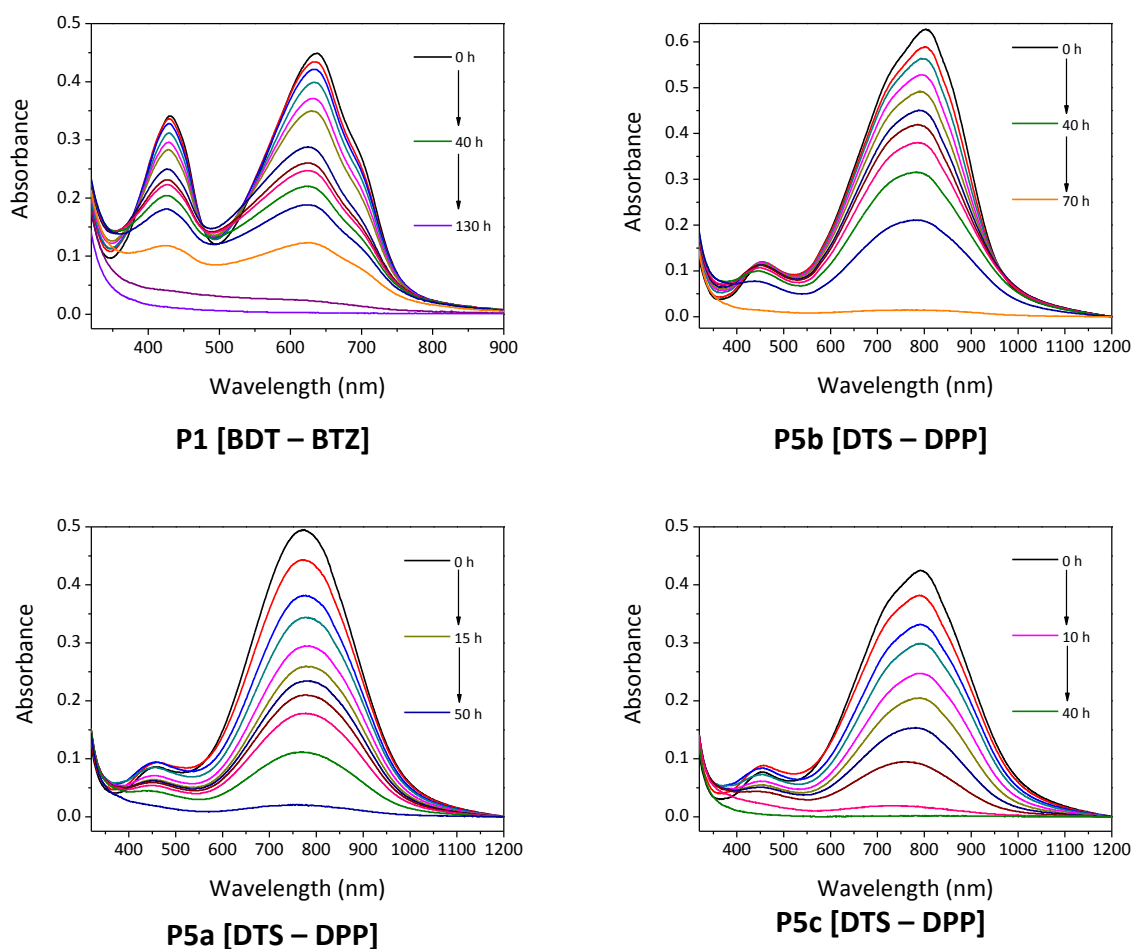
Figure 3.29. Absorbance decay for polymers P1 and P5a-c exposed to photooxidative conditions.

P2 [BDT – TzTz]

P3 [DTS – BTZ]

P4 [DTS – TzTz]
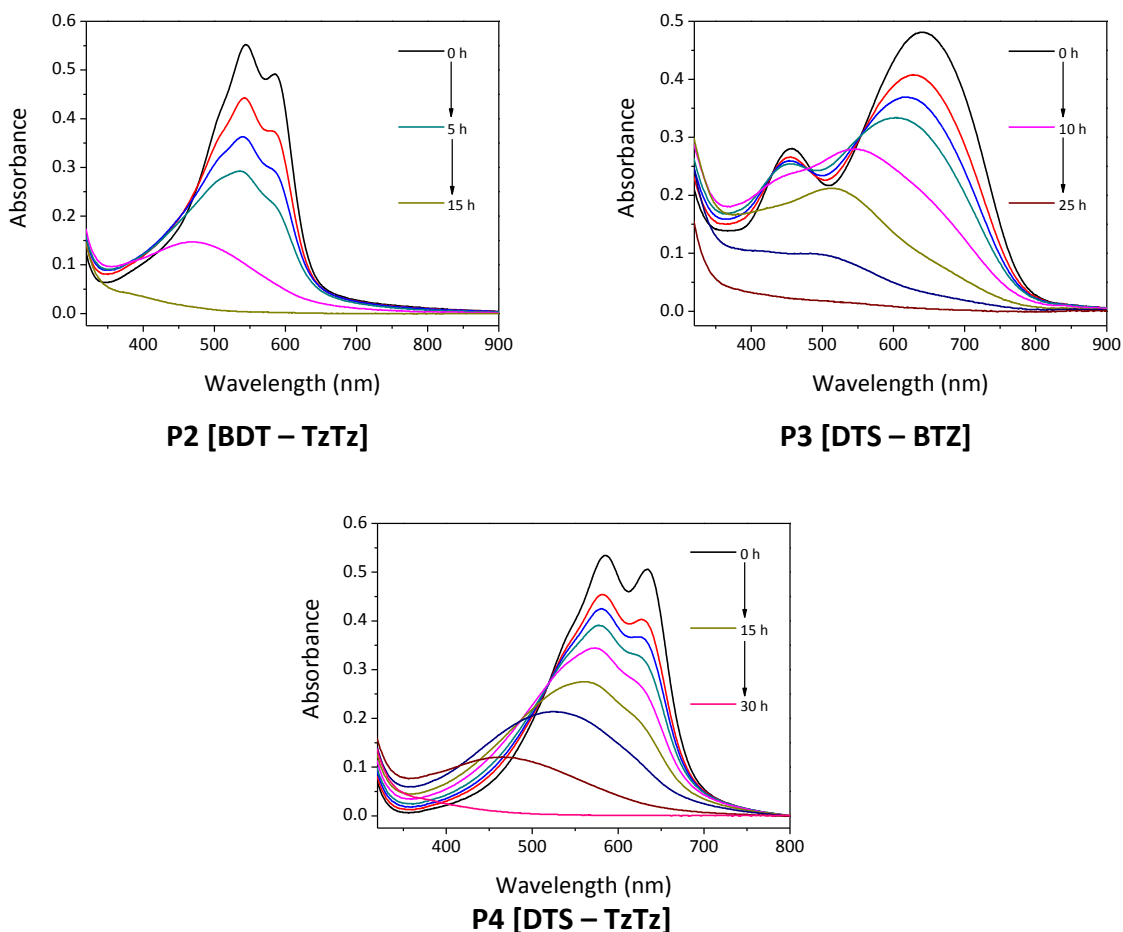
Figure 3.30. Absorbance decay for polymers P2-P4 exposed to photooxidative conditions.

(a)

(b)

Polymer	Rate / h^{-1}
P1	-0.0121 ± 0.0009
Si-PCPDTBT	-0.013 ± 0.003
C-PCPDTBT	-0.016 ± 0.001
P5b	-0.0190 ± 0.0006
P5a	-0.026 ± 0.004
P4	-0.0263 ± 0.0008
P5c	-0.028 ± 0.003
P3HT	-0.036 ± 0.005
P3	-0.0474 ± 0.0005
P2	-0.059 ± 0.001
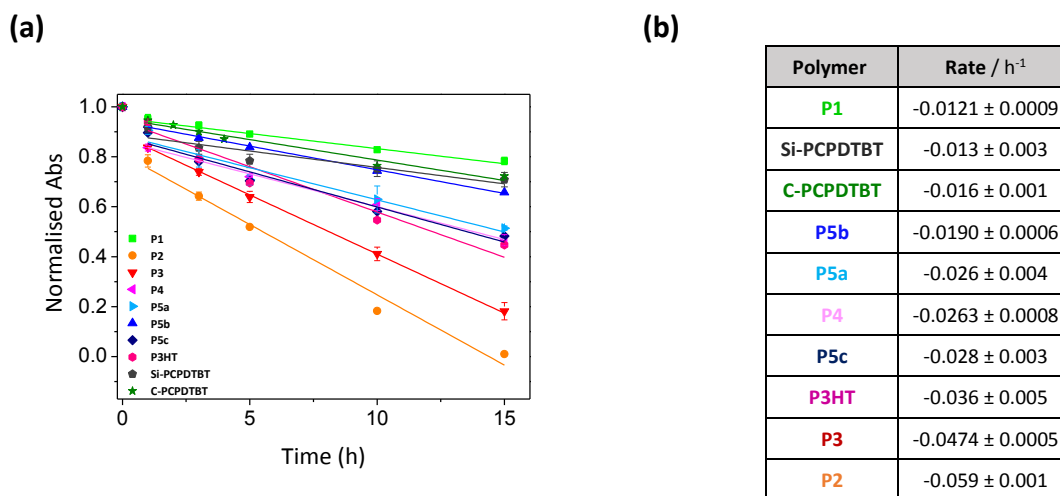
Figure 3.31. (a) Normalised absorbance decay at the maximum absorption wavelength for the different polymers exposed to photooxidative conditions, together with the corresponding linear fits. (b) Calculated slopes obtained from the linear fits of the data between t_{1h} and t_{15h}.

3.3.2.2.2. <u>Polymer thermooxidation</u>

The photochemical stability of the polymers was then compared to their thermal behaviour in the presence of oxygen. To this end, polymer thin films were aged in a thermoregulated oven at 100 °C. Similarly to what was observed when the films were degraded photochemically, the thermal treatment provoked a continuous loss of UV-Vis absorption of the polymer films (see Figure 3.32). However, this occurred at lower rates than photooxidation in all cases [see Figure 3.31 (b) and Figure 3.32 (b)]. Indeed, thermooxidation brings down the degradation rates to very similar values for all the polymers (on average $r_{thermoox}$ = -0.012 h^{-1}). A clear deviation from this behaviour is P5a, which was particularly unstable under these conditions compared to the other polymers, degrading at a rate of -0.021 h^{-1}.

(a)   **(b)**

Polymer	Rate / h^{-1}
Si-PCPDTBT	-0.008 ± 0.001
P1	-0.0090 ± 0.0008
C-PCPDTBT	-0.0092 ± 0.0009
P5b	-0.011 ± 0.001
P3	-0.0113 ± 0.0008
P5c	-0.0124 ± 0.0009
P3HT	-0.013 ± 0.001
P2	-0.013 ± 0.002
P4	-0.015 ± 0.002
P5a	-0.021 ± 0.005
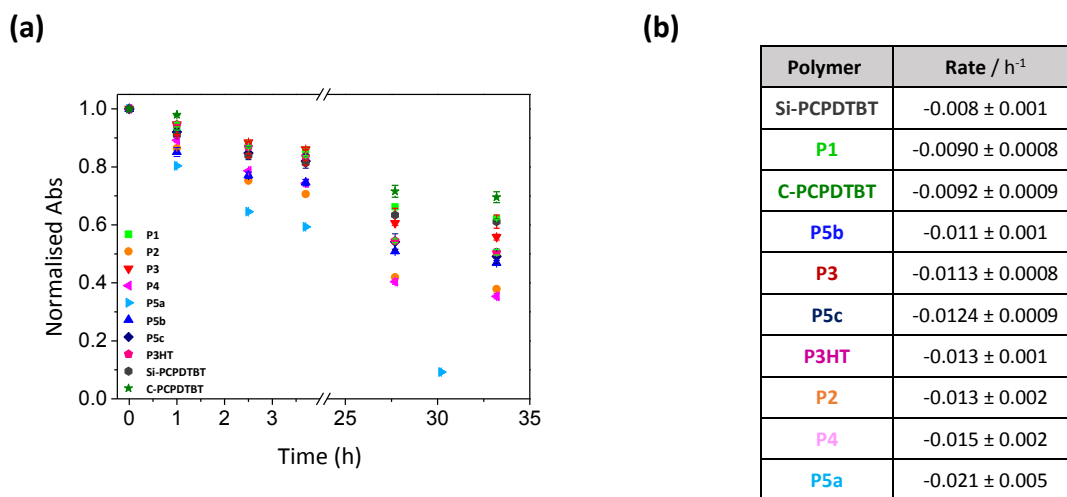
Figure 3.32. (a) Normalised absorbance decay at the maximum absorption wavelength for the different polymers exposed to thermooxidative conditions (100 °C). (b) Calculated slopes obtained from the linear fits of the data between t_{1h} and t_{35h} (linear fits not shown).

The general observation concerning the existence or absence of a blue-shift for samples during photooxidation is still valid for the polymers under thermooxidative conditions (*i.e.* blue-shift only observable for P2-P4). Interestingly, the polymers of the P5 series exhibited a particular behaviour when thermally annealed in air, as illustrated in Figure 3.33. In contrast to the continuous decay of both polymer absorption bands (around 800 nm and 450 nm), as recognised in photooxidation, thermal degradation induced the vertical decay of only the band at higher wavelength (800 nm, corresponding to the ICT donor-acceptor), whereas the band at 450 nm ($\pi \rightarrow \pi^*$ transitions) increases with time. This is clearly exemplified by t_{25h} in Figure 3.33 (b), in which, despite the total disappearance of the band at 800 nm, an increased absorbance around 0.15 of the band at 450 nm is evident.

(a)   **(b)**
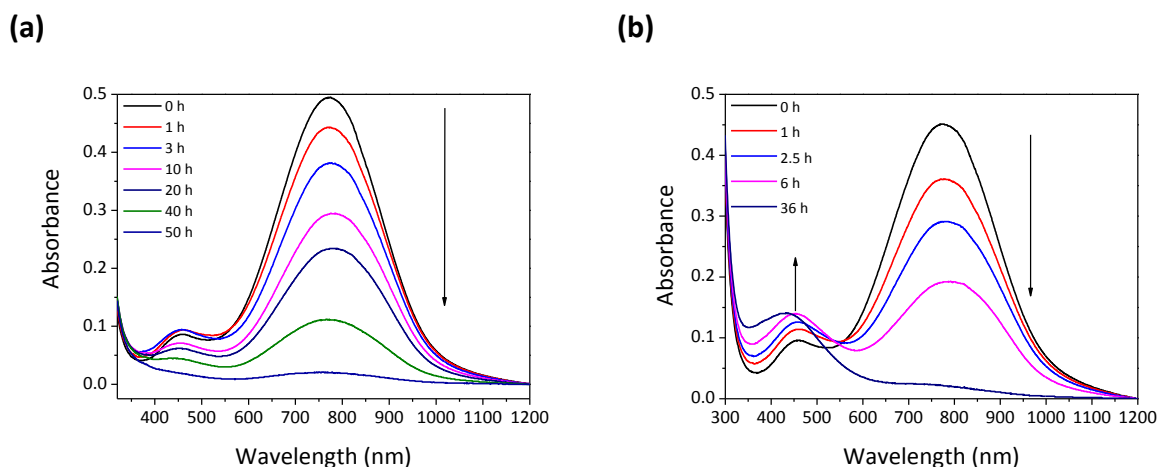
Figure 3.33. Absorbance decay for P5a under photooxidative (a) and thermooxidative (b) conditions. This behaviour is representative of the entire P5 series.

3.3.2.2.3. Discussion

Polymers photooxidation: influence of the structure

The polymers under study exhibited differences in terms of their photooxidation rates, and could be classified into different groups depending on their photostability, see Table 3.8. Looking at the polymers with high photostability, P1 (BDT-DTBT) and P5b (DTS-DPP), these two polymers do not have any structural units in common. Indeed, different donor-acceptor combinations yield polymers that can be classified into different stability groups; for instance, DTS-based polymers can be stable (P5b), intermediately stable (P5a, P5c), and rather unstable (P3).

Table 3.8. Classification of the photochemical stability of the low bandgap polymers under study.

Stability	Polymer	Donor	Acceptor
High (~Si/C-PCPDTBT)	**P1**	BDT	DTBT
	P5b	DTS	DPP
Intermediate (~ P3HT)	**P5a**	DTS	DPP
	P4	DTS	TzTz
	P5c	DTS	DPP
Low (< P3HT)	**P3**	DTS	DTBT
	P2	BDT	TzTz

Interestingly, P3 is structurally similar to one of the most stable polymers analysed, namely Si-PCPDTBT. These two polymers rely on the combination of DTS (donor) and BT (acceptor), and the

only difference between them is the incorporation of alkyl-substituted thiophene moieties as spacers in the acceptor unit of P3. According to the reported photooxidation mechanism of P3HT, the addition of two substituted thiophenes could be a source of instability of the resulting polymer, since radical formation *via* hydrogen abstraction in the alpha position of a thiophene is highly favoured.[214] Indeed, in the stability raking established in this study, P3 does exhibit lower photostability than P3HT, reinforcing the idea of the DTBT unit being a source of instability. However, this acceptor is also contained in P1, which is, in turn, the most stable polymer in these series. It could be then proposed that the donor BDT has an extremely high intrinsic photostability, making the combination of BDT-DTBT in P1 very stable despite the alkyl-substituted thiophenes of the DTBT unit. However, this argument is completely refuted by the fact that the other BDT polymer analysed in this series, P2, was the most unstable.

This clearly exemplifies the difficulty in attributing the higher or lower photostability of a low bandgap polymer to the presence or absence of a certain building block. For the analysed polymers, photostability seems to be determined by a certain donor-acceptor combination rather than caused by the specific stability or instability of a certain building block. However, this might not be the case for some other polymers (outside of this investigation) actually containing structures very prone to degradation. These results contrast with the 'rule of thumb' proposed by Manceau *et al.*,[210] actually establishing a stability ranking for different donor and acceptor units. Taking a closer look at their study, it is noticed that, consistent with the results herein, a same donor unit can lead to very distinct photodegradation rates depending on the acceptor it is coupled with (and *vice versa*). This is exemplified by the t_{80} values (time at which 20 % of the initial absorbance is lost) observed for the DTS-based polymers, which is clearly different depending on the acceptor. Indeed, DTS coupled with dithienylthienopyrazine displays t_{80} ~75 h (or even ~150 h if the side chains in the acceptor unit are thermally cleaved), whereas the DTS-DTBT combination leads to t_{80} < 10 h, in line with the results herein presented for P3 (see Figure 3.31). Nevertheless, this paper provides consistent data concerning the modifications in stability due to structural variations. For instance, a systematically higher relative stability is observed for Si-bridged *versus* C-bridged CPDT donors, independent of the chosen acceptor units. In contrast to these results, and as mentioned in Section 3.3.1.3.3, several studies on the comparison of Si-PCPDTBT and C-PCPDTBT actually attribute a higher photostability to the carbon analogous,[237, 278] clearly indicating that, in addition to the chemical structure, other parameters can effectively determine the stability of the polymers.

The results presented herein concerning the photooxidation of Si-PCPDTBT and C-PCPDTBT indicate that both polymers display a similar degradation rate, at least for the analysed interval, in contrast to what observed in the literature.[237, 278] Comparing the results herein to the work of Aygül *et al.*, Si-PCPDTBT exhibited a very similar photodegradation rate (0.013 h^{-1}) to the value they obtained for the decay of the band at 694 nm (0.014 h^{-1}). However, the degradation rate for C-PCPDTBT (0.0054 h^{-1}), was more than half of the value calculated in the study herein (0.016 h^{-1}). Seemingly, the intrinsic photostability of these two polymer films is not drastically different, since the results are on the same order of magnitude in both cases. Thus, slight differences in the processing conditions, irradiation or data treatment can effectively modify the obtained results. For example, Aygül *et al.*[278] compared films of initial Abs ~1, whilst the films in our study were of Abs ~0.5. Notably, the coincidence between the values obtained for Si-PCPDTBT in both studies, despite the differences in thickness, supports the idea discussed in Section 3.3.1.3 about an absolute degradation rate for Si-PCPDTBT in this absorbance interval. Additionally, EPR characterisation of the different polymers allowed the identification of a high content in paramagnetic species in C-PCPDTBT (and P5a) compared to the rest of the polymers (see Figure 3.26). These species could be potentially photochemically activated, thus explaining the higher photodegradation rate obtained for C-PCPDTBT in our study.

In general, and according to literature,[210, 232] reducing the number of solubilising alkyl side chains seems a reasonable strategy for increasing the photochemical stability the polymer. In this sense, limiting the attachment of alkyl side chains uniquely to the donor unit (as exemplified in the structure of the Si(C)-PCPDTBT polymers, see Figure 3.25) *or* the acceptor unit seems desirable for improving the stability of the resulting polymer. The position (and nature) of such side chains in the quest for more stable polymers and solar cells is, however, not a trivial topic, and has received considerable attention over the past years.[210, 232, 283-286] Very generally, and uniquely considering photochemical degradation *via* predominant radical chain oxidation, the attachment of an alkyl side chain to an electron-rich donor unit would only favour radical creation (since the created radical can be readily stabilised). According to this, side chains should be attached to an electron deficient moiety, which would induce lower stabilisation of the created radical. In addition, it should play a role if the side chain is attached directly to a sp^2 carbon involved in the conjugated system, or a sp^3 hybridised atom which consequently cannot stabilise a radical mesomerically. Nonetheless, the role of the side chains in the photochemical degradation is beyond the scope of this work, and has been separately

addressed in a joint study with Aurélien Tournebize and Dr Graham E Morse (ESR10 and ER3 in the ESTABLIS project, respectively).[285]

Polymers photooxidation: crystallinity of the films

A clearer correlation between the photooxidation kinetics and the absorbance loss (in terms of the aforementioned blue-shift) is obtained if one takes into account the crystalline properties of the films according to the XRD data in Figure 3.28. Whereas the low crystallinity polymers are in the range medium to low photostability (P2, P3, P4), more crystalline P5a-c and P1 are located in the range medium to high stability (see Table 3.8). Furthermore, this classification is coincident with the presence or absence of a blue-shift; *i.e.* a blue-shift was observed for polymers P2, P3, and P4, whilst an absence of blue shift was evident for P1 and the polymers in the P5 series (see Figure 3.29 and Figure 3.30). As aforementioned, a higher level of crystallinity is associated with a higher resistance to photooxidation. Several explanations have been proposed in the literature to explain this behaviour. Dupuis *et al.*[181] have indicated that the more crystalline phases exhibit lower oxygen-permeability in comparison to the amorphous ones, thus reducing the quantity of oxygen able to irreversibly degrade the polymer. Besides, a higher level of triplets in the amorphous regions could also explain the higher reactivity in less crystalline films. Hintz *et al.*[233] have proposed that overall longer conjugation lengths are achieved for more crystalline films, leaving less non-conjugated points for attack of oxygen. In line with the assumption of higher conjugation lengths achieved for the more crystalline films, the typical blue-shift of the absorption peak, indicative of loss of π-conjugation, has been found to appear earlier for more disordered (amorphous) films.[233] This correlation between crystallinity and blue-shift is coincident with the trend obtained in the study herein presented.

Concerning the polymers in the P5 series with different side chains linked to the nitrogen in the lactam units, medium to low photooxidation rates were observed (r_{P5b} = -0.0190 h^{-1}, r_{P5a} = -0.026 h^{-1}, r_{P5c} = -0.028 h^{-1}). Interestingly, according to the XRD data in Figure 3.28, the most stable P5b displays a peak at 2θ = 5.5 ° corresponding to an interchain distance of 16 Å, whilst for the others (P5a, P5c) distances were slightly longer. Indeed, P5b contains a shorter side chain than P5a and P5c. Presumably, the denser packing achieved for P5b explains the higher stability achieved compared to the other DTS-DPP polymers. Finally, the higher content in organic paramagnetic species as calculated by EPR in for P5a (see Figure 3.26) does not seem to significantly affect the photochemical behaviour

of the polymer, since the calculated photooxidation rates are of the same order as the rest of the P5 polymers.

Thermal oxidation

Compared to photooxidation, the thermooxidation rates are very similar for the analysed polymers, as illustrated in Figure 3.34. All of the polymers display similar thermooxidation rates (around 0.012 h^{-1}), with the exception of P5a (0.021 h^{-1}). This is attributed to the aforementioned content in (organic) paramagnetic species in this polymer (see Figure 3.26) is responsible for this behaviour. Since the photooxidation rate is not drastically different from that of other P5 polymers, these species seem to be thermally initiated only. Furthermore, the significantly disparate values between the photooxidation and thermooxidation rates for polymers P2, P3, and P3HT indicate that photoinitiated processes (either reaction with oxygen species or light absorption by chromophores present in the polymer) are significantly effective for the degradation of these polymers. Interestingly, no structural accordance is observed for the three polymers (P2, P3, and P3HT) for which this effect is markedly higher, see Figure 3.24.
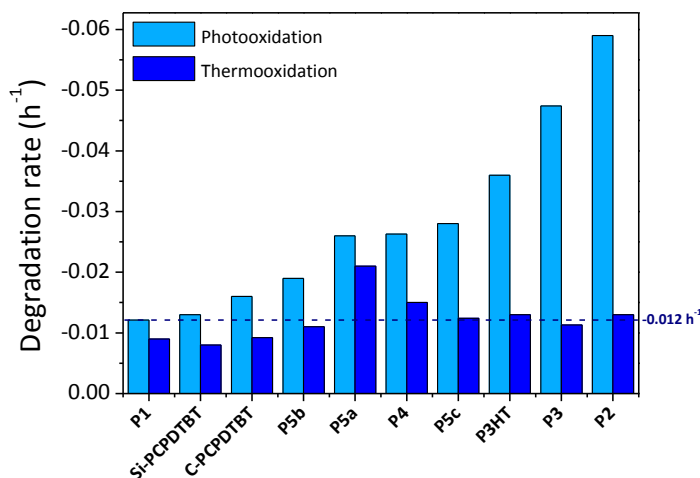
Figure 3.34. Comparison of the photo- and thermooxidation rates of the analysed polymers.

Concerning the thermooxidative behaviour of the P5 series, higher thermal stability of one of the building blocks (*i.e.*, DTS *or* DPP) is assumed. Indeed, the rapid destruction of one unit over the other upon thermooxidation would explain the absence of intramolecular charge transfer (leading to absorption at higher wavelengths, 800 nm), whereas the absorption at lower wavelengths indicates the existence of remaining π-conjugated material in the sample. Since this behaviour is uniquely observed

for the P5 series, it would appear that the DPP unit (only present in the P5 polymers) is the responsible for this behaviour.

3.3.2.3. Evaluation of blend stability

3.3.2.3.1. Blend photostability in air

In order to obtain relevant information about how these low bandgap polymers would behave when incorporated into solar cells (in terms of photochemical stability), the effect of neighbouring PCBM needs to be considered.[238] To this end, polymers were blended with PCBM at a 1:2 ratio, and the resulting thin films were aged using light under ambient air conditions (photooxidative conditions). As observed for the polymer films, irradiation provoked a decrease in the UV-Vis absorption bands with destruction of the π-system of the polymer. However, this occurred at different (and generally lower) rates compared to the photooxidation of the neat polymers, see Figure 3.35. Importantly, the C-PCPDTBT:PCBM blend actually degrades faster than the polymer on its own, in line with the literature.[237] Furthermore, upon addition of PCBM, the stability order established for the polymers is not maintained, which underlines the versatile nature of the effect of PCBM on different polymers regarding stabilisation and destabilisation.

(a)   **(b)**

Polymer	Rate / h^{-1}
P1	-0.0033 ± 0.0007
P5a	-0.005 ± 0.002
P5c	-0.0063 ± 0.0008
P2	-0.0074 ± 0.0006
P3HT	-0.0085 ± 0.0003
Si-PCPDTBT	-0.010 ± 0.002
P5b	-0.011 ± 0.002
P4	-0.0173 ± 0.0009
C-PCPDTBT	-0.027 ± 0.004
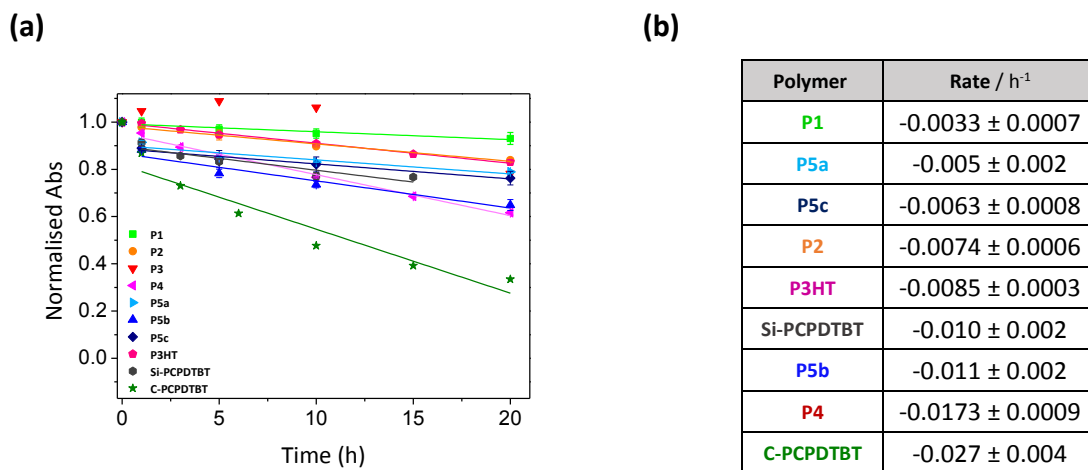
Figure 3.35. (a) Normalised absorbance decay at the maximum absorption wavelength for the different blends exposed to photooxidative conditions, together with the corresponding linear fits. (b) Calculated slopes obtained from the linear fits of the data between t_{1h} and t_{20h}.

It must be noted that the degradation rate of P3:PCBM has not been calculated due to the hypsochromic effect observed for this blend when exposed to light. After very short exposure (1 h), the band at 630 nm completely shifted to lower wavelengths, after which, bleaching of the sample followed, see Figure 3.36. In this work, efforts have been unsuccessfully undertaken to recover the

initial position of the absorption band by applying thermal stress or irradiating the sample with monochromatic light, in line with studies on other compounds exhibiting photothermal isomerisation.[287] Besides, the fact that this effect is only observed in the presence of PCBM suggests involvement of the fullerene acceptor in a possible macromolecular reorganisation leading to the shift to lower wavelengths. Although very interesting, to date no satisfactory explanation for the observed behaviour has been found. Nevertheless, this result highlights the value of measurements on separate active layers (in addition to the individual components), which can provide with useful information about unexpected behaviour upon testing the electrical performance of the corresponding devices.
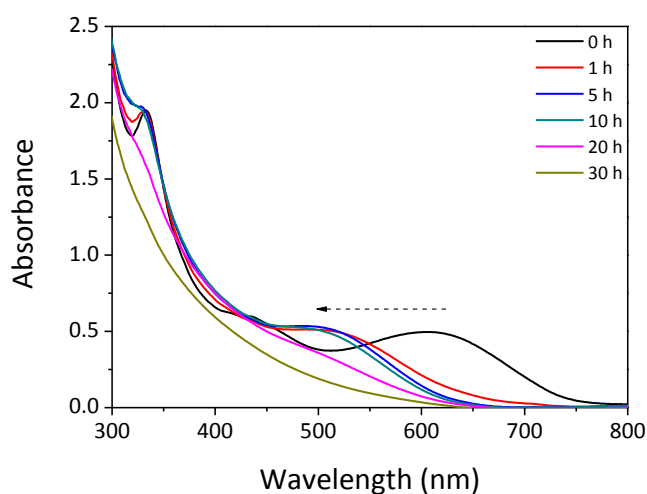
Figure 3.36. Hypsochromic shift observed for P3:PCBM when exposed to light and oxygen.

3.3.2.3.2. Blend photostability under vacuum

The prediction of the stability of the solar cells based on these polymers was examined further by analysing the photostability of their blends with PCBM under vacuum (low oxygen content), emulating the behaviour of barrier-encapsulated solar cells. Under these conditions, the degradation of the polymer is no longer the bottleneck in terms of photodegradation, see Figure 3.37 (a). In fact, the band corresponding to the polymer remains untouched, and only a modification in the UV domain (rise of the absorption at 320 nm) can be observed. This modification in the UV region has been identified in the literature as the dimerisation of the fullerene.[238, 243]

Distler *et al.*[238] have reported that the rate and extent of dimerisation correlates with the average size of the polymer and fullerene domains; in fact, well distributed domains of appropriate length lead to higher extents of dimerisation. Accordingly, the extent of dimerisation, calculated as the

relative increase in absorbance at 320 nm, was measured in order to characterise the miscibility of the different polymers with PCBM. This is summarised in Figure 3.37 (b). According to these results, the lowest extents of dimerisation were observed for C-PCPDTBT, P3 and Si-PCPDTBT, followed by P2, P4 and P5, and the highest being P1 and P5a.

(a)

(b)
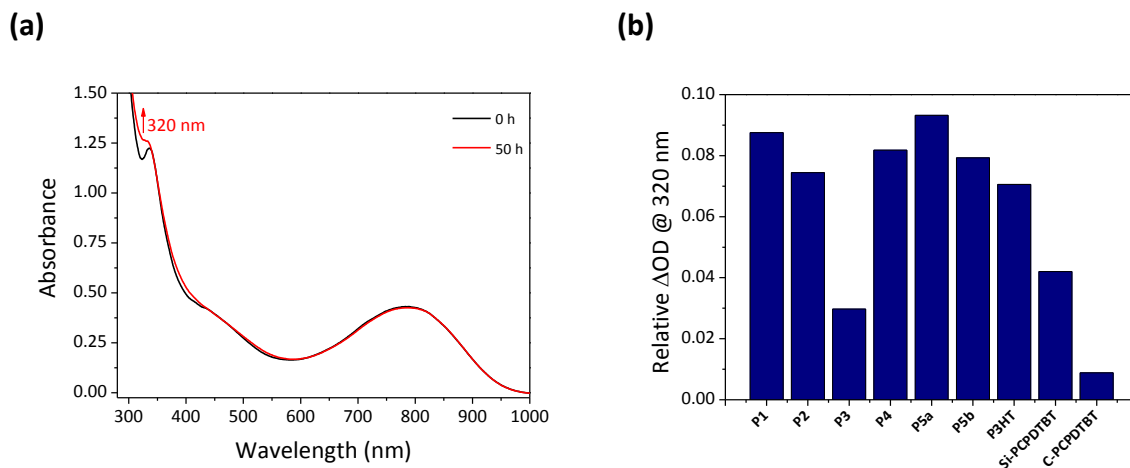
Figure 3.37. (a) Sample of P5a exposed to light in absence of oxygen (under vacuum). (b) Extent of dimerisation, calculated as the relative increase in absorbance at 320 nm.

3.3.2.3.3. Discussion

The study of the photooxidative behaviour of the polymer upon addition of PCBM completely modified the previously established photooxidation trends, as shown in Figure 3.38 (a), summarising the photooxidation rates of all the polymer and blends with PCBM. For instance, P2, identified as the most unstable polymer upon photooxidation, is highly stabilised by PCBM (stabilisation factor ~8) leading to a photooxidation rate comparable to that of the blends of the P5 series or P3HT, for instance. Furthermore, the photooxidation of C-PCPDTBT (among the most stable polymers upon photooxidation) is actually accelerated by PCBM (destabilisation factor ~2), making the combination C-PCPDTBT:PCBM the most unstable in the blend series. Importantly, P1 is identified as a very robust material, behaving very consistently and exhibiting low photooxidation rates in all cases (neat or blended with PCBM).

Accordingly, the difficulty in relating photostability of a low bandgap polymer to its structural characteristics is further increased when it is blended with PCBM. Once again, no particular relationship can be established between the structure and the resulting blend photooxidation rates. Furthermore, upon addition of PCBM, the considerations established in Section 3.3.2.2.3 regarding the clear

relationship between crystallinity and stability can be called into question. Indeed, the amorphous P2 is stabilised by PCBM, reaching a similar stability to more crystalline blend combinations such as the polymers in the P5 series. Furthermore, while the conditions utilised for processing P1 on its own created (semi)crystalline films (see Figure 3.28), XRD analysis of P1:PCBM (ratio 1:2) revealed an absence of diffraction peaks. Nevertheless, and as indicated above, this combination is the most stable, and this polymer, in general, is the most robust under the tested conditions. Independent of the verified 'good' behaviour under photooxidative conditions, if this material is to be employed in organic solar cells, optimisation of the processing leading to increased crystalline (of appropriate size) domains should be considered to lead to optimum charge transport and separation.

(a) **(b)**
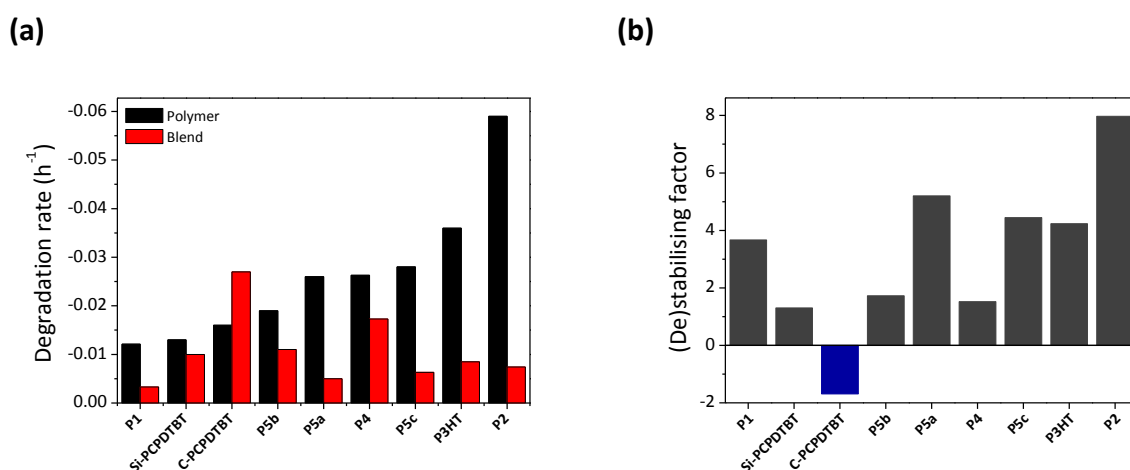
Figure 3.38. (a) Polymer and blend photooxidation rates. (b) Stabilising and destabilising factor imparted by PCBM when blended with the different polymers, calculated from the ratio of the rates in (a).

Overall, the effect of PCBM seems the most decisive parameter controlling the resulting photostability of the studied polymers. Discussed in Section 3.1.2.1, PCBM can impart several stabilising effects (radical scavenging, UV filtering, quenching of polymer singlet states) and destabilising effects, such as the sensitisation of reactive oxygen species.[237, 247-249, 251] Depending on which of these effects prevails for each specific polymer, their stability upon photooxidation when blended with PCBM can be drastically different.[237] Furthermore, although this section examines uniquely the effect of the commonly employed PCBM, different fullerenes can stabilise or destabilise the same polymer differently, mainly depending on the electron affinity of the fullerene derivative.[238, 247] It must be noted as well that fullerenes are not the only materials that can be used as acceptors in the active layer.[60]

Thus, the study of the photochemical stability of polymers for application in organic solar cells requires the consideration of the characteristics of the donor, the acceptor, and their combination.

In order to obtain information relevant to the photochemical stability of these blends under cells operating conditions, blend films were exposed to light irradiation while encapsulated under vacuum (thus reducing the presence of oxygen). Under these conditions, the degradation of the polymer is insignificant, as shown in Figure 3.37 (a). However, a rise in absorption at 320 nm caused by the dimerisation of PCBM is clearly visible, to different extents, for the majority of the samples (see Figure 3.37). This modification, although thermally reversible, can be considered as a solar cell degradation mechanism. In fact, PCBM dimerisation leads to a reduction in effective charge carrier mobility, and this is translated into a drop of solar cell efficiency mainly due to a loss of fill factor (FF) and short circuit current (j_{sc}). However, it is noteworthy that photoinduced dimerisation can be prevented when using other fullerene derivatives, such as $PC_{70}BM$ or bis-substituted fullerenes like ICBA.[238] Furthermore, some groups have reported the value of this reaction in the stabilisation of the active layer morphology,[245-246] in a way that long-term stability under thermal stress can be actually benefitted from this *a priori* detrimental mechanism.

The extent of dimerisation, calculated as the relative rise of the band at 320 nm (see Figure 3.37) was then employed to qualitatively assess the polymer/fullerene domain separation in the investigated blends. Distler *et al.*[238] calculated the extent of PCBM dimerisation when blended with four of the polymers in the series investigated herein, namely P4 (PDTSTzTz in their study), P3HT, Si-PCPDTBT, and C-PCPDTBT. Their obtained trend (C-PCPDTBT:PCBM < Si-PCPDTBT:PCBM < P4:PCBM < P3HT:PCBM) is similar to the trend observed in this study, although slightly higher extents of dimerisation with P4 were observed here, inverting the order at the end of the list. In their study, they attributed the supressed fullerene dimerisation to the finely dispersed morphology achieved when mixing C-PCPDTBT with PCBM. The increased dimerisation in the rest of the cases was then explained in terms of the growing domain sizes (Si-PCPDTBT:PCBM < P4:PCBM < P3HT:PCBM).[46] [288-289] Based on this assumption, P3 would favourably mix with PCBM, leading to not much domain separation, P2 and P5b would create bigger domains and especially high phase-separation would be created for P1 and P5a. Certainly, further investigations on this are needed to qualify and quantify the phase separation in each case, which, in turn, has a direct implication in charge separation and transport processes and blend stability.

In light of these results, it is clear that PCBM plays a vital role in the photostability of the different polymers. Whilst upon photooxidation conditions, photobleaching of the polymer prevails, under exclusion of oxygen, the observed degradation mechanism is ascribed to the dimerisation of PCBM. Overall, in addition to the selection of stable polymers (such as P1), the election of an appropriate fullerene acceptor is of prime importance. In this regard, fullerene acceptors are expected to both prevent dimerisation from happening and impart a stabilising effect on the photooxidation of the polymer when oxygen diffuses into the device. Given the dramatic effect that polymer photooxidation causes in the overall efficiency of the device,[16, 290] the identification of stable donor-acceptor combinations is mandatory to hamper these photoinduced processes.

3.4. Conclusions

The evolution of Si-PCPDTBT thin films under photooxidation conditions has been monitored using several analytical techniques in order to obtain a multiscale analysis from the molecular to the nanomechanical properties. Moreover, combining IR experimental analysis with modelling has allowed accurate elucidation of the radical photooxidation mechanism of Si-PCPDTBT. The results indicate that the polymer side chains that continuously degrade from the beginning of irradiation, evolve through the formation of chain oxidation products, crosslinking reactions and formation (and loss) of low molar mass oxidation products. The overall photodegradation process in the polymer backbone takes place *via* oxidation of the sulfur units of the thiophene rings, although bands related to the oxidation of the N and Si atoms could also be identified. The degradation rate of Si-PCPDTBT, measured in terms of the absorbed photons, is calculated faster when irradiating the samples using SEPAP 12/24 (higher in UV photons) compared to the commonly employed Suntest CPS/XLS. Interestingly, the absolute degradation rate (ΔAbs *versus* time) is identified independent from the initial thickness of the sample discarding light penetration as the rate-limiting factor. In turn, a layer-by-layer oxidation profile determined by oxygen diffusion is proposed. Finally, the absorbance loss in Si-PCPDTBT is found to be slower than that of other commonly employed p-type polymers, such as P3HT and PCDTBT. In order to explain this, the pertinence of employing silicon as a bridging atom for the solubilising alkyl chains was approached by comparing the macroradicals created upon hydrogen abstraction in the alkyl chain of both Si-PCPDTBT and the analogous C-PCPDTBT. The calculations revealed that the inclusion of Si as a bridging atom appears to be an interesting structural strategy, since macroradical creation after hydrogen abstraction is less favoured in this case.

Further insight into the parameters and structural factors influencing the polymer photostability in air was obtained from the analysis of a series of low bandgap polymers (P1 – P5c) with systematically modified backbones (P1 – P5) and/or alkyl side chains (P5a-c). The polymers under study exhibited photochemical stabilities similar to that of reference polymers such as Si(C)-PCPDTBT (polymers P1 and P5b) or P3HT (polymers P5a, P5c, P4), and especially low photostabilities (below that of P3HT) were found for P2 and P3. According to our results, the stability of each polymer is not determined by the presence of a certain donor or acceptor but is dictated by each specific donor-acceptor combination. However, more crystalline polymers films (such as P1 or the P5 series) present medium to high photostability, whereas more amorphous polymer films such as P4, P3 and P2 display medium to low photostabilities (the average value set by the photooxidation rate of P3HT).

The lack of crystallinity also correlates with the observation of blue-shifts in the UV-Vis spectra of the samples upon photooxidation. Furthermore, the higher content in organic paramagnetic species in P5a and C-PCPDTBT, as determined by EPR, is found to accelerate their thermooxidation and photooxidation rates, respectively.

Analysis of the photochemical behaviour in air of these polymers in the presence of PCBM reveals a complete modification of the relative stabilities of the different polymers, due to the stabilising and destabilising effects imposed by the fullerene derivative. This, in turn, further confirms the difficulty in establishing a relationship between the constitution of the polymer backbone and the resulting stability of each polymer. The photochemical treatment of the blends under vacuum caused, in all cases (but to different extents), dimerisation of PCBM, a process that has been also related to a drop in power conversion efficiency of the solar cells. Overall, the analysis of these polymers leads to the conclusion that the identification of a stable p-type polymer goes hand in hand with the selection of a suitable fullerene acceptor, able to both prevent dimerisation and stabilise the photooxidation rate of the active layer.

Chapter 4. Multiscale Approach to the Stability of Inverted Solar Cells: from the Polymer to the Cell

4.1. Introduction

Among the different degradation mechanisms present in organic solar cells (see Section 1.4.2), (photo)chemical and morphological processes occurring in the active layer can drastically affect the performance of the cell, as they directly affect the steps of the charge generation process.[6-7] Comprehensive understanding of these degradation mechanisms requires both the evaluation of the electrical parameters of the cells and analysis of single cell components or layers as they are influenced by relevant degradation triggers (*e.g.*, light or temperature, in this case). Furthermore, and in line with the main conclusions of Chapter 3, it is important to note that information about the degradation of low bandgap polymers can only be extrapolated to the behaviour of the corresponding cells when the actual constitution of the blend (*i.e.*, a certain polymer-acceptor combination) is considered. In this context, this chapter reports the use of a multiscale analysis to the photothermal degradation processes occurring in the active layer of P4:PCBM-based inverted solar cells, by evaluating the degradation of polymer films, blend films, and inverted solar cells subjected to several degradation conditions (see Figure 4.1).

The first part of the chapter is devoted to the elucidation of the degradation pathways of low bandgap poly[4,4'-bis(2-ethylhexyl) dithieno[3,2-b:2',3'-d]silole)-2,6-diyl-*alt*-[2,5-bis(3-tetradecyl-thiophen-2-yl)thiazole[5,4-d]thiazole)-1,8-diyl], denoted as P4 in the polymer series studied in Section 3.3.2, and its blend with PCBM. To this end, chemical and morphological modifications in P4 and P4:PCBM thin films were probed using UV-Vis and IR spectroscopy, as they were treated using both artificial ageing conditions and natural outdoor illumination. Concerning the former, films were irradiated (Suntest CPS/XLS Atlas) and thermally treated (thermoregulated oven at 100 °C) in the presence of oxygen, in so-called photooxidation and thermooxidation experiments, respectively. Comparison between photo- and thermal oxidation of polymer and blend films was employed to identify the main mechanisms responsible for the oxidation of both the polymer and blend films. Additionally, samples were sealed under vacuum to resemble the behaviour of encapsulated solar cells. Irradiation and thermal treatment of encapsulated samples were used to obtain information about processes induced by mere light and temperature exposure. Finally, illumination of vacuum-encapsulated thin films in natural outdoor exposure was employed to assess if the artificial ageing conditions are representative of natural irradiation and to establish a correlation between the degradation rates in both cases.

In the second part of the chapter, the photostability of P4:PCBM-based solar cells in an inverted structure was examined by studying the j-V characteristics of the cells as a function of irradiation time. Firstly, the role of light in combination with oxygen was assessed by studying the photoelectrical behaviour of non-encapsulated cells illuminated in dry synthetic air. Secondly, cells were encapsulated using a flexible barrier foil in order to limit the effect of oxygen in the degradation process; after which, devices were illuminated and their electrical parameters were monitored over time. Furthermore, the influence that interlayers can have on cell degradation upon illumination was evaluated by preparing two sets of cells, either comprising ZnO or polyethylenimine (PEI) as electron transport layers. Finally, estimation of the cell lifetime under operating conditions was obtained by comparing the electrical behaviour of the cells to the degradation of polymer and blend films exposed to illumination under artificial and natural outdoor exposure. The general strategy followed in this chapter is illustrated in Figure 4.1.
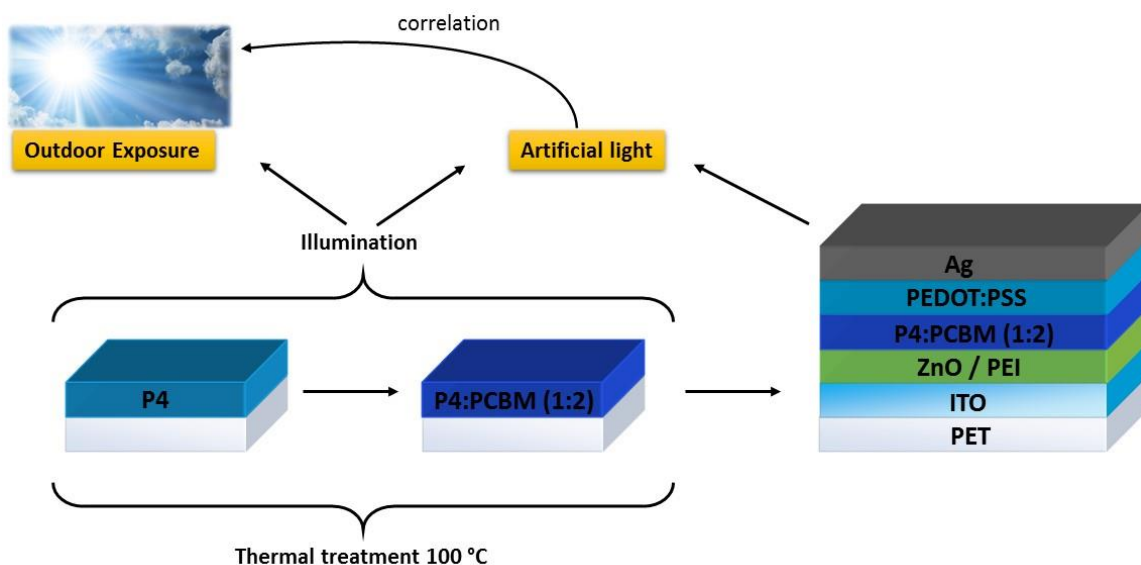
Figure 4.1. Multiscale approach to the stability of P4 and P4:PCBM films and P4:PCBM-based inverted solar cells.

4.2. Experimental

4.2.1. Materials

P4 (M_n = 45 kg mol^{-1}, Đ = 3.5) was synthesised by Dr Graham E Morse (ER3 in the ESTABLIS project) at Merck Chemicals, and was used without further purification. ZnO nanoparticle solution (5 % in ethanol) was obtained from IBUtec. Polyethylenimine (PEI) was purchased from Sigma Aldrich. PEDOT:PSS suspension (HTL Solar) was purchased from Heraeus GmbH. *Ortho*-dichlorobenzene (ODCB) HPLC grade (99 %), *para*-xylene HPLC grade (99 %), anhydrous *ortho*-xylene (97 %) and 1-methylnaphtalene (1-MN) (≥ 95 %) were obtained from Sigma Aldrich.

4.2.2. Methods

4.2.2.1. Sample preparation

4.2.2.1.1. Polymer and blend films

P4 films on KBr were prepared *via* doctor blading (Erichsen Coatmaster 809 MC) from a polymer solution 0.9 % (w/v) in *p*-xylene:*o*-dichlorobenzene (7:1). The solution stirred overnight at 100 °C, after which, films of absorbance 0.5–0.7 were prepared. Active layer films were coated on KBr using doctor blading, from a solution P4:PCBM (1:2) in a solvent mixture o-xylene:1-MN (95:5), total solids concentration 3 % (w/v). The solution stirred overnight at 120 °C prior to deposition, and the absorbance of the prepared films was 0.7-0.8. Deposition of the active layers was followed by 5 minutes of thermal annealing at 130 °C.

4.2.2.1.2. Inverted solar cells

Solar cells in an inverted structure were processed on flexible substrates (PET), according to the following structure: PET-ITO/ETL/AL/HTL/Ag. All layers, namely electron transport layer (ETL), active layer (AL), and hole transport layer (HTL), were deposited by doctor blading at ambient atmosphere (in cleanroom environment). The employed ETL was ZnO or polyethyleneimine (30 cells of each variation were prepared) and the hole transport layer was PEDOT:PSS. The active layer composition was P4:PCBM (1:2), Abs ~0.7 – 0.8, and it was processed according to the parameters specified above for the preparation of blend films. Deposition of the active layer was followed by 5 min of thermal annealing at 130 °C. A silver top electrode (500 nm) was deposited by evaporation, and the active layer of the cells was 27 mm^2. Cells were encapsulated at ambient atmosphere using a flexible barrier foil by Mitsubishi with a WVTR of ~3 10^{-3} g m^{-2} day^{-1}. For photooxidation experiments, a set of

16 cells with PEI used as electron transport layer and a permeable silver top electrode of only 50 nm thickness was prepared.

4.2.2.2. Sample ageing

4.2.2.2.1. <u>Photochemical degradation</u>

Illumination of polymer films, blend films, and encapsulated solar cells was performed using a Suntest CPS/XLS Atlas device, provided with a Xenon lamp from ATLAS (NXE1700) configured at 750 W m^{-2} (300 – 800 nm); a filter cutting off IR irradiation and UV photons below 300 nm. A thermostat maintained the Black Standard Temperature (BST) at 60 °C, corresponding with a chamber temperature of 35 °C. Photooxidation experiments were carried out in ambient air conditions, therefore in presence of oxygen. Photolysis experiments, corresponding to irradiation in absence of (or with strongly reduced) oxygen content, were performed in glass-encapsulated samples subjected to secondary vacuum (10^{-6} Pa). Samples were encapsulated, illuminated, analysed, and resealed under vacuum after each measurement. 'Control' films on KBr were only analysed initially and at the final degradation step, to determine and/or avoid the possible error caused by the encapsulation and measurement of the samples at each time step. Photolysis experiments were carried out in the Suntest device and exposing the samples to solar irradiation under natural conditions (Clermont-Ferrand, France) over a 10 months period between October 2014 and September 2015. Illumination of cells under photooxidative conditions was carried out exposing them to a steady flow of dry synthetic air while being irradiated with a metal halide lamp at an intensity of 1000 W m^{-2}.

4.2.2.2.2. <u>Thermal degradation</u>

Polymer and blend thermal ageing experiments were performed in a thermoregulated oven at T = 100 °C. Samples were irradiated both in the presence and absence of oxygen (thermooxidation and thermolysis, respectively), the latter encapsulated under vacuum as described for the photolysis experiments.

4.2.2.3. Sample characterisation

4.2.2.3.1. <u>Spectroscopies</u>

UV-Vis absorption spectra were registered using a Shimadzu UV-2600 spectrophotometer provided with an integration sphere. Infrared transmission spectra were recorded by a Nicolet 760 Magna spectrophotometer purged with dry air (32 acquisitions and 4 cm^{-1} resolution).

4.2.2.3.2. <u>Electrical Measurements</u>

Current-voltage characteristics of the solar cells were recorded under a calibrated solar simulator providing 1 sun (AM 1.5, 1000 W m^{-2}) using a Keithley 2400 Source Measurement Unit in combination with a Keithley 7001 Multiplexer system and custom software.

4.3. Results and discussion

4.3.1. Degradation of P4 and P4:PCBM films upon artificial and natural exposure

4.3.1.1. Initial characterisation

Firstly, pristine polymer and blend samples were spectroscopically characterised. As shown in Figure 4.2, P4 displays a main absorption band at around 600 nm, with two local maxima at 580 and 630 nm, together with a low absorption band (due to $\pi \rightarrow \pi^*$ transitions) at 280 nm. Mixing P4 with PCBM slightly shifts the main polymer absorption band to higher wavelengths (maxima at 590 and 640 nm); in addition, the absorption bands of PCBM (215, 265 and 335 nm) can be clearly distinguished. It is to note that conditions for processing the blend in this chapter and in Chapter 3 (see Section 3.2.2.1) were not identical. Herein, a different solvent system was used [*o*-xylene:1-MN (95:5)], and an annealing step (5 min at 130 °C) was applied after depositing the film to optimise the morphology. In fact, this same procedure was applied in the fabrication of the solar cells in Section 4.3.2. Although no significant differences were observed on the shape of the UV-Vis spectra of the P4:PCBM blends in both chapters (other than the different initial absorbance), the different processing conditions can indeed have an influence on the resulting morphology and/or crystallinity of the films. As a result, this can affect the response of the blend films to the different degradation treatments.
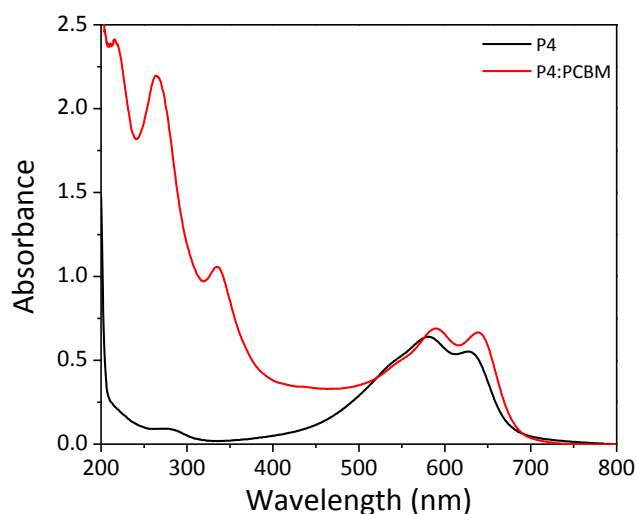
Figure 4.2. UV-Vis absorption spectra of pristine P4 (black line) and P4:PCBM (red line).

Polymer and blend films were also characterised using IR spectroscopy [see Figure 4.3 (b)]; the most characteristic IR bands were assigned according to the calculations performed in Section 3.3.1 and consulted literature,[223, 248, 291-293] as summarised in Table 4.1. The chemical structures of P4 and PCBM have been reproduced in Figure 4.3 (a) to enable the reader a better understanding of the IR assignments. In accordance with other studied p-type polymers, P4 is characterised by an intense band in the interval 2850 – 2950 cm^{-1} due to the aliphatic side chains, together with multiple vibrations in the fingerprint region (1500 – 500 cm^{-1}). Overall, the IR spectrum is similar to that of Si-PCPDTBT (see Figure 3.12) since the individual backbone constituents are also similar in both cases. On the one hand, the donor unit, dithienosilole, is the same in both P4 and Si-PCPDTBT. On the other hand, the acceptor unit in P4 is based on thiazolothiazole (with two thiophene spacers), whereas in Si-PCPDTBT, the acceptor unit is a benzothiadiazole group (and no spacers).

(a) **(b)**
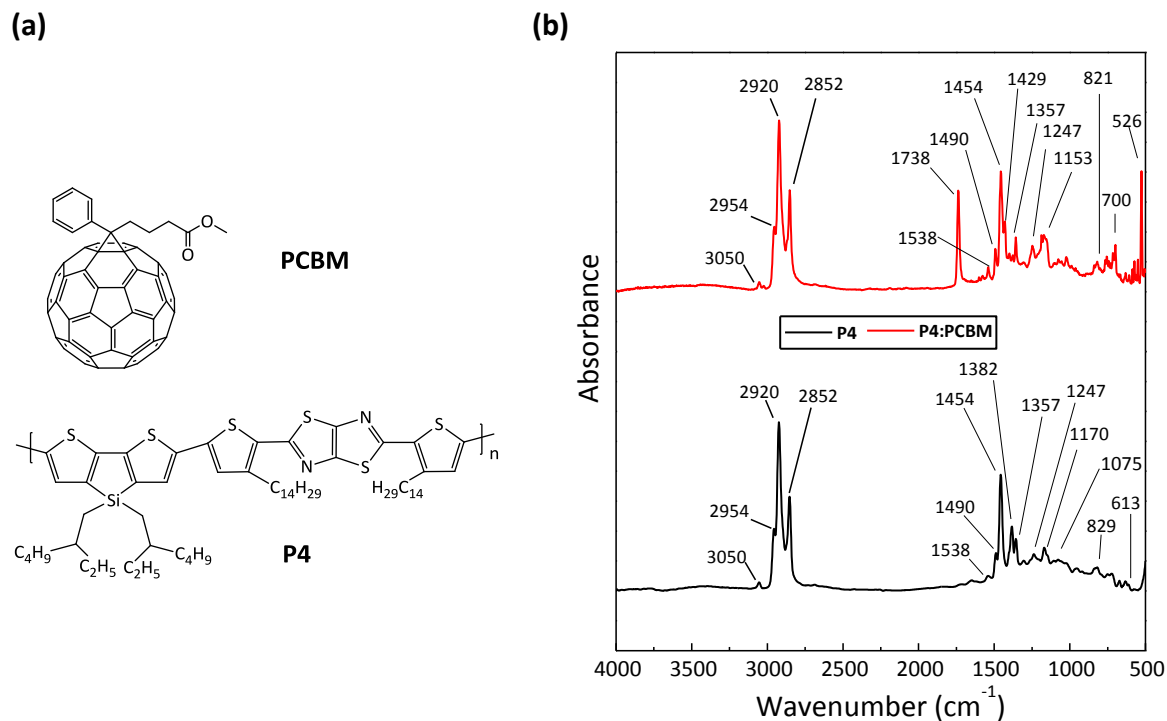
Figure 4.3. (a) Chemical structure of PCBM and P4. (b) IR spectra of pristine P4 (black line) and P4:PCBM (red line), including the labelling of main absorption bands. Traces have been translated along the 'absorbance' axis for clarity purposes.

Table 4.1. Attribution of the IR bands in P4 and PCBM.

$\tilde{\nu}$ / cm^{-1}	Assignment	
	P4	PCBM
526		C$_{60}$ (vibration skeleton)
573		C$_{60}$ (vibration skeleton)
613	ω thiophene rings	
698		δ (out-of-plane) aromatic C-H
742		δ (out-of-plane) aromatic C-H
794	thiophene rings deformations + C$_4$Si ω + C-H wagging thiazole	
829	pulsation thiophene ring	
881	δ thiophene ring + ν_{CS} thiophene + ν_{C-Si} ring deformation + thiazole ring deformation	
1075	β (C-H) thiophene and thiazole rings	
1105	α_{CCC} rings + δ_{CH} alkyl chains ν_{CC} rings + δ_{CH} alkyl chains	
1153	pulsation thiazole cycle	ν C-O Ester
1187		C$_{60}$ (vibration skeleton)
	δ_{CC} thiophene ring + δ_{C-H} alkyl chain	
1247	'breathing' C$_4$Si cycle + δ_{C-H} alkyl chain + C-H rocking thiazole	ν C-O ester
1357	$\nu_{a,C=C}$ C$_4$Si ring + $\nu_{C=C}$ all rings	
1382	$\nu_{C=N}$ thiazole	
1429		C$_{60}$ (vibration skeleton)
1454	$\nu_{C=C}$ all rings	
1490	$\nu_{C=C}$, $\nu_{C=N}$ fused dithiazole	ν C-C fullerene
1538	ν dithiazole cycle	
1738		ν C=O ester
2852	ν_s CH$_2$	
2920	ν_a CH$_2$	
2954	ν_a CH$_3$	

Importantly, the alkyl signal (~2850 – 2950 cm^{-1}) is especially intense in P4 due to the presence of four solubilising chains, namely the two branched ethylhexyl chains attached to the Si in the DTS unit, and another two linear tetradecyl chains directly linked to the conjugated thiophene spacers in the acceptor. Since the backbone constituents contribute to the development of IR bands at similar wavenumbers, attribution of each band to a single backbone unit is challenging and sometimes not possible. However, certain distinctions can be established; for instance, some bands are mostly related to the thiophene rings (1187 cm^{-1}), to the four-member silicon cycle (1245 cm^{-1}) or to the thiazolothiazole (1538 and 1490 cm^{-1}). Additionally, blend films also display IR bands characteristic of PCBM, among which, probably the most distinctive are the intense band 526 cm^{-1} due to the vibration of the fullerene cage and that of the ester bond at 1738 cm^{-1}.

(a)   **(b)**
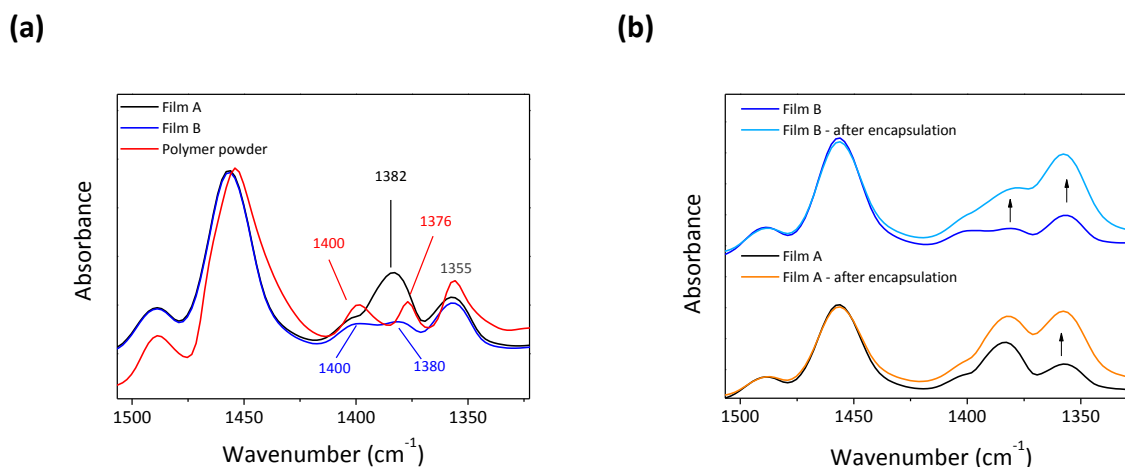
Figure 4.4. (a) IR spectra for two polymer films (Film A, Film B), processed from the same solution and following the same deposition conditions, and for a sample of polymer powder (red line). (b) IR spectra of films A and B as coated and after encapsulation under vacuum.

Interestingly, P4 films displayed different band distributions in the interval 1350-1380 cm^{-1}, as shown in Figure 4.4. In general, three bands could be observed in this region, with maxima at 1400, 1380 and 1355 cm^{-1}; however, the relative intensity of these bands varied in the set of coated films. Exemplifying this, film A in Figure 4.4 (a) displays a higher intensity for the maximum at 1380 cm^{-1} and lower intensity for the other two bands, whereas film B is characterised by two bands at 1400 and 1380 cm^{-1}, together with a higher intensity maxima at 1355 cm^{-1}. These results were then compared to the IR spectrum of the polymer powder in this interval [red line in Figure 4.4 (a)]. The band disposition is more similar to film B, since the two maxima at 1400 and 1380 cm^{-1} exhibit identical intensity, with slightly higher absorbance for the band at 1355 cm^{-1}. Importantly, in addition to the observed differences in pristine films, this region changed upon encapsulation of the samples under vacuum; the procedure employed to eliminate oxygen from the samples in the photolysis and thermolysis experiments. Similar behaviour was observed in the region 650 – 700 cm^{-1}, with maxima at 690, 670 and 660 cm^{-1}, varying in intensity in the different films and after the vacuum treatment (not shown). This same observation was detected for the set of blend films prepared (not shown), although less markedly due to overall lower intensity of these bands in the spectrum.

According to literature, the bands observed in these two regions of the spectrum reflect changes in the packing or crystallinity of polymer chains.[294] Thus, although these films were prepared from the same solution, in the same run, and following identical processing conditions, different degrees of crystallinity seemed to be achieved, which also changed upon vacuum treatment

[Figure 4.4 (b)]. However, it is recalled that the polymer film is a two-phase system in which a crystalline phase coexists with an amorphous phase, the distribution of which can be spatially inhomogeneous (both laterally and throughout the thickness/depth). In order to better characterise the films, attempts were made to correlate the different distributions in the IR spectra with the UV-Vis spectrum of the polymer. More specifically, the distribution in IR was compared to the relative intensity of the maxima in the main polymer absorption bands (580 and 630 nm), since the feature at higher wavelengths reflects changes in the aggregation/crystallinity.[278, 281] However, no correlation between the IR and UV-Vis data could be established. Finally, according to XRD data, the polymer is predominantly amorphous, both before (see Figure 3.28) and after vacuum sealing (not shown). Nevertheless, and as aforementioned in Chapter 3, further work is needed to better characterise the crystallinity of the polymer. Overall, this analysis confirmed the existence of amorphous and crystalline phases in the polymer, as well as the contribution of the vacuum process towards the modification of the crystallinity of the sample. In the following studies upon thermal and photochemical treatments, results observed in this area are treated with caution, due to both the lack of reproducibility of these bands among the different pristine films and the additional modifications imparted by external factors, such as the encapsulation of the samples under vacuum (used in photolysis and thermolysis experiments).

4.3.1.2. Treatments in presence of oxygen

4.3.1.2.1. <u>Photooxidation</u>

Figure 4.5 displays the UV-Vis spectra of polymer and blend films irradiated in the presence of air (photooxidation) using Suntest CPS/XLS. In line with the results in Chapter 3 (Section 3.3.2.2), the loss of optical absorption in the polymer in Figure 4.5 (a) is characterised by a strong blue-shift, ascribed to the predominantly amorphous character of this polymer and evidencing the loss of π-conjugation in the film. In turn, Figure 4.5 (c), illustrating the UV-Vis changes of P4:PCBM thin films, shows a continuous decrease of the polymer and fullerene absorption bands upon irradiation. In this case, a blue-shift is not clearly discernible [see Figure 4.5 (b)], although it could be occurring in the last degradation steps (after 100 hours of treatment). Furthermore, PCBM imparts a stabilising effect on the degradation of P4, as exemplified by the overall longer irradiation time needed to achieve total bleaching of the sample in the case of the blend.

(a)

(b)

(c)
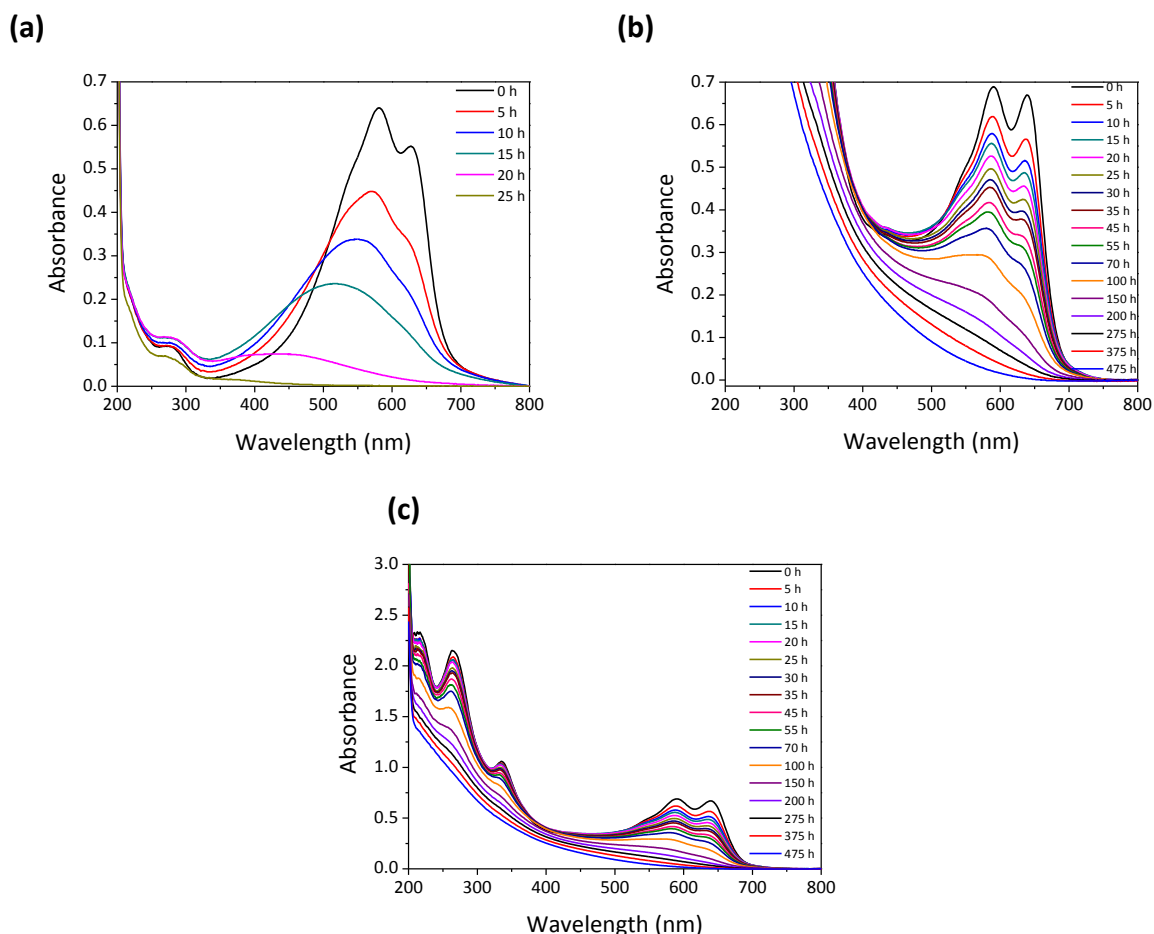
Figure 4.5. UV-Vis evolution for (a) P4 films and (b, c) P4:PCBM films upon photochemical treatment under ambient air conditions.

Figure 4.6 summarises the absorbance loss of P4 and P4:PCBM films irradiated using Suntest under ambient air conditions. Linear fits have been applied to calculate the rate of absorbance loss (established as the degradation rate) for both polymer and blend films; and the stabilisation factor imparted by PCBM under these conditions has been calculated as the quotient rate$_{polymer}$/ rate$_{blend}$. According to this, upon irradiation under ambient air conditions, the degradation rate of the polymer is stabilised by factor of 5 in the presence of PCBM. This value contrasts with the stabilisation factor of less than 2 that we obtained for this same polymer blended with PCBM and exposed to the same irradiation conditions in Chapter 3 (see Section 3.3.2.3.3). As previously indicated, it is important to note that processing of the films was carried out differently in both cases. Whilst the P4:PCBM ratio was kept the same in both experiments (1:2), different solvent mixtures were employed; *p*-xylene:ODCB (7:1) in one case (Chapter 3) and *o*-xylene:1-MN (95:5) in the other (Chapter 4).

Furthermore, in the latter, a post-deposition annealing step (5 min at 130 °C) was applied to optimise the achieved morphologies; in fact, the procedure reported in this chapter has allowed the preparation of solar cells in Section 4.3.2. The different morphologies obtained in both cases can certainly explain the different stabilisation factors obtained, since modifications in the interfacial area between polymer and fullerene (for example *via* incorporation of a processing additive that enhances phase separation in the active layer) can vary the extent of stabilisation or destabilisation that PCBM has over a certain polymer.[237]
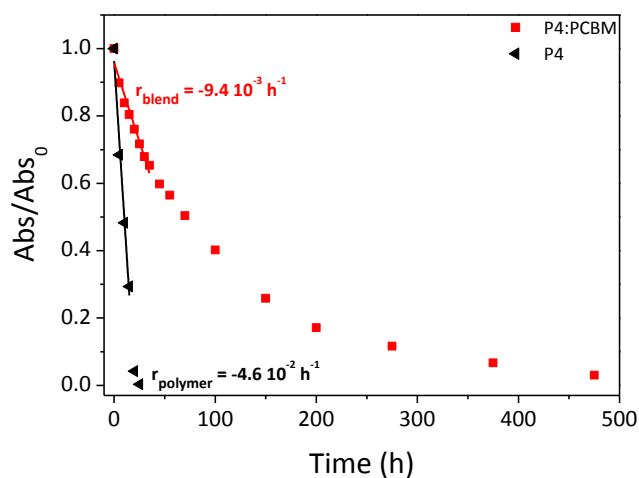
Figure 4.6. Normalised absorbance loss (at the polymer maximum absorption wavelength) for P4 and P4:PCBM films upon photooxidation.

(a) **(b)**
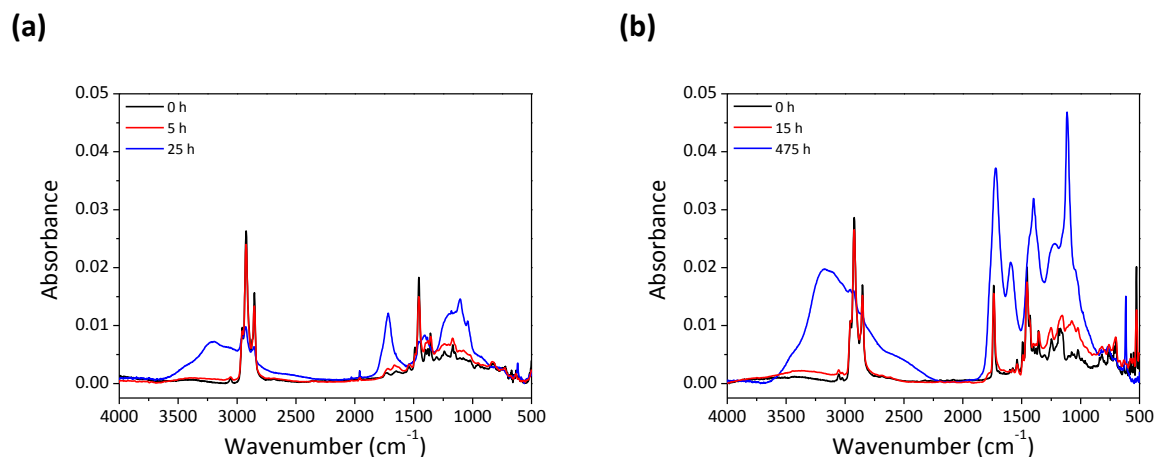
Figure 4.7. IR evolution for (a) P4 films and (b) P4:PCBM films upon photochemical treatment at ambient air conditions.

Figure 4.7 shows the IR spectra for both polymer and blend as pristine materials, at their corresponding t_{80} (20 % absorbance loss) and after total bleaching of the sample. Changes in the polymer IR spectra [see Figure 4.7 (a)] are characterised by the rise of bands in the hydroxyl and carbonyl regions (centred at 3200 and 1720 cm^{-1}, respectively) and in the fingerprint region (1384, 1105, and 617 cm^{-1}), attributed to the oxidation of the sulfur atom in the thiophene rings and indicative of an advanced stage of polymer oxidation.[210, 214] A decrease in the intensity of the bands was also observed in the alkyl domain (2950 - 2850 cm^{-1}) and other polymer characteristic bands, for instance at 1492, 1456, and 1355 cm^{-1}. As shown in Figure 4.7 (b), the behaviour of the blend is markedly different. Certain changes are similar to that observed for the neat polymer, *e.g.* the loss of alkyl side chains and the decrease in the band at 1456 cm^{-1} (C=C rings vibration), the latter suggesting the disruption of the π-conjugation system. However, other major modifications are related to the degradation of the fullerene derivative (*e.g.*, the marked decrease at 526 cm^{-1}). Furthermore, the large absorption band in the region 1500 – 1000 cm^{-1}, with maxima at 1380, 1219, and 1059 cm^{-1}, has also been reported for the photothermal oxidation of C_{60} and PCBM, and has been ascribed to the vibration of C-O bands.[295] In light of these results and the consulted literature, it is proposed that there is a clear involvement of the fullerene acceptor in the oxidative reactions taking place. Under these conditions, PCBM can act as a radical acceptor, consequently saturating the fullerene cage with alcohols, epoxides and other moieties,[239-240, 295] and provoking the loss of fullerene absorbance in the UV domain, see Figure 4.5 (c). In turn, this behaviour reduces the rate of polymer degradation compared to the photooxidation of the neat polymer (Figure 4.6).

4.3.1.2.2. <u>Thermooxidation</u>

Figure 4.8 displays the UV-Vis decay for P4 and P4:PCBM films thermally treated in air at 100 °C. In line with what was observed upon photooxidation, photobleaching of the polymer in Figure 4.8 (a) occurs, and a strong blue-shift can be observed. The absorbance of the film drops to approximately 20 % of the initial value after 100 hours of thermal treatment. In turn, thermal oxidation of the blend, observed in Figure 4.8 (b,c), provokes a rapid initial change of absorption in the fullerene region within the first 5 hours of treatment, due to phase segregation causing a reorganisation of the active layer morphology. This aspect was also observed and further explained in the study of the thermal behaviour of P3HT:PCBM at 150 °C in Section 2.3.2.2. Overall, the UV-Vis absorption changes in the blend upon thermal treatment indicate a thermally-driven morphological reorganisation of polymer and fullerene, leading to an inhomogeneous lateral distribution of PCBM and consequently to an initial drop in the

overall absorption in the UV region. From this moment, thermal treatment in air provokes a steady decrease of absorption loss in the polymer [Figure 4.8 (b,c)], although at a lower rate compared to the absorbance loss in neat P4 films. Additionally, the absorption corresponding to the fullerene remains constant up to 700 h, after which, loss in PCBM absorption proceeds rapidly [Figure 4.8 (c)]. This apparent delay in PCBM absorption loss is ascribed to the precedent morphological reorganisation. In fact, the created PCBM crystallites can shield the absorption of the already degraded PCBM, in a way that only when a sufficient amount of material has been degraded (after 700 h in this case), the consequent changes in the UV-Vis spectra can be observed.
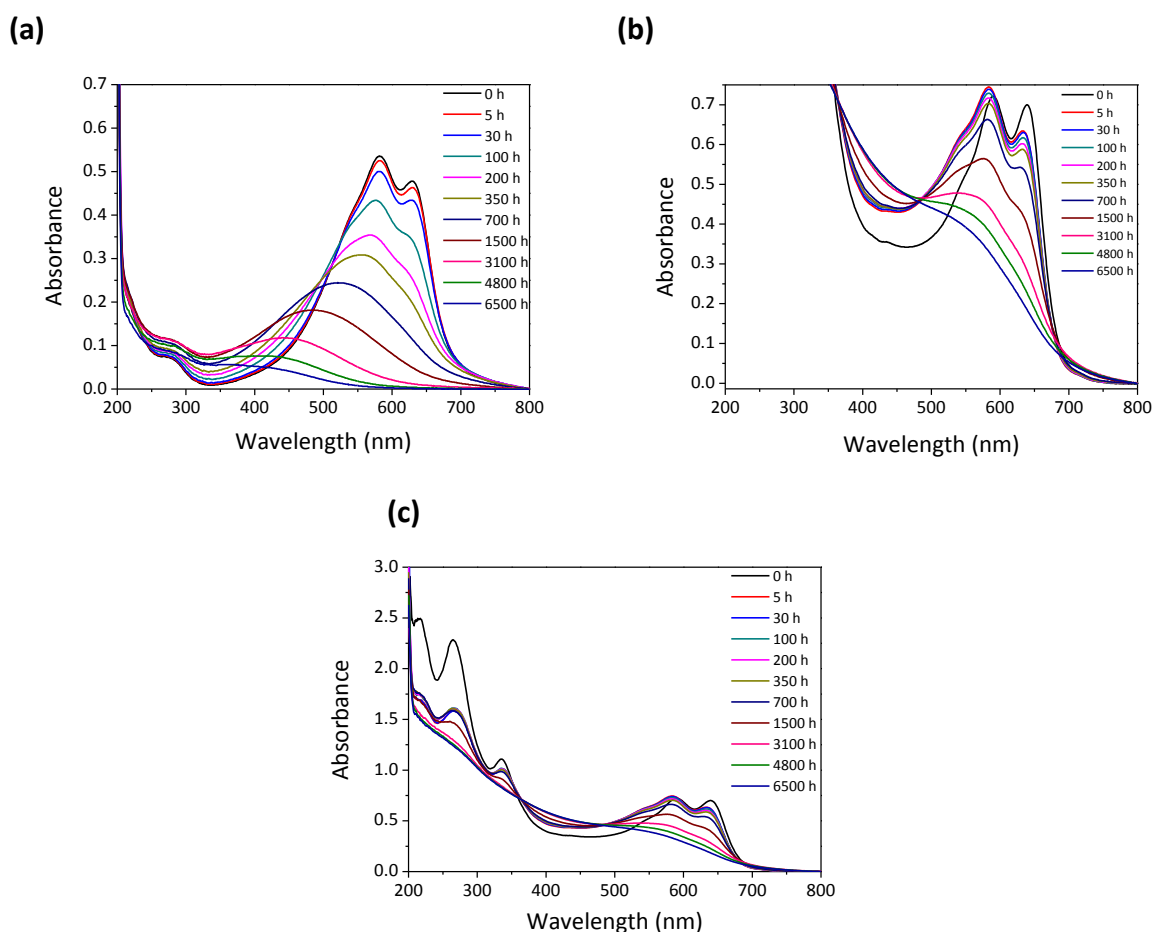
Figure 4.8. UV-Vis evolution for (a) P4 films and (b, c) P4:PCBM films exposed to thermal oxidation at 100 °C.

Figure 4.9 shows the normalised absorbance loss for polymer and blend films under thermal stress in air at 100 °C. Linear fits have been applied to the absorbance decay to calculate the degradation rates in polymer and blend. Accordingly, it is verified that PCBM suppresses the

degradation of P4 by a factor of 10 (higher than for photooxidation). A higher stabilisation under these conditions could be also ascribed to the morphological reorganisation, in a way that PCBM aggregated as crystallites in the surface hinder the access of oxygen to the polymer, thus leading to a reduction in the degradation rate of the polymer.
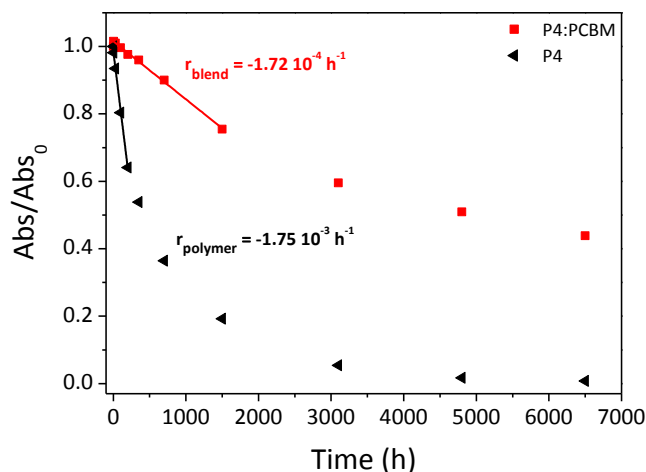
Figure 4.9. Normalised absorbance loss (at the polymer maximum absorption wavelength) for P4 and P4:PCBM films upon thermooxidation.

Figure 4.10 includes the IR spectra of both polymer and blend at different stages of their degradation upon thermal treatment in air, namely as pristine materials (0 h), at their corresponding t_{80} and at the last measured time step (6500 h). In the case of the blend, the IR spectrum after 5 h of thermal degradation [time corresponding to the morphological reorganisation observed in Figure 4.8 (c)] is also included. A strong decrease is noticeable in the aliphatic chains domain (~2850 – 2950 cm^{-1}), together with the increase of a convoluted band in the carbonyl domain (~1600 -1800 cm^{-1}) and several modifications in the fingerprint region, namely a decrease of the band at 1456 cm^{-1} ($\upsilon_{C=C}$ all rings) and creation of bands at 1384, 1122, and 617 cm^{-1}, attributed to the oxidation of the sulfur atoms in the thiophene rings.[210, 214] Modifications in the IR spectra of P4:PCBM films [Figure 4.10 (b)] are similar to what observed upon photooxidation, and include a marked increase in the hydroxyl domain (~3000 - 3600 cm^{-1}), carbonyl domain (~1600 - 1800 cm^{-1}, centred at 1734 cm^{-1}), and multiple bands in the interval 1400 - 920 cm^{-1}. Furthermore, it is clearly noticeable a decrease of the aliphatic chains band (~2850 – 2950 cm^{-1}) and of the bands at 1456 cm^{-1} ($\upsilon_{C=C}$ all rings) and 526 cm^{-1} (vibration of the fullerene cage). Interestingly, despite the near total absorbance loss achieved for the polymer after 6500 hours, compared to the absorbance loss slightly below 50 % in the

case of the blend for the same period (see Figure 4.9), the modifications in the IR spectra are drastically more pronounced for the oxidised blend. This is summarised in Figure 4.11, displaying the subtracted IR spectrum after 6500 h of thermal treatment in both cases.

(a)   **(b)**
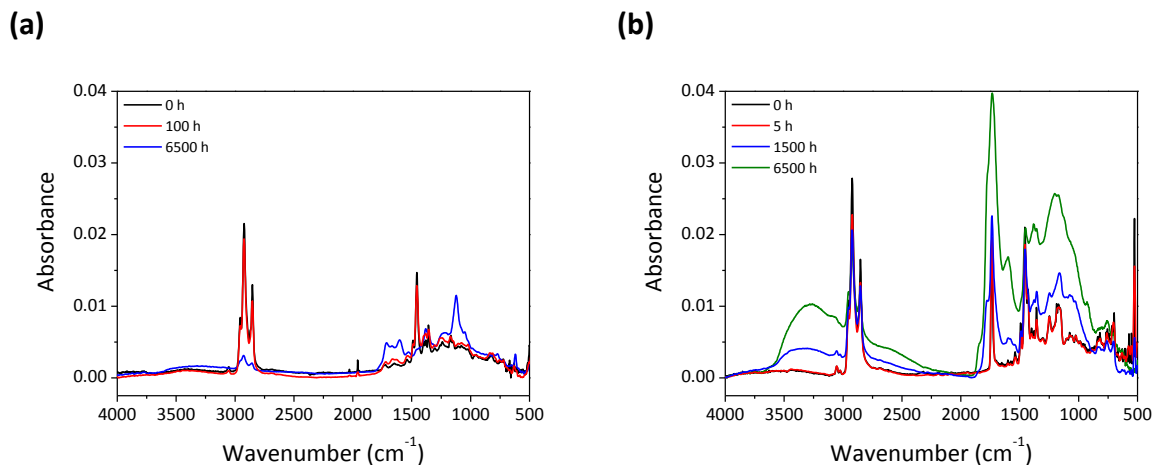
Figure 4.10. IR evolution for (a) P4 films and (b) P4:PCBM films under thermal oxidation at 100 °C.
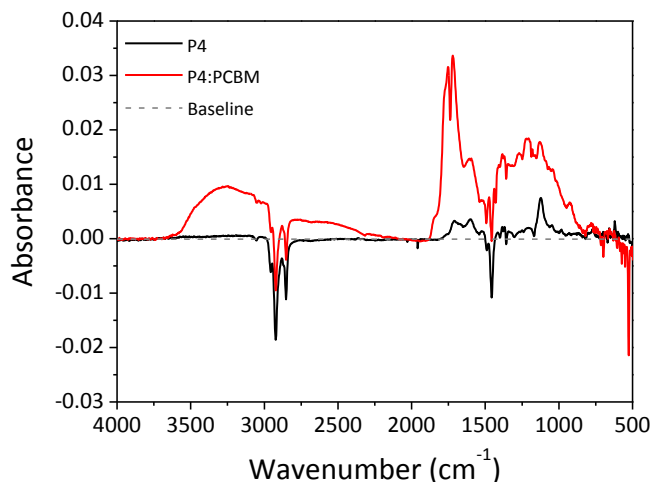
Figure 4.11. Subtracted IR spectra of P4 (black) and P4:PCBM (red) after 6500 h of thermal treatment in air.

4.3.1.2.3. <u>Comparison thermooxidation *versus* photooxidation</u>

The IR modifications for P4 thin films exposed to photo- and thermooxidative conditions have been compared at a similar UV-Vis absorbance loss (*i.e.*, total bleaching of the main absorption band in the polymer), see subtracted spectra in Figure 4.12. As can be observed, photooxidation creates a broad band in the hydroxyl domain (3200 cm^{-1}), which was non-existent under thermooxidative conditions.

Furthermore, modifications in the region below 1500 cm^{-1} are more intense in photooxidation, especially around 1200 cm^{-1}. Additionally, in the last stages of polymer photobleaching, the convoluted band created in the carbonyl region evolves to produce a sharp band with maxima at 1720 cm^{-1} [Figure 4.13 (a)]. In turn, thermal oxidation produces a band with several maxima (1720, 1670, and 1600 cm^{-1}), among which, the maximum at 1720 cm^{-1} starts to decrease for the last recorded spectrum at 6500 h [Figure 4.13 (b)].
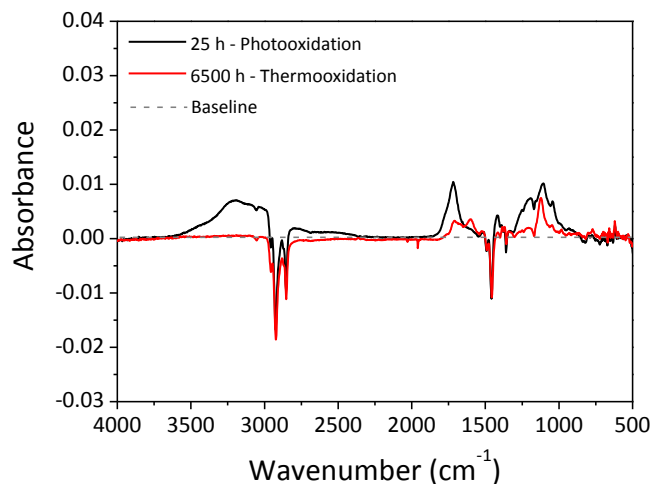
Figure 4.12. IR subtracted (calculated as 'aged – pristine') spectra for P4 films irradiated in air (black line) or thermally treated in air (red line). These spectra correspond to a stage in which total bleaching of the polymer main absorption band has been completed.
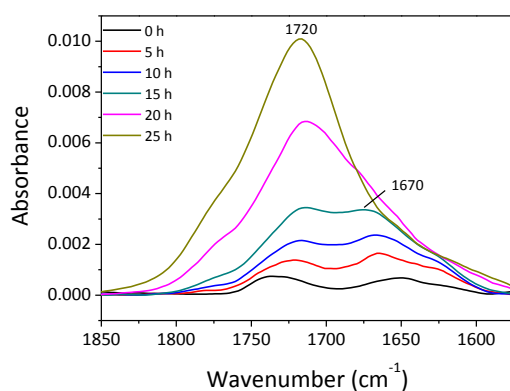
(a)   **(b)**
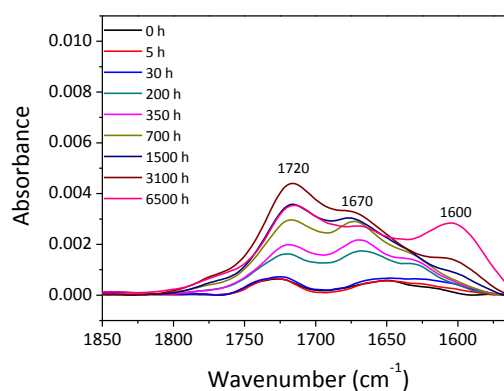
Figure 4.13. Evolution in the carbonyl domain upon (a) photooxidation and (b) thermooxidation for polymer thin films.
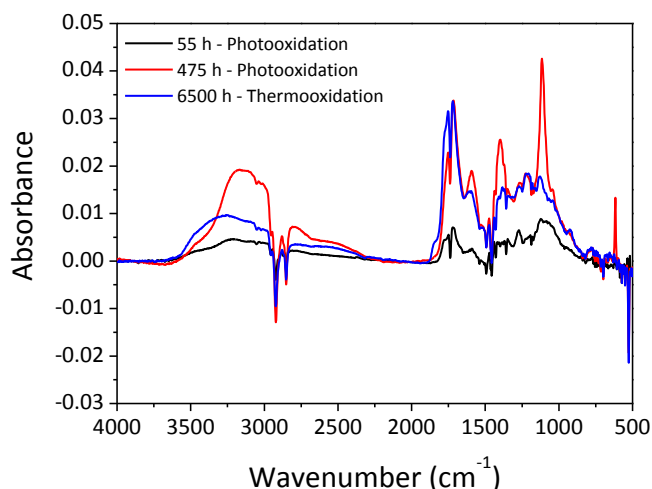
Figure 4.14. IR subtracted (calculated as 'aged – pristine') spectra for P4:PCBM films irradiated in air (black and red line) or thermally treated in air (blue line). The '55 h – Photooxidation' and '6500 h – Thermooxidation' spectra correspond to a polymer absorbance loss of slightly more than 50 % in each case.

(a)   **(b)**
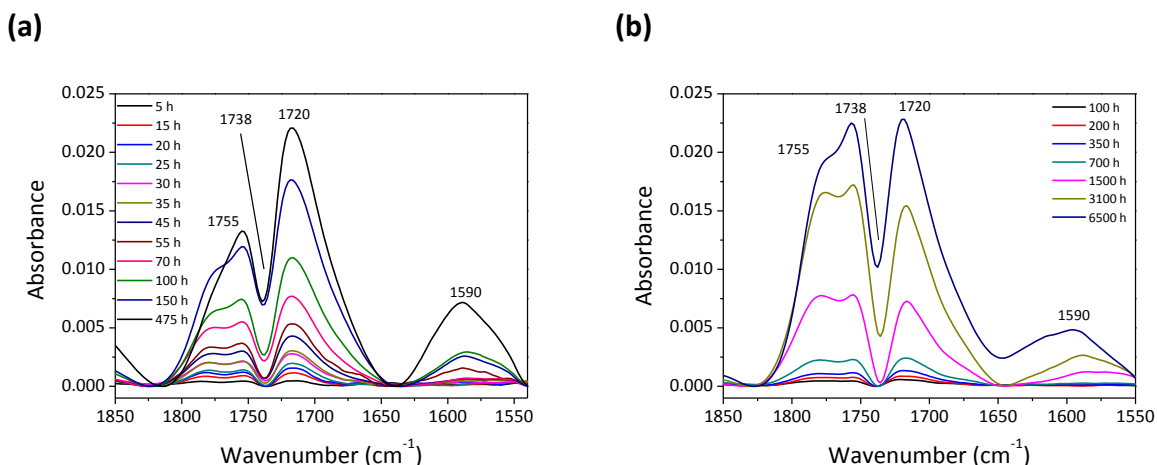
Figure 4.15. Evolution in the carbonyl region upon (a) photooxidation and (b) thermooxidation for P4:PCBM thin films.

In the same manner, IR changes in the blend upon photooxidation were compared to the changes that occurred upon thermooxidation. To this end, a similar degradation extent (established as 50 % polymer absorbance loss) was compared in both cases, namely 55 h of photooxidation and 6500 h in thermooxidation (Figure 4.14). The overall shape of the bands is very similar; however, changes are remarkably more pronounced in the case of the thermooxidised sample. This is most notable in the hydroxyl and carbonyl products and the products giving rise to bands in the finger print region.

Nevertheless, the spectrum after 475 h of photooxidation (corresponding to a total bleaching of the sample), reveals that when the reaction proceeds further, the absorption of these bands increases to a similar, or even more enhanced, extent than upon thermal oxidation. Furthermore, 475 h of photooxidation create a marked development of the bands at 1380, 1105, and 617 cm^{-1}. The evolution in the carbonyl domain is very similar in both cases, characterised by the loss of the ester function of the PCBM at 1738 cm^{-1}, and the creation of a band in the carbonyl domain with maxima at 1755, 1720, and 1590 cm^{-1} (see Figure 4.15).

(a)   **(b)**
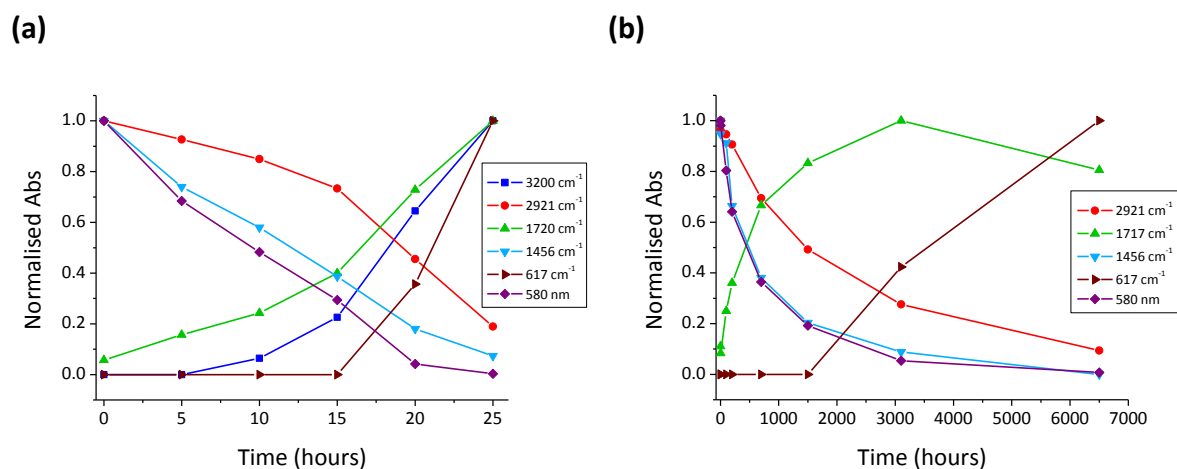
Figure 4.16. Evolution of selected IR and Vis bands upon (a) irradiation or (b) thermal treatment (100 °C) in air of P4 films.

Figure 4.16 compares the evolution of selected IR wavenumbers, corresponding to characteristic bands of the polymer or oxidation products, with the absorption loss of the main polymer band at 580 nm. Accordingly, photooxidation induces the decay of the polymer band at 1456 cm^{-1} (C=C rings), occurring in parallel with the loss of UV-Vis absorbance (580 nm), whilst the band corresponding to the alkyl side chains (2921 cm^{-1}) evolves at a different rate. Furthermore, photooxidation of the polymer provokes a steady increase of carbonyl products (1720 cm^{-1}) from the beginning of the irradiation, whereas formation of hydroxyl products (3200 cm^{-1}) and sulfinic esters (617 cm^{-1}) occurs after 10 h and 20 h of exposure, respectively. Conversely, no hydroxyl products were observed upon thermal oxidation, and the rise of the carbonyl band at 1720 cm^{-1} is characterised by a subsequent decrease after 3100 h of treatment. Sulfinic esters (617 cm^{-1}) are formed after 3000 h of thermal oxidation, at a stage when the UV-Vis absorbance of the polymer has practically vanished. Similarly to what was observed in photooxidation, a direct (and probably even more evident in this case) relationship between the band 1456 cm^{-1} and the loss of

polymer absorbance at 580 cm^{-1} is shown, whilst the alkyl side chain band (2921 cm^{-1}) decreases at a lower rate.

(a)   **(b)**
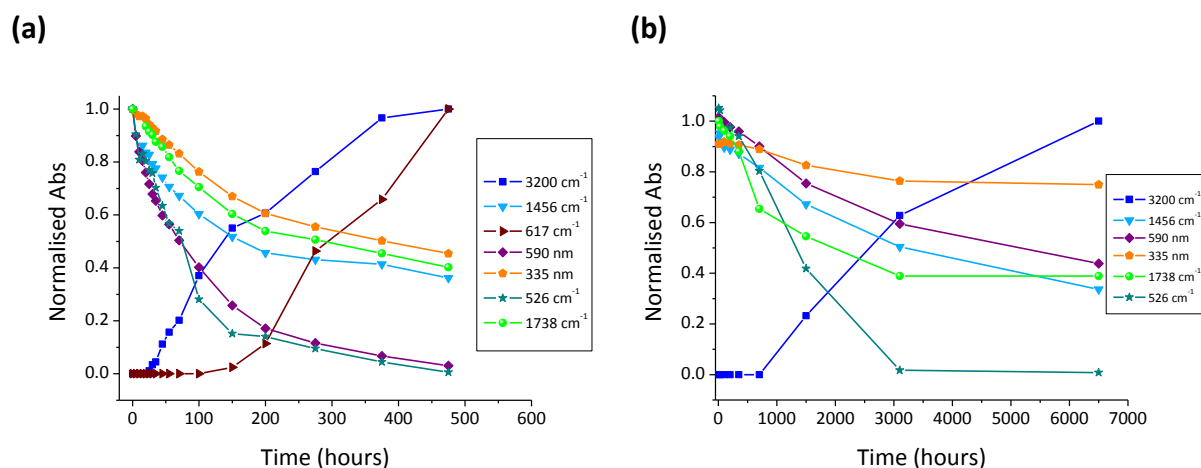
Figure 4.17. Evolution of selected IR and UV-Vis bands upon (a) irradiation or (b) thermal treatment (100 °C) in air of P4:PCBM films.

Similarly, Figure 4.17 compiles the modifications for selected polymer and fullerene bands, as well as their oxidation products upon photo- and thermooxidation. As for photochemically treated samples, the selected markers of oxidation, namely the hydroxyl band at 3200 cm^{-1} and the band at 617 cm^{-1}, appear after approximately 25 h and 150 h, respectively. In this case, the appearance of carbonyl products was difficult to monitor due to the presence of the ester band of PCBM from the start. Interestingly, the decrease in the polymer main absorption band at 590 nm occurs together with the loss of the band 526 cm^{-1}, characteristic of the fullerene. In turn, the decrease in the UV band of PCBM (335 nm) and its ester function (1738 cm^{-1}) comes together with the loss of the band at 1456 cm^{-1} (C=C rings). Finally, the changes in thermooxidation are determined by an overall lower extent of degradation and by the aforementioned morphological reorganisation (Figure 4.9). On the one hand, although the growth of the band in the hydroxyl domain (3200 cm^{-1}) can be observed after 1500 h of treatment, the band at 617 cm^{-1} did not developed at this stage. On the other hand, a similar decay in absorbance is observed for the bands at 1456 cm^{-1}, 1738 cm^{-1}, and 590 nm. Notably, the UV absorbance of the polymer (335 nm) remains almost constant up to 700 hours, and then steadily decays; whilst the fullerene IR characteristic band at 526 cm^{-1} rapidly decays from the beginning of the exposure.

4.3.1.3. Treatments under vacuum

4.3.1.3.1. <u>Photolysis</u>

Subsequently, the effect of light and temperature was re-evaluated by encapsulating polymer and blend films in glass tubes sealed under vacuum, with the aim of obtaining conditions more representative of the behaviour of encapsulated solar cells, thus excluding the effect of oxygen in the system as much as possible.

(a)

(b)

(c)
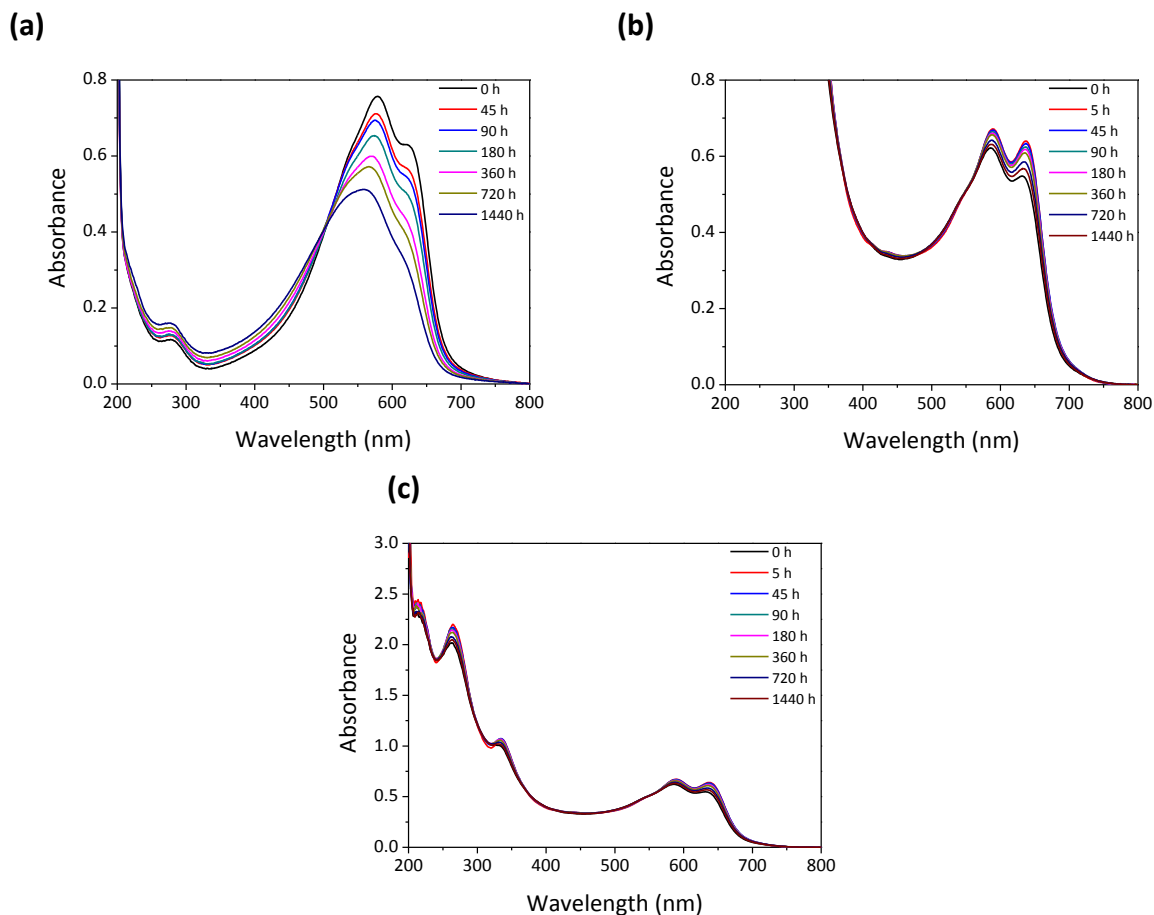
Figure 4.18. UV-Vis evolution for (a) P4 films and (b, c) P4:PCBM films exposed to irradiation under vacuum using Suntest as ALT.

Accordingly, Figure 4.18 indicates the UV-Vis absorption changes occurring upon irradiation of P4 and P4:PCBM thin films exposed to irradiation under vacuum. Overall, the behaviour of the UV-Vis spectra resembles that observed upon photooxidation; however, occurring at a lower rate. Accordingly, whilst 20 % absorbance loss was observed in less than 5 hours of photooxidation (Figure 4.5), almost 360 hours were needed to achieve the same extent of degradation in this case. Similarly, the

UV-Vis absorption spectra of blends encapsulated under vacuum displayed in Figure 4.18 (b, c) indicate both a low loss of absorption in the main polymer band (~5 % at 590 nm) and a slight rise in absorption at 320 nm, the latter being characteristic for the photoinduced dimerisation of PCBM.[238]

(a)   **(b)**
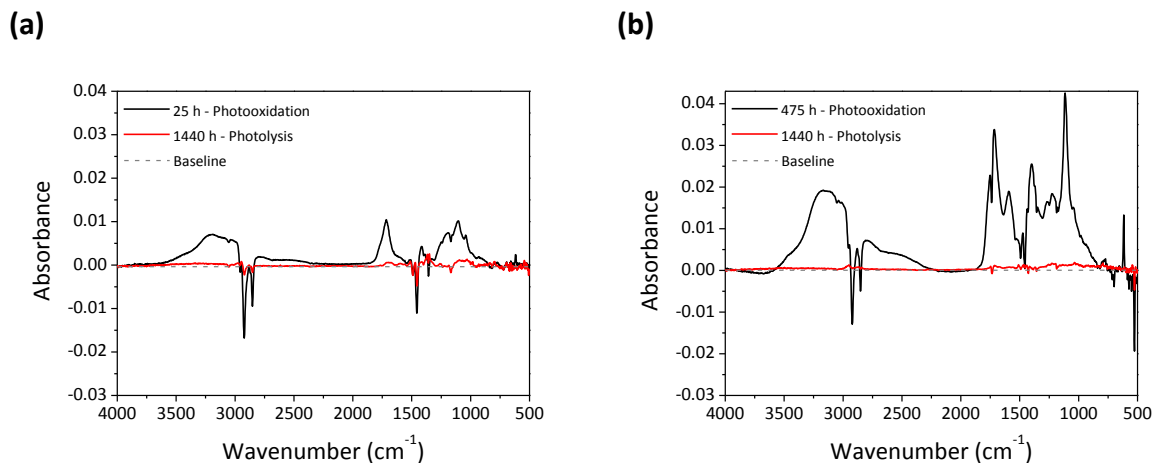
Figure 4.19. IR subtracted (calculated as 'aged – pristine') spectra for samples irradiated in air (black line) or under vacuum (red line), for (a) P4 films and (b) P4:PCBM films.

Figure 4.19 compares the modifications created in the IR spectra of polymer and blend films subjected to photooxidation and photolysis. As shown, subtracted spectra corresponding to polymer films [Figure 4.19 (a)] share several characteristics, notably the decrease of bands in the interval 2850-2950 cm^{-1} or the bands at 1456 cm^{-1} and 1164 cm^{-1}. A certain rise of a band in the carbonyl domain (1600 - 1800 cm^{-1}) is detected, although this feature is not as marked as upon photooxidation. Furthermore, no hydroxyl or sulfinic products can be detected at this stage. As for the blend, and in line with the minor modifications in the UV-Vis spectra [Figure 4.18 (b,c)], the changes in the IR spectra are very slight; probably the most marked modification being the reduction of the band at 526 cm^{-1}, characteristic of the fullerene [Figure 4.19 (b)]. Having confirmed the existence of certain oxidation of the analysed samples, most notably in the polymer films, the influence that the (re)encapsulation process may have towards the introduction of oxygen in the system was assessed. To this end, polymer and blend 'control' samples were initially characterised, encapsulated and re-analysed uniquely after 1440 hours, with no intermediate measurements steps. Interestingly, for these samples, an absorbance loss of only 15 % (polymer, 580 nm) and 3 % (blend, 590 nm) was observed after completion of 1440 hours of photochemical treatment (see Figure 4.20). The different extents of degradation in the two cases indicate that each time the tube is opened to obtain the measurement of the sample, a certain amount of oxygen is introduced in the system. Samples analysed at several irradiation steps

(Figure 4.19) have been in contact with higher amounts of oxygen, thus explaining the higher absorption loss. The absorption loss of polymer and blend films under 'normal' and 'control' conditions is summarised in Figure 4.21.

(a)

(b)
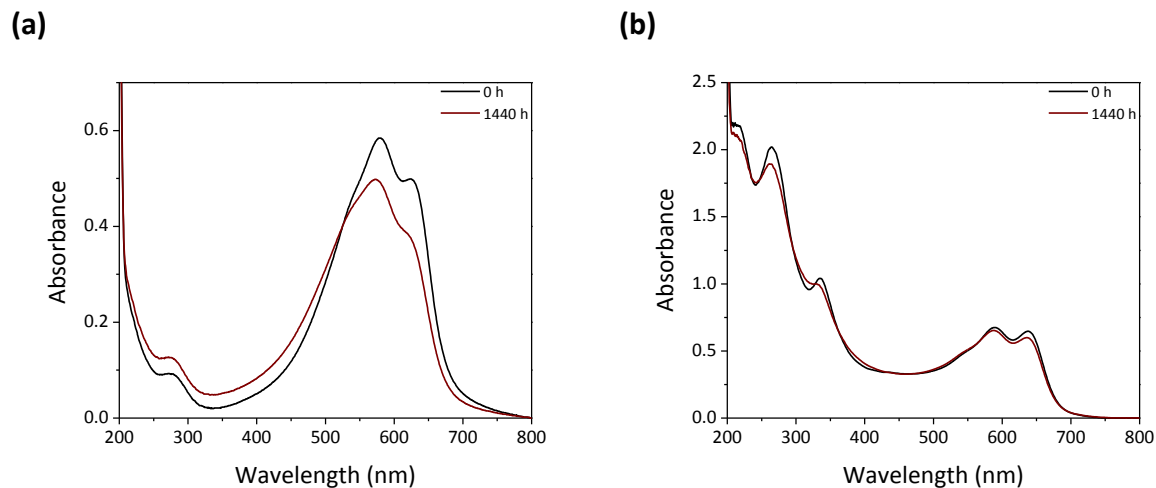
Figure 4.20. UV-Vis absorption spectra of 'control' (a) P4 and (a) P4:PCBM films encapsulated under vacuum irradiated using Suntest for 1440 h.
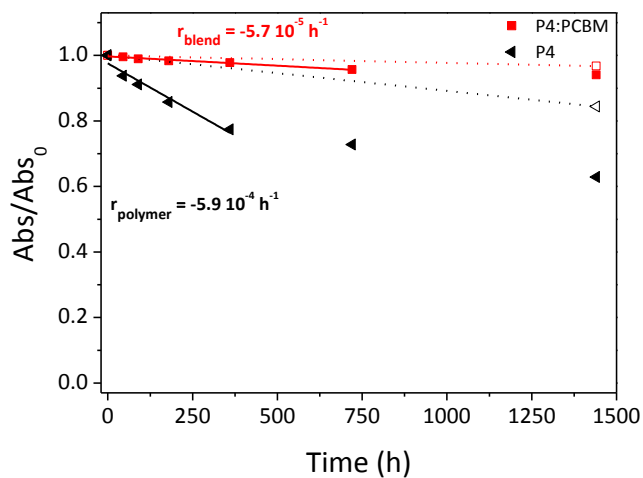
Figure 4.21. Normalised absorbance loss (at the polymer maximum absorption wavelength) for P4 and P4:PCBM films in photolysis experiments using Suntest. Open symbols indicate the absorbance loss for control samples analysed uniquely at the end of the exposure time.

(a)   **(b)**

Figure 4.22. IR subtracted spectra (calculated as 'aged − pristine') for (a) P4 and (b) P4:PCBM films irradiated in air (black line) or under vacuum (blue line).

In order to evaluate the level of oxidation occurring in the 'normal' samples, the IR spectra of both polymer and blend films irradiated under vacuum were compared to those of films irradiated in air. IR spectra were compared for a similar absorbance loss at the polymer main absorption band, namely 20 % for polymer films and 2 % for blend films, see Figure 4.22. Figure 4.22 (a) shows that, despite the same absorbance loss observed in UV-Vis for the analysed samples, IR changes in P4 films are more pronounced for samples irradiated in ambient air. This is clear when comparing the modifications in the alkyl side chain domain (2950 - 2850 cm^{-1}) and carbonyl domain (1800 − 1600 cm^{-1}), the decrease of the polymer band at 1456 cm^{-1} or the rise of bands in the interval 1300 - 1000 cm^{-1}. As for the sample irradiated under vacuum, the more noticeable changes were the decrease of the band at 1456 cm^{-1} and the decrease of the band at ~1360 cm^{-1}, the latter related to a loss of crystallinity in the polymer. However, as indicated in Section 4.3.1.1, modifications in this band can be purely induced by the vacuum-encapsulation process, thus, the observed modifications cannot be only ascribed to the effect of mere light exposure. Similarly, changes in the IR spectra of blends for a 2 % polymer absorbance loss [Figure 4.22 (b)] are less marked for photochemical treatment under vacuum, arguably the major difference being the decrease of the band at 526 cm^{-1}. Overall, the discrepancy between the IR spectra of samples irradiated under ambient air conditions and sealed under vacuum for the same degradation extent (measured as a similar UV-Vis absorption loss), indicated that degradation in the photolysis experiments does not uniquely stem from the reaction with the residual oxygen present in the tubes. Furthermore, since the reaction leading to PCBM

dimerisation is effectively supressed by oxygen,[238, 243] the observation of PCBM dimerisation in Figure 4.18 (b), corroborates a high level of exclusion of oxygen in the vacuum-encapsulated tubes.

4.3.1.3.2. Thermolysis

Figure 4.23 (a) displays the UV-Vis decay for P4 and P4:PCBM films encapsulated under vacuum and thermally treated at 100 °C. The general behaviour of the polymer films is similar to that observed under thermal oxidation [see Figure 4.8 (a)]. However, absorbance loss occurs to a clearly lower rate, as exemplified by the 20 % absorbance loss observed after approximately 1600 h of treatment.

(a)

(b)

(c)
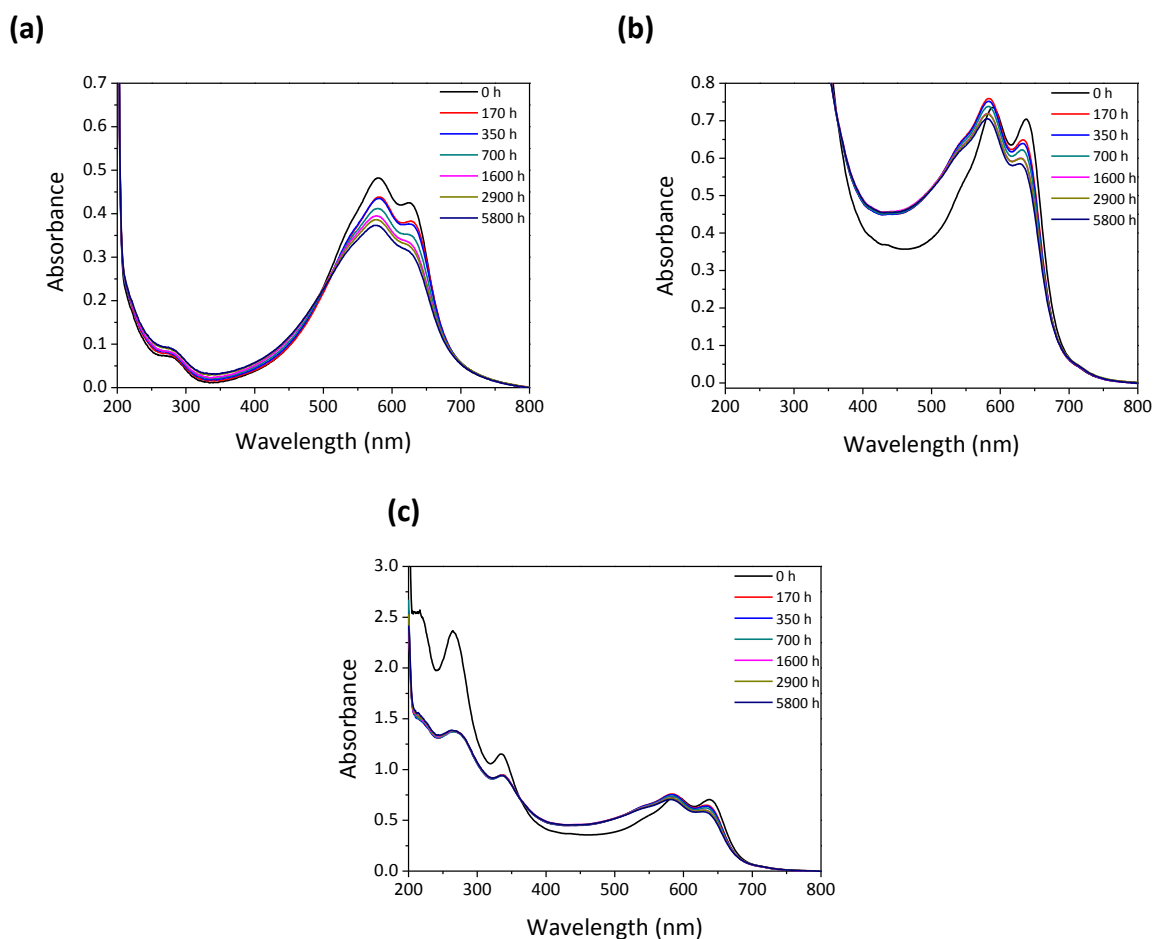
Figure 4.23. UV-Vis evolution for (a) P4 films and (b, c) P4:PCBM films exposed to thermal treatment under vacuum at 100 °C.

In the case of P4:PCBM films [Figure 4.23 (b)], changes in the UV-Vis absorption spectra of the films indicate an initial of loss absorption in the fullerene phase due to morphological reorganisation of the active layer, after which, degradation proceeds very slowly and mainly affects the polymer.

The comparison between the absorbance loss of the polymer main absorption band in the neat polymer and that in the blend is depicted in Figure 4.24.
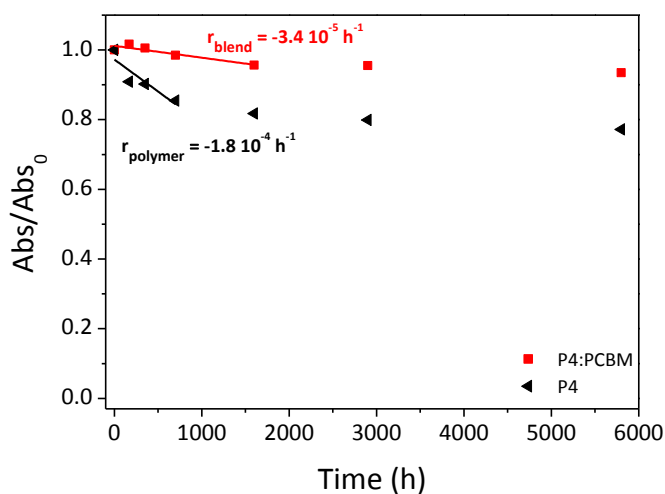
Figure 4.24. Normalised absorbance loss (at the polymer maximum absorption wavelength) for P4 and P4:PCBM films upon thermolysis at 100 °C.

Figure 4.26 compares the IR modifications (subtracted spectra) for P4 and P4:PCBM samples thermally treated in air or sealed under vacuum for a treatment period leading to a similar UV-Vis absorption loss (namely 20 % in polymer films and 5 % for the blend films). The IR evolution during thermolysis for both polymer and blend is similar to what was observed upon thermooxidation, *albeit* to a lesser extent for a similar irradiation period. This is exemplified by the decrease of the bands corresponding to the aliphatic chains ($\sim$2850 – 2950 cm^{-1}), the slight reduction of the band at 1456 cm^{-1}, and the modest increase in the carbonyl domain ($\sim$1600 - 1800 cm^{-1}). Similarly to that observed while comparing photooxidation and photolysis, the increase of bands in the carbonyl domain indicates that traces of oxygen are present in the system, leading to observed sample oxidation. Furthermore, pronounced modifications in the region below 1500 cm^{-1} were detected for both polymer and blend films subject to thermal treatment under vacuum, provoking a modification of the baseline. It could be proposed that these changes stem from mere morphological changes in the samples, produced by the prolonged thermal treatment under vacuum. Finally, although thermal treatment of encapsulated P4 and P4:PCBM films induces several modifications in the corresponding IR spectrum, these are certainly less pronounced than upon thermooxidation for a similar treatment interval (see Figure 4.26).

(a)   **(b)**
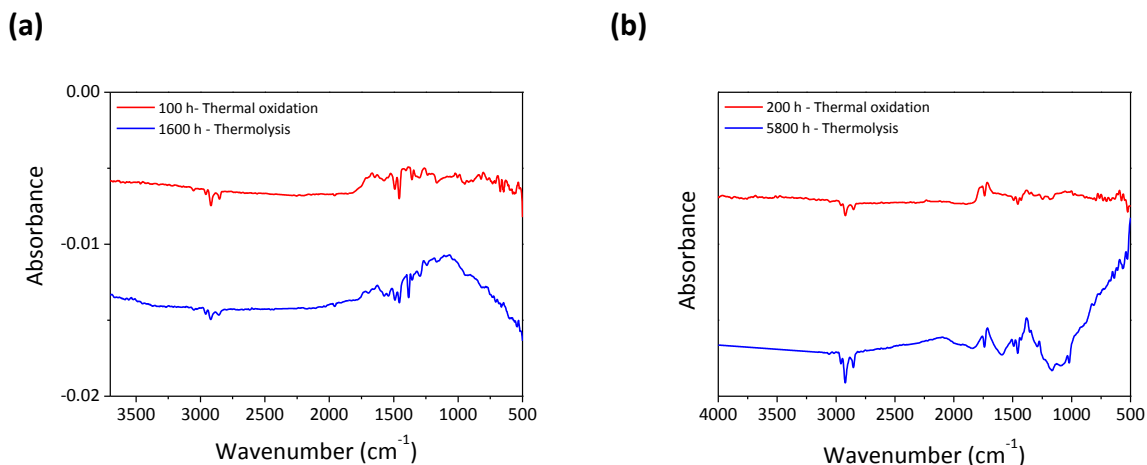
Figure 4.25. IR subtracted (calculated as 'aged – pristine') spectra of (a) P4 and (b) P4:PCBM films thermally treated in air (red line) or under vacuum (blue). For blend films, the spectra after 5 hours of thermal treatment haven been used as 'pristine' spectra in order to eliminate the influence of the initial morphological reorganisation.

(a)   **(b)**
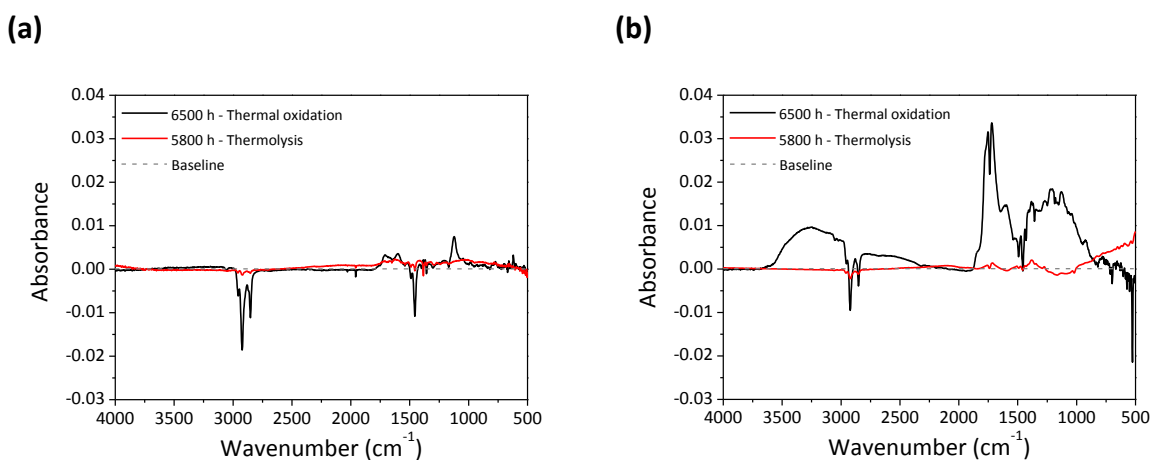
Figure 4.26. IR subtracted spectra (calculated as 'aged – pristine') of (a) P4 and (b) P4:PCBM films thermally treated in air (black line) or under vacuum (red line). For blend films, the spectrum after 5 hours of thermal treatment haven been used as 'pristine' spectrum in order to eliminate the influence of the initial morphological reorganisation.

4.3.1.3.3. <u>Natural outdoor exposure</u>

The study was completed with the irradiation of vacuum-encapsulated samples using natural outdoor exposure, carried out in Clermont-Ferrand (France) over a 10 month period between October 2014 and September 2015. As indicated in Figure 4.27, the evolution using natural illumination is clearly similar to that observed using irradiation of Suntest except that the induced modifications occurred at a much lower rate, since after 10 months (which, considering only 5 hours of average solar

irradiation per day would correspond to approximately 1500 hours of irradiation), the absorbance loss is less than after 1440 hours, both for polymer and blend films. Importantly, in the case of the blend films, the absorbance loss of the polymer is almost negligible (~2 %) and the most marked effect is probably the increase of absorbance in the fullerene domain (320 nm) due to the dimerisation of fullerene. This effect is also observed in the control sample exposed to illumination for a period of 6 months without intermediate analysis steps [Figure 4.27 (c)]. Remarkably, this observation of PCBM dimerisation under outdoor exposure conditions is, to our knowledge, the first report of this photochemical reaction under natural illumination conditions.

(a)

(b)

(c)
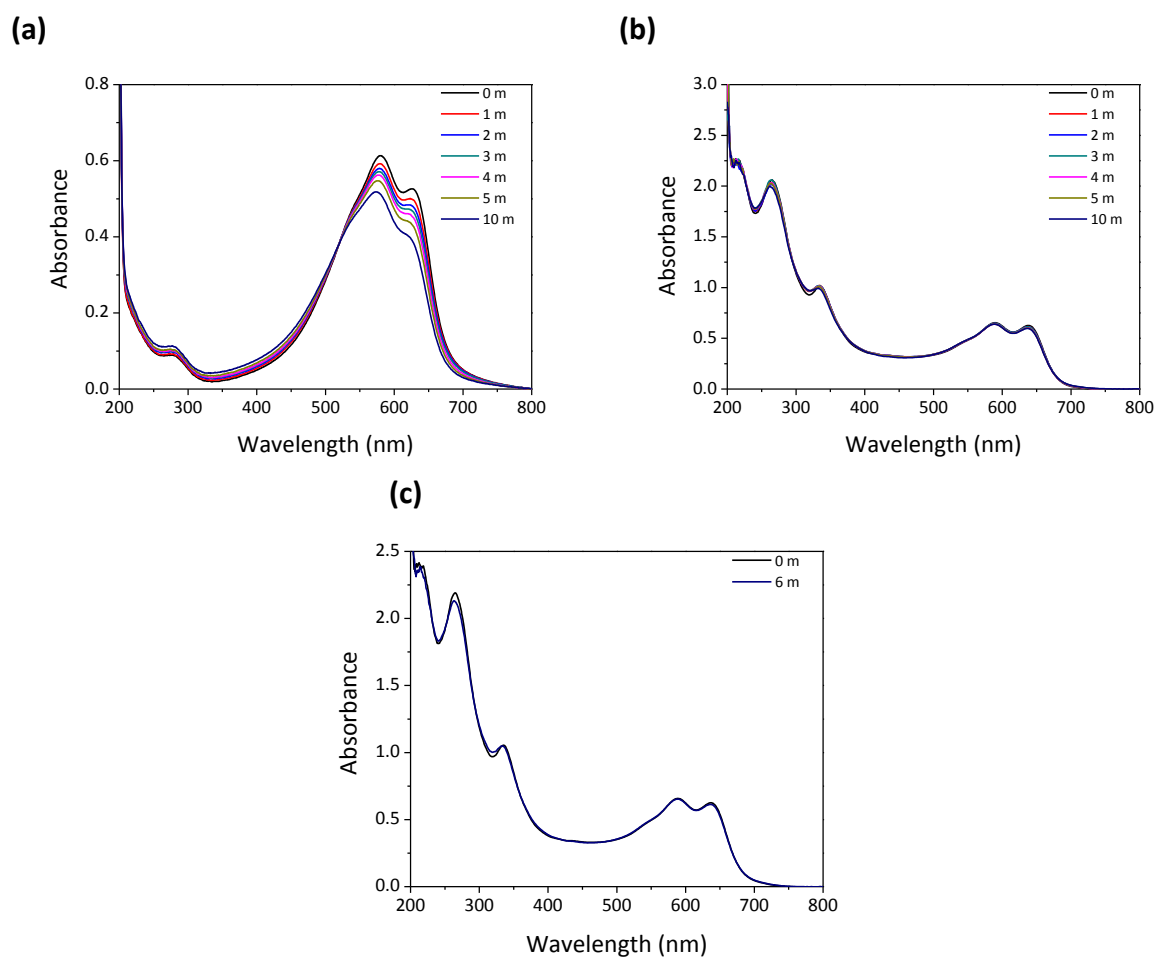
Figure 4.27. UV-Vis absorption spectra for (a) P4 and (b,c) P4:PCBM thin films encapsulated under vacuum and irradiated using natural outdoor illumination. P4:PCBM in (c) corresponds to a 'control' samples, uniquely analysed after 6 months of outdoor exposure.

In order to obtain more information about the relationship between the UV-Vis changes provoked in both polymer and blend samples using both types of irradiation, the normalised

absorbance decay for polymer and blend films aged using Suntest as Accerelated Lifetime Test (ALT) and natural Outdoor Exposure (OE) are compared in Figure 4.28. This plot highlights the good correspondence between the degradation carried out using natural and artificial illumination. Given the almost negligible modifications in terms of absorbance at 590 nm for blends photochemically treated both in Suntest and using outdoor illumination, the relationship between ALT and OE is established on the basis of the absorbance decay of neat polymer films under these conditions. According to this, approximately 100 hours of ALT degradation corresponds to 4 months of degradation under natural illumination.
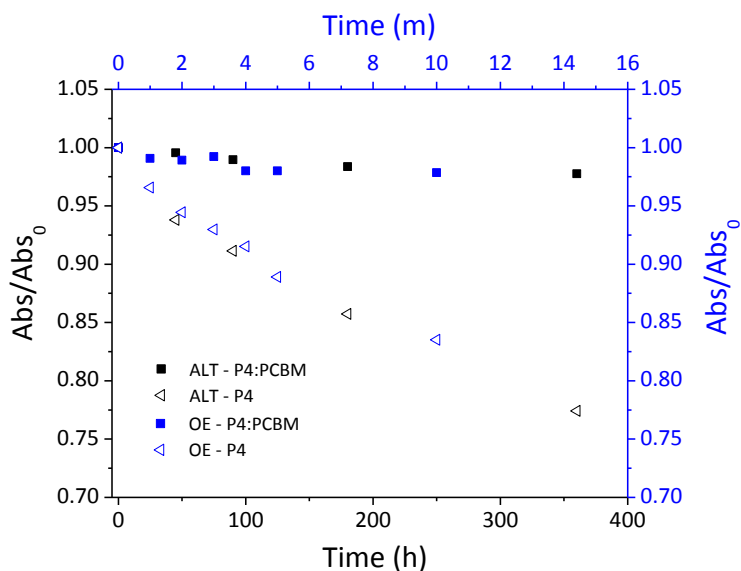
Figure 4.28. Normalised absorbance decay for thin films (P4 and P4:PCBM) exposed to irradiation using Suntest as Accelerated Lifetime Test (ALT, in black) and using natural Outdoor Exposure (OE, in blue).

Finally, the modifications in the IR spectra for both polymer and blend are equivalent to those observed for the photolysis experiments using Suntest (see Figure 4.29), particularly in the region below 1800 cm^{-1}. Interestingly, a slight increase of the characteristic band of the alkyl side chains can be observed, contrary to what was observed for the ensemble of accelerated tests, which could be due to a modification in the stretching of the aliphatic groups due to the prolonged treatment under vacuum. Focusing on the finger print region, the main modifications for polymer and blend are the decrease of the bands at 1456 cm^{-1} and 526 cm^{-1}, respectively.

(a)   **(b)**
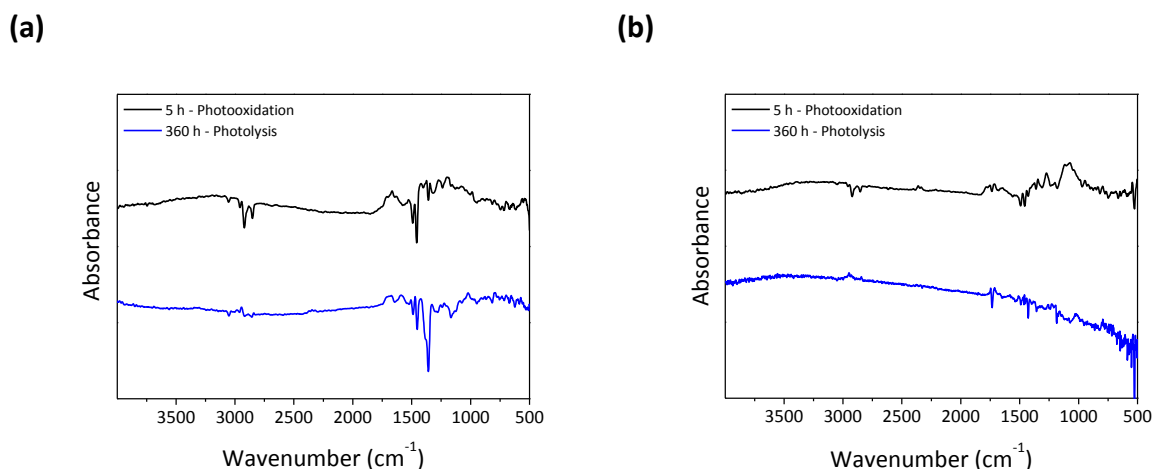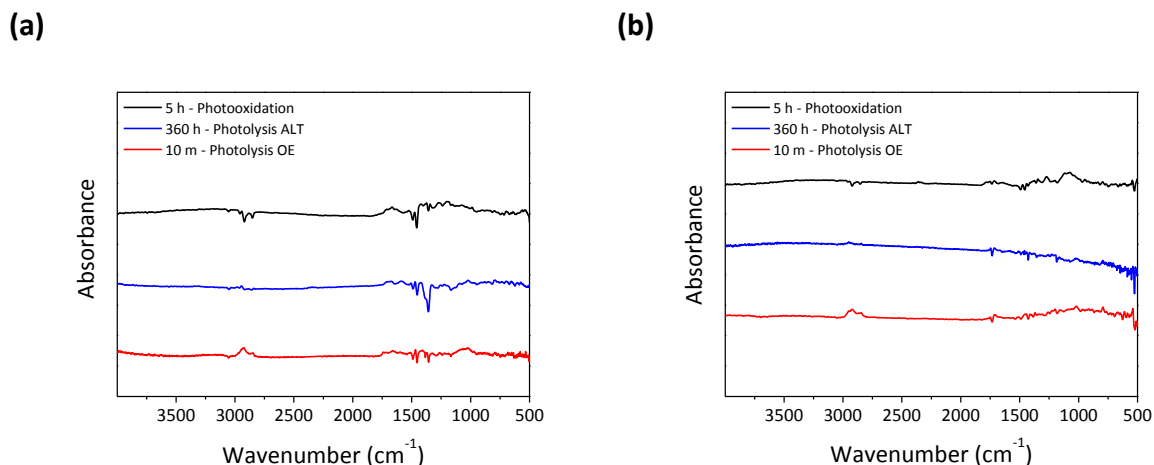

Figure 4.29. IR subtracted spectra (calculated as 'aged – pristine') for (a) P4 and (b) P4:PCBM films irradiated using an ALT in air (black line) or under vacuum (blue line), and irradiated using natural illumination (red line).

As for P4 films, the decrease of the band at 1456 cm^{-1} occurs in parallel to the decrease in absorbance (not shown), as also observed upon photooxidation or thermooxidation of the samples (see Figure 4.16). Concerning P4:PCBM films, Figure 4.30 displays the evolution of the polymer main absorption band (590 nm) and the two bands at 1456 cm^{-1} and 526 cm^{-1}, indicating slight modifications in both the absorption at 590 nm and 1456 cm^{-1}, whilst the band at 526 cm^{-1} is found to steadily decrease upon irradiation, independent of the irradiation conditions.

(a)   **(b)**
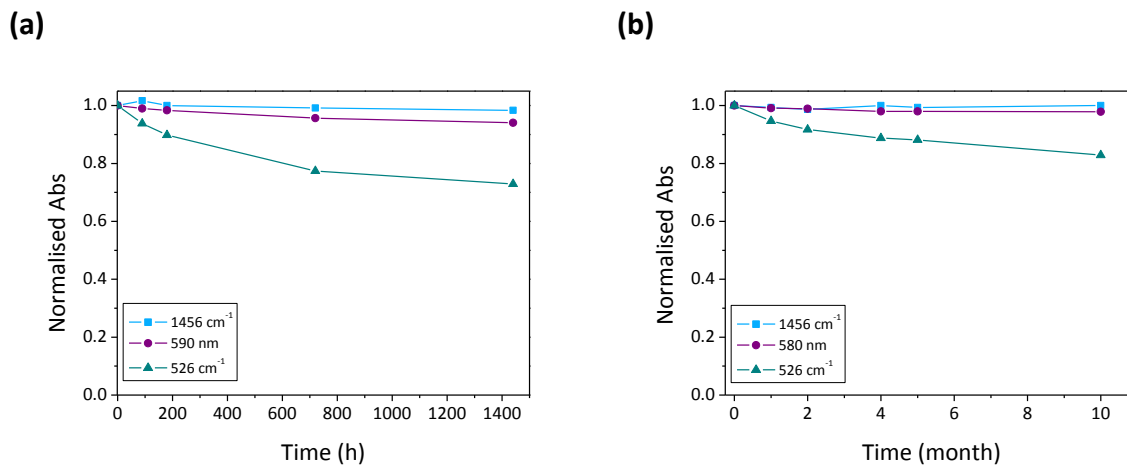
Figure 4.30. Evolution of selected bands corresponding to the polymer (590 nm) and fullerene (526 cm^{-1}) upon irradiation of P4:PCBM films using (a) an artificial or accelerated lifetime test and (b) outdoor illumination.

Notably, if the decrease of the band at 526 cm^{-1} is used as a marker of blend degradation to establish the relationship between natural and artificial conditions Figure 4.31, the aforementioned equivalence (100 hours of ALT degradation corresponding to 4 months of OE degradation) can be again demonstrated.
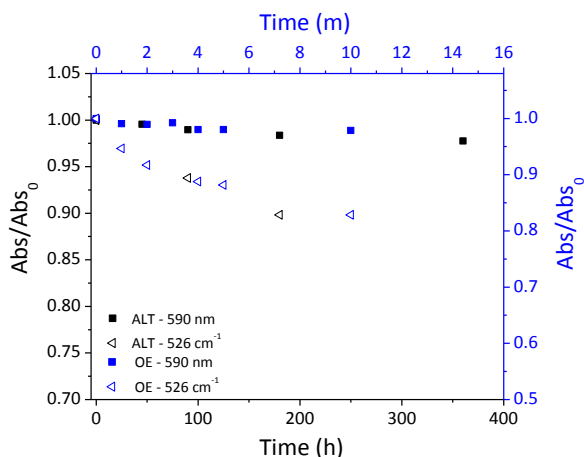
Figure 4.31. Normalised absorbance decay for the bands at 590 nm and 526 cm^{-1} exposed to irradiation using Suntest as Accelerated Lifetime Test (ALT, in black) and using natural Outdoor Exposure (OE, in blue).

4.3.1.4. Summary

Table 4.2 summarises the absorbance loss in polymer and blend films exposed to the different degradation conditions examined in this chapter. Linear fits have been applied in all cases to calculate the rate of absorbance loss (established as the degradation rate) and the stabilisation factor imparted by PCBM under these conditions has been calculated as the quotient rate$_{polymer}$/rate$_{blend}$.

Table 4.2. Summary of the degradation rates calculated for the different experiments in this chapter, where SF is the stabilising factor imparted by PCBM.

		Thermal treatment at 100 °C		Suntest		Natural Outdoor Exposure	
		Rate h^{-1}	SF	Rate h^{-1}	SF	Rate m^{-1}	SF
Ambient air	P4	$(-1.75 \pm 0.05)\ 10^{-3}$	~10	$(-4.6 \pm 0.4)\ 10^{-2}$	~5		
	P4:PCBM	$(-1.72 \pm 0.03)\ 10^{-4}$		$(-9.4 \pm 0.7)\ 10^{-3}$			
Vacuum	P4	$(-1.8 \pm 0.6)\ 10^{-4}$	~5	$(-5.9 \pm 0.7)\ 10^{-4}$	~10	$(-2.0 \pm 0.2)\ 10^{-2}$	~10
	P4:PCBM	$(-3.4 \pm 0.8)\ 10^{-5}$		$(-5.7 \pm 0.4)\ 10^{-5}$		$(-1.9 \pm 0.9)\ 10^{-3}$	

According to Table 4.2, PCBM imparts a stabilising factor between 5 and 10 depending on the degradation conditions. It is noteworthy that this factor is highly dependent on several factors, such as

morphology or oxygen content, and can substantially vary depending on the marker employed to calculate it. It can also be seen from Table 4.2 that the combination of temperature with oxygen, and most notably, light with oxygen, are the most destructive for the polymer, leading to a rapid decrease in polymer absorption. Furthermore, it was demonstrated that the initial modification in thermally treated blend films is a change in morphology, which has an impact on the subsequent thermal oxidation steps. Encapsulating the samples under vacuum allowed monitoring changes occurring by light and temperature in the presence of a strongly reduced oxygen content, thus obtaining more representative conditions of encapsulated solar cells. Under these conditions, photothermal treatment of the samples led to reduced degradation rates in all cases. Furthermore, UV-Vis and IR analysis of samples treated under vacuum permitted the identification of changes due to mere exposure to light or temperature (*i.e.*, PCBM dimerisation or reduction in polymer crystallinity), although the contribution of prolonged vacuum encapsulation towards certain modifications should not be neglected. Finally, irradiation under photolysis conditions has allowed the comparison between artificial and natural light exposure, indicating that 100 h of irradiation using Suntest corresponds to approximately 4 months of natural sunlight illumination.

4.3.2. Photochemical degradation of P4-based inverted solar cells

4.3.2.1. Photoelectrical behaviour of non-encapsulated solar cells

This section reports the behaviour under photooxidative conditions of inverted solar cells comprising a P4:PCBM (1:2) active layer, with PEDOT:PSS and PEI used as hole transport layer and electron transport layer, respectively. Cells were not encapsulated, and a permeable silver top electrode of only 50 nm thickness was evaporated in order to prevent the degradation from being oxygen diffusion controlled.
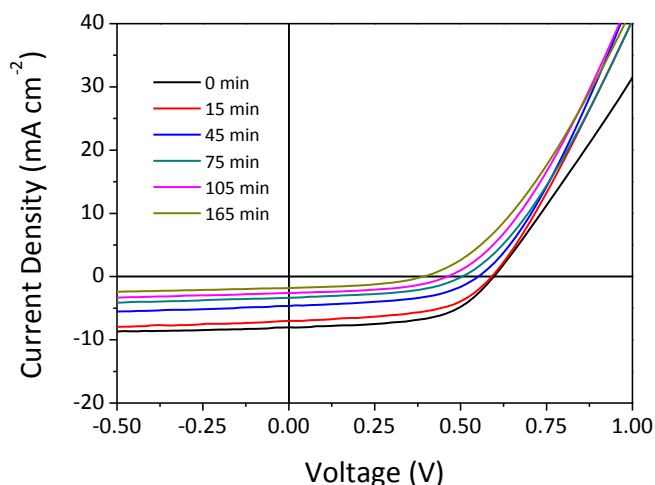
Figure 4.32. Current-voltage characteristics of an inverted solar cell based on P4:PCBM upon irradiation in dry synthetic air.

Figure 4.32 shows the recorded current-voltage characteristics of one representative cell during the course of degradation. The injection current under forward bias conditions (*i.e.*, the current density at +1 V) is found to slightly increase during the very early stages, which can be attributed to a certain heating-up of the samples (to ~40 °C) upon illumination, facilitating charge mobility. After which, the injection current remains, however, constant. Moreover, the open-circuit voltage (V_{OC}), the fill factor (FF), and especially the short-circuit current density (j_{SC}) dramatically decreases within minutes (see also Figure 4.33). After 45 min, the PCE already dropped to ~50% of its initial value, which is mainly the result of a loss in j_{SC} by ~40%. By this time, the V_{OC} and the FF decreased by 6% and 13%, respectively. It is noteworthy that the degradation in all parameters was partially reversible upon annealing for 5 min at 130 °C under inert atmosphere (not shown). Overall, the observed changes follow

typical degradation behaviour, in terms of both quality and rate, compared to previous studies on organic solar cells with this architecture.[16, 238, 290]

Figure 4.33. Temporal evolution of the power conversion efficiency (PCE), the fill factor (FF), the short-circuit current density (j_{SC}), and the open-circuit voltage (V_{OC}) of inverted P4:PCBM solar cells upon irradiation in dry synthetic air.

The origin of this degradation is reported to undoubtedly stem from photooxidation of the conjugated polymer.[6-8] The underlying reaction mechanism of this photooxidation, as well as the way it affects the device performance, is, however, of a two-fold nature. Firstly, chemical photooxidation of the polymer leads to the formation of oxidation products (see Sections 3.3.1 and 4.3.1), which can, on the one hand, act as quenching centres for excitons and, by this, reduce the overall charge generation. On the other hand, these oxygen-containing defects form deep trap states for charges and consequently impede charge extraction in the device. This type of photooxidation of the polymer and the related device performance losses are not reversible upon annealing. Furthermore, and in line with the results presented in Section 4.3.1, oxidation of the fullerene itself could similarly contribute towards this reduction in charge generation.

Secondly, as discussed in Section 3.1.1.1.2, irradiation of conjugated polymers in air can lead to the formation of a charge-transfer complex with superoxide *via* electron transfer from the polymer exciton to molecular oxygen.[199-201] This species causes an increased steady-state concentration of charge carriers in the active layer. More precisely, it concerns mobile holes, which are delocalised over the polymer backbone, and immobile electrons being trapped on the oxygen. In the photovoltaic device, this mismatch of charge mobilities leads to the formation of a space charge region close to the negative electrode, which shields the internal electric field and consequently hinders charge extraction.[16] Remarkably, the charge-transfer complex between polymer cation and superoxide anion is a metastable complex at room temperature that can be split-up by heat or vacuum treatment,[200-201] which also makes the related device degradation reversible under these conditions (not shown).

The results presented herein on the degradation of solar cells under photooxidative conditions are now compared to those obtained upon photochemical treatment in air of isolated P4:PCBM films (see Section 4.3.1.2.1). As aforementioned, inverted photovoltaic devices based on P4:PCBM lose ~50 % of their initial power conversion efficiency within 45 min under these conditions (see Figure 4.33). In turn, considering the linear fit applied to the polymer absorbance loss in the blend films in Figure 4.6, an exposure time of 45 min correlates with a loss of only ~0.7 % in polymer absorbance. This factor of ~70 between the PCE loss of P4:PCBM-based solar cells and the corresponding decrease in polymer absorbance proves that the reduction in absorption is not directly responsible for the decrease in device performance, as still 99.3 % of the absorbance is maintained while already half of the efficiency is lost. Furthermore, the sensitivity of IR spectroscopy is not sufficient for detecting the low concentration of polymer oxidation products at a stage in which these species already significantly impact the solar cell performance. In this regard, very sensitive techniques, such as electronic paramagnetic resonance or pump-probe spectroscopy, have been revealed as powerful tools to unveil the cause for device degradation under photooxidative conditions.[200-201, 290] Using to the latter, Karuthedath *et al.*[290] indicated, for different polymer:fullerene blends, that such degrees of photooxidation (< 2 % absorbance loss) do not even significantly influence the overall charge generation yield. They reported instead that an enhanced charge recombination yield, caused by a reduction in charge carrier mobility, was responsible for the observed losses in device performance.

4.3.2.2. Photoelectrical behaviour of encapsulated solar cells

The fast degradation of organic solar cells under operation in air, as shown for P4:PCBM in Section 4.3.2.1, requires good packaging of the devices to ensure sufficient lifetimes. Thus, focus now is placed on the behaviour of encapsulated inverted solar cells based on a P4:PCBM layer upon irradiation in Suntest. The device architecture and layer stack are the same as used in the previous chapter, but with an additional variation in the electron transport layer, namely PEI *versus* ZnO. The initial statistics of all cells are depicted in a boxplot in Figure 4.34.
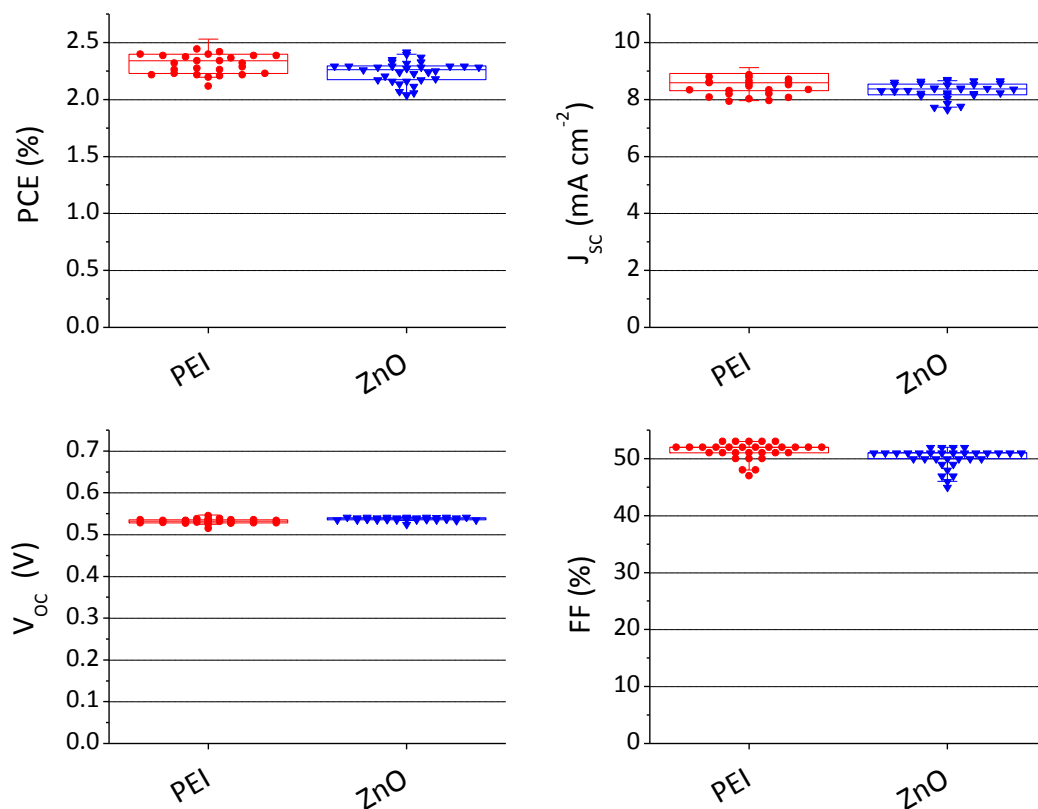
Figure 4.34. Initial performance of encapsulated inverted P4:PCBM solar cells comprising two different electron transport layers, namely PEI and ZnO.

The initial performance of all manufactured devices was similar, independent of the type of electron transport layer; the average values of the key parameters being PCE = 2.3%, j_{SC} = 8.5 mA cm^{-2}, V_{OC} = 0.54 V, and FF = 51 %. Deviation from these mean values was relatively low. All of these cells (30 of each variation) were exposed to irradiation using Suntest, configured at 750 W m^{-2} at 60 °C just as for the polymer and blend films in Section 4.3.1.3.1. Figure 4.35 shows the recorded current-voltage characteristics of one representative cell of each variation during the course of degradation.

(a)　　　　　　　　　　　　　　　　　　　　**(b)**
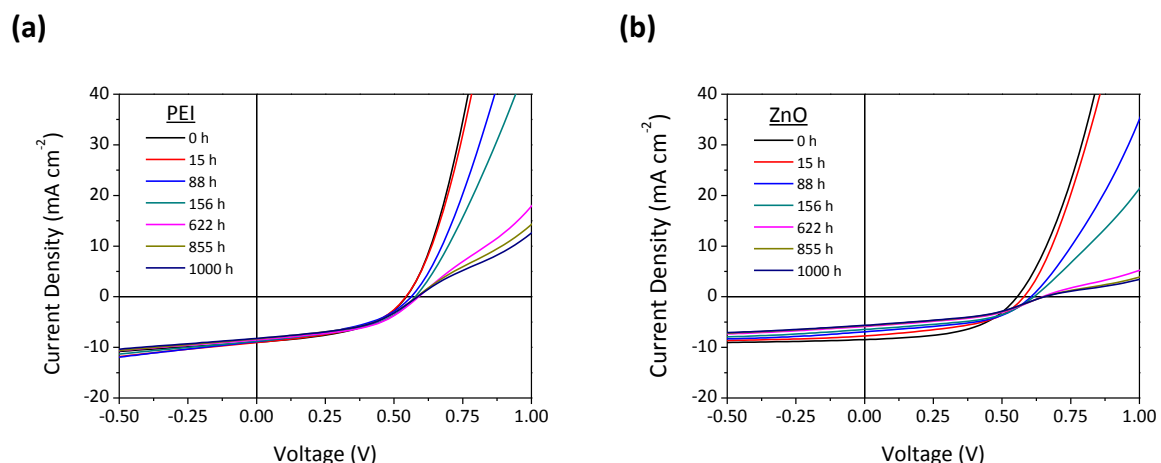
Figure 4.35. Current-voltage characteristics of encapsulated inverted P4:PCBM solar cells comprising two different electron transport layers, namely (a) PEI and (b) ZnO, upon irradiation in Suntest.

PEI-containing cells [Figure 4.35 (a)] exhibit a slight shunt in their initial state which becomes less prominent at later stages of the experiment, as shown by the slopes of the j-V curves at reverse bias (-0.50 V). In addition, a steady decrease in injection current (upper right quadrant of the plot) during the course of degradation was observed, which led to the formation of an S-shape (also known as 'second diode') after 622 h. However, this second diode does not influence the maximum power point of the j-V curve in the fourth quadrant, meaning that it does not decrease the solar cell efficiency. For devices containing ZnO as electron transport layer [Figure 4.35 (b)] the same decrease in injection current occurs, but even more pronounced than in the case of PEI. Such a decrease in injection current was not observed in the photooxidation experiment in Section 4.3.2.1, which indicates that slow oxygen ingress through the encapsulation foil is not the reason for this evolution. Instead, the injection loss might be caused by any intrinsic degradation, for instance induced by light or heat. Moreover, the ZnO cells exhibit another type of degradation behavior in their j-V curves, which dramatically affects the operation regime of the photovoltaic device (*i.e.* the fourth quadrant). This second mechanism, which is not present in the case of PEI, mainly decreases the short-circuit current and the fill factor of the solar cell (see also Figure 4.36).

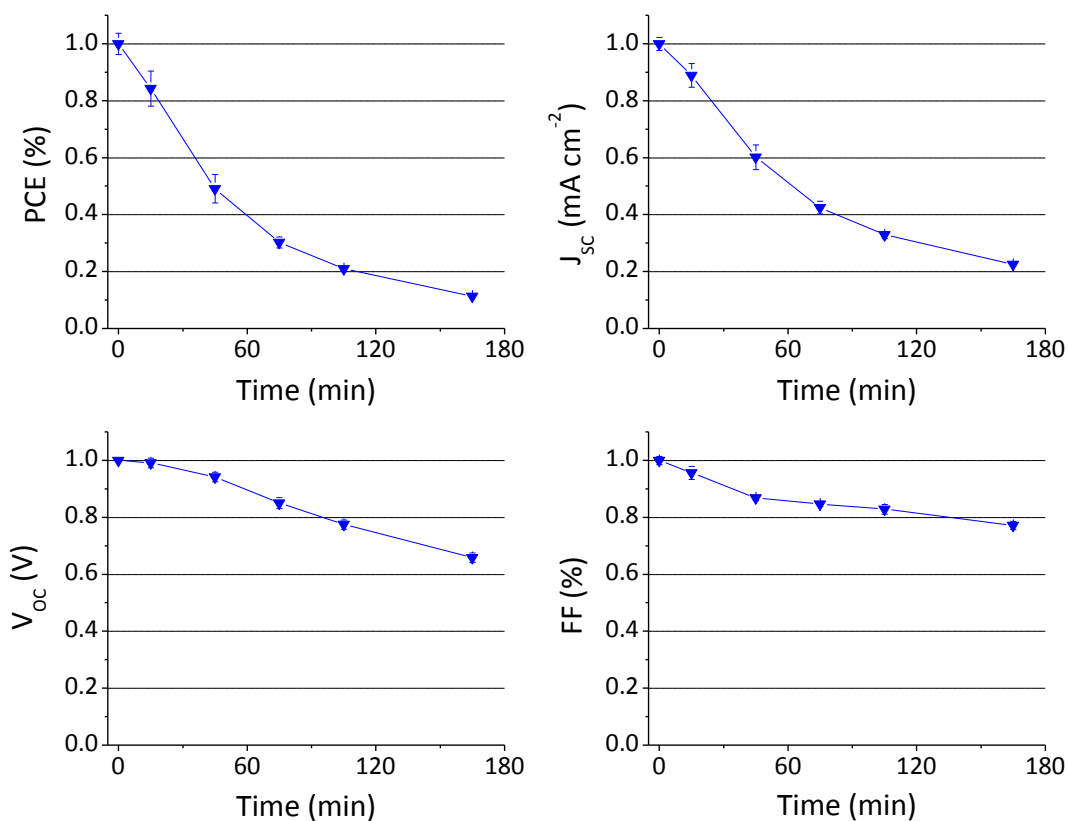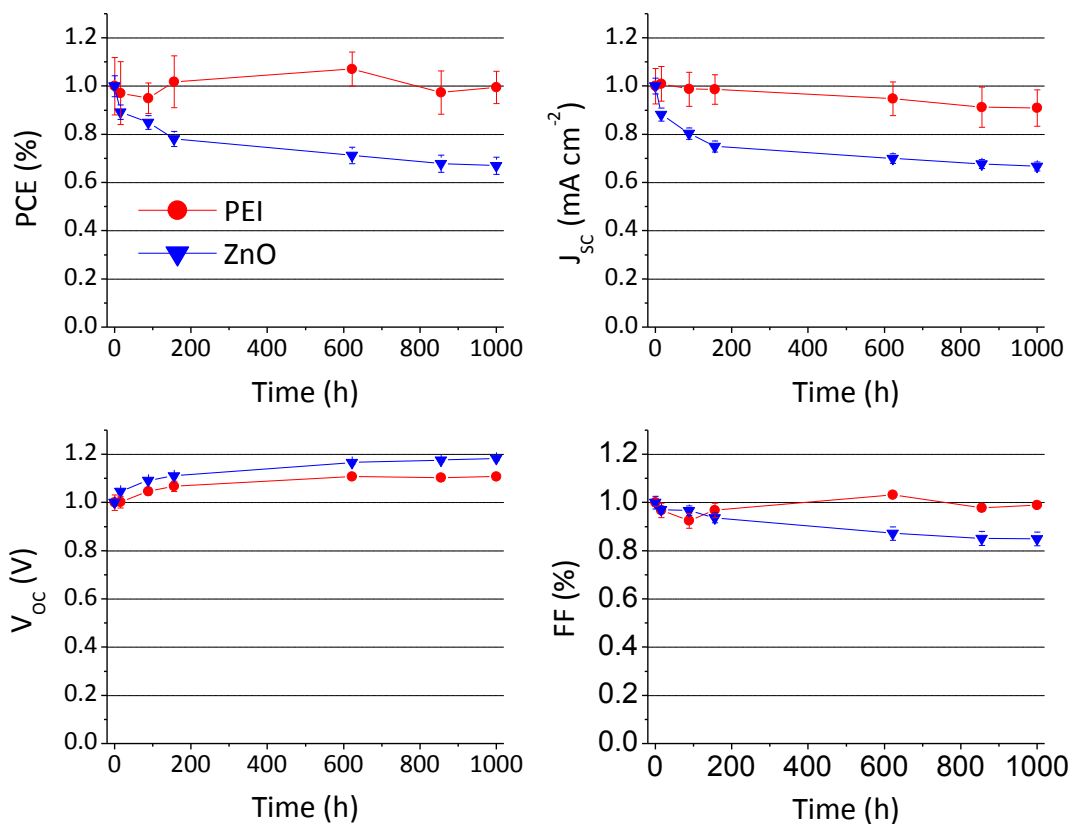**Figure 4.36. Temporal evolution of the power conversion efficiency (PCE), the short-circuit current density (j$_{SC}$), the open-circuit voltage (V$_{OC}$), and the fill factor (FF) of encapsulated inverted P4:PCBM solar cells comprising two different electron transport layers, namely PEI (red circles) and ZnO (blue triangles) upon irradiation in Suntest.**

Figure 4.36 shows the evolution of the device parameters during the course of the experiment. After 1000 h of irradiation, the PCE of the ZnO devices decreased by 33 %, whereas no loss at all was observed for the cells comprising PEI. In the case of PEI, 10 % loss in j$_{SC}$ was compensated by a 10 % rise in V$_{OC}$. The increase in V$_{OC}$ may correlate with the decrease in injection current, as both effects are more pronounced for ZnO compared to PEI. Accordingly, a slow, but steady, morphological change inside the active layer induced by temperature could be responsible for both observations. Also, the initial decrease in FF for both PEI and ZnO-containing devices could be due to PCBM photodimerisation.[243] The main difference in degradation between the devices comprising two different electron transport layers was the pronounced loss in short-circuit current by > 30 % within 1000 h in the case of ZnO. Such an exponential loss in j$_{SC}$ upon irradiation of ZnO-containing organic solar cells under inert atmosphere has already been reported in the literature, however, the exact origin remains unclear.[296-297] This observation suggests intrinsic light stability problems inside the ZnO layer or at the

interface with the active layer. Conversely, the stable performance of the PEI devices up to 1000 h indicates that no crucial degradation takes place in the other parts of the solar cell, including the active layer.

Finally, these results were combined with the outcome of the study on isolated films correlating Suntest and outdoor exposure (Section 4.3.1.3.3), in order to obtain an estimation of the lifetime of these devices under real operating conditions. In these experiments, 100 h of irradiation in Suntest has been correlated to an outdoor exposure period of 4 months. According to which, the device degradation experiment of 1000 h in Suntest herein presented is equivalent to 40 months of outdoor operation (assuming a linear relationship between the protocols). This implies that P4:PCBM devices with PEI, which exhibited absolutely no PCE loss during 1000 h in Suntest, would probably show a stable performance for at least 3.3 years under outdoor operation. As the 'lifetime' of a solar cell usually tolerates a loss of 20 % in power conversion efficiency,[298] the expected lifetime of these cells can be even higher, most likely > 10 years, if no other degradation takes place.

4.4. Conclusions

Chemical and morphological changes in P4 and P4:PCBM films upon degradation using both artificial ageing conditions (light, temperature) and natural outdoor illumination have been monitored using IR and UV-Vis spectroscopy. Thermal and photochemical treatment of samples in the presence of oxygen led to markedly higher degradation rates than upon vacuum encapsulation of the samples. Furthermore, it was verified the stabilising effect imparted by PCBM towards the degradation of the polymer, to different extents depending on the degradation treatment and the blend morphology. Overall, treatments in the presence of oxygen led to the oxidation of both polymer and fullerene; additionally, temperature was observed to cause changes in the morphology of the blend. Samples encapsulated under vacuum (which are more representative of the behaviour of encapsulated solar cells) displayed modifications due to pure temperature treatment (*e.g.*, morphological reorganisation of the blend) or light exposure, such as PCBM dimerisation. Importantly, PCBM dimerisation was also observed for samples exposed to outdoor illumination. Finally, comparison between artificial and natural illumination indicated that 100 h of irradiation using Suntest corresponds to approximately 4 months of outdoor exposure.

Concerning the photostability of P4:PCBM-based inverted solar cells, the very detrimental effect caused by light in combination with oxygen was firstly verified for non-encapsulated samples, provoking a 50 % PCE loss within 45 min. In turn, such a decay in efficiency stems from photoinduced reversible and irreversible oxidation in the active layer, which leads to a reduction in charge mobility and enhanced charge recombination. In agreement with this, encapsulated solar cells were shown to be more resistant to light exposure due to the reduced presence of oxygen, although clear effects ascribed to the use of different electron transport layers were identified. Major degradation issues were observed for cells using ZnO as ETL, indicating intrinsic stability problems of this layer or at its interface with the active layer. Notably, cells containing PEI as ETL displayed no PCE losses for the entire duration of the experiment (1000 h), which could be extrapolated to an outdoor operation of 3.3 years owing to the study on separate active layers exposed to irradiation under natural and artificial illumination.

General Conclusions

The establishment of OSCs in the market requires the improvement of device operational lifetimes, for which the development of materials with higher intrinsic stabilities is mandatory. To this end, research within the ESTABLIS project has been conducted towards the elucidation and amendment of OSC degradation mechanisms, among which are delamination, arising from a lack of adhesion between the active layer and the hole transport layer, and photochemical degradation of the active layer.

The first part of the work (Chapter 2) concerned the synthesis and application of an amphiphilic block copolymer as a thin adhesive interlayer, to overcome the delamination issues reported at the interface between the active layer and PEDOT:PSS (hole transport layer) in inverted devices. The adhesive material proposed in this work is poly(3-hexylthiophene)-*block*-poly(*p*-styrene sulfonate) (P3HT-*b*-PSS), whose structural characteristics reflect a combination of the components in the active layer (P3HT:PCBM) and the hole transport layer (PEDOT:PSS). The strategy adopted to produce such an amphiphilic block copolymer included separate synthesis of the P3HT block and an alkyl-protected precursor of the PSS block, both conveniently functionalised to be subsequently coupled using 'click' chemistry. After which, thermal treatment allowed for deprotection of the alkyl-protected sulfonic groups in PSS, yielding the target P3HT-*b*-PSS amphiphilic block copolymer. Since microphase separation of block copolymers is highly dependent on both the chemical characteristics and the size of the different blocks, the synthesis of these segments requires great control over the polymer molar mass and dispersity. Thus, the first part of this chapter was devoted to studies of the controlled synthesis of poly(*p*-neopentyl styrene sulfonate), PNSS, using Reversible Addition-Fragmentation chain Transfer (RAFT) polymerisation. To this end, different chain transfer agents (BTTC-N_3 and DTTC-N_3, bearing a primary or tertiary leaving group, respectively), initial monomer concentrations (0.8, 1.3, and 4.0 M), solvents (THF, anisole, and toluene) and temperatures (60 °C, 75 °C) were investigated to identify the optimum conditions ([NSS]$_0$ = 4.0 M, DTTC-N_3 in anisole at 75 °C) to obtain well-defined PNSS of varied molar masses and unimodal distributions. After which, the synthesis of the triblock poly(neopentyl *p*-styrene sulfonate)-*b*-polybutadiene-*b*-poly(neopentyl *p*-styrene sulfonate) by azide-alkyne 'click' chemistry and its subsequent thermal treatment to yield its amphiphilic analogous, allowed verifying both the end group fidelity (N_3) in the RAFT process and the utility of the general

strategy to produce amphiphilic block copolymers. Accordingly, this same approach was developed to synthesise poly(3-hexylthiophene)-*block*-poly(neopentyl *p*-styrene sulfonate), P3HT-*b*-PNSS, copolymers with varying PNSS block lengths.[111] Surface characterisation of P3HT$_{50}$-*b*-PNSS$_{10}$, P3HT$_{50}$-*b*-PNSS$_{30}$, P3HT, and PNSS thin films was carried out by means of Atomic Force Microscopy (AFM) working in classical Tapping mode and Peak Force mode in order to obtain information about the modifications induced by the thermal deprotection treatment (5 h at 150 °C). Analysis of the topography images and the adhesion forces established between the AFM tip and the different samples led to the conclusion that, in the investigated copolymers, the PNSS block could be possibly located at the surface level and at least partially deprotected even before thermal treatment. Finally, on the basis of the results obtained for the polymerisation of NSS, RAFT polymerisation was further explored to produce a series of systematically varied alkyl-protected PSS derivatives, in the quest for materials with improved thermal lability.[180] Thermogravimetric analysis (TGA) of the different R-varied polymers identified poly(isobutyl *p*-styrene sulfonate) as the best performing alkyl-protected derivative, exhibiting a fine compromise between lability upon thermal treatment and room temperature stability. Accordingly, incorporation of this polymer into P3HT$_{50}$-*b*-PiBSS$_{14}$ indicated shorter deprotection times (around 45 minutes) compared to the 3 hours required for the PNSS-based analogous copolymer.

In summary, the work developed towards the fabrication of thin interlayers for OSCs has successfully led to the synthesis of thermally-triggerable, alkyl-protected PSS-based block copolymers. Furthermore, the characteristics of these block copolymers towards their application in OSCs have been improved, as reflected in the reduction in deprotection time needed in P3HT-*b*-PiBSS compared to previously synthesised P3HT-*b*-PNSS.[111, 180] Nevertheless, the work herein would benefit from additional experiments to complete the presented results. Concerning the length of the PSS segment in the synthesised block copolymers, although PNSS with varied molar masses and low dispersity ($Đ \leq 1.50$) has been obtained, achieving high molar mass PNSS was difficult using the optimised RAFT system. A possible approach to resolve this issue would be to conduct the RAFT polymerisation using higher pressures than ambient or under emulsion conditions, as modifying these parameters has been reported to yield higher molar mass polymers.[135, 299] Thus, analysing the systematic influence of these parameters would complement the study and optimisation of the RAFT polymerisation of PNSS. Besides, studies on the incorporation and effect of this interlayer in inverted solar cells are inexistent so far. This would require, firstly, optimisation of the processing conditions (solvent, layer thickness, thermal annealing conditions), so that the introduction of this interlayer in the device would not

detrimentally affect device performance, or, more pertinently, even enhance it. Since the proposed interlayer is to be coated on top of the active layer, applying the thermal deprotection step can dramatically influence the bulk heterojunction morphology, and, consequently, device performance. In this sense, and in light of the results obtained with AFM on the thermal deprotection of P3HT-*b*-PNSS which suggest surface deprotection pre-thermal treatment, it would be interesting to analyse the implementation of this interlayer applying no thermal annealing or shorter annealing steps than those dictated by TGA of these copolymers. Finally, characterisation of the effect of this interlayer towards adhesion at the interface between the active layer and PEDOT:PSS would be required, using techniques like the double cantilever beam[11] or tack tests,[300] and subjecting devices with and without this interlayer to severe tests like damp heat (65 °C/ 85 °C, 85 % relative humidity).[6]

The second major component of the manuscript, comprising Chapters 3 and 4, examines the photostability of low bandgap polymers and blends for the active layer. Firstly, the photooxidation of poly[(4,4'-bis(2-ethylhexyl) dithieno [3,2-b:2',3'-d]silole)-2,6- diyl-*alt*-(4,7-bis(2-thienyl)-2,1,3-benzothiadiazole)-5,5'-diyl] (Si-PCPDTBT) thin films was monitored using a range of analytic techniques (UV-Vis and IR spectroscopy, headspace solid-phase microextraction coupled with gas chromatography/mass spectrometry, HS-SPME-GC-MS, AFM), combined with theoretical calculations. In line with studies on other p-type polymers, side chains continuously degraded from the beginning of irradiation, and oxidation processes in the polymer backbone involve the oxidation of the thiophene rings. Furthermore, calculations indicated that including silicon as a bridging atom to the side chains makes hydrogen abstraction in the side chain less favoured than when the bridging atom is a carbon. The absolute degradation rate in Si-PCPDTBT was identified to be independent of initial thickness of the films, whilst irradiating the samples with higher UV content increased the rate of oxidation. After this, the parameters and structural factors determining the photooxidation rate of a series of low bandgap polymers with systematically modified backbones and/or alkyl side chains (denoted as P1 – P4, and P5a,b,c) were assessed and compared to reference polymers (Si-PCPDTBT, its carbon-analogous C-PCPDTBT, and P3HT). According to the results presented herein, the stability of each polymer was dictated by the specific donor-acceptor combination in each case, and not by the intrinsic (de)stability of a certain building block. A clearer correlation concerning the photooxidation rate in these polymers, was established when the crystallinity of the different polymer films, as determined by XRD, was taken into account. The predominantly crystalline polymer (P1 and P5a-c) films displayed medium to high photostability (and no blue-shift in the UV-Vis spectra upon degradation), whereas

more amorphous polymers (P2, P3, P4) showed medium to low photostabilities (and strong blue-shift in their absorption spectra). Furthermore, the higher content of organic paramagnetic species in P5a and C-PCPDTBT, as determined by means of EPR, was found to enhance their oxidation rates. Finally, the analysis of these polymers blended with [6,6]-phenyl-C61-butyric acid methyl ester (PCBM) indicated that, independent of the stability of the neat polymer, the photooxidation rate of the blend is dictated by the (de)stabilising effect that PCBM has over each polymer, whilst under highly reduced oxygen content, photodimerisation of PCBM prevails.

Finally, Chapter 4 constitutes a multiscale approach to the photothermal degradation processes occurring in the active layer of P4:PCBM-based inverted solar cells. To this end, chemical and morphological changes in P4 and P4:PCBM films upon degradation in air/under vacuum, using both artificial ageing conditions (light, temperature) content and/or natural outdoor illumination, were monitored using IR and UV-Vis spectroscopy. Similarly, cells were exposed to artificial illumination either in the presence of oxygen or encapsulated using a flexible barrier foil. In all cases, degradation was enhanced in the presence of oxygen, both concerning the photothermal degradation of polymer and blend films and the photoelectrical behaviour of the cells. Furthermore, under strongly reduced oxygen content, changes due to pure thermal and photochemical treatments were observed, *i.e.* morphological reorganisation of the blend and photodimerisation of PCBM. Importantly, PCBM dimerisation was also observed for samples exposed to outdoor illumination. As for encapsulated solar cells, whilst major degradation issues were observed for cells containing ZnO, cells processed with polyethyleneimine (PEI) exhibited no performance losses for an irradiation period of 1000 h using artificial light, which could be extrapolated to 3.3 years of operation under ambient conditions. Furthermore, since the definition of device 'lifetime' tolerates up to 20 % of performance loss, the operational lifetime of these devices could be even longer, possibly over 10 years if no other degradation mechanism takes place. Overall, these results highlight the need for considering the cell as a whole, in which the judicious selection of solar cell constituents and suitable encapsulating materials plays a decisive role towards the preservation of power conversion efficiencies over the operating lifetime of devices.

Given the strong relationship between resistance to photooxidation and polymer crystallinity, further work includes the optimisation of the methods employed in X-ray diffraction (XRD) and Rapid Heat-Cool Calorimetry (RHC) to obtain information about the crystallinity in different polymers films. To this end, polymer and blend films are currently being characterised using RHC, complementing the

study reported herein on the polymers as powder. Furthermore, X-ray characterisation of the films should be optimised to permit one to detect all the diffraction peaks in the samples. Additionally, despite the ability of PCBM to stabilise, in the majority of cases, the photothermal oxidation of the polymers in the active layer (possibly in detriment to its own stability), there exist stability issues associated with its use in the blend, namely dimerisation[243] and phase-segregation.[89-90] Thus, it appears interesting studying the stability of blends composed by other (non-fullerene) acceptors, for example, in all-polymer solar cells. It must be noted that reports on the stability of these all-polymer blends are scarce, so far. Finally, given the sensitivity of pump probe spectroscopy to discern the causes for power efficiency loss due photooxidation in the active layer, blend films exposed to irradiation using outdoor exposure and accelerated lifetime tests have been analysed by Shafkath Karuthedath and Dr. Larry Lüer, also members of the ESTABLIS project, working at IMDEA Nanociencia, Madrid. This study is expected to complement the information obtained by UV-Vis and IR spectroscopy.

Bibliography

1.   Morton, O., Solar Energy: A New Day Dawning?: Silicon Valley Sunrise. *Nature* **2006**, *443*, 19-22.

2.   Kippelen, B.; Bredas, J.-L., Organic Photovoltaics. *Energy & Environmental Science* **2009**, *2*, 251-261.

3.   Zhang, M.; Lin, P.; Yang, M.; Yan, F., Fabrication of Organic Electrochemical Transistor Arrays for Biosensing. *Biochimica et Biophysica Acta (BBA) - General Subjects* **2013**, *1830*, 4402-4406.

4.   Nguyen, T. P.; Le Rendu, P.; Long, P. D.; De Vos, S. A., Chemical and Thermal Treatment of PEDOT:PSS Thin Films for Use in Organic Light Emitting Diodes. *Surface and Coatings Technology* **2004**, *180-181*, 646-649.

5.   http://www.nrel.gov/ncpv/images/efficiency_chart.jpg. (accessed 8/10/2015).

6.   Jørgensen, M.; Norrman, K.; Gevorgyan, S. A.; Tromholt, T.; Andreasen, B.; Krebs, F. C., Stability of Polymer Solar Cells. *Advanced Materials* **2012**, *24*, 580-612.

7.   Grossiord, N.; Kroon, J. M.; Andriessen, R.; Blom, P. W. M., Degradation Mechanisms in Organic Photovoltaic Devices. *Organic Electronics* **2012**, *13*, 432-456.

8.   Jørgensen, M.; Norrman, K.; Krebs, F. C., Stability/Degradation of Polymer Solar Cells. *Solar Energy Materials and Solar Cells* **2008**, *92*, 686-714.

9.   Etxebarria, I.; Ajuria, J.; Pacios, R., Solution-Processable Polymeric Solar Cells: A Review on Materials, Strategies and Cell Architectures to Overcome 10%. *Organic Electronics* **2015**, *19*, 34-60.

10.   Rivaton, A.; Tournebize, A.; Gaume, J.; Bussière, P.-O.; Gardette, J.-L.; Therias, S., Photostability of Organic Materials Used in Polymer Solar Cells. *Polymer International* **2014**, *63*, 1335-1345.

11.   Dupont, S. R.; Oliver, M.; Krebs, F. C.; Dauskardt, R. H., Interlayer Adhesion in Roll-to-Roll Processed Flexible Inverted Polymer Solar Cells. *Solar Energy Materials and Solar Cells* **2012**, *97*, 171-175.

12.   Brand, V.; Bruner, C.; Dauskardt, R. H., Cohesion and Device Reliability in Organic Bulk Heterojunction Photovoltaic Cells. *Solar Energy Materials and Solar Cells* **2012**, *99*, 182-189.

13.   Voroshazi, E.; Verreet, B.; Buri, A.; Müller, R.; Di Nuzzo, D.; Heremans, P., Influence of Cathode Oxidation Via the Hole Extraction Layer in Polymer:Fullerene Solar Cells. *Organic Electronics* **2011**, *12*, 736-744.

14.   Yamanari, T.; Taima, T.; Sakai, J.; Tsukamoto, J.; Yoshida, Y., Effect of Buffer Layers on Stability of Polymer-Based Organic Solar Cells. *Japanese Journal of Applied Physics* **2010**, *49*, 01AC02-4pp.

15.   Norrman, K.; Madsen, M. V.; Gevorgyan, S. A.; Krebs, F. C., Degradation Patterns in Water and Oxygen of an Inverted Polymer Solar Cell. *Journal of the American Chemical Society* **2010**, *132*, 16883-16892.

16.   Seemann, A.; Sauermann, T.; Lungenschmied, C.; Armbruster, O.; Bauer, S.; Egelhaaf, H. J.; Hauch, J., Reversible and Irreversible Degradation of Organic Solar Cell Performance by Oxygen. *Solar Energy* **2011**, *85*, 1238-1249.

17.   Mateker, W. R.; Sachs-Quintana, I. T.; Burkhard, G. F.; Cheacharoen, R.; McGehee, M. D., Minimal Long-Term Intrinsic Degradation Observed in a Polymer Solar Cell Illuminated in an Oxygen-Free Environment. *Chemistry of Materials* **2015**, *27*, 404-407.

18.   Becquerel, A. E., Mémoire sur les Effets Électriques Produits sous L'influence des Rayons Solaires. *Comp. Rend. Acad. Sci.* **1839**, *9*, 561-567.

19.   Smith, W., Effect of Light on Selenium During the Passage of an Electric Current. *Nature* **1873**, *7*, 303.

20.   Pochettino, A. S., A., Photoelectric Behavior of Anthracene. *Acad. Lincei Rend.* **1906**, *15*, 355-363.

21.   McNeill, R., Siudak, R., Wardlaw, J.H., Weiss, D.E., Electronic Conduction in Polymers. I. The Chemical Structure of Polypyrrole. *Aust. J. Chem* **1963**, *16*, 1056-1075.

22.   Shirakawa, H.; Louis, E. J.; MacDiarmid, A. G.; Chiang, C. K.; Heeger, A. J., Synthesis of Electrically Conducting Organic Polymers: Halogen Derivatives of Polyacetylene. *Journal of the Chemical Society, Chemical Communications* **1977**, 578-580.

23.   http://depts.washington.edu/cmditr/mediawiki/index.php?title=the_polyene_series. (accessed 28/09/2015).

24.   Chamberlain, G. A., Organic Solar Cells: A Review. *Solar Cells* **1983**, *8*, 47-83.

25.   Deibel, C.; Dyakonov, V., Polymer–Fullerene Bulk Heterojunction Solar Cells. *Reports on Progress in Physics* **2010**, *73*, 096401-39pp.

26.   Nelson, J., Polymer:Fullerene Bulk Heterojunction Solar Cells. *Materials Today* **2011**, *14*, 462-470.

27.   Su, Y.-W.; Lan, S.-C.; Wei, K.-H., Organic Photovoltaics. *Materials Today* **2012**, *15*, 554-562.

28.   Tang, C. W., Two-Layer Organic Photovoltaic Cell. *Applied Physics Letters* **1986**, *48*, 183-185.

29.   Fung, D. D. S., Choy, W. C. H., Introduction to Organic Solar Cells. In *Organic Solar Cells: Materials and Device Physics*, Choy, W. C. H., Ed. Springer-Verlag London, 2013; pp 1-16.

30.   Yu, G.; Gao, J.; Hummelen, J. C.; Wudl, F.; Heeger, A. J., Polymer Photovoltaic Cells: Enhanced Efficiencies Via a Network of Internal Donor-Acceptor Heterojunctions. *Science* **1995**, *270*, 1789-1791.

31.   van Bavel, S. S.; Bärenklau, M.; de With, G.; Hoppe, H.; Loos, J., P3HT/PCBM Bulk Heterojunction Solar Cells: Impact of Blend Composition and 3D Morphology on Device Performance. *Advanced Functional Materials* **2010**, *20*, 1458-1463.

32.   He, Z.; Zhong, C.; Su, S.; Xu, M.; Wu, H.; Cao, Y., Enhanced Power-Conversion Efficiency in Polymer Solar Cells Using an Inverted Device Structure. *Nat Photon* **2012**, *6*, 591-595.

33.   Brabec, C., Waldauf, C. Photovoltaic Component and Production Method Therefor. 2006.

34.   You, J., et al., A Polymer Tandem Solar Cell with 10.6% Power Conversion Efficiency. *Nat Commun* **2013**, *4*, 1446-10pp.

35.   Nunzi, J.-M., Organic Photovoltaic Materials and Devices. *C. R. Physique* **2002**, *3*, 523–542.

36.   Shaheen, S. E.; Brabec, C. J.; Sariciftci, N. S.; Padinger, F.; Fromherz, T.; Hummelen, J. C., 2.5% Efficient Organic Plastic Solar Cells. *Applied Physics Letters* **2001**, *78*, 841-843.

37.   Brabec, C. J.; Shaheen, S. E.; Winder, C.; Sariciftci, N. S.; Denk, P., Effect of LiF/Metal Electrodes on the Performance of Plastic Solar Cells. *Applied Physics Letters* **2002**, *80*, 1288-1290.

38.   Dang, M. T.; Hirsch, L.; Wantz, G., P3HT:PCBM, Best Seller in Polymer Photovoltaic Research. *Advanced Materials* **2011**, *23*, 3597-3602.

39.   Kim, Y., et al., A Strong Regioregularity Effect in Self-Organizing Conjugated Polymer Films and High-Efficiency Polythiophene:Fullerene Solar Cells. *Nat Mater* **2006**, *5*, 197-203.

40.   Bundgaard, E.; Krebs, F. C., Low Band Gap Polymers for Organic Photovoltaics. *Solar Energy Materials and Solar Cells* **2007**, *91*, 954-985.

41.   Roncali, J., Synthetic Principles for Bandgap Control in Linear π-Conjugated Systems. *Chemical Reviews* **1997**, *97*, 173-206.

42.   Chochos, C. L.; Choulis, S. A., How the Structural Deviations on the Backbone of Conjugated Polymers Influence Their Optoelectronic Properties and Photovoltaic Performance. *Progress in Polymer Science* **2011**, *36*, 1326-1414.

43.   Boudreault, P.-L. T.; Najari, A.; Leclerc, M., Processable Low-Bandgap Polymers for Photovoltaic Applications. *Chemistry of Materials* **2011**, *23*, 456-469.

44.   Mühlbacher, D.; Scharber, M.; Morana, M.; Zhu, Z.; Waller, D.; Gaudiana, R.; Brabec, C., High Photovoltaic Performance of a Low-Bandgap Polymer. *Advanced Materials* **2006**, *18*, 2884-2889.

45.   Scharber, M. C., et al., Influence of the Bridging Atom on the Performance of a Low-Bandgap Bulk Heterojunction Solar Cell. *Advanced Materials* **2010**, *22*, 367-370.

46.   Morana, M., et al., Nanomorphology and Charge Generation in Bulk Heterojunctions Based on Low-Bandgap Dithiophene Polymers with Different Bridging Atoms. *Advanced Functional Materials* **2010**, *20*, 1180-1188.

47.   Peet, J.; Kim, J. Y.; Coates, N. E.; Ma, W. L.; Moses, D.; Heeger, A. J.; Bazan, G. C., Efficiency Enhancement in Low-Bandgap Polymer Solar Cells by Processing with Alkane Dithiols. *Nat Mater* **2007**, *6*, 497-500.

48.   Dennler, G.; Scharber, M. C.; Brabec, C. J., Polymer-Fullerene Bulk-Heterojunction Solar Cells. *Advanced Materials* **2009**, *21*, 1323-1338.

49.   Meager, I., et al., Photocurrent Enhancement from Diketopyrrolopyrrole Polymer Solar Cells through Alkyl-Chain Branching Point Manipulation. *Journal of the American Chemical Society* **2013**, *135*, 11537-11540.

50.   Wang, D. H.; Kim, J. K.; Seo, J. H.; Park, I.; Hong, B. H.; Park, J. H.; Heeger, A. J., Transferable Graphene Oxide by Stamping Nanotechnology: Electron-Transport Layer for Efficient Bulk-Heterojunction Solar Cells. *Angewandte Chemie International Edition* **2013**, *52*, 2874-2880.

51.   Blouin, N.; Michaud, A.; Leclerc, M., A Low-Bandgap Poly(2,7-Carbazole) Derivative for Use in High-Performance Solar Cells. *Advanced Materials* **2007**, *19*, 2295-2300.

52.   Liang, Y.; Xu, Z.; Xia, J.; Tsai, S.-T.; Wu, Y.; Li, G.; Ray, C.; Yu, L., For the Bright Future—Bulk Heterojunction Polymer Solar Cells with Power Conversion Efficiency of 7.4%. *Advanced Materials* **2010**, *22*, E135-E138.

53.   Chen, J.-D.; Cui, C.; Li, Y.-Q.; Zhou, L.; Ou, Q.-D.; Li, C.; Li, Y.; Tang, J.-X., Single-Junction Polymer Solar Cells Exceeding 10% Power Conversion Efficiency. *Advanced Materials* **2015**, *27*, 1035-1041.

54.   He, Y.; Li, Y., Fullerene Derivative Acceptors for High Performance Polymer Solar Cells. *Physical Chemistry Chemical Physics* **2011**, *13*, 1970-1983.

55.   Sariciftci, N. S.; Smilowitz, L.; Heeger, A. J.; Wudl, F., Photoinduced Electron Transfer from a Conducting Polymer to Buckminsterfullerene. *Science* **1992**, *258*, 1474-1476.

56.   Sariciftci, N. S.; Braun, D.; Zhang, C.; Srdanov, V. I.; Heeger, A. J.; Stucky, G.; Wudl, F., Semiconducting Polymer-Buckminsterfullerene Heterojunctions: Diodes, Photodiodes, and Photovoltaic Cells. *Applied Physics Letters* **1993**, *62*, 585-587.

57.   Hummelen, J. C.; Knight, B. W.; LePeq, F.; Wudl, F.; Yao, J.; Wilkins, C. L., Preparation and Characterization of Fulleroid and Methanofullerene Derivatives. *The Journal of Organic Chemistry* **1995**, *60*, 532-538.

58.   He, Y.; Chen, H.-Y.; Hou, J.; Li, Y., Indene–C_{60} Bisadduct: A New Acceptor for High-Performance Polymer Solar Cells. *Journal of the American Chemical Society* **2010**, *132*, 1377-1382.

59.   Lenes, M.; Wetzelaer, G.-J. A. H.; Kooistra, F. B.; Veenstra, S. C.; Hummelen, J. C.; Blom, P. W. M., Fullerene Bisadducts for Enhanced Open-Circuit Voltages and Efficiencies in Polymer Solar Cells. *Advanced Materials* **2008**, *20*, 2116-2119.

60.   Hwang, Y.-J.; Courtright, B. A. E.; Ferreira, A. S.; Tolbert, S. H.; Jenekhe, S. A., 7.7% Efficient All-Polymer Solar Cells. *Advanced Materials* **2015**, *27*, 4578-4584.

61.   Hoppe, H.; Sariciftci, N. S., Morphology of Polymer/Fullerene Bulk Heterojunction Solar Cells. *Journal of Materials Chemistry* **2006**, *16*, 45-61.

62.   Reisdorffer, F.; Haas, O.; Le Rendu, P.; Nguyen, T. P., Co-Solvent Effects on the Morphology of P3HT:PCBM Thin Films. *Synthetic Metals* **2012**, *161*, 2544-2548.

63.   Pivrikas, A.; Neugebauer, H.; Sariciftci, N. S., Influence of Processing Additives to Nano-Morphology and Efficiency of Bulk-Heterojunction Solar Cells: A Comparative Review. *Solar Energy* **2011**, *85*, 1226-1237.

64.   Zhao, J.; Swinnen, A.; Van Assche, G.; Manca, J.; Vanderzande, D.; Mele, B. V., Phase Diagram of P3HT/PCBM Blends and Its Implication for the Stability of Morphology. *The Journal of Physical Chemistry B* **2009**, *113*, 1587-1591.

65.   Müller, C.; Ferenczi, T. A. M.; Campoy-Quiles, M.; Frost, J. M.; Bradley, D. D. C.; Smith, P.; Stingelin-Stutzmann, N.; Nelson, J., Binary Organic Photovoltaic Blends: A Simple Rationale for Optimum Compositions. *Advanced Materials* **2008**, *20*, 3510-3515.

66.   Stingelin, N., On the Phase Behaviour of Organic Semiconductors. *Polymer International* **2012**, *61*, 866-873.

67.   Cabanetos, C.; El Labban, A.; Bartelt, J. A.; Douglas, J. D.; Mateker, W. R.; Fréchet, J. M. J.; McGehee, M. D.; Beaujuge, P. M., Linear Side Chains in Benzo[1,2-B:4,5-B']Dithiophene–Thieno[3,4-C]Pyrrole-4,6-Dione Polymers Direct Self-Assembly and Solar Cell Performance. *Journal of the American Chemical Society* **2013**, *135*, 4656-4659.

68.   Yiu, A. T.; Beaujuge, P. M.; Lee, O. P.; Woo, C. H.; Toney, M. F.; Fréchet, J. M. J., Side-Chain Tunability of Furan-Containing Low-Band-Gap Polymers Provides Control of Structural Order in Efficient Solar Cells. *Journal of the American Chemical Society* **2012**, *134*, 2180-2185.

69.   Groenendaal, L.; Jonas, F.; Freitag, D.; Pielartzik, H.; Reynolds, J. R., Poly(3,4-Ethylenedioxythiophene) and Its Derivatives: Past, Present, and Future. *Advanced Materials* **2000**, *12*, 481-494.

70.   Kirchmeyer, S.; Reuter, K., Scientific Importance, Properties and Growing Applications of Poly(3,4-Ethylenedioxythiophene). *Journal of Materials Chemistry* **2005**, *15*, 2077-2088.

71.   Ouyang, J.; Xu, Q.; Chu, C.-W.; Yang, Y.; Li, G.; Shinar, J., On the Mechanism of Conductivity Enhancement in Poly(3,4-Ethylenedioxythiophene):Poly(Styrene Sulfonate) Film through Solvent Treatment. *Polymer* **2004**, *45*, 8443-8450.

72.   Hu, Z.; Zhang, J.; Hao, Z.; Zhao, Y., Influence of Doped PEDOT:PSS on the Performance of Polymer Solar Cells. *Solar Energy Materials and Solar Cells* **2011**, *95*, 2763-2767.

73.   Ko, C.-J.; Lin, Y.-K.; Chen, F.-C.; Chu, C.-W., Modified Buffer Layers for Polymer Photovoltaic Devices. *Applied Physics Letters* **2007**, *90*, 063509-3pp.

74.   Xiao, T.; Cui, W.; Anderegg, J.; Shinar, J.; Shinar, R., Simple Routes for Improving Polythiophene:Fullerene-Based Organic Solar Cells. *Organic Electronics* **2011**, *12*, 257-262.

75.   Kim, G.-H.; Song, H.-K.; Kim, J. Y., The Effect of Introducing a Buffer Layer to Polymer Solar Cells on Cell Efficiency. *Solar Energy Materials and Solar Cells* **2011**, *95*, 1119-1122.

76.   Norrman, K.; Larsen, N. B.; Krebs, F. C., Lifetimes of Organic Photovoltaics: Combining Chemical and Physical Characterisation Techniques to Study Degradation Mechanisms. *Solar Energy Materials and Solar Cells* **2006**, *90*, 2793-2814.

77.   Dennler, G.; Lungenschmied, C.; Neugebauer, H.; Sariciftci, N. S.; Latrèche, M.; Czeremuszkin, G.; Wertheimer, M. R., A New Encapsulation Solution for Flexible Organic Solar Cells. *Thin Solid Films* **2006**, *511–512*, 349-353.

78.   Sarkar, S.; Culp, J. H.; Whyland, J. T.; Garvan, M.; Misra, V., Encapsulation of Organic Solar Cells with Ultrathin Barrier Layers Deposited by Ozone-Based Atomic Layer Deposition. *Organic Electronics* **2010**, *11*, 1896-1900.

79.   Lewis, J. S.; Weaver, M. S., Thin-Film Permeation-Barrier Technology for Flexible Organic Light-Emitting Devices. *Selected Topics in Quantum Electronics, IEEE Journal of* **2004**, *10*, 45-57.

80.   Wang, G.-F.; Tao, X.-M.; Wang, R.-X., Flexible Organic Light-Emitting Diodes with a Polymeric Nanocomposite Anode. *Nanotechnology* **2008**, *19*, 145201-5pp.

81.   Kim, J. S.; Friend, R. H.; Cacialli, F., Improved Operational Stability of Polyfluorene-Based Organic Light-Emitting Diodes with Plasma-Treated Indium–Tin–Oxide Anodes. *Applied Physics Letters* **1999**, *74*, 3084-3086.

82.	Shrotriya, V.; Li, G.; Yao, Y.; Chu, C.-W.; Yang, Y., Transition Metal Oxides as the Buffer Layer for Polymer Photovoltaic Cells. *Applied Physics Letters* **2006**, *88*, 073508-3pp.

83.	de Jong, M. P.; van IJzendoorn, L. J.; de Voigt, M. J. A., Stability of the Interface between Indium-Tin-Oxide and Poly(3,4-Ethylenedioxythiophene)/Poly(Styrenesulfonate) in Polymer Light-Emitting Diodes. *Applied Physics Letters* **2000**, *77*, 2255-2257.

84.	Chen, M.-C.; Chiou, Y.-S.; Chiu, J.-M.; Tedla, A.; Tai, Y., Marked Improvement in the Stability of Small Molecule Organic Photovoltaics by Interfacial Modification Using Self-Assembled Monolayers to Prevent Indium Diffusion into the Active Layer. *Journal of Materials Chemistry A* **2013**, *1*, 3680-3687.

85.	Wilken, S.; Hoffmann, T.; von Hauff, E.; Borchert, H.; Parisi, J., ITO-Free Inverted Polymer/Fullerene Solar Cells: Interface Effects and Comparison of Different Semi-Transparent Front Contacts. *Solar Energy Materials and Solar Cells* **2012**, *96*, 141-147.

86.	Carle, J. E.; Helgesen, M.; Madsen, M. V.; Bundgaard, E.; Krebs, F. C., Upscaling from Single Cells to Modules - Fabrication of Vacuum- and ITO-Free Polymer Solar Cells on Flexible Substrates with Long Lifetime. *Journal of Materials Chemistry C* **2014**, *2*, 1290-1297.

87.	Song, W.; So, S. K.; Moulder, J.; Qiu, Y.; Zhu, Y.; Cao, L., Study on the Interaction between Ag and Tris(8-Hydroxyquinoline) Aluminum Using X-Ray Photoelectron Spectroscopy. *Surface and Interface Analysis* **2001**, *32*, 70-73.

88.	Brand, V.; Levi, K.; McGehee, M. D.; Dauskardt, R. H., Film Stresses and Electrode Buckling in Organic Solar Cells. *Solar Energy Materials and Solar Cells* **2012**, *103*, 80-85.

89.	Klimov, E.; Li, W.; Yang, X.; Hoffmann, G. G.; Loos, J., Scanning near-Field and Confocal Raman Microscopic Investigation of P3HT–PCBM Systems for Solar Cell Applications. *Macromolecules* **2006**, *39*, 4493-4496.

90.	Swinnen, A.; Haeldermans, I.; vande Ven, M.; D'Haen, J.; Vanhoyland, G.; Aresu, S.; D'Olieslaeger, M.; Manca, J., Tuning the Dimensions of C_{60}-Based Needlelike Crystals in Blended Thin Films. *Advanced Functional Materials* **2006**, *16*, 760-765.

91.	Nam, C.-Y.; Qin, Y.; Park, Y. S.; Hlaing, H.; Lu, X.; Ocko, B. M.; Black, C. T.; Grubbs, R. B., Photo-Cross-Linkable Azide-Functionalized Polythiophene for Thermally Stable Bulk Heterojunction Solar Cells. *Macromolecules* **2012**, *45*, 2338-2347.

92.	Wantz, G.; Derue, L.; Dautel, O.; Rivaton, A.; Hudhomme, P.; Dagron-Lartigau, C., Stabilizing Polymer-Based Bulk Heterojunction Solar Cells Via Crosslinking. *Polymer International* **2014**, *63*, 1346-1361.

93.	Derue, L.; Lecourtier, C.; Gorisse, T.; Hirsch, L.; Dautel, O.; Wantz, G., A Solvent Additive to Enhance the Efficiency and the Thermal Stability of Polymer:Fullerene Solar Cells. *RSC Advances* **2015**, *5*, 3840-3843.

94.	Goubard, F.; Wantz, G., Ternary Blends for Polymer Bulk Heterojunction Solar Cells. *Polymer International* **2014**, *63*, 1362-1367.

95.	Gardette, J.-L., Fundamental and Technical Aspects of the Photo-Oxidation of Polymers. In *Handbook of Polymer Degradation*, 2 ed.; S., H. H., Ed. 2000; Vol. 1, pp 671–698

96.	Schafferhans, J.; Baumann, A.; Wagenpfahl, A.; Deibel, C.; Dyakonov, V., Oxygen Doping of P3HT:PCBM Blends: Influence on Trap States, Charge Carrier Mobility and Solar Cell Performance. *Organic Electronics* **2010**, *11*, 1693-1700.

97.	Okamura, H.; Takatori, Y.; Tsunooka, M.; Shirai, M., Synthesis of Random and Block Copolymers of Styrene and Styrenesulfonic Acid with Low Polydispersity Using Nitroxide-Mediated Living Radical Polymerization Technique. *Polymer* **2002**, *43*, 3155-3162.

98.	Elschner, A., The Spectral Sensitivity of PEDOT:PSS Films. *Solar Energy Materials and Solar Cells* **2011**, *95*, 1333-1338.

99.   Vitoratos, E.; Sakkopoulos, S.; Dalas, E.; Paliatsas, N.; Karageorgopoulos, D.; Petraki, F.; Kennou, S.; Choulis, S. A., Thermal Degradation Mechanisms of PEDOT:PSS. *Organic Electronics* **2009**, *10*, 61-66.

100.   Huang, J.; Miller, P. F.; de Mello, J. C.; de Mello, A. J.; Bradley, D. D. C., Influence of Thermal Treatment on the Conductivity and Morphology of PEDOT/PSS Films. *Synthetic Metals* **2003**, *139*, 569-572.

101.   Kawano, K.; Pacios, R.; Poplavskyy, D.; Nelson, J.; Bradley, D. D. C.; Durrant, J. R., Degradation of Organic Solar Cells Due to Air Exposure. *Solar Energy Materials and Solar Cells* **2006**, *90*, 3520-3530.

102.   Bulle-Lieuwma, C. W. T.; van Gennip, W. J. H.; van Duren, J. K. J.; Jonkheijm, P.; Janssen, R. A. J.; Niemantsverdriet, J. W., Characterization of Polymer Solar Cells by TOF-SIMS Depth Profiling. *Applied Surface Science* **2003**, *203–204*, 547-550.

103.   Abetz, V.; Simon, P. W., Phase Behaviour and Morphologies of Block Copolymers. In *Block Copolymers I*, Abetz, V., Ed. Springer Berlin Heidelberg: 2005; Vol. 189, pp 125-212.

104.   Topham, P. D.; Parnell, A. J.; Hiorns, R. C., Block Copolymer Strategies for Solar Cell Technology. *Journal of Polymer Science Part B: Polymer Physics* **2011**, *49*, 1131-1156.

105.   Schacher, F. H.; Rupar, P. A.; Manners, I., Functional Block Copolymers: Nanostructured Materials with Emerging Applications. *Angewandte Chemie International Edition* **2012**, *51*, 7898-7921.

106.   Matsen, M. W., Effect of Architecture on the Phase Behavior of Ab-Type Block Copolymer Melts. *Macromolecules* **2012**, *45*, 2161-2165.

107.   Miyanishi, S.; Zhang, Y.; Tajima, K.; Hashimoto, K., Fullerene Attached All-Semiconducting Diblock Copolymers for Stable Single-Component Polymer Solar Cells. *Chemical Communications* **2010**, *46*, 6723-6725.

108.   Lim, B.; Jo, J.; Na, S.-I.; Kim, J.; Kim, S.-S.; Kim, D.-Y., A Morphology Controller for High-Efficiency Bulk-Heterojunction Polymer Solar Cells. *Journal of Materials Chemistry* **2010**, *20*, 10919-10923.

109.   Boudouris, B. W.; Frisbie, C. D.; Hillmyer, M. A., Nanoporous Poly(3-Alkylthiophene) Thin Films Generated from Block Copolymer Templates. *Macromolecules* **2008**, *41*, 67-75.

110.   Brendel, J. C.; Lu, Y.; Thelakkat, M., Polymer Templated Nanocrystalline Titania Network for Solid State Dye Sensitized Solar Cells. *Journal of Materials Chemistry* **2010**, *20*, 7255-7265.

111.   Erothu, H., et al., Synthesis, Thermal Processing, and Thin Film Morphology of Poly(3-Hexylthiophene)–Poly(Styrenesulfonate) Block Copolymers. *Macromolecules* **2015**, *48*, 2107-2117.

112.   Liang, L.; Astruc, D., The Copper(I)-Catalyzed Alkyne-Azide Cycloaddition (CuAAC) "Click" Reaction and Its Applications. An Overview. *Coordination Chemistry Reviews* **2011**, *255*, 2933-2945.

113.   Higashihara, T.; Liu, C.-L.; Chen, W.-C.; Ueda, M., Synthesis of Novel Π-Conjugated Rod-Rod-Rod Triblock Copolymers Containing Poly(3-Hexylthiophene) and Polyacetylene Segments by Combination of Quasi-Living Grim and Living Anionic Polymerization. *Polymers* **2011**, *3*, 236-251.

114.   Moad, G.; Rizzardo, E.; Thang, S. H., Toward Living Radical Polymerization. *Accounts of Chemical Research* **2008**, *41*, 1133-1142.

115.   Wang, J.-S.; Matyjaszewski, K., Controlled/"Living" Radical Polymerization. Halogen Atom Transfer Radical Polymerization Promoted by a Cu(I)/Cu(II) Redox Process. *Macromolecules* **1995**, *28*, 7901-7910.

116.   Ando, T.; Kato, M.; Kamigaito, M.; Sawamoto, M., Living Radical Polymerization of Methyl Methacrylate with Ruthenium Complex: Formation of Polymers with Controlled Molecular Weights and Very Narrow Distributions1. *Macromolecules* **1996**, *29*, 1070-1072.

117.   Georges, M. K.; Veregin, R. P. N.; Kazmaier, P. M.; Hamer, G. K., Narrow Molecular Weight Resins by a Free-Radical Polymerization Process. *Macromolecules* **1993**, *26*, 2987-2988.

118.   Solomon, D. H., Genesis of the Csiro Polymer Group and the Discovery and Significance of Nitroxide-Mediated Living Radical Polymerization. *Journal of Polymer Science Part A: Polymer Chemistry* **2005**, *43*, 5748-5764.

119.   Chiefari, J., et al., Living Free-Radical Polymerization by Reversible Addition-Fragmentation Chain Transfer: The RAFT Process. *Macromolecules* **1998**, *31*, 5559-5562.

120.   Moad, G.; Rizzardo, E.; Thang, S. H., Living Radical Polymerization by the RAFT Process: A Second Update. *Australian Journal of Chemistry* **2009**, *62*, 1402-1472.

121.   Moad, G.; Rizzardo, E.; Thang, S. H., Living Radical Polymerization by the RAFT Process. *Australian Journal of Chemistry* **2005**, *58*, 379-410.

122.   Keddie, D. J., A Guide to the Synthesis of Block Copolymers Using Reversible-Addition Fragmentation Chain Transfer (RAFT) Polymerization. *Chemical Society Reviews* **2014**, *43*, 496-505.

123.   Gody, G.; Maschmeyer, T.; Zetterlund, P. B.; Perrier, S., Rapid and Quantitative One-Pot Synthesis of Sequence-Controlled Polymers by Radical Polymerization. *Nat Commun* **2013**, *4*, 2505-9pp.

124.   Braunecker, W. A.; Matyjaszewski, K., Controlled/Living Radical Polymerization: Features, Developments, and Perspectives. *Progress in Polymer Science* **2007**, *32*, 93-146.

125.   Tulig, T. J.; Tirrell, M., Molecular Theory of the Trommsdorff Effect. *Macromolecules* **1981**, *14*, 1501-1511.

126.   Lowe, A. B.; McCormick, C. L., Reversible Addition–Fragmentation Chain Transfer (RAFT) Radical Polymerization and the Synthesis of Water-Soluble (Co)Polymers under Homogeneous Conditions in Organic and Aqueous Media. *Progress in Polymer Science* **2007**, *32*, 283-351.

127.   Thomas, D. B.; Convertine, A. J.; Hester, R. D.; Lowe, A. B.; McCormick, C. L., Hydrolytic Susceptibility of Dithioester Chain Transfer Agents and Implications in Aqueous RAFT Polymerizations†. *Macromolecules* **2004**, *37*, 1735-1741.

128.   Sato, T.; Shimizu, T.; Seno, M.; Tanaka, H.; Ota, T., Solvent Effect on the Propagation Rate-Constant in the Radical Polymerization of Bis(2-Ethylhexyl) Itaconate. *Makromolekulare Chemie-Macromolecular Chemistry and Physics* **1992**, *193*, 1439-1444.

129.   Sato, T.; Masaki, K.; Kondo, K.; Seno, M.; Tanaka, H., Solvent Effects on the Radical Polymerization of N-Dodecylmaleimide. *Polymer Bulletin* **1995**, *35*, 345-350.

130.   Benaglia, M.; Rizzardo, E.; Alberti, A.; Guerra, M., Searching for More Effective Agents and Conditions for the RAFT Polymerization of MMA: Influence of Dithioester Substituents, Solvent, and Temperature. *Macromolecules* **2005**, *38*, 3129-3140.

131.   Wood, M. R.; Duncalf, D. J.; Findlay, P.; Rannard, S. P.; Perrier, S., Investigation of the Experimental Factors Affecting the Trithiocarbonate-Mediated RAFT Polymerization of Methyl Acrylate. *Australian Journal of Chemistry* **2007**, *60*, 772-778.

132.   Pullan, N.; Liu, M.; Topham, P. D., Reversible Addition-Fragmentation Chain Transfer Polymerization of 2-Chloro-1,3-Butadiene. *Polymer Chemistry* **2013**, *4*, 2272-2277.

133.   Abreu, C. M. R.; Mendonca, P. V.; Serra, A. C.; Coelho, J. F. J.; Popov, A. V.; Grynova, G.; Coote, M. L.; Guliashvili, T., Reversible Addition-Fragmentation Chain Transfer Polymerization of Vinyl Chloride. *Macromolecules* **2012**, *45*, 2200-2208.

134.   Arita, T.; Buback, M.; Janssen, O.; Vana, P., RAFT-Polymerization of Styrene up to High Pressure: Rate Enhancement and Improved Control. *Macromolecular Rapid Communications* **2004**, *25*, 1376-1381.

135.   Rzayev, J.; Penelle, J., Hp-RAFT: A Free-Radical Polymerization Technique for Obtaining Living Polymers of Ultrahigh Molecular Weights. *Angewandte Chemie International Edition* **2004**, *43*, 1691-1694.

136.   Cauët, S. I.; Wooley, K. L., Kinetic Investigation of the RAFT Polymerization of p-Acetoxystyrene. *Journal of Polymer Science Part A: Polymer Chemistry* **2010**, *48*, 2517-2524.

137.   Guimard, N. K.; Gomez, N.; Schmidt, C. E., Conducting Polymers in Biomedical Engineering. *Progress in Polymer Science* **2007**, *32*, 876-921.

138.   Andreoli, E.; Liao, K.-S.; Haldar, A.; Alley, N. J.; Curran, S. A., PPy:PSS as Alternative to PEDOT:PSS in Organic Photovoltaics. *Synthetic Metals* **2013**, *185-186*, 71-78.

139.   Ghosh, S.; Inganäs, O., Self-Assembly of a Conducting Polymer Nanostructure by Physical Crosslinking: Applications to Conducting Blends and Modified Electrodes. *Synthetic Metals* **1999**, *101*, 413-416.

140.   Fehse, K.; Walzer, K.; Leo, K.; Lövenich, W.; Elschner, A., Highly Conductive Polymer Anodes as Replacements for Inorganic Materials in High-Efficiency Organic Light-Emitting Diodes. *Advanced Materials* **2007**, *19*, 441-444.

141.   Ding, J.; Chuy, C.; Holdcroft, S., A Self-Organized Network of Nanochannels Enhances Ion Conductivity through Polymer Films. *Chemistry of Materials* **2001**, *13*, 2231-2233.

142.   Yu, J.; Yi, B.; Xing, D.; Liu, F.; Shao, Z.; Fu, Y.; Zhang, H., Degradation Mechanism of Polystyrene Sulfonic Acid Membrane and Application of its Composite Membranes in Fuel Cells. *Physical Chemistry Chemical Physics* **2003**, *5*, 611-615.

143.   Chen, S.-L.; Krishnan, L.; Srinivasan, S.; Benziger, J.; Bocarsly, A. B., Ion Exchange Resin/Polystyrene Sulfonate Composite Membranes for PEM Fuel Cells. *Journal of Membrane Science* **2004**, *243*, 327-333.

144.   Bauman, W. C.; Eichhorn, J., Fundamental Properties of a Synthetic Cation Exchange Resin. *Journal of the American Chemical Society* **1947**, *69*, 2830-2836.

145.   Kim, J.; Kim, B.; Jung, B., Proton Conductivities and Methanol Permeabilities of Membranes Made from Partially Sulfonated Polystyrene-Block-Poly(Ethylene-Ran-Butylene)-Block-Polystyrene Copolymers. *Journal of Membrane Science* **2002**, *207*, 129-137.

146.   Athanasekos, L.; El Sachat, A.; Pispas, S.; Riziotis, C., Amphiphilic Diblock Copolymer-Based Multiagent Photonic Sensing Scheme. *Journal of Polymer Science Part B: Polymer Physics* **2013**, *52*, 46-54.

147.   Li, D.; Jiang, Y.; Li, Y.; Yang, X.; Lu, L.; Wang, X., Fabrication of a Prototype Humidity-Sensitive Capacitor Via Layer-by-Layer Self-Assembling Technique. *Materials Science and Engineering: C* **2000**, *11*, 117-119.

148.   Rubinger, C. P. L.; Martins, C. R.; De Paoli, M. A.; Rubinger, R. M., Sulfonated Polystyrene Polymer Humidity Sensor: Synthesis and Characterization. *Sensors and Actuators B: Chemical* **2007**, *123*, 42-49.

149.   Al-Marhoun, M. A.; Rahman, S. S., Treatment of Drilling Fluid to Combat Drill Pipe Corrosion. *Corrosion* **1990**, *46*, 778-782.

150.   Saleh, M. M., Water Softening Using Packed Bed of Polypyrrole from Flowing Solutions. *Desalination* **2009**, *235*, 319-329.

151.   Bouix, M.; Gouzi, J.; Charleux, B.; Vairon, J.-P.; Guinot, P., Synthesis of Amphiphilic Polyelectrolyte Block Copolymers Using "Living" Radical Polymerization. Application as Stabilizers in Emulsion Polymerization. *Macromolecular Rapid Communications* **1998**, *19*, 209-213.

152.   Bélanger, D. R.; Tierney, M. G.; Dickinson, G., Effect of Sodium Polystyrene Sulfonate on Lithium Bioavailability. *Annals of Emergency Medicine* **1992**, *21*, 1312-1315.

153.   Antipina, M. N.; Sukhorukov, G. B., Remote Control over Guidance and Release Properties of Composite Polyelectrolyte Based Capsules. *Advanced Drug Delivery Reviews* **2011**, *63*, 716-729.

154.   Watson, M. A.; Baker, T. P.; Nguyen, A.; Sebastianelli, M. E.; Stewart, H. L.; Oliver, D. K.; Abbott, K. C.; Yuan, C. M., Association of Prescription of Oral Sodium Polystyrene Sulfonate with Sorbitol in an Inpatient Setting with Colonic Necrosis: A Retrospective Cohort Study. *American Journal of Kidney Diseases* **2012**, *60*, 409-416.

155.   Girard, J.; Brunetto, P. S.; Braissant, O.; Rajacic, Z.; Khanna, N.; Landmann, R.; Daniels, A. U.; Fromm, K. M., Development of a Polystyrene Sulfonate/Silver Nanocomposite with Self-Healing Properties for Biomaterial Applications. *Comptes Rendus Chimie* **2013**, *16*, 550-556.

156.   Gibson, H. W.; Bailey, F. C., Chemical Modification of Polymers. 13. Sulfonation of Polystyrene Surfaces. *Macromolecules* **1980**, *13*, 34-41.

157.   Akovali, G.; Ozkan, A., Notes on Modification of Polystyrene by Sulphonation: Some Properties of Poly(Styrenesulphonic Acid). *Polymer* **1986**, *27*, 1277-1280.

158.   Kucera, F.; Jancar, J., Sulfonation of Solid Polystyrene Using Gaseous Sulfur Trioxide. *Polymer Engineering & Science* **2009**, *49*, 1839-1845.

159.   Keoshkerian, B.; Georges, M. K.; Boilsboissier, D., Living Free-Radical Aqueous Polymerization. *Macromolecules* **1995**, *28*, 6381-6382.

160.   Mannan, A.; Fukuda, K.; Miura, Y., Living Radical Polymerization of Sodium 4-Styrenesulfonate Mediated by New Water-Soluble Nitroxides. *Polym. J.* **2007**, *39*, 500-501.

161.   Wang, X. S.; Jackson, R. A.; Armes, S. P., Facile Synthesis of Acidic Copolymers Via Atom Transfer Radical Polymerization in Aqueous Media at Ambient Temperature. *Macromolecules* **1999**, *33*, 255-257.

162.   Choi, C.-K.; Kim, Y.-B., Atom Transfer Radical Polymerization of Styrenesulfonic Acid Sodium Salts (SSNa) in Aqueous Phase. *Polymer Bulletin* **2003**, *49*, 433-439.

163.   Iddon, P. D.; Robinson, K. L.; Armes, S. P., Polymerization of Sodium 4-Styrenesulfonate Via Atom Transfer Radical Polymerization in Protic Media. *Polymer* **2004**, *45*, 759-768.

164.   Mitsukami, Y.; Donovan, M. S.; Lowe, A. B.; McCormick, C. L., Water-Soluble Polymers. 81. Direct Synthesis of Hydrophilic Styrenic-Based Homopolymers and Block Copolymers in Aqueous Solution Via RAFT. *Macromolecules* **2001**, *34*, 2248-2256.

165.   Sumerlin, B. S.; Lowe, A. B.; Stroud, P. A.; Zhang, P.; Urban, M. W.; McCormick, C. L., Modification of Gold Surfaces with Water-Soluble (Co)Polymers Prepared Via Aqueous Reversible Addition-Fragmentation Chain Transfer (RAFT) Polymerization. *Langmuir* **2003**, *19*, 5559-5562.

166.   Baek, K.-Y., Synthesis and Characterization of Sulfonated Block Copolymers by Atom Transfer Radical Polymerization. *Journal of Polymer Science Part A: Polymer Chemistry* **2008**, *46*, 5991-5998.

167.   Kollisch, H. S.; Barner-Kowollik, C.; Ritter, H., Amphiphilic Block Copolymers Based on Cyclodextrinhost-Guest Complexes Via RAFT-Polymerization in Aqueous Solution. *Chemical Communications* **2009**, 1097-1099.

168.   Brusseau, S.; D'Agosto, F.; Magnet, S.; Couvreur, L.; Chamignon, C.; Charleux, B., Nitroxide-Mediated Copolymerization of Methacrylic Acid and Sodium 4-Styrenesulfonate in Water Solution and One-Pot Synthesis of Amphiphilic Block Copolymer Nanoparticles. *Macromolecules* **2011**, *44*, 5590-5598.

169.   Brendel, J. C.; Burchardt, H.; Thelakkat, M., Semiconductor Amphiphilic Block Copolymers for Hybrid Donor-Acceptor Nanocomposites. *Journal of Materials Chemistry* **2012**, *22*, 24386-24393.

170.   Matsumoto, K.; Hasegawa, H.; Matsuoka, H., Synthesis of Sodium-Polystyrenesulfonate-Grafted Nanoparticles by Core-Cross-Linking of Block Copolymer Micelles. *Tetrahedron* **2004**, *60*, 7197-7204.

171.   Matsumoto, K.; Hirabayashi, T.; Harada, T.; Matsuoka, H., Synthesis of Shell Cross-Linked Block Copolymer Micelles with Poly(p-Styrenesulfonic Acid) in the Micelle Core. *Macromolecules* **2005**, *38*, 9957-9962.

172.   Matsumoto, K.; Kage, S.; Matsuoka, H., Synthesis of Water-Dispersible, Fluorinated Particles with Grafting Sulfonate Chains by the Core Crosslinking of Block Copolymer Micelles. *Journal of Polymer Science Part A: Polymer Chemistry* **2007**, *45*, 1316-1323.

173.   Baek, K.-Y., Synthesis and Characterization of UV Crosslinkable and Highly Sulfonated Block Copolymer by Living Radical Polymerization. *Molecular Crystals and Liquid Crystals* **2010**, *520*, 256/[532]-261/[537].

174.   Baek, K.-Y.; Kim, H.-J.; Lee, S.-H.; Cho, K.-Y.; Kim, H. T.; Hwang, S. S., Morphology Control of Highly Sulfonated Block Copolymers by a Simple Thermal Process. *Macromolecular Chemistry and Physics* **2010**, *211*, 613-617.

175.   Li, X.; Jiang, Y.; Shuai, L.; Wang, L.; Meng, L.; Mu, X., Sulfonated Copolymers with SO_3H and COOH Groups for the Hydrolysis of Polysaccharides. *Journal of Materials Chemistry* **2012**, *22*, 1283-1289.

176.   Guo, X.; Baumgarten, M.; Müllen, K., Designing Pi-Conjugated Polymers for Organic Electronics. *Progress in Polymer Science* **2013**, *38*, 1832-1908.

177.   Zhu, J.; Zhu, X.; Kang, E. T.; Neoh, K. G., Design and Synthesis of Star Polymers with Hetero-Arms by the Combination of Controlled Radical Polymerizations and Click Chemistry. *Polymer* **2007**, *48*, 6992-6999.

178.   Stenzel, M. H.; Davis, T. P., Star Polymer Synthesis Using Trithiocarbonate Functional Β-Cyclodextrin Cores (Reversible Addition–Fragmentation Chain-Transfer Polymerization). *Journal of Polymer Science Part A: Polymer Chemistry* **2002**, *40*, 4498-4512.

179.   Vora, A.; Singh, K.; Webster, D. C., A New Approach to 3-Miktoarm Star Polymers Using a Combination of Reversible Addition-Fragmentation Chain Transfer (RAFT) and Ring Opening Polymerization (ROP) Via "Click" Chemistry. *Polymer* **2009**, *50*, 2768-2774.

180.   Kolomanska, J.; Johnston, P.; Gregori, A.; Fraga Domínguez, I.; Egelhaaf, H.-J.; Perrier, S.; Rivaton, A.; Dagron-Lartigau, C.; Topham, P., Design, Synthesis and Thermal Behaviour of a Series of Well-Defined Clickable and Triggerable Sulfonate Polymers. *RSC Advances* **2015**, *5*, 66554-66562.

181.   Schön, P. M. G., M.; Vancso, G. J., Imaging of Mechanical Properties of Soft Matter. From Heterogeneous Polymer Surfaces to Single Biomolecules. *Imaging & Microscopy* **2012**.

182.   Derjaguin, B. V.; Muller, V. M.; Toporov, Y. P., Effect of Contact Deformations on the Adhesion of Particles. *Journal of Colloid and Interface Science* **1975**, *53*, 314-326.

183.   Schuh, K.; Prucker, O.; Rühe, J., Surface Attached Polymer Networks through Thermally Induced Cross-Linking of Sulfonyl Azide Group Containing Polymers. *Macromolecules* **2008**, *41*, 9284-9289.

184.   Gondi, S. R.; Vogt, A. P.; Sumerlin, B. S., Versatile Pathway to Functional Telechelics Via RAFT Polymerization and Click Chemistry. *Macromolecules* **2007**, *40*, 474-481.

185.   Skey, J.; O'Reilly, R. K., Facile One Pot Synthesis of a Range of Reversible Addition-Fragmentation Chain Transfer (RAFT) Agents. *Chemical Communications* **2008**, 4183-4185.

186.   Li, M.; De, P.; Gondi, S. R.; Sumerlin, B. S., End Group Transformations of RAFT-Generated Polymers with Bismaleimides: Functional Telechelics and Modular Block Copolymers. *J Polym Sci Pol Chem* **2008**, *46*, 5093-5100.

187.   Lowe, A. B., Thiol-Ene "Click" Reactions and Recent Applications in Polymer and Materials Synthesis. *Polymer Chemistry* **2010**, *1*, 17-36.

188.   Li, M.; De, P.; Li, H.; Sumerlin, B. S., Conjugation of RAFT-Generated Polymers to Proteins by Two Consecutive Thiol-Ene Reactions. *Polymer Chemistry* **2010**, *1*, 854-859.

189.   Lai, J. T.; Filla, D.; Shea, R., Functional Polymers from Novel Carboxyl-Terminated Trithiocarbonates as Highly Efficient RAFT Agents. *Macromolecules* **2002**, *35*, 6754-6756.

190.   Topham, P. D.; Sandon, N.; Read, E. S.; Madsen, J.; Ryan, A. J.; Armes, S. P., Facile Synthesis of Well-Defined Hydrophilic Methacrylic Macromonomers Using ATRP and Click Chemistry. *Macromolecules* **2008**, *41*, 9542-9547.

191.   Binder, W. H.; Sachsenhofer, R., 'Click' Chemistry in Polymer and Materials Science. *Macromolecular Rapid Communications* **2007**, *28*, 15-54.

192.   Vogt, A. P.; Sumerlin, B. S., An Efficient Route to Macromonomers Via ATRP and Click Chemistry. *Macromolecules* **2006**, *39*, 5286-5292.

193.   Agut, W.; Taton, D.; Lecommandoux, S., A Versatile Synthetic Approach to Polypeptide Based Rod-Coil Block Copolymers by Click Chemistry. *Macromolecules* **2007**, *40*, 5653-5661.

194.   Kimani, S. M.; Hardman, S. J.; Hutchings, L. R.; Clarke, N.; Thompson, R. L., Synthesis and Surface Activity of High and Low Surface Energy Multi-End Functional Polybutadiene Additives. *Soft Matter* **2012**, *8*, 3487-3496.

195.   Tahk, D.; Lee, H. H.; Khang, D.-Y., Elastic Moduli of Organic Electronic Materials by the Buckling Method. *Macromolecules* **2009**, *42*, 7079-7083.

196.   Ruud, C. J.; Jia, J.; Baker, G. L., Synthesis and Characterization of Poly[(1-Trimethylsilyl-1-Propyne)-Co-(1-(4-Azidobutyldimethylsilyl)-1-Propyne)] Copolymers. *Macromolecules* **2000**, *33*, 8184-8191.

197.   Bräse, S.; Gil, C.; Knepper, K.; Zimmermann, V., Organic Azides: An Exploding Diversity of a Unique Class of Compounds. *Angewandte Chemie International Edition* **2005**, *44*, 5188-5240.

198.   Rabek, J. F., *Photodegradation of Polymers*; Springer: Berlin, 1996.

199.   Abdou, M. S. A.; Orfino, F. P.; Son, Y.; Holdcroft, S., Interaction of Oxygen with Conjugated Polymers: Charge Transfer Complex Formation with Poly(3-Alkylthiophenes). *Journal of the American Chemical Society* **1997**, *119*, 4518-4524.

200.   Aguirre, A.; Meskers, S. C. J.; Janssen, R. A. J.; Egelhaaf, H. J., Formation of Metastable Charges as a First Step in Photoinduced Degradation in Π-Conjugated Polymer:Fullerene Blends for Photovoltaic Applications. *Organic Electronics* **2011**, *12*, 1657-1662.

201.   Sperlich, A.; Kraus, H.; Deibel, C.; Blok, H.; Schmidt, J.; Dyakonov, V., Reversible and Irreversible Interactions of Poly(3-Hexylthiophene) with Oxygen Studied by Spin-Sensitive Methods. *The Journal of Physical Chemistry B* **2011**, *115*, 13513-13518.

202.   Carlsson, D. J.; Garton, A.; Wiles, D. M., Initiation of Polypropylene Photooxidation. 2. Potential Processes and Their Relevance to Stability. *Macromolecules* **1976**, *9*, 695-701.

203.   Cicchetti, O., Mechanisms of Oxidative Photodegradation and of UV Stabilization of Polyolefins. In *Fortschritte Der Hochpolymeren-Forschung*, Springer Berlin Heidelberg: 1970; Vol. 7/1, pp 70-112.

204.   Frolova, L. A.; Piven, N. P.; Susarova, D. K.; Akkuratov, A. V.; Babenko, S. D.; Troshin, P. A., Esr Spectroscopy for Monitoring the Photochemical and Thermal Degradation of Conjugated Polymers Used as Electron Donor Materials in Organic Bulk Heterojunction Solar Cells. *Chemical Communications* **2015**, *51*, 2242-2244.

205.   Susarova, D. K.; Piven, N. P.; Akkuratov, A. V.; Frolova, L. A.; Polinskaya, M. S.; Ponomarenko, S. A.; Babenko, S. D.; Troshin, P. A., Esr Spectroscopy as a Powerful Tool for Probing the Quality of Conjugated Polymers Designed for Photovoltaic Applications. *Chemical Communications* **2015**, *51*, 2239-2241.

206.   Chambon, S.; Rivaton, A.; Gardette, J.-L.; Firon, M.; Lutsen, L., Aging of a Donor Conjugated Polymer: Photochemical Studies of the Degradation of Poly[2-Methoxy-5-(3',7'-Dimethyloctyloxy)-1,4-Phenylenevinylene]. *Journal of Polymer Science Part A: Polymer Chemistry* **2007**, *45*, 317-331.

207.   Bussière, P. O.; Mailhot, B.; Rivaton, A.; Barthe, M. F.; Gardette, J. L.; Baba, M., Photocrosslinking of Poly(N-Vinylcarbazole): Implementing a Complementary Set of Techniques to Characterize the Three-Dimensional Network Formation. *Polymer Degradation and Stability* **2008**, *93*, 1376-1382.

208.   Bussière, P.-O.; Rivaton, A.; Thérias, S.; Gardette, J.-L., Multiscale Investigation of the Poly(N-Vinylcarbazole) Photoageing Mechanism. *The Journal of Physical Chemistry B* **2011**, *116*, 802-812.

209.   Tournebize, A.; Bussière, P.-O.; Wong-Wah-Chung, P.; Thérias, S.; Rivaton, A.; Gardette, J.-L.; Beaupré, S.; Leclerc, M., Impact of UV-Visible Light on the Morphological and Photochemical Behavior

of a Low-Bandgap Poly(2,7-Carbazole) Derivative for Use in High-Performance Solar Cells. *Advanced Energy Materials* **2013**, *3*, 478-487.

210.   Manceau, M.; Bundgaard, E.; Carle, J. E.; Hagemann, O.; Helgesen, M.; Sondergaard, R.; Jorgensen, M.; Krebs, F. C., Photochemical Stability of [Small Pi]-Conjugated Polymers for Polymer Solar Cells: A Rule of Thumb. *Journal of Materials Chemistry* **2011**, *21*, 4132-4141.

211.   Hintz, H.; Egelhaaf, H. J.; Peisert, H.; Chassé, T., Photo-Oxidation and Ozonization of Poly(3-Hexylthiophene) Thin Films as Studied by UV/Vis and Photoelectron Spectroscopy. *Polymer Degradation and Stability* **2010**, *95*, 818-825.

212.   Hintz, H.; Sessler, C.; Peisert, H.; Egelhaaf, H. J.; Chassé, T., Wavelength-Dependent Pathways of Poly-3-Hexylthiophene Photo-Oxidation. *Chemistry of Materials* **2012**, *24*, 2739-2743.

213.   Tournebize, A., et al., Is There a Photostable Conjugated Polymer for Efficient Solar Cells? *Polymer Degradation and Stability* **2015**, *112*, 175-184.

214.   Manceau, M.; Rivaton, A.; Gardette, J.-L.; Guillerez, S.; Lemaître, N., The Mechanism of Photo- and Thermooxidation of Poly(3-Hexylthiophene) (P3HT) Reconsidered. *Polymer Degradation and Stability* **2009**, *94*, 898-907.

215.   Abdou, M. S. A.; Holdcroft, S., Mechanisms of Photodegradation of Poly(3-Alkylthiophenes) in Solution. *Macromolecules* **1993**, *26*, 2954-2962.

216.   Soon, Y. W.; Cho, H.; Low, J.; Bronstein, H.; McCulloch, I.; Durrant, J. R., Correlating Triplet Yield, Singlet Oxygen Generation and Photochemical Stability in Polymer/Fullerene Blend Films. *Chemical Communications* **2013**, *49*, 1291-1293.

217.   Holdcroft, S., A Photochemical Study of Poly(3-Hexylthiophene). *Macromolecules* **1991**, *24*, 4834-4838.

218.   Scurlock, R. D.; Wang, B.; Ogilby, P. R.; Sheats, J. R.; Clough, R. L., Singlet Oxygen as a Reactive Intermediate in the Photodegradation of an Electroluminescent Polymer. *Journal of the American Chemical Society* **1995**, *117*, 10194-10202.

219.   Manceau, M.; Rivaton, A.; Gardette, J.-L., Involvement of Singlet Oxygen in the Solid-State Photochemistry of P3HT. *Macromolecular Rapid Communications* **2008**, *29*, 1823-1827.

220.   Tournebize, A.; Bussière, P.-O.; Rivaton, A.; Gardette, J.-L.; Medlej, H.; Hiorns, R. C.; Dagron-Lartigau, C.; Krebs, F. C.; Norrman, K., New Insights into the Mechanisms of Photodegradation/Stabilization of P3HT:PCBM Active Layers Using Poly(3-Hexyl-D13-Thiophene). *Chemistry of Materials* **2013**, *25*, 4522-4528.

221.   Rivaton, A.; Chambon, S.; Manceau, M.; Gardette, J.-L.; Lemaître, N.; Guillerez, S., Light-Induced Degradation of the Active Layer of Polymer-Based Solar Cells. *Polymer Degradation and Stability* **2010**, *95*, 278-284.

222.   Manceau, M.; Chambon, S.; Rivaton, A.; Gardette, J.-L.; Guillerez, S.; Lemaître, N., Effects of Long-Term UV–Visible Light Irradiation in the Absence of Oxygen on P3HT and P3HT:PCBM Blend. *Solar Energy Materials and Solar Cells* **2010**, *94*, 1572-1577.

223.   Chambon, S.; Rivaton, A.; Gardette, J.-L.; Firon, M., Durability of MDMO-PPV and MDMO-PPV:PCBM Blends under Illumination in the Absence of Oxygen. *Solar Energy Materials and Solar Cells* **2008**, *92*, 785-792.

224.   Mateker, W. R.; Douglas, J. D.; Cabanetos, C.; Sachs-Quintana, I. T.; Bartelt, J. A.; Hoke, E. T.; El Labban, A.; Beaujuge, P. M.; Frechet, J. M. J.; McGehee, M. D., Improving the Long-Term Stability of PBDTTPD Polymer Solar Cells through Material Purification Aimed at Removing Organic Impurities. *Energy & Environmental Science* **2013**, *6*, 2529-2537.

225.   Kong, J., et al., Long-Term Stable Polymer Solar Cells with Significantly Reduced Burn-in Loss. *Nat Commun* **2014**, *5*, 5688-8pp.

226.   Liang, Z.; Nardes, A.; Wang, D.; Berry, J. J.; Gregg, B. A., Defect Engineering in π-Conjugated Polymers. *Chemistry of Materials* **2009**, *21*, 4914-4919.

227.   Liang, Z.; Reese, M. O.; Gregg, B. A., Chemically Treating Poly(3-Hexylthiophene) Defects to Improve Bulk Heterojunction Photovoltaics. *ACS Applied Materials & Interfaces* **2011**, *3*, 2042-2050.

228.   Nielsen, K. T.; Bechgaard, K.; Krebs, F. C., Removal of Palladium Nanoparticles from Polymer Materials†. *Macromolecules* **2005**, *38*, 658-659.

229.   Rivaton, A.; Mailhot, B.; Derderian, G.; Bussiere, P. O.; Gardette, J. L., Investigation of the Photophysical Processes and Photochemical Reactions Involved in PVK Films Irradiated at λ > 300 Nm. *Macromolecules* **2003**, *36*, 5815-5824.

230.   Arnaud, R.; Fanton, E.; Gardette, J.-L., Photochemical Behaviour of Semi-Aromatic Polyamides. *Polymer Degradation and Stability* **1994**, *45*, 361-369.

231.   Himmelberger, S.; Duong, D. T.; Northrup, J. E.; Rivnay, J.; Koch, F. P. V.; Beckingham, B. S.; Stingelin, N.; Segalman, R. A.; Mannsfeld, S. C. B.; Salleo, A., Role of Side-Chain Branching on Thin-Film Structure and Electronic Properties of Polythiophenes. *Advanced Functional Materials* **2015**, *25*, 2616-2624.

232.   Manceau, M.; Helgesen, M.; Krebs, F. C., Thermo-Cleavable Polymers: Materials with Enhanced Photochemical Stability. *Polymer Degradation and Stability* **2010**, *95*, 2666-2669.

233.   Hintz, H.; Egelhaaf, H. J.; Lüer, L.; Hauch, J.; Peisert, H.; Chassé, T., Photodegradation of P3HT–a Systematic Study of Environmental Factors. *Chemistry of Materials* **2010**, *23*, 145-154.

234.   Dupuis, A.; Wong-Wah-Chung, P.; Rivaton, A.; Gardette, J.-L., Influence of the Microstructure on the Photooxidative Degradation of Poly(3-Hexylthiophene). *Polymer Degradation and Stability* **2012**, *97*, 366-374.

235.   Madsen, M. V.; Tromholt, T.; Böttiger, A.; Andreasen, J. W.; Norrman, K.; Krebs, F. C., Influence of Processing and Intrinsic Polymer Parameters on Photochemical Stability of Polythiophene Thin Films. *Polymer Degradation and Stability* **2012**, *97*, 2412-2417.

236.   Tromholt, T.; Madsen, M. V.; Carle, J. E.; Helgesen, M.; Krebs, F. C., Photochemical Stability of Conjugated Polymers, Electron Acceptors and Blends for Polymer Solar Cells Resolved in Terms of Film Thickness and Absorbance. *Journal of Materials Chemistry* **2012**, *22*, 7592-7601.

237.   Distler, A.; Kutka, P.; Sauermann, T.; Egelhaaf, H.-J.; Guldi, D. M.; Di Nuzzo, D.; Meskers, S. C. J.; Janssen, R. A. J., Effect of Pcbm on the Photodegradation Kinetics of Polymers for Organic Photovoltaics. *Chemistry of Materials* **2012**, *24*, 4397-4405.

238.   Distler, A. The Role of Fullerenes in the Photo-Degradation of Organic Solar Cells. Doctoral Thesis, Friedrich-Alexander-Universität Erlangen-Nürnberg (FAU), 2015.

239.   Hamed, A.; Sun, Y. Y.; Tao, Y. K.; Meng, R. L.; Hor, P. H., Effects of Oxygen and Illumination on the in Situ Conductivity of C_{60} Thin Films. *Physical Review B* **1993**, *47*, 10873-10880.

240.   Creegan, K. M.; Robbins, J. L.; Robbins, W. K.; Millar, J. M.; Sherwood, R. D.; Tindall, P. J.; Cox, D. M.; McCauley, J. P.; Jones, D. R., Synthesis and Characterization of C_{60}>O, the First Fullerene Epoxide. *Journal of the American Chemical Society* **1992**, *114*, 1103-1105.

241.   Rao, A. M., et al., Photoinduced Polymerization of Solid C_{60} Films. *Science* **1993**, *259*, 955-957.

242.   Rao, A. M.; Menon, M.; Wang, K.-A.; Eklund, P. C.; Subbaswamy, K. R.; Cornett, D. S.; Duncan, M. A.; Amster, I. J., Photoinduced Polymerization of Solid C_{70} Films. *Chemical Physics Letters* **1994**, *224*, 106-112.

243.   Distler, A.; Sauermann, T.; Egelhaaf, H.-J.; Rodman, S.; Waller, D.; Cheon, K.-S.; Lee, M.; Guldi, D. M., The Effect of PCBM Dimerization on the Performance of Bulk Heterojunction Solar Cells. *Advanced Energy Materials* **2014**, *4*, 1-6.

244.	Dzwilewski, A.; Wågberg, T.; Edman, L., Photo-Induced and Resist-Free Imprint Patterning of Fullerene Materials for Use in Functional Electronics. *Journal of the American Chemical Society* **2009**, *131*, 4006-4011.

245.	Piersimoni, F., et al., Influence of Fullerene Photodimerization on the Pcbm Crystallization in Polymer: Fullerene Bulk Heterojunctions under Thermal Stress. *Journal of Polymer Science Part B: Polymer Physics* **2013**, *51*, 1209-1214.

246.	Li, Z.; Wong, H. C.; Huang, Z.; Zhong, H.; Tan, C. H.; Tsoi, W. C.; Kim, J. S.; Durrant, J. R.; Cabral, J. T., Performance Enhancement of Fullerene-Based Solar Cells by Light Processing. *Nat Commun* **2013**, *4*, 2227-7pp.

247.	Hoke, E. T.; Sachs-Quintana, I. T.; Lloyd, M. T.; Kauvar, I.; Mateker, W. R.; Nardes, A. M.; Peters, C. H.; Kopidakis, N.; McGehee, M. D., The Role of Electron Affinity in Determining Whether Fullerenes Catalyze or Inhibit Photooxidation of Polymers for Solar Cells. *Advanced Energy Materials* **2012**, *2*, 1351-1357.

248.	Chambon, S.; Rivaton, A.; Gardette, J.-L.; Firon, M., Photo- and Thermal Degradation of Mdmo-PPV:PCBM Blends. *Solar Energy Materials and Solar Cells* **2007**, *91*, 394-398.

249.	Yamakoshi, Y.; Umezawa, N.; Ryu, A.; Arakane, K.; Miyata, N.; Goda, Y.; Masumizu, T.; Nagano, T., Active Oxygen Species Generated from Photoexcited Fullerene (C_{60}) as Potential Medicines: $O_2^{-\bullet}$ Versus $^1O_2$. *Journal of the American Chemical Society* **2003**, *125*, 12803-12809.

250.	Di Nuzzo, D.; Aguirre, A.; Shahid, M.; Gevaerts, V. S.; Meskers, S. C. J.; Janssen, R. A. J., Improved Film Morphology Reduces Charge Carrier Recombination into the Triplet Excited State in a Small Bandgap Polymer-Fullerene Photovoltaic Cell. *Advanced Materials* **2010**, *22*, 4321-4324.

251.	Grancini, G., et al., The Critical Role of Interfacial Dynamics in the Stability of Organic Photovoltaic Devices. *Physical Chemistry Chemical Physics* **2014**, *16*, 8294-8300.

252.	Chen, L.; Mizukado, J.; Suzuki, Y.; Kutsuna, S.; Aoyama, Y.; Yoshida, Y.; Suda, H., An Esr Study on Superoxide Radical Anion Generation and Its Involvement in the Photooxidative Degradation of Poly-3-Hexylthiophene in Chlorobenzene Solution. *Chemical Physics Letters* **2014**, *605–606*, 98-102.

253.	Tournebize, A.; Rivaton, A.; Gardette, J.-L.; Lombard, C.; Pépin-Donat, B.; Beaupré, S.; Leclerc, M., How Photoinduced Crosslinking under Operating Conditions Can Reduce PCDTBT-Based Solar Cell Efficiency and Then Stabilize It. *Advanced Energy Materials* **2014**, 1301530-8pp.

254.	Wouters, S.; Demir, F.; Beenaerts, L.; Van Assche, G., Calibration and Performance of a Fast-Scanning Dsc—Project Rhc. *Thermochimica Acta* **2012**, *530*, 64-72.

255.	Wilhelm, C.; Gardette, J.-L., Infrared Identification of Carboxylic Acids Formed in Polymer Photooxidation. *Journal of Applied Polymer Science* **1994**, *51*, 1411-1420.

256.	Oliver, W. C.; Pharr, G. M., An Improved Technique for Determining Hardness and Elastic Modulus Using Load and Displacement Sensing Indentation Experiments. *Journal of Materials Research* **1992**, *7*, 1564-1583.

257.	Hehre, W. J. D., R.; Pople, J. A. , Self-Consistent Molecular Orbital Methods. XII. Further Extensions of Gaussian-Type Basis Sets for Use in Molecular Orbital Studies of Organic Molecules. *J. Chem. Phys.* **1972**, *56*, 2257-2261.

258.	Dill, J. D. P., J. A., Self-Consistent Molecular Orbital Methods. XV. Extended Gaussian-Type Basis Sets for Lithium, Beryllium, and Boron. *J. Chem. Phys.* **1975**, 2921-2923.

259.	Francl, M. M. P., W. J.; Hehre, W. J.; Binkley, J. S.; Gordon, M. S.; DeFrees, D. J.; Pople J. A., Self-Consistent Molecular Orbital Methods. XXIII. A Polarization Type Basis Set for Second-Row Elements. *J. Chem. Phys.* **1982**, 3654-3665.

260.	Becke, A. D., Density-Functional Thermochemistry. III. The Role of Exact Exchange. *J. Chem. Phys.* **1993**, 5648–5652.

261.	Frisch, M. J. *Gaussian 09, Revision D.01*, Gaussian Inc. : Wallingford CT 2009.

262.   Löwdin, P.-O., On the Non-Orthogonality Problem Connected with the Use of Atomic Wave Functions in the Theory of Molecules and Crystals. *J. Chem. Phys.* **1950**, *18*, 365-375.

263.   Löwdin, P.-O., On the Non-Orthogonality Problem. *Adv. Quantum Chem.* **1970**, *5*, 185-199.

264.   Rosch, R., et al., Investigation of the Degradation Mechanisms of a Variety of Organic Photovoltaic Devices by Combination of Imaging Techniques-the ISOS-3 Inter-Laboratory Collaboration. *Energy & Environmental Science* **2012**, *5*, 6521-6540.

265.   Bégué, D.; Elissalde, S.; Pere, E.; Iratcabal, P.; Pouchan, C., New Theoretical and Experimental Infrared Results on Formaldehyde in Solution. *The Journal of Physical Chemistry A* **2006**, *110*, 7793-7800.

266.   Bégué, D.; Qiao, G. G.; Wentrup, C., Nitrile Imines: Matrix Isolation, IR Spectra, Structures, and Rearrangement to Carbodiimides. *Journal of the American Chemical Society* **2012**, *134*, 5339-5350.

267.   Manceau, M.; Gaume, J.; Rivaton, A.; Gardette, J.-L.; Monier, G.; Bideux, L., Further Insights into the Photodegradation of Poly(3-Hexylthiophene) by Means of X-Ray Photoelectron Spectroscopy. *Thin Solid Films* **2010**, *518*, 7113-7118.

268.   Carlsson, D. J.; Brousseau, R.; Zhang, C.; Wiles, D. M., Identification of Products from Polyolefin Oxidation by Derivatization Reactions. In *Chemical Reactions on Polymers*, American Chemical Society: 1988; Vol. 364, pp 376-389.

269.   Lowry, T. H. R., K.S. , *Mechanism and Theory in Organic Chemistry*; Harper & Row, 1987.

270.   McKellar, J. F. A., N. S. , *Photochemistry of Man-Made Polymers*; Elsevier Applied Science Publishers Ltd, London, 1979.

271.   Grassie, N., Scott, G., *Polymer Degradation and Stabilization*; Cambridge University Press: Cambridge, 1985.

272.   Hamid, S. H., Amin, M. B.; Maadhah, A. G., *Handbook of Polymer Degradation*; Marcel Dekker, Inc.: New York, 1992.

273.   Bolland, J. L.; Gee, G., Kinetic Studies in the Chemistry of Rubber and Related Materials. II. The Kinetics of Oxidation of Unconjugated Olefins. *Transactions of the Faraday Society* **1946**, *42*, 236-243.

274.   Audouin, L.; Langlois, V.; Verdu, J.; de Bruijn, J. C. M., Role of Oxygen Diffusion in Polymer Ageing: Kinetic and Mechanical Aspects. *Journal of Materials Science* **1994**, *29*, 569-583.

275.   Mark, J. E. A., H.R., West, R., In *Inorganic Polymers*, Prentice Hall: New Jersey, 1992.

276.   Miller, R. D.; Michl, J., Polysilane High Polymers. *Chemical Reviews* **1989**, *89*, 1359-1410.

277.   Alem, S., et al., Effect of Mixed Solvents on PCDTBT:$PC_{70}BM$ Based Solar Cells. *Organic Electronics* **2011**, *12*, 1788-1793.

278.   Aygül, U.; Egelhaaf, H.-J.; Nagel, P.; Merz, M.; Schuppler, S.; Eichele, K.; Peisert, H.; Chassé, T., Photodegradation of C-PCPDTBT and Si-PCPDTBT: Influence of the Bridging Atom on the Stability of a Low-Band-Gap Polymer for Solar Cell Application. *ChemPhysChem* **2015**, *16*, 428-435.

279.   Pan, H.; Li, Y.; Wu, Y.; Liu, P.; Ong, B. S.; Zhu, S.; Xu, G., Low-Temperature, Solution-Processed, High-Mobility Polymer Semiconductors for Thin-Film Transistors. *Journal of the American Chemical Society* **2007**, *129*, 4112-4113.

280.   Walker, B.; Tamayo, A. B.; Dang, X.-D.; Zalar, P.; Seo, J. H.; Garcia, A.; Tantiwiwat, M.; Nguyen, T.-Q., Nanoscale Phase Separation and High Photovoltaic Efficiency in Solution-Processed, Small-Molecule Bulk Heterojunction Solar Cells. *Advanced Functional Materials* **2009**, *19*, 3063-3069.

281.   Liu, Y.; Zhao, J.; Li, Z.; Mu, C.; Ma, W.; Hu, H.; Jiang, K.; Lin, H.; Ade, H.; Yan, H., Aggregation and Morphology Control Enables Multiple Cases of High-Efficiency Polymer Solar Cells. *Nat Commun* **2014**, *5*, 5293-8pp.

282.   Zhao, Y.; Yuan, G.; Roche, P.; Leclerc, M., A Calorimetric Study of the Phase Transitions in Poly(3-Hexylthiophene). *Polymer* **1995**, *36*, 2211-2214.

283.   Silva, H. S.; Tournebize, A.; Begue, D.; Peisert, H.; Chasse, T.; Gardette, J. L.; Therias, S.; Rivaton, A.; Hiorns, R. C., A Universal Route to Improving Conjugated Macromolecule Photostability. *RSC Advances* **2014**, *4*, 54919-54923.

284.   Morse, G. E.; Tournebize, A.; Rivaton, A.; Chasse, T.; Taviot-Gueho, C.; Blouin, N.; Lozman, O. R.; Tierney, S., The Effect of Polymer Solubilizing Side-Chains on Solar Cell Stability. *Physical Chemistry Chemical Physics* **2015**, *17*, 11884-11897.

285.   Tournebize, A. M., Graham E; Fraga Domínguez, Isabel; Peisert, Heiko; Chassé, Thomas; Rivaton, Agnès, Photostability of Low Band Gap Polymers, Is There a Rule of Thumb? *Unpublished results*.

286.   Kesters, J.; Verstappen, P.; Raymakers, J.; Vanormelingen, W.; Drijkoningen, J.; D'Haen, J.; Manca, J.; Lutsen, L.; Vanderzande, D.; Maes, W., Enhanced Organic Solar Cell Stability by Polymer (PCPDTBT) Side Chain Functionalization. *Chemistry of Materials* **2015**, *27*, 1332-1341.

287.   Yan, H.; Zhu, L.; Li, X.; Kwok, A.; Li, X.; Agren, H.; Zhao, Y., Photothermal-Responsive [2]Rotaxanes. *RSC Advances* **2013**, *3*, 2341-2350.

288.   Peet, J.; Wen, L.; Byrne, P.; Rodman, S.; Forberich, K.; Shao, Y.; Drolet, N.; Gaudiana, R.; Dennler, G.; Waller, D., Bulk Heterojunction Solar Cells with Thick Active Layers and High Fill Factors Enabled by a Bithiophene-Co-Thiazolothiazole Push-Pull Copolymer. *Applied Physics Letters* **2011**, *98*, 043301-3pp.

289.   Guo, J.; Ohkita, H.; Benten, H.; Ito, S., Charge Generation and Recombination Dynamics in Poly(3-Hexylthiophene)/Fullerene Blend Films with Different Regioregularities and Morphologies. *Journal of the American Chemical Society* **2010**, *132*, 6154-6164.

290.   Karuthedath, S.; Sauermann, T.; Egelhaaf, H.-J.; Wannemacher, R.; Brabec, C. J.; Luer, L., The Effect of Oxygen Induced Degradation on Charge Carrier Dynamics in P3HT:PCBM and Si-PCPDTBT:PCBM Thin Films and Solar Cells. *Journal of Materials Chemistry A* **2015**, *3*, 3399-3408.

291.   Cox, D. M.; Behal, S.; Disko, M.; Gorun, S. M.; Greaney, M.; Hsu, C. S.; Kollin, E. B.; Millar, J.; Robbins, J., Characterization of C_{60} and C_{70} Clusters. *Journal of the American Chemical Society* **1991**, *113*, 2940-2944.

292.   Hegelund, F.; Larsen, R. W.; Palmer, M. H., The Vibrational Spectrum of Thiazole between 600 and 1400 cm^{-1} Revisited: A Combined High-Resolution Infrared and Theoretical Study. *Journal of Molecular Spectroscopy* **2007**, *244*, 63-78.

293.   Lin-Vien, D. C., Norman B.; Fateley, William G.; Grasselli, Jeanette G. , *The Handbook of Infrared and Raman Characteristic Frequencies of Organic Molecules* Academic Press: San Diego, 1991.

294.   Zerbi, G. G., Germana; Del Fanti, N.; Baini, L. , Structural Depth Profiling in Polyethylene Films by Multiple Internal Reflection Infra-Red Spectroscopy. *Polymer* **1989**, *30*, 23424-2327.

295.   Chambon, S. Etude Du Vieillissement De Cellules Solaires Photovoltaïques Plastiques. Doctoral Thesis, Université Blaise Pascal - Clermont-Ferrand II, 2006.

296.   Kam, Z.; Wang, X.; Zhang, J.; Wu, J., Elimination of Burn-in Open-Circuit Voltage Degradation by ZnO Surface Modification in Organic Solar Cells. *ACS Applied Materials & Interfaces* **2015**, *7*, 1608-1615.

297.   MacLeod, B. A., et al., Stability of Inverted Organic Solar Cells with ZnO Contact Layers Deposited from Precursor Solutions. *Energy & Environmental Science* **2015**, *8*, 592-601.

298.   Krebs, F. C., *Stability and Degradation of Organic and Polymer Solar Cells* 1st Ed.; John Wiley and Sons: Chichester, 2012.

299.   Perrier, S.; Takolpuckdee, P., Macromolecular Design Via Reversible Addition-Fragmentation Chain Transfer (RAFT)/Xanthates (MADIX) Polymerization. *J Polym Sci Pol Chem* **2005**, *43*, 5347-5393.

300.   Gregori, A. Synthesis of Conjugated Polymers and Adhesive Properties of Thin Layers in OPV Devices. Doctoral Thesis, Université de Pau et des Pays de l'Adour, 2015.
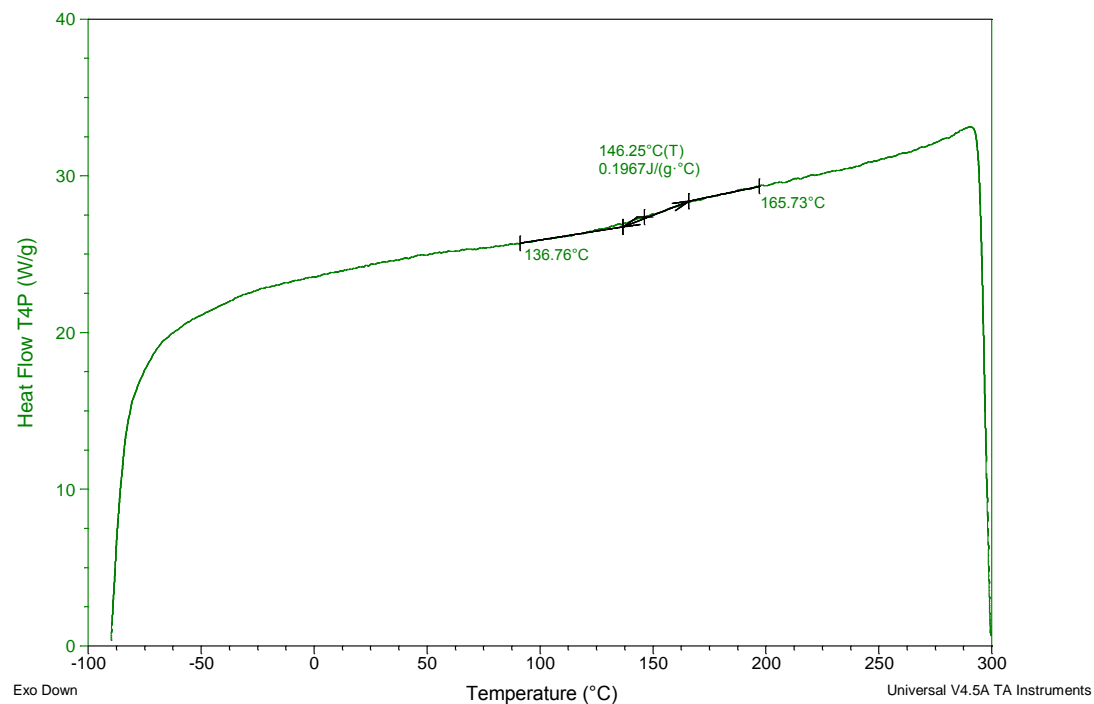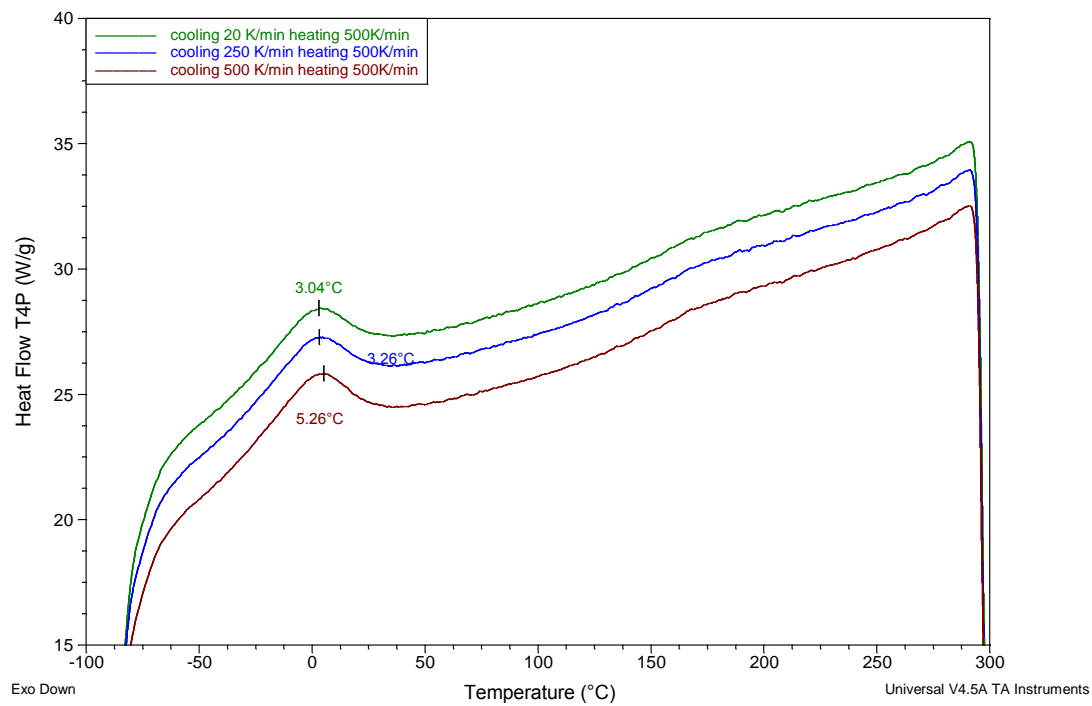
Annex

Rapid Heat-Cool Calorimetry

Rapid Heat-Cool Calorimetry (RHC) analysis were carried out by Maxime Defour, PhD student at the Vrije Universiteit Brussel. The measurements were performed on a TA Instruments Rapid Heat-Cool Differential Scanning Calorimeter (RHC) using a liquid nitrogen cooling system and purged with neon (12 mL min^{-1}). The RHC cell is heated by four quartz halogen lamps with an almost instantaneous response. More details on the procedure can be found in the literature.[254]

The results obtained are summarised in Table 3.7 in page 169. These results were extracted for the different polymers from the following thermograms.
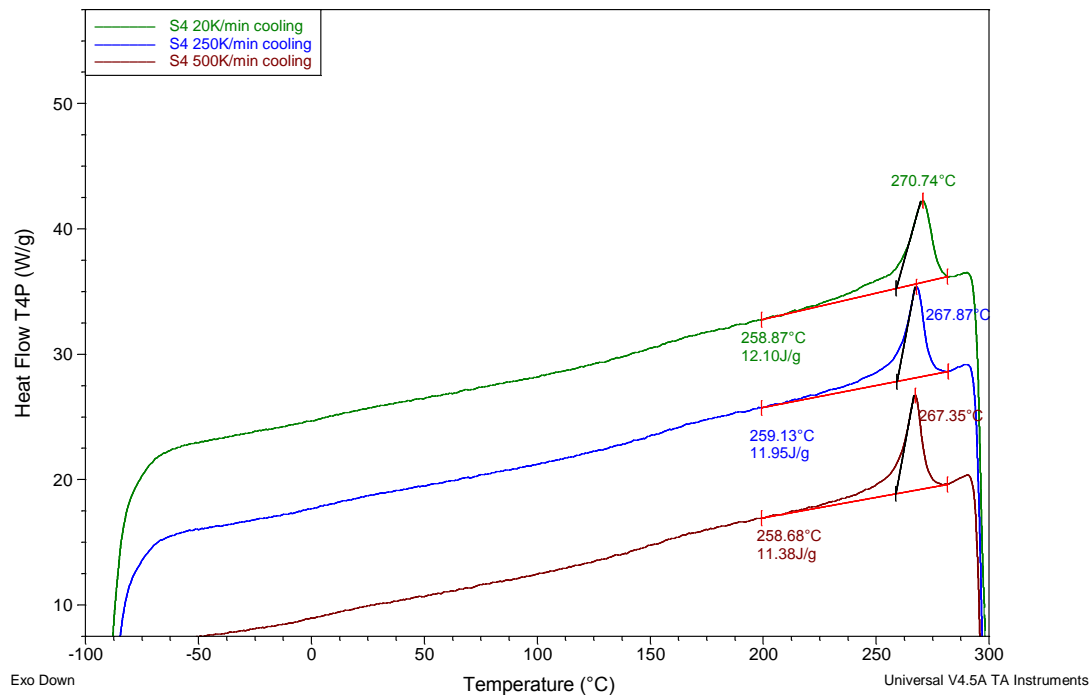
P1

P2

P3
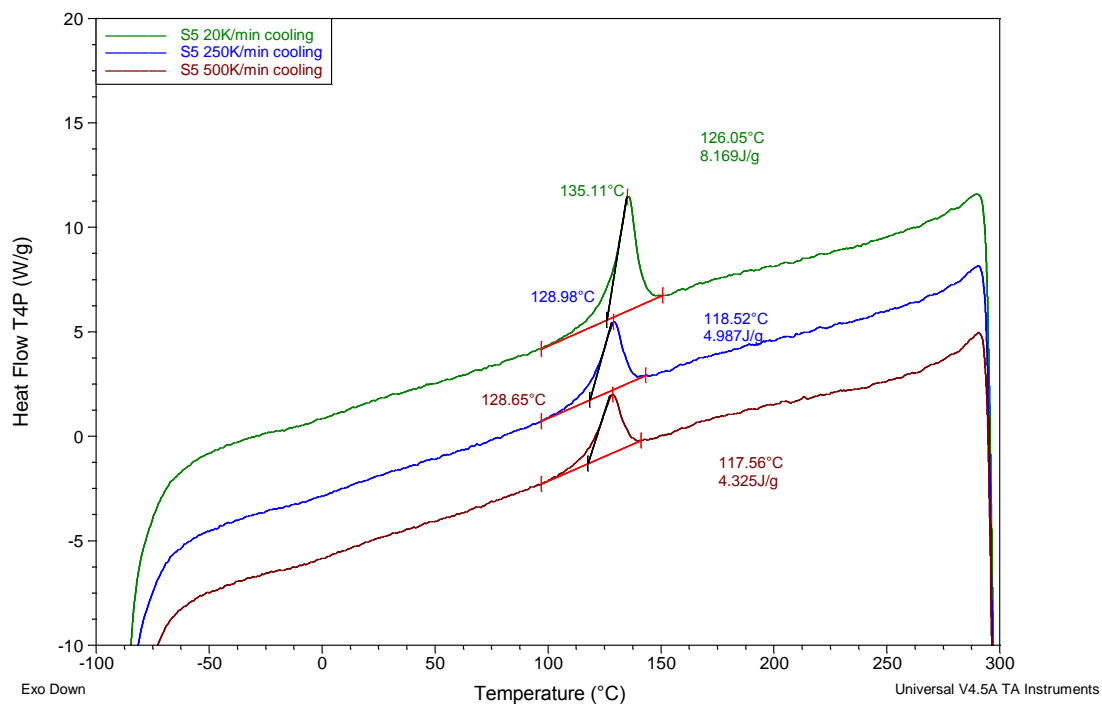
P4
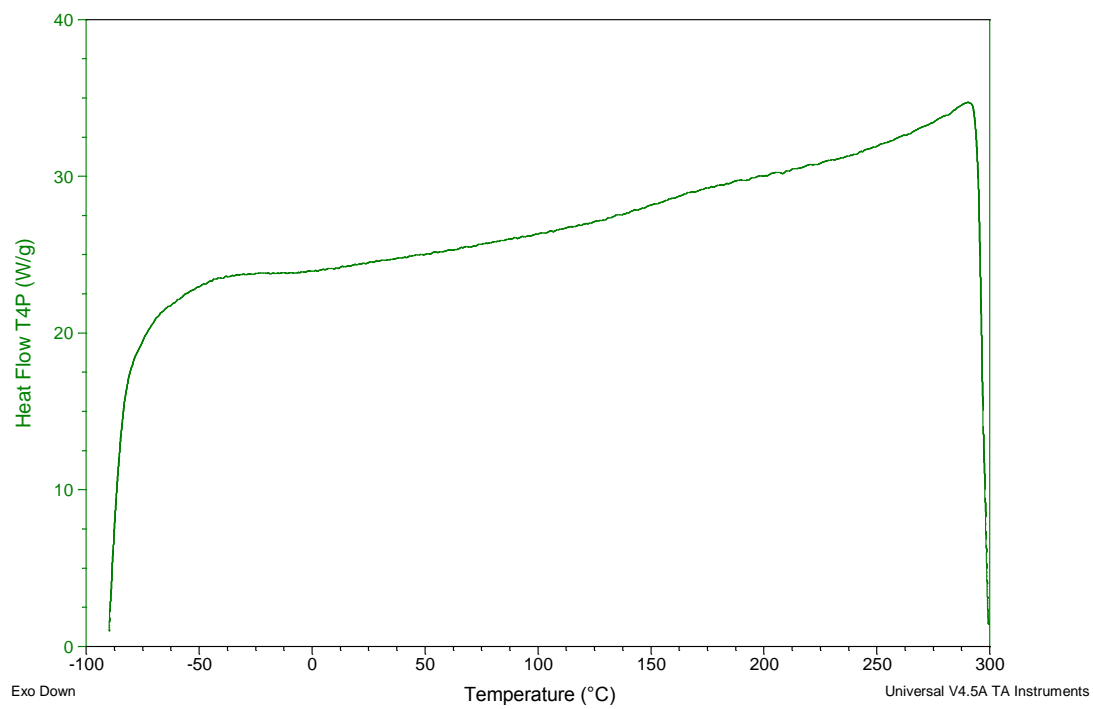
P5a

P5b

P5c

P3HT

Si-PCPDTBT

C-PCPDTBT

Exo Down   Temperature (°C)   Universal V4.5A TA Instruments